Synthesis, Characterization, and Reactivity of Transition Metal Complexes Stabilized by Naphthalene and Naphthyl-substituted *N*-heterocyclic Carbenes

Dissertation

zur Erlangung des Doktorgrades der Naturwissenschaften (Dr. rer. nat.)
an der Fakultät für Chemie und Pharmazie der Universität Regensburg

vorgelegt von
Dirk Herrmann
aus Burghausen

Regensburg 2018

Der experimentelle Teil der vorliegenden Arbeit wurde in der Zeit zwischen November 2012 und Oktober 2016 unter Anleitung von Prof. Dr. Robert Wolf am Institut für Anorganische Chemie der Universität Regensburg angefertigt.

Die Arbeit wurde angeleitet von: Prof. Dr. Robert Wolf

Promotionsgesuch eingereicht am: 29.06.2018

Tag der mündlichen Prüfung: 30.08.2018

Prüfungsausschuss:	Vorsitzender:	Prof. Dr. Rainer Müller
	Erstgutachter:	Prof. Dr. Robert Wolf
	Zweitgutachter:	Prof. Dr. Manfred Scheer
	Dritter Prüfer:	Prof. Dr. Frank-Michael Matysik

Abstract

This thesis reports on the synthesis and characterization of transition metal complexes with naphthalene, 1,5-cyclooctadiene, and naphthyl-substituted N-heterocyclic carbene ligands. The first part (chapter 3) deals with the preparation of low-valent ruthenium complexes stabilized by naphthalene and 1,5-cyclooctadiene. The structure and reactivity of these compounds is discussed, and the symmetric diruthenium complex **2** is analyzed in depth in terms of its electronic structure and redox properties.

The second part of the thesis (chapters 4-6) is concerned with *N*-heterocyclic carbene ligands featuring naphthyl substituents, which were employed with the aim of generating hemilabile chelate complexes. Chapter 4 discusses the preparation of NHC precursor materials and NHC-silver complexes which were subsequently used as carbene transfer agents. Chapter 5 reports on the preparation and characterization of NHC complexes of gold, rhodium, and ruthenium complexes as well as catalytic experiments using rhodium and ruthenium complexes as catalysts. Chapter 6 deals with NHC complexes of iron and cobalt, prepared from strongly basic starting materials, and their structural, spectroscopic, and electrochemical characterization. Furthermore, the magnetic properties of the cobalt complexes and catalytic reactions with the iron complexes are discussed, as are chemical reduction experiments.

Zusammenfassung

Die vorliegende Arbeit beschäftigt sich mit der Synthese und Charakterisierung von Übergangsmetallkomplexen mit Naphthalin-, 1,5-Cyclooctadien- und naphthylsubstituierten *N*-heterocyclischen Carbenliganden. Der erste Teil der Arbeit (Kapitel 3) behandelt die Darstellung und Charakterisierung niedervalenter Rutheniumkomplexe, die durch Naphthalin bzw. 1,5-Cyclooctadien stabilisiert sind. Die elektronische Struktur und die Redoxeigenschaften des symmetrischen Dirutheniumkomplexes **2** werden diskutiert.

Der zweite Teil der Arbeit beschäftigt sich mit naphthylsubstituierten *N*-heterocyclischen Carbenliganden, die mit dem Ziel eingesetzt wurden, halblabile Chelatkomplexe zu erzeugen. Kapitel 4 beschreibt die Herstellung von NHC-Vorläuferverbindungen und von NHC-Silberkomplexen, die nachfolgend als Carbentransfer-Reagenzien eingesetzt wurden. Kapitel 5 beschreibt die Synthese und Charakterisierung von Gold-, Rhodium- und Ruthenium-komplexen sowie katalytische Testreaktionen mit Rhodium- und Rutheniumkomplexen. Kapitel 6 behandelt die Darstellung von Eisen- und Cobaltkomplexen aus basischen Ausgangs-verbindungen sowie ihre strukturelle, spektroskopische und elektrochemische Charakterisierung. Daneben werden die magnetischen Eigenschaften der Cobaltkomplexe und Katalyseversuche mit den Eisenkomplexen sowie Reduktionsversuche diskutiert.

Table of Contents

1. Introduction

1.1 Polyaromatic Hydrocarbon Ligands in Organometallic Chemistry

Polyaromatic hydrocarbons constitute a highly useful class of ligands in synthetic organometallic chemistry. Their unique properties include a strong π-acceptor character and thus an affinity for electron-rich metal centers, as well as a distinct lability with respect to displacement by other ligands. Due to these features, which can be rationalized in terms of the electronic structure, the use of polyarenes enables the synthesis of reactive transition metal complexes that can serve as organometallic building blocks for a wide range of compounds and materials.

While monocyclic arenes such as benzene prefer a symmetric η^6-coordination to metal centers, polycyclic arenes like naphthalene or anthracene show a degree of flexibility in their coordination which include η^6-, η^4-, and η^2-modes. The η^4-mode is particularly interesting since the arene ligand undergoes a significant deformation. Parkin and co-workers studied this phenomenon in detail.[1] Analyzing the bond dissociation energies of a series of $[(Ar)Mo(PR_3)]$ and $[(Ar)Mo(PR_3)(H)_2]$ complexes (Ar = benzene, naphthalene, and anthracene), they concluded that the energy required to fold the arene along the C1–C4 axis is compensated by the increase in bond dissociation energy for naphthalene and anthracene, whereas benzene remains in a coplanar conformation and assumes η^6-coordination.

Parkin further investigated the cause of this preference for an η^4-mode in fused polyarenes. A comparison the shapes of the HOMOs of benzene, naphthalene, and anthracene showed that the overlap with metal centered d-orbitals was increased when the fused polyarenes slipped towards an η^4-coordination (Figure 1.1). The interaction of the occupied d_{xz}-orbital with the arene LUMO is increased when the arene "slips" to an η^4-coordination. Folding along the C1–C4 axis minimizes the antibonding interaction, thereby further reducing the energy of the orbital resulting from this interaction (Figure 1.2).[1] This strong back-bonding explains the π-acceptor character of polyarene ligands which enables the synthesis of complexes with transition metals in low oxidation states.

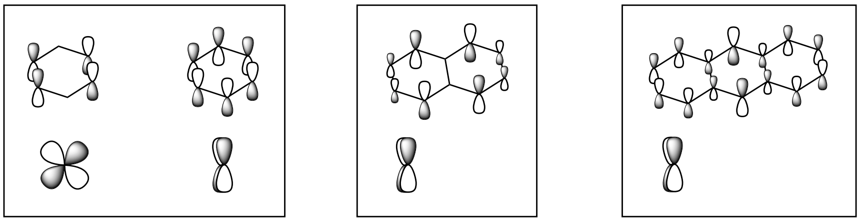

Figure 1.1. Interaction of metal-centered d-orbitals with HOMOs of benzene (left), naphthalene (center), and anthracene (right).

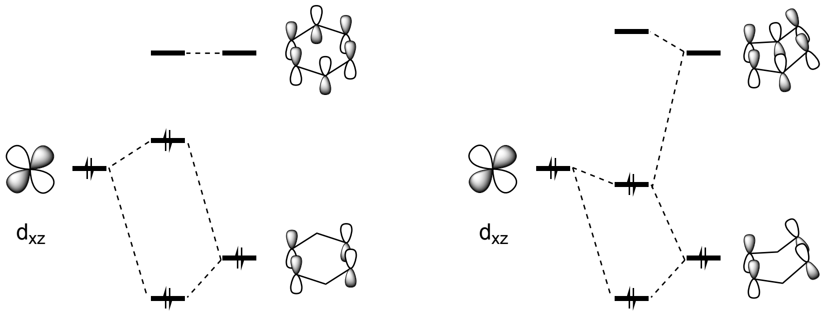

Figure 1.2. Interaction of the d_{xz}-orbital with the HOMO and LUMO of η^6-benzene (left) and η^4-benzene (right). Slipping and folding of the arene ligand increases the overlap of the d_{xz}-orbital with the arene LUMO and and reduces the antibonding interaction.[1]

While M–(η^4-polyarene) interactions are strong, the addition of other ligands can cause the displacement of the polyarene even at mild conditions. Upon dissociation from the metal center, the folding energy is released as the polyarene assumes a planar conformation. This facile ligand exchange makes polyarene complexes powerful synthetic building blocks.

Metalates such as tris(naphthalene)titanate(2–) (**I**) and bis(anthracene)-cobaltate(1–) (**II**) are prominent examples of the utility of polyarene ligands. **I** and **II** serve as synthetic equivalents of "naked" metal anions, as demonstrated by the synthesis of the first carbon-free sandwich complex [Ti(P_5)$_2$] by the group of Ellis (Scheme 1.1, top) and the cyclodimerization of phosphaalkynes in the coordination sphere of Co(–I) generated from **II** by Wolf and co-workers (Scheme 1.1, bottom).[2,3]

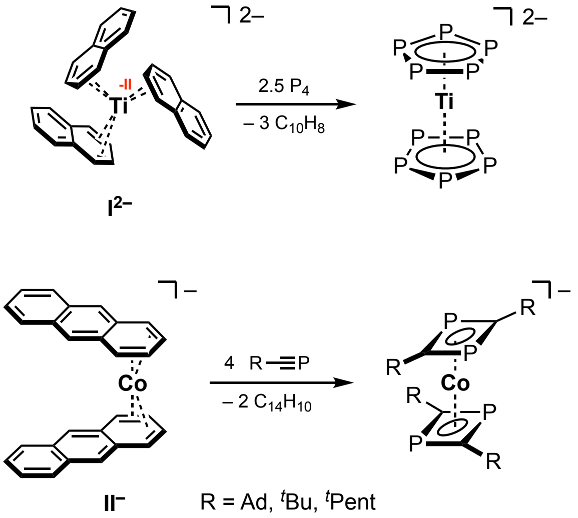

Scheme 1.1. Formation of a carbon-free sandwich complex by reaction of **I** with white phosphorus (top); cyclodimerization of phosphaalkynes via reaction with **II** (bottom).

1.2 *N*-heterocyclic Carbenes

In comparison to the labile π-acceptor ligands described in section 1.1, *N*-heterocyclic carbenes (NHCs) display a starkly contrasting coordination chemistry. Their electronic properties (*vide infra*) makes them strong σ-donors with little to no π-acceptor character.

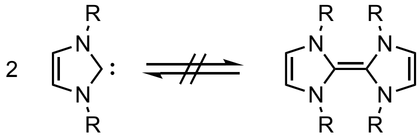

Scheme 1.2. Wanzlick's postulated equilibrium between a free NHC and its dimer.

First reports by Wanzlick on the stability of NHCs were greeted with scepticism, as was his proposal of an equilibrium between the carbene and its dimer (Scheme 1.2).[4] Even though some examples of transition metal complexes featuring NHC ligands were reported, it was not until 1991, when Arduengo and co-workers managed to isolate 1,3-diadamantylimidazolin-2-ylidene (IAd),[5] that NHCs became popular tools in synthetic organometallic chemistry. The high stability of the carbene–metal bond and the ease with which the steric and electronic properties of the NHC can be modified have led to an upsurge in research activity, and a vast array of transition metal NHC complexes have since been reported.

The factors determining the favorable ligand properties of *N*-heterocyclic carbenes are evident from the molecular orbital scheme of a $C(NR_2)_2$ fragment (Figure 1.3).[6] The vacant p_π-orbital of the singlet carbene carbon atom interacts with the lone pairs of the adjacent nitrogen atoms, leading to an increase in energy of the LUMO while the HOMO is not influenced. The large HOMO-LUMO gap stabilizes the singlet ground state of the carbene. In addition to the stabilization by conjugation (+M effect), electronegative nitrogen atoms decrease the energy of the HOMO (–I effect), which further stabilizes the singlet state. The low-lying HOMO is responsible for the nucleophilicity and strong σ-donor character, while the high-lying LUMO is the reason for the weak π-acceptor character.

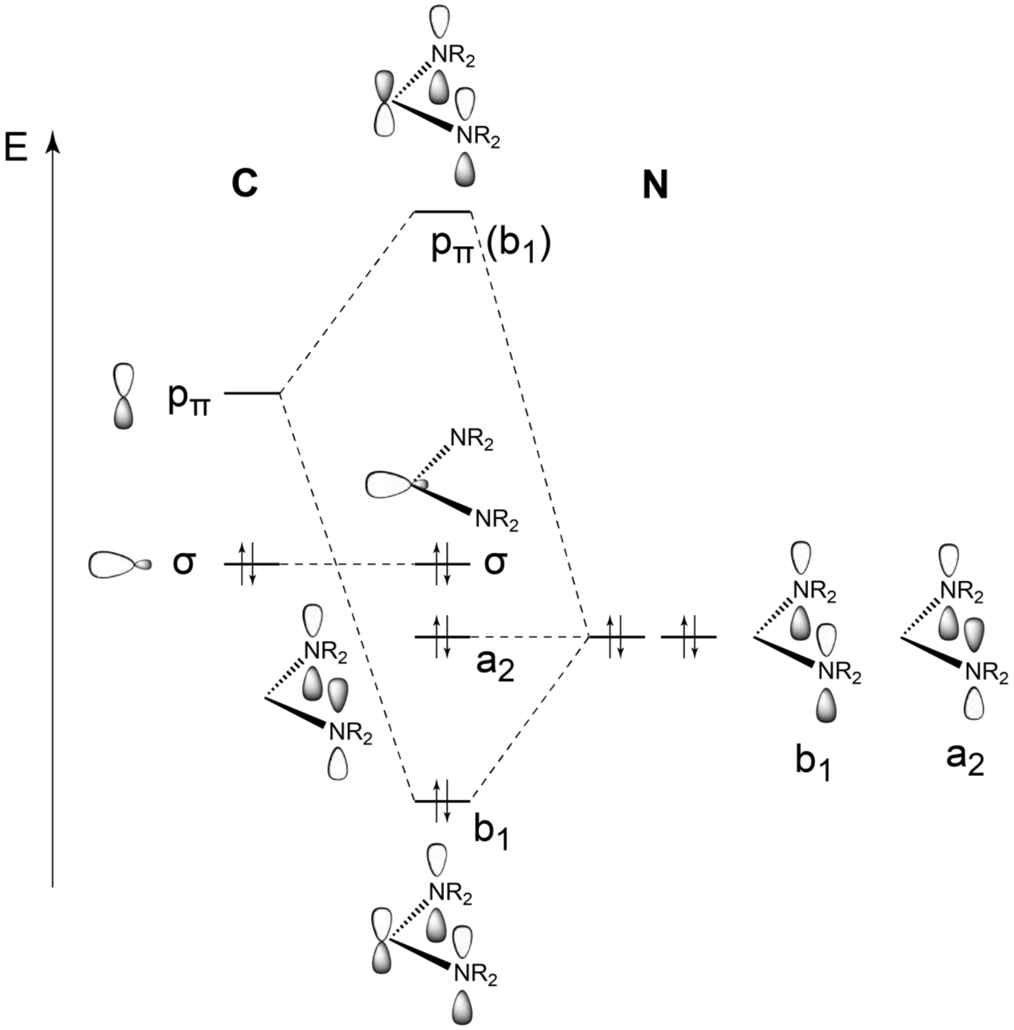

Figure 1.3. MO scheme of $C(NR_2)_2$.

What makes *N*-heterocyclic carbenes particularly attractive is the high degree of variability that makes it possible to adjust the steric and electronic properties as required. Three parameters can be modified: The number and nature of the heteroatoms adjacent to the carbene center, the substituents R attached to these heteroatoms, and the backbone.

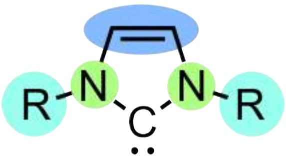

Figure 1.4. Parameters to modify the steric and electronic properties of an NHC: heteroatoms (green), substituents (turquoise), and backbone (blue).

In order to quantify and compare the donor properties of NHCs, several metrics have been developed using methods such as IR spectroscopy, NMR spectroscopy, and electrochemistry.[7] The most frequently used one is the *Tolman Electronic Parameter* (TEP), which was originally introduced to compare the donor ability of phosphane ligands. The TEP is the CO stretching frequency ν_{CO} of $[Ni(CO)_3(NHC)]$, which is dependent on the electron density on the Ni atom and, consequently, the donor strength of the NHC. [(NHC)IrCl(CO)$_2$] and [(NHC)RhCl(CO)$_2$] complexes can be used in cases where the nickel complex is not accessible. The *Huynh Electronic Parameter* (HEP) is obtained via ^{13}C NMR spectroscopy of [PdBr$_2$(B*i*Pr)(NHC)] complexes.[8] The ^{13}C chemical shift of the carbene carbon of the B*i*Pr ligand is influenced by the *trans* ligand, and thus serves as a measure for NHCs as well as a variety of other ligands. The *Lever Electronic Parameter* (LEP) relies on the electrochemical oxidation of complexes such as [Ru(bpy)$_2$(NHC)$_2$].[7] The redox potential depends on the electron density at the metal center, which, in turn, is influenced by the NHC ligand. Besides these methods, computational studies compared different carbene ligands, and the influence of parameters such as the number of heteroatoms, the backbone, and the substituents were analyzed in detail.[7]

The heteroatoms influence the carbene center through mesomeric and inductive effects (*vide supra*). Therefore the electronic properties of the carbene are strongly dependent on the number of heteroatoms present. While in the vast majority of NHCs found in the literature, the carbene is surrounded by two nitrogen atoms (Figure 1.5, b), the cyclic alkyl amino carbenes (cAACs) developed by Bertrand et. al. feature a carbene center with an adjacent carbon and a nitrogen (Figure 1.5, a) and are stronger σ-donors; carbenes with a triazole core (Figure 1.5, c) feature three nitrogen atoms and are weaker σ donors. Replacing one nitrogen of an imidazole-based NHC by a sulfur atom (Figure 1.5, d) results in a more weakly donating thiazolin-2-ylidene.

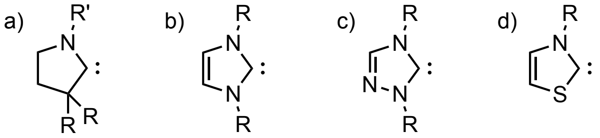

Figure 1.5. a) Cyclic alkyl amino carbene (cAAC), b) imidazolin-2-ylidene, c) triazolin-2-ylidene, d) thiazolin-2-ylidene.

After Arduengo's discovery of IAd, it was assumed that the aromatic five-membered ring is responsible for the stability of the carbene. While aromaticity may contribute to the stability, the successful synthesis of NHCs with a saturated backbone proved that the presence of an aromatic system is not necessary. In comparison to imidazolin-2-ylidenes with an unsaturated backbone, saturated imidazolidin-2-ylidenes are stronger σ-donors due to the +I effect of the alkyl backbone as opposed to the –I effect of an unsaturated backbone. The introduction of substituents to the backbone of the NHC core allows fine-tuning of the donor strength. Carbenes with a polycyclic aromatic core, such as benzimidazolin-2-ylidenes (Figure 1.6, a), are weaker donors than imidazolin-2-ylidenes. Substituents on the backbone can have an important steric influence as well: chiral backbones (Figure 1.6, b and c) are a widely used tool in asymmetric catalysis.[9]

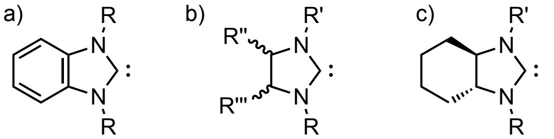

Figure 1.6. a) benzimidazolin-2-ylidene, b) imidazolidin-2-ylidene with chiral backbone, and c) (*R*,*R*)-tetrahydrobenzimidazolin-2-ylidene.

The substituents on the nitrogen atoms provide a versatile handle to influence the properties of an NHC. Introducing electron-withdrawing groups can decrease the donor strength of the carbene, while electron-donating substituents can increase it. Besides the electronic properties, the steric bulk of the substituents can substantially influence the reactivity of a carbene or an NHC metal complex. Very bulky substituents can stabilize low-coordinate metal centers and lead to increased catalytic activity in hydrogenation and cross-coupling reactions.[10]

Apart from adjusting the sterics of the NHC, modifying the *N*-substituents makes it possible to introduce additional functional groups such as alcohols, amines, imines, carboxylic esters, and many others.[11] These functionalized NHCs can act as chelating ligands, and metal complexes of imine-substituted NHCs have become popular in catalysis.[12] Ligands with both strong and weak binding sites (often referred to as "hemilabile" ligands) are useful tools in catalysis. In the presence of a suitable substrate, the weak ligand–metal bond is cleaved, opening a coordination site on the catalytically active center; in the absence of substrate, the weakly binding end of the ligand is reattached to the metal center, thus stabilizing the resting state of the catalyst.[13]

1.3 *N*-heterocyclic Carbenes with Labile Chelating Groups

While large numbers of chelating NHC ligands are known, particularly imino- and pyridyl-NHCs,[11] there are relatively few examples of NHCs with substitutionally labile substituents such as alkenes or polyarenes. Lai, Li, and co-workers successfully used the allyl-NHC rhodium complex **III** (Figure 1.7, left) in catalytic hydrogenations and hydrosilylations.[14] The related iridium complexes **IV** and **V** (Figure 1.7, center and right), reported by Hahn, Oro, and co-workers and Mata and co-workers, were used in transfer hydrogenation of ketones and hydrosilylation of alkenes.[15] Albrecht and co-workers used the allyl-NHC ruthenium complex

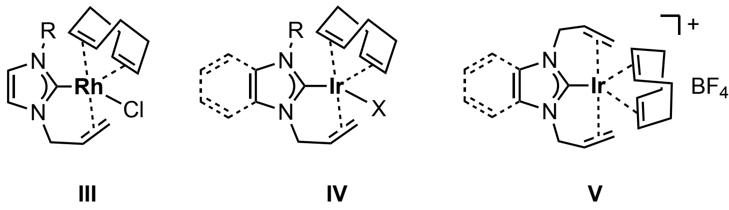

Figure 1.7. Chelating allyl-NHC complexes of rhodium and iridium.[14,15]

VI (Figure 1.8, left) for the transfer hydrogenation of alkenes using alcohols as the hydrogen source.[16] The groups of Çetinkaya, Dixneuf, and Özdemir reported ruthenium complexes with η^1:η^6-chelating NHCs carrying sterically encumbered aryl groups, such as **VII** (Figure 1.8, right), which were used in the transfer hydrogenation of ketones.[17]

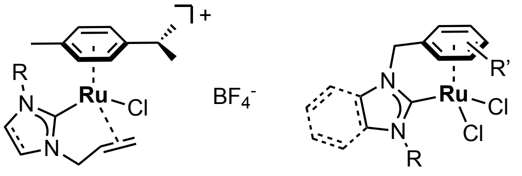

VI **VII**

Figure 1.8. Chelating NHC-ruthenium complexes **VI** and **VII**.[16,17]

There are some reports of NHCs featuring polyarene substituents. Kündig and co-workers, for example, reported palladium complex **VIII** (Figure 1.9, left) and gold complex **IX** (Figure 1.9, center) of the chiral carbene ligand [(*S*,*S*)INpC(*t*Bu)], which were used as catalysts in asymmetric C–C coupling reactions.[18] Dorta and co-workers synthesized a series of α-naphthyl-substituted NHC ligands and corresponding palladium complexes **X** (Figure 1.9, right), which were used as catalysts in C–C and C–N coupling reactions.[19]

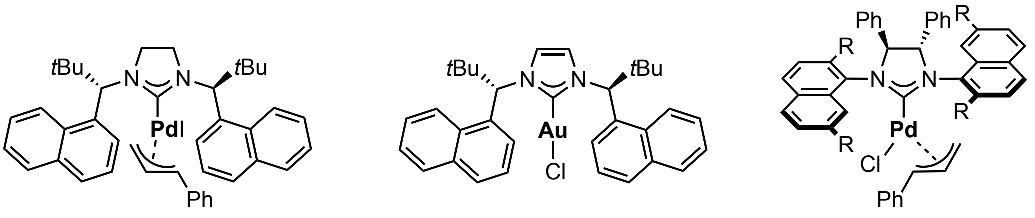

VIII **IX** **X**

Figure 1.9. NHC complexes **VII**-**X** featuring naphthyl stereodirecting groups.[18,19]

Larger polyarenes, such as anthracene or pyrene, were used as fluorescent tags on NHC complexes such as **XI** (Figure 1.10, far left) reported by Liu, Zhang, and co-workers, and **XII** (Figure 1.10, center-left) reported by Cresteil, Roland, and co-workers.[20] The latter used fluorescence microscopy to localize cytotoxic complex **XII** in cancer cells.

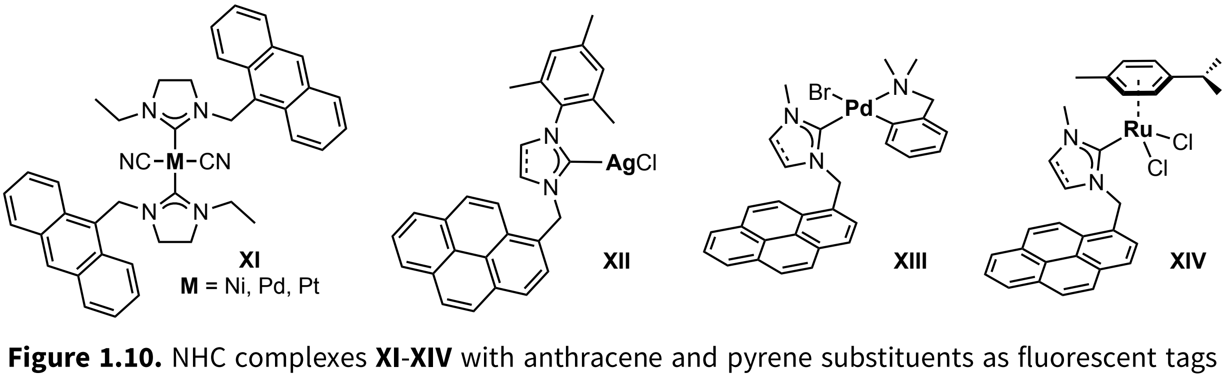

XI
M = Ni, Pd, Pt
XII **XIII** **XIV**

Figure 1.10. NHC complexes **XI**-**XIV** with anthracene and pyrene substituents as fluorescent tags and for immobilization on graphene surfaces.

Pyrene substituents have also found use in immobilizing NHC complexes on graphene surfaces via noncovalent interactions. The groups of Mata and Peris reported that palladium complex **XIII** (Figure 1.10, center-right) and ruthenium complex **XIV** (Figure 1.10, far right) showed improved catalytic properties and recyclability when immobilized on graphene.[21]

These examples illustrate that the steric and electronic properties of polyarenes have found use in NHC chemistry. However, only very few compounds are known in which the polyarene substituents actually function as coordinating groups.

Ruthenium complex **XV** (Figure 1.11, left) is a prominent and inspiring example of this type of NHC–polyarene chelation. An extensive collaborative study of the groups of Glorius and Wolf was concerned with ruthenium-based hydrogenation catalysts, and **XV** emerged as an extremely powerful catalyst for the asymmetric hydrogenation of a wide range of (hetero-) arenes.[22] Single-crystal X-ray crystallography revealed the unique and remarkable molecular structure of **XV**. The ruthenium center is ligated by two NHCs, one of which is deprotonated at a methyl group and a naphthyl moiety, forming two Ru–C bonds. The second NHC ligand shows no C–H activation, but one of the naphthyl groups coordinates to the Ru center in the η^4-mode typical for polyarenes. As η^4-coordinating polyarenes are easily displaced by other ligands, this bonding situation contributes to the high catalytic activity of **XV**. A mechanistic study by Glorius and Wolf revealed that, under H_2 pressure, the Ru–C bonds are cleaved and the polyarene substituents are partially hydrogenated, thus freeing up the coordination sphere of the Ru center for H_2 and substrate molecules.

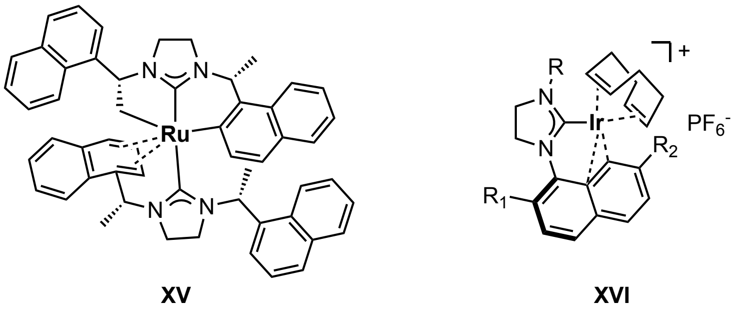

Figure 1.11. Naphthyl-NHC complexes **XV** and **XVI** showing polyarene chelation.

More recently, the group of Dorta presented another example of a highly active catalyst exhibiting NHC–polyarene chelation.[23] Iridium complex **XVI** (Figure 1.11, right) was formed by removing a chloride ligand from [(cod)IrCl(NHC)] using a silver salt containing a weakly coordinating anion. **XVI** exhibits η^2-coordination of one of the α-naphthyl substituents and was found to catalyze intramolecular hydroamination reactions.

The unique molecular structures of **XV** and **XVI** as well as their catalytic activity demonstrate the great potential of combining the strong bonding exhibited by NHCs with the lability of polyarenes. Hemilabile chelating ligands made up of NHCs and polyarenes hold great promise for the development of new, highly active transition metal catalysts.

1.4 References

[1] G. Zhu, K. E. Janak, J. S. Figueroa, G. Parkin, *J. Am. Chem. Soc.* **2006**, *128*, 5452-5461.

[2] a) M. Jang, J. E. Ellis, *Angew. Chem.* **1994**, *106*, 2036-2038; b) R. E. Jilek, M. Jang, E. D. Smolensky, J. D. Britton, J. E. Ellis, *Angew. Chem. Int. Ed.* **2008**, *47*, 8692-8695; c) E. Urnezius, W. W. Brennessel, C. J. Cramer, J. E. Ellis, P. v. R. Schleyer, *Science* **2002**, *295*, 832-834.

[3] a) R. Wolf, A. W. Ehlers, J. C. Slootweg, M. Lutz, D. Gudat, M. Hunger, A. L. Spek, K. Lammertsma, *Angew. Chem. Int. Ed.* **2008**, *47*, 4584-4587; b) R. Wolf, A. W. Ehlers, M. M. Khusniyarov, F. Hartl, B. de Bruin, G. J. Long, F. Grandjean, F. M. Schappacher, R. Pöttgen, J. C. Slootweg, M. Lutz, A. L. Spek, K. Lammertsma, *Chem. Eur. J.* **2010**, *16*, 14322-14334; c) J. Malberg, T. Wiegand, H. Eckert, M. Bodensteiner, R. Wolf, *Chem. Eur. J.* **2013**, *19*, 2356-2369; d) J. Malberg, T. Wiegand, H. Eckert, M. Bodensteiner, R. Wolf, *Eur. J. Inorg. Chem.* **2014**, 1638-1651; e) J. Malberg, M. Bodensteiner, D. Paul, T. Wiegand, H. Eckert, R. Wolf, *Angew. Chem. Int. Ed.* **2014**, *53*, 2771-2775; f) C. Rödl, R. Wolf, *Eur. J. Inorg. Chem.* **2016**, 736-742.

[4] a) H.-W. Wanzlick, E. Schikora, *Chem. Ber.* **1961**, *94*, 2389-2393; b) H.-W. Wanzlick, F. Esser, H.-J. Kleiner, *Chem. Ber.* **1963**, *96*, 1208-1212; c) H.-W. Wanzlick, H.-J. Schönherr, *Angew. Chem. Int. Ed.* **1968**, *7*, 141-142.

[5] A. J. Arduengo III, R. L. Harlow, M. Kline, *J. Am. Chem. Soc.* **1991**, *113*, 361-363.

[6] D. Bourissou, O. Guerret, F. P. Gabbaï, G. Bertrand, *Chem. Rev.* **2000**, *100*, 39-91.

[7] D. J. Nelson, S. P. Nolan, *Chem. Soc. Rev.* **2013**, *42*, 6723-6753.

[8] Q. Teng, H. Vinh Huynh, *Dalton Trans.* **2017**, *46*, 614-627.

[9] a) F. Guillen, C. L. Winn, A. Alexakis, *Tet. Asymmetry* **2001**, *12*, 2083-2086; b) C. Michon, A. Ellern, R. J. Angelici, *Inorg. Chim. Acta* **2006**, *359*, 4549-4556; c) V. Jurčík, M. Gilani, R. Wilhelm, *Eur. J. Org. Chem.* **2006**, 5103-5109; d) D. Baskakov, W. A. Herrmann, E. Herdtweck, S. D. Hoffmann, *Organometallics* **2007**, *26*, 626-632; e) S. Zinner, W. A. Herrmann, F. E. Kühn, *J. Organomet. Chem.* **2008**, *693*, 1543-1546; f) X. Luan, R. Mariz, C. Robert, M. Gatti, S. Blumentritt, A. Linden, R. Dorta, *Org. Lett.* **2008**, *10*, 5569-5572; g) K. Hirano, S. Urban, C. Wang, F. Glorius, *Org. Lett.* **2009**, *11*, 1019-1022.

[10] A. Gómez-Suárez, D. J. Nelson, S. P. Nolan, *Chem. Commun.* **2017**, *53*, 2650-2660.

[11] E. Peris, *Chem. Rev.* **2017**, available online: DOI: 10.1021/acs.chemrev.6b00695.

[12] a) M. Frøseth, A. Dhindsa, H. Røise, M. Tilset, *Dalton Trans.* **2003**, 4516-4524; b) S. Dastgir, K. S. Coleman, A. R. Cowley, M. L. H. Green, *Organometallics* **2006**, *25*, 300-306; c) J. Al Thagfi, S. Dastgir, A. J. Lough, G. G. Lavoie, *Organometallics* **2010**, *29*, 3133-3138; d) Q.

Zhou, Y.-N. Wang, X.-Q. Guo, X.-H. Zhu, Z.-M. Li, X.-F. Hou, *Organometallics* **2015**, *34*, 1021-1028.

[13] a) C. S. Slone, D. A. Weinberger, C. A. Mirkin, *Prog. Inorg. Chem.* **1999**, *48*, 233-350; b) P. Braunstein, F. Naud, *Angew. Chem. Int. Ed.* **2001**, *40*, 680-699.

[14] J. Li, J. Peng, Y. Bai, G. Lai, X. Li, *J. Organomet. Chem.* **2011**, *696*, 2116-2121.

[15] a) F. E. Hahn, C. Holtgrewe, T. Pape, M. Martin, E. Sola, L. A. Oro, *Organometallics* **2005**, *24*, 2203-2209; b) A. Zanardi, E. Peris, J. A. Mata, *New J. Chem.* **2008**, *32*, 120-126.

[16] a) C. Gandolfi, M. Heckenroth, A. Neels, G. Laurenczy, M. Albrecht, *Organometallics* **2009**, *28*, 5112-5121; b) S. Horn, M. Albrecht, *Chem. Commun.* **2011**, *47*, 8802-8804; c) S. Horn, C. Gandolfi, M. Albrecht, *Eur. J. Inorg. Chem.* **2011**, 2863-2868.

[17] Selected references: a) M. Yiğit, B. Yiğit, İ. Özdemir, E. Çetinkaya, B. Çetinkaya, *Appl. Organomet. Chem.* **2006**, *20*, 322-327; b) N. Gürbüz, S. Yaşar, E. Özcan, İ. Özdemir, B. Çetinkaya, *Eur. J. Inorg. Chem.* **2010**, 3051-3056; c) N. Gürbüz, E. Özcan, İ. Özdemir, B. Çetinkaya, O. Şahin, O. Büyükgüngör, *Dalton Trans.* **2012**, *41*, 2330-2339.

[18] a) M. Nakanishi, D. Katayev, C. Besnard, E. P. Kündig, *Angew. Chem. Int. Ed.* **2011**, *50*, 7438-7441; b) D. Banerjee, A. K. Buzas, C. Besnard, E. P. Kündig, *Organometallics* **2012**, *31*, 8348-8354; c) L. Benhamou, C. Besnard, E. P. Kündig, *Organometallics* **2014**, *33*, 260-266.

[19] a) X. Luan, R. Mariz, M. Gatti, C. Costabile, A. Poater, L. Cavallo, A. Linden, R. Dorta, *J. Am. Chem. Soc.* **2008**, *130*, 6848-6858; b) X. Luan, R. Mariz, C. Robert, M. Gatti, S. Blumentritt, A. Linden, R. Dorta, *Org. Lett.* **2008**, *10*, 5569-5572; c) L. Vieille-Petit, X. Luan, R. Mariz, S. Blumentritt, A. Linden, R. Dorta, *Eur. J. Inorg. Chem.* **2009**, 1861-1870; d) L. Wu, E. Drinkel, F. Gaggia, S. Capolicchio, A. Linden, L. Falivene, L. Cavallo, R. Dorta, *Chem. Eur. J.* **2011**, *17*, 12886-12890.

[20] a) Q.-X. Liu, F.-B. Xu, Q.-S. Li, H.-B. Song, Z.-Z. Zhang, *Organometallics* **2004**, *23*, 610-614; b) L. Eloy, A.-S. Jarrousse, M.-L. Teyssot, A. Gautier, L. Morel, C. Jolivalt, T. Cresteil, S. Roland, *ChemMedChem* **2012**, *7*, 805-814.

[21] S. Sabater, J. A. Mata, E. Peris, *ACS Catal*. **2014**, *4*, 2038-2047.

[22] Representative examples: a) S. Urban, N. Ortega, F. Glorius, *Angew. Chem. Int. Ed.* **2011**, *50*, 3803-3806; b) N. Ortega, S. Urban, B. Beiring, F. Glorius, *Angew. Chem. Int. Ed.* **2012**, *51*, 1710-1713; c) S. Urban, B. Beiring, N. Ortega, D. Paul, F. Glorius, *J. Am. Chem. Soc.* **2012**, *134*, 15241-15244; d) M. Plois, Dissertation, WWU Münster, **2012**; e) D. Paul, B. Beiring, M. Plois, N. Ortega, S. Kock, D. Schlüns, J. Neugebauer, R. Wolf, F. Glorius, *Organometallics* **2016**, *35*, 3641-3646.

[23] a) G. Sipos, A. Ou, B. W. Skelton, L. Falivene, L. Cavallo, R. Dorta, *Chem. Eur. J.* **2016**, *22*, 6939-6946; b) G. Sipos, P. Gao, D. Foster, B. W. Skelton, N. Sobolev, R. Dorta, *Organometallics* **2017**, *36*, 801-817; c) P. Gao, G. Sipos, D. Foster, R. Dorta, *ACS Catal.* **2017**, *7*, 6060-6064.

2. Objectives

In their research on low-valent transition metal complexes, the group of Wolf investigated the ferrate complex [K(18-crown-6){Cp*Fe($C_{10}H_8$)}] (**XVII**, Figure 2.1, left), which is a powerful organometallic building block and was used extensively as a synthetic equivalent of the “Cp*Fe$^-$“ synthon.[1] **XVII** was used to prepare dinuclear complexes [Cp*Fe(μ-$C_{10}H_8$)MCp*] (**XVIII** (M = Fe; Figure 2.2, far left), **XIX** (M = Ru; Figure 2.2, center left)). Polyarene complexes like **XVIII** and **XIX** have been mentioned in the literature as model compounds for molecular electronics due to the strong electronic coupling across the naphthalene ligand.[2]

The aim of the first part of the present work was to expand on this research by finding a ruthenium analogue of ferrate **XVII**. The synthesis of the direct analogue [K]$^+$[Cp*Ru($C_{10}H_8$)]$^-$ (**K1**, Figure 2.1, center) should be possible either in analogy to **XVII**, by reacting [Cp*RuCl]$_4$ with K$C_{10}H_8$, or by reduction of [Cp*Ru($C_{10}H_8$)]PF_6 ([**XXI**]PF_6) with a strong reducing agent such as KC_8. Since recent results from the group of Wolf showed that the cobaltate [Co(cod)$_2$]$^-$ is a good alternative to the anthracene complex [Co($C_{14}H_{10}$)2]$^-$ as a source of “Co$^-$“ anions,[3] the ruthenate [Cp*Ru(cod)]$^-$ was envisaged as an alternative to **K1**.

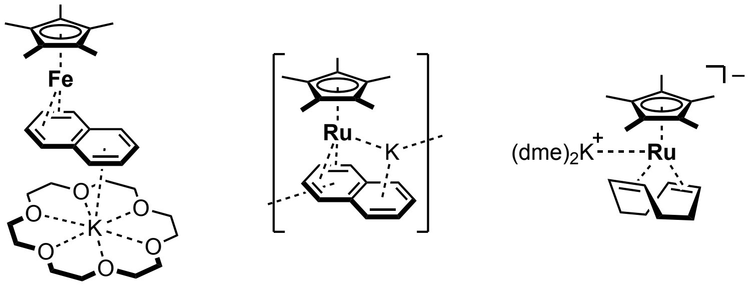

XVII **K1** **K3**

Figure 2.1. Low-valent metalates **XVII**, **K1**, and **K3**.

Building on previous studies of dinuclear naphthalene complexes such as **XVIII** and **XIX** (Figure 2.2), the diruthenium complex [Cp*Ru(μ-$C_{10}H_8$)RuCp*] (**2**; Figure 2.2, far right) was another focus of this work. Recently, Chin and co-workers described the diruthenium complex **XX** (Figure 2.2, center right), which features a *syn*-bridging naphthalene ligand rather than the *anti*-bridging naphthalene observed in **XVIII** and **XIX**.[4] The ruthenium atom in **XX** were described as electronically distinct (one Ru(0) and one (Ru(+II) center), whereas centrosymmetric **XVIII** displayed two equivalent iron centers in a formal oxidation state of +I. In order to understand whether this difference is due to the different molecular structure or the presence of ruthenium rather than iron, complex **2** serves as a useful middle ground. Therefore, a detailed analysis of **2** and its oxidation product **2**$^+$ was a subject of this thesis.

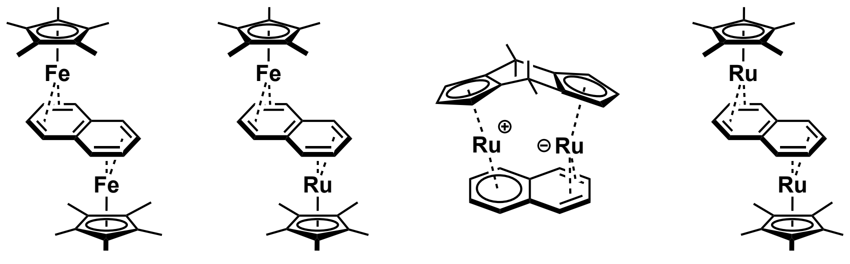

XVIII **XIX** **XX** **2**

Figure 2.2. Dinuclear iron and ruthenium complexes with bridging naphthalene ligands.

The second part of this work is concerned with incorporating naphthalene moieties into the framework of *N*-heterocyclic carbene ligands. The collaborative study by the groups of Glorius and Wolf on ruthenium-catalyzed asymmetric hydrogenations[5] demonstrated the enormous potential of combining the properties of NHC ligands with those of polyarenes into hemilabile chelating ligands (section 1.3). Inspired by the unique structure and catalytic performance of **XV** (Figure 1.11, left), we decided to explore how modifying the ligands and using different metals could afford complexes displaying hemilabile chelation and, possibly, catalytic activity. NHC-iridium complex **XVI** reported by Dorta and co-workers (section 1.3, Figure 1.11, right)[6] motivated us to include α-naphthyl substituents in the group of NHC ligands to be tested.

A series of ligands was selected that represent variations of the chiral NHC used in **XV**, with modified *N*-substituents (1-naphthylmethyl, 1-(1-naphthyl)ethyl, and α-naphthyl) and different backbones (saturated, unsaturated, fused aromatic). Different synthesis routes were envisaged for synthesizing these azolium salts, based on related compounds found in the literature.

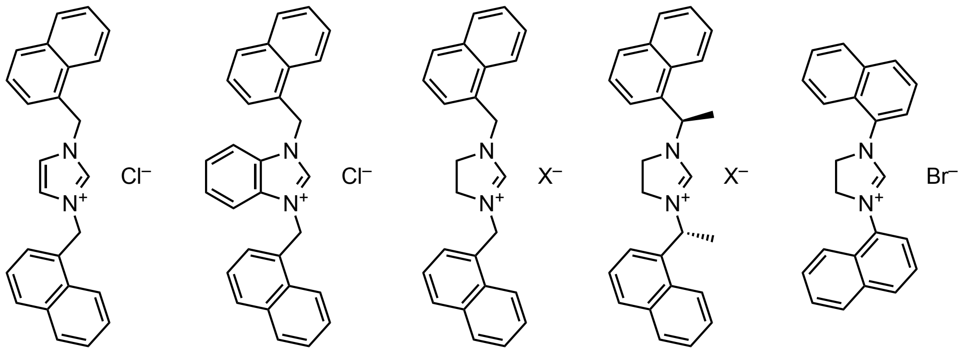

X = Cl, BF_4

XXXIX **XL** **XLI** **XLII** (X = BF_4) **4** (X = Cl) **5**

Figure 2.3. Naphthyl-substituted NHC precursors used in the present work.

Since the selected NHCs cannot be isolated, two common strategies were employed for the synthesis of transition metal complexes: The reaction of an azolium salt with a basic metal precursor and carbene transfer from silver to other metals.

Braunstein and Danopoulos described the straightforward synthesis of heteroleptic iron- and cobalt-NHC complexes from $[M\{N(SiMe_3)_2\}_2]$ (M = Fe, Co) and azolium salts.[7] Building upon this report, the selected azolium salts (vide supra) were reacted with $[M\{N(SiMe_3)_2\}_2]$. However, we were more interested in obtaining halide complexes of the type $[(NHC)MX_2]_2$ and tricoordinate amido complexes $[(NHC)M\{N(SiMe_3)_2\}_2]$. Since these compounds are usually prepared from the free NHCs and MX_2 or $[M\{N(SiMe_3)_2\}_2]$, respectively, we envisaged alternative synthetic procedures that involved generating the carbene *in situ*. The base needed to deprotonate the azolium salt was added in the form of $M^I[N(SiMe_3)_2]$ to $[M\{N(SiMe_3)_2\}_2]$ or by mixing equimolar amounts of $[M\{N(SiMe_3)_2\}_2]$ and MX_2 (Scheme 2.1, left).

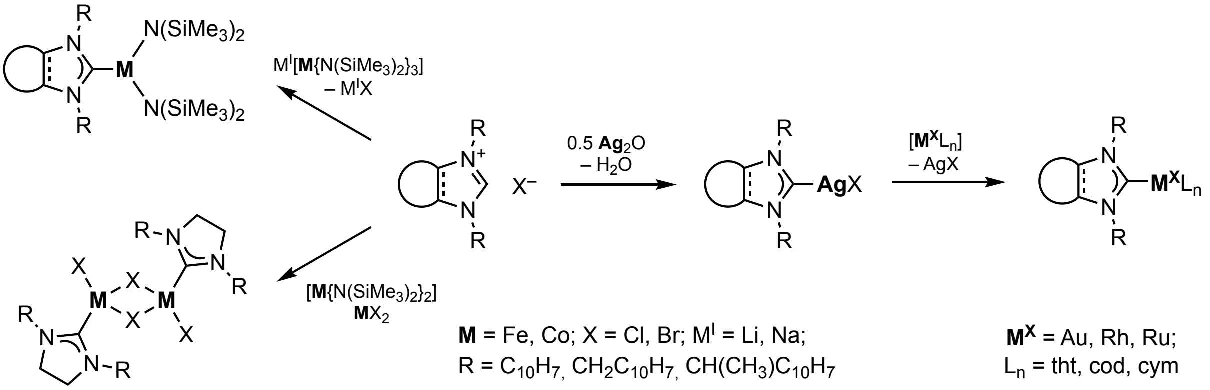

Scheme 2.1. Synthesis of NHC complexes by reaction with basic metal precursors.

The preparation of NHC-silver complexes from azolium salts and silver oxide is well known in the literature. We therefore decided to follow this route to prepare silver complexes and use these subsequently as NHC transfer agents. Carbene transfer from silver is a straightforward method to obtain precious metal carbene complexes. Based on the continued interest in using gold, rhodium, and ruthenium complexes in catalysis, and motivated especially by the work of Glorius and co-workes on ruthenium-catalyzed hydrogenations, we decided to use the silver NHC-transfer route to prepare gold, rhodium, and ruthenium complexes (Scheme 2.1, right). The silver-NHC transfer agents were either prepared as described above and isolated, or they were generated *in situ* simply by adding silver oxide to a mixture of azolium salt and a suitable precursor of the respective precious metal.

Many reports on catalysis using NHC-precious metal complexes explain that, in order to obtain a catalytically active species, a ligand has to be removed from the precatalyst.[8] Usually a halide is abstracted from the metal center using a silver salt of a weakly coordinating anion. The allyl-NHC complexes described by Hahn, Oro, and Mata (see section 1.3) show that halide abstraction may lead to chelation by the *N*-substituent(s) of the carbene ligand. Motivated by these reports, we wanted to synthesize chelate complexes by reacting the gold and rhodium complexes with halide scavengers. Besides the redox-neutral dissociation of halide ligands, reduction of the metal complexes should also lead to complexation by the π-accepting *N*-substituents. Therefore, the various NHC complexes were reacted with reducing agents such as Grignard reagents, KC_8, and hydrides.

Finally, we wanted to assess the catalytic activity of some of the carbene complexes. Our test systems included the ruthenium-catalyzed hydrosilylation of alkenes, rhodium-catalyzed hydrogenation of ketones and arenes (in collaboration with Dr. D. Paul, group of F. Glorius, WWU Münster), and the iron-catalyzed hydrogenation of arenes (in collaboration with Dr. T. Gieshoff, group of A. Jacobi von Wangelin).

---

[1] See reference 7 in chapter 3.

[2] See references 13 and 14 in chapter 3.

[3] See for example: S. Pelties, T. Maier, D. Herrmann, B. de Bruin, C. Rebreyend, S. Gärtner, I. G. Shenderovich, R. Wolf, *Chem. Eur. J.* **2017**, *23*, 6094-6102.

[4] See reference 19d in chapter 3.

[5] See reference 22 in chapter 1.

[6] See reference 23 in chapter 1.

[7] See reference 9 in chapter 6.

[8] See references 5f-h, 10, 35, 36, and 46 in chapter 5.

3. Low-valent Ruthenium Complexes Stabilized by Naphthalene or 1,5-Cyclooctadiene*

3.1 Introduction

Polyaromatic hydrocarbons and related dienes such as 1,5-cyclooctadiene possess unique ligand properties. While they can stabilize metal centers in low oxidation states via strong π backbonding, they are also easily displaced by other ligands. This makes transition metal complexes containing polyarene or cod ligands powerful organometallic reagents that can serve as synthetic equivalents for low-valent metal fragments or even transition metal anions. The pioneering work of the groups of Jonas and Ellis[1] demonstrates the great potential of this compound class.[2] Ellis and co-workers reported the synthesis of some early transition metalates such as tris(naphthalene)titanate which, upon reaction with white phosphorus, gave a unique sandwich complex containing only P_5^- ligands (Scheme 3.1).[2]

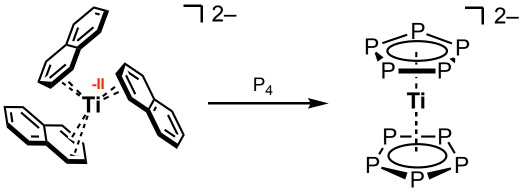

Scheme 3.1. Synthesis of a carbon-free metallocene from tris(naphthalene)titanate.

Related metalates such as bis(anthracene)cobaltate(–I)[3] were used by Wolf and co-workers for the synthesis of various anionic sandwich complexes (Scheme 3.2) as well as a catalyst for the hydrogenation of arenes and olefins.[4] The bis(1,5-cycloooctadiene)cobaltate(–I) developed by Jonas and co-workers[5] has found application in the synthesis of anionic diamine complexes which show a rich and interesting reactivity (Scheme 3.3).[6]

---

* The experiments and results discussed in this chapter, with the exception of complexes **K1** and **K3**, have been published as a full paper in *Dalton Transactions*: "Synthesis, electronic structure and redox properties of the diruthenium sandwich complexes $[Cp^*Ru(\mu\text{-}C_{10}H_8)RuCp^*]^x$ (x = 0, +1; $Cp^* = C_5Me_5$; $C_{10}H_8$ = naphthalene)", Dirk Herrmann, Christian Rödl, Bas de Bruin, František Hartl, Robert Wolf, *Dalton Trans.* **2018**, *47*, 11058-11069.

The DFT calculations and analyses were performed by Christian Rödl (University of Regensburg), who also created the visualizations (Figures 3.12, 3.18, and 3.19). The EPR measurements, analyses, and simulations were performed by Prof. Dr. Bas de Bruin (University of Amsterdam), who created Figure 3.17 and supplied the data given in Table 3.5. Spectroelectrochemical measurements and analyses were performed with the guidance of Prof. Dr. František Hartl (University of Reading).

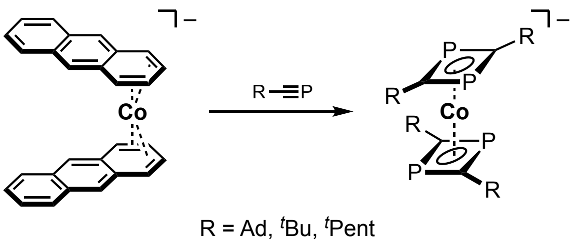

Scheme 3.2. Synthesis of bis(diphosphacyclobutadiene)cobaltate(-I) sandwich complexes from bis(anthracene)cobaltate(-I).

The heteroleptic ferrate [K(18-crown-6){Cp*Fe($C_{10}H_8$)}] (**XVII**), developed by the group of Wolf on the basis of the work of Jonas[1b], was the starting point for detailed investigations including the activation of white phosphorus, cyclodimerization of alkynes, ligand substitution of naphthalene by phosphinines and subsequent studies of the reactivity and catalytic activity of these compounds (Scheme 3.4).[7]

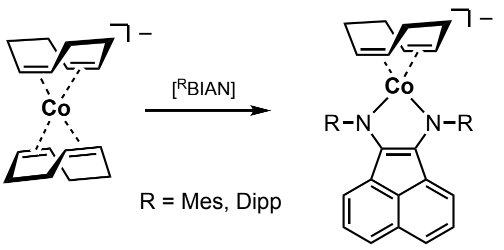

Scheme 3.3. Synthesis of bis(imino)acenaphthene cobaltates from bis(1,5-cyclooctadiene)-cobaltate(-I).

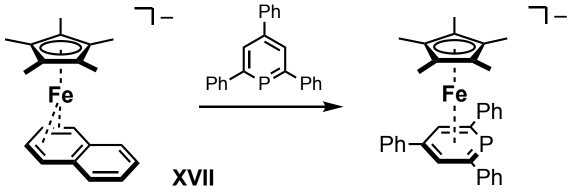

Scheme 3.4. Synthesis of phosphinine ferrates from **XVII**.

The lability of the naphthalene ligand has made the heteroleptic ruthenium sandwich complexes [Cp*Ru($C_{10}H_8$)]$^+$ (**XXI**$^+$) and [CpRu($C_{10}H_8$)]$^+$ (**XXII**$^+$) popular building blocks that provide easy access to the Cp*Ru$^+$ and CpRu$^+$ synthons (Figure 3.1).[8] The substitution of naphthalene was investigated in great detail by the group of Kudinov.[9] **XXI**$^+$ and **XXII**$^+$ have found application in catalysis, e.g. in the hydration of alkynes as well as alkene-alkyne couplings.[10] The high reactivity of ferrates such as **XVII** and the catalytic properties of ruthenium sandwich complexes such as **XXI**$^+$ encouraged us to investigate the chemistry of low-valent Cp*Ru complexes (section 3.2).

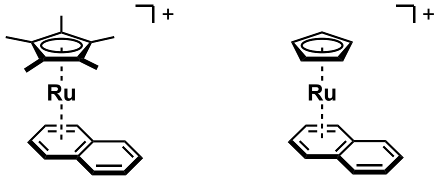

XXI$^+$ **XXII**$^+$

Figure 3.1. Heteroleptic ruthenium sandwich complexes featuring naphthalene ligands.

A series of related ruthenium half-sandwich complexes featuring diene ligands [Cp*RuCl(diene)] were reported in 1990 by the group of Fagan.[11] In particular, the 1,5-cyclooctadiene complex [Cp*RuCl(cod)] (**XXIII**) received a great deal of attention for its catalytic properties. Abstraction of the chloride ligand or displacement of the cod by phosphanes or other ligands provide activation pathways, making **XXIII** a potent (pre-)catalyst for the dimerization and hydrogenation of alkynes as well as the 1,4-hydrogenation of dienes.[12] While Fagan and co-workers also reported on the reduction of **XXIII** and other diene complexes to give anionic Ru(0) complexes, these have not been investigated any further thus far. We were therefore interested to probe the reactivity of such anionic half-sandwich complexes of ruthenium (section 3.3).

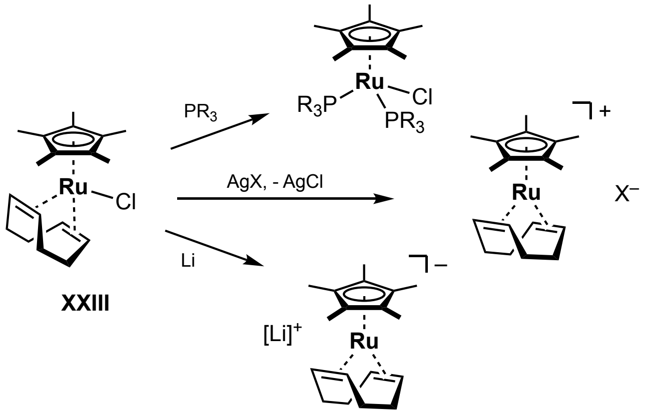

Scheme 3.4. Activation pathways of ruthenium half-sandwich complex **XXIII**.

A notable property of polyarenes is their tendency to act as bridging ligands in oligonuclear complexes. Sustained interest in these compounds stems from the fact that such systems are discussed as potential building blocks for molecular electronics.[13] The ability to tune the degree of the electronic communication between the metal centers is a key aspect in this area. Polyaromatic bridging ligands provide a varying degree of electronic coupling between the coordinated metal atoms through their conjugated π-system.[14]

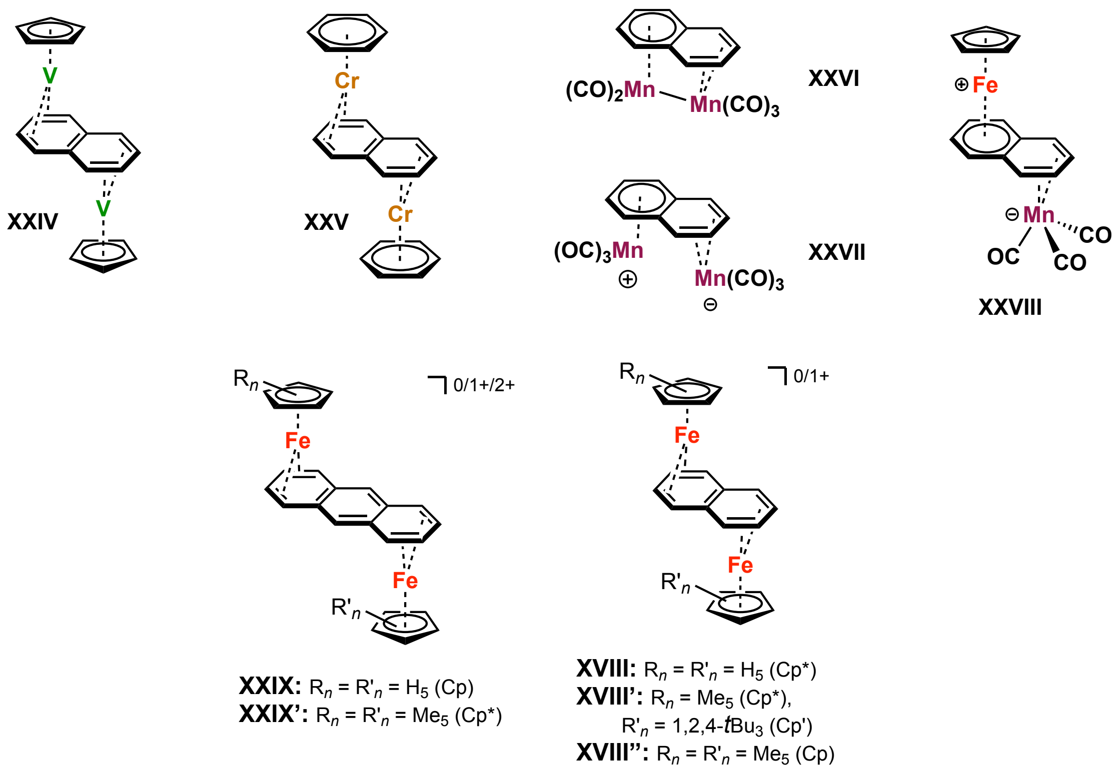

Figure 3.2. Selected examples of dinuclear polyarene-bridged transition metal complexes with M = V-Fe.

The two simplest polyarenes, naphthalene and anthracene, enable a particularly strong electronic coupling between the metal atoms, yet the number of known bimetallic naphthalene and anthracene complexes is still relatively small. Early examples include vanadium, chromium, and manganese complexes (e.g. complexes **XXIV–XXVIII** in Figure 3.2).[15] A related diiron complex, $[CpFe(\mu\text{-}C_{14}H_{10})FeCp]^{2+}$ (**XXIX**$^{2+}$), was reported by Hendrickson *et al.*[16] Jonas and coworkers subsequently extended the family by synthesizing the related naphthalene complexes $[CpFe(\mu\text{-}C_{10}H_8)FeCp]$ (**XVIII'**) and $[Cp^*Fe(\mu\text{-}C_{10}H_8)FeCp^*]$ (**XVIII**).[17] A single-crystal X-ray structure analysis of **XVIII** confirmed the a *trans* arrangement of the CpFe moieties.

While mononuclear ruthenium complexes of type $[(C_5R_5)Ru(polyarene)]^+$ have found widespread use in organometallic chemistry and catalysis (*vide supra*), polyarene-bridged diruthenium complexes have also attracted attention (Figure 3.3).[18,19] Dicationic diruthenium complexes *anti*-$[Cp^*Ru(\mu\text{-}\eta^6\text{:}\eta^6\text{-L})RuCp^*]^{2+}$ (**XXX–XXXIII**, x = 1+ or 2+, L = anthracene [**XXX**], phenanthrene [**XXXI**], pyrene [**XXXII**], and chrysene [**XXXIII**]) were prepared by the groups of Kölle and Román.[19a-c] The redox behavior of these complexes was investigated by electrochemical methods. A single X-ray diffraction study of the triflate salt [**XXXIII**]$(OTf)_2$ of the chrysene complex revealed the *anti*-facial configuration of the metal centers.[19c] The μ-

η^6:η^4-naphthalene diruthenium complex [(η^4-cod)Ru(μ-η^6:η^4-$C_{10}H_8$)Ru(η^4-cod)(L)] (**XXXIV**, cod = 1,5-cyclooctadiene, L = PMe_3, PEt_3, and $P(OMe)_3$) reported by Bennett *et al.* also displays an *anti*-facial structure,[20] while Chin *et al.* recently described the *syn*-facial the naphthalene and anthracene-bridged complexes **XX** and **XXXV**$^{2+}$. The *syn*-facial arrangement is due to the presence of a doubly-bridged dicyclopentadienyl ligand connecting the ruthenium atoms.[19d]

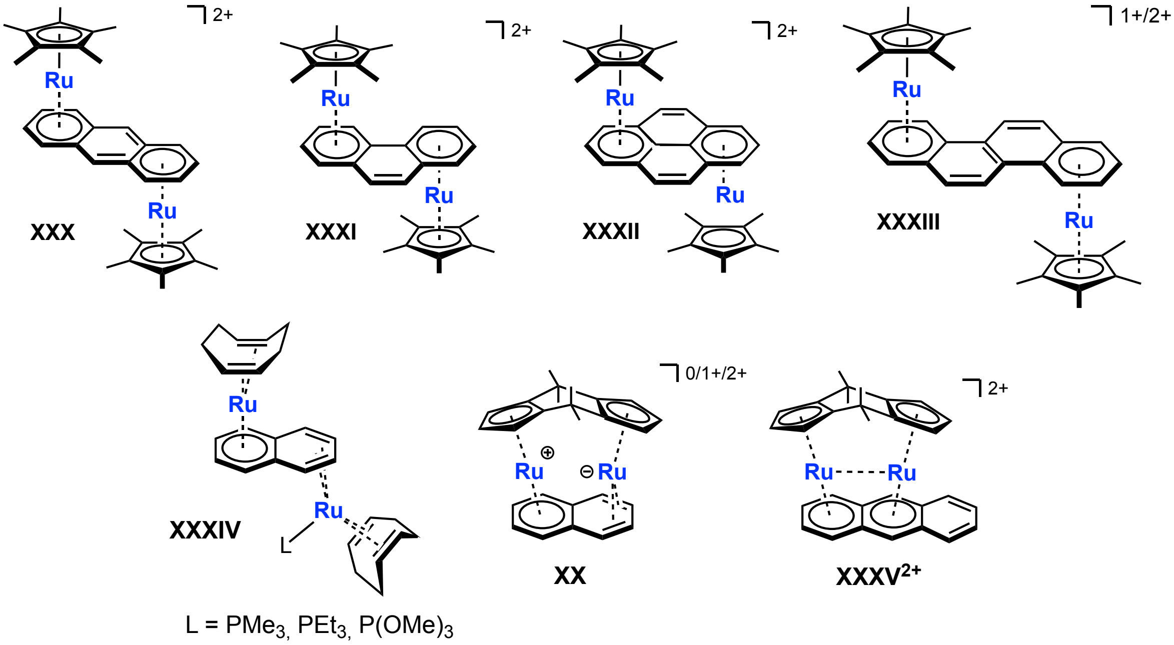

Figure 3.3. Previously characterized polyarene-bridged diruthenium complexes.

During their investigations of synthetic applications of low-valent polyarene transition metalates (*vide supra*), Wolf and co-workers also studied the chemistry of bimetallic polyarene iron and ruthenium complexes. They reported a new route to the previously reported diiron complex **XVIII**, and synthesized and characterized the closely related diiron and iron-ruthenium complexes **XVIII''**, **XIX**, and **XIX'**.[21] In an independent study, Ohki, Tatsumi *et al.* prepared and characterized the Cp*-substituted compounds **XXIX'** and **XVIII**. Monocationic oxidation products [**XXIX'**]BAr^F_4 and [**XVIII**]BAr^F_4 were isolated by oxidizing these neutral precursors with $[Cp_2Fe]PF_6$ followed by anion exchange with $NaBAr^F_4$.[22] Wolf and co-workers similarly obtained the monocationic diiron and iron-ruthenium complexes [Cp'Fe(μ-$C_{10}H_8$)FeCp*]PF_6 ([**XXIX''**]PF_6), and [Cp'Fe(μ-$C_{10}H_8$)RuCp*]PF_6 ([**XIX'**]PF_6) by oxidizing neutral **XVIII** and **XIX'** with $[Cp_2Fe]PF_6$.[21c]

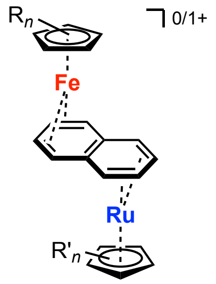

XIX: R$_n$ = R'$_n$ = Me$_5$ (Cp*)
XIX': R$_n$ = 1,2,4-*t*Bu$_3$ (Cp'); R'$_n$ = Me$_5$ (Cp*)

Figure 3.4. Naphthalene-bridged iron-ruthenium complexes.

Combined spectroscopic, electrochemical and quantum chemical studies revealed similar electronic structures for the diiron and iron-ruthenium complexes of type **XVIII** and **XIX**, which are only marginally influenced by different substituent patterns on the Cp ligand (Cp* vs. Cp'). Substituting one of the iron centers by ruthenium in the heterometallic complexes **XIX** only had a very modest effect on the structural and spectroscopic properties as well. This observation was explained by the similar composition of the frontier molecular orbitals in the diiron and iron-ruthenium complexes, which are dominated by contributions from iron and ligand-based atomic orbitals whereas the Ru-based orbitals appeared to be of secondary importance.[21c] Therefore we were interested to study the consequences of replacing both iron centers in **XVIII** by ruthenium (sections 3.4-3.5).

3.2 Attempted Synthesis of [Cp*Ru($C_{10}H_8$)]$^-$ (1$^-$)

The ferrate [K(18-crown-6)][Cp*Fe($C_{10}H_8$)] (**XVII**) is prepared by the reduction of "Cp*FeCl", generated *in situ* from $FeCl_2(thf)_{1.5}$ and Cp*Li, by potassium naphthalenide ($KC_{10}H_8$). Our first approach towards the synthesis of the corresponding ruthenium complex, K[Cp*Ru($C_{10}H_8$)] (**K1**) followed an analogous route, involving the reduction of $[Cp^*RuCl]_4$ by $KC_{10}H_8$. However, no product could be isolated.

We therefore considered the reduction of the well-known cationic Ru(II) complex [Cp*Ru($C_{10}H_8$)]PF_6 ([**XXI**]PF_6). The group of Kölle investigated the electrochemistry of **XXI**$^+$ and related ruthenium-arene complexes and observed a reduction of **XXI**$^+$ at –1.96 V vs. Fc^+/Fc that was reversible only at a very high scan rate of $v = 2000$ mV s^{-1}. They concluded that, upon electrochemical reduction in CH_2Cl_2, "short-lived neutral Cp*Ru(η^6-arene) complexes undergo decomplexation rather than dimerization or hydrogen abstraction". In a subsequent study, Gusev and coworkers observed a reversible reduction of **XXI**$^+$ at –2.10 V in acetonitrile and a second, irreversible reduction at –3.16 V. They identified the mononuclear benzocyclohexadienyl complex [Cp*Ru($C_{10}H_9$)] (**XXXVI**) as the major product (62% isolated yield) of the chemical reduction of [**XI**]PF_6 with an excess of Na/Hg in THF (Scheme 3.5). They did not comment on the source of the hydrogen atom.

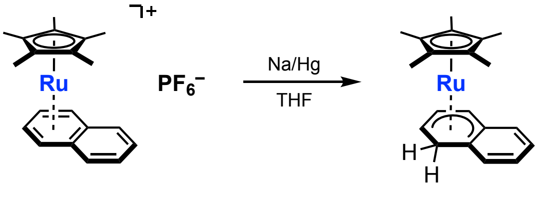

[**XXI**]PF_6 **XXXVI**

Scheme 3.5. Reduction of **[XXI]**PF_6 to the cyclohexadienyl complex **XXIII**.

In light of these reports, we decided to perform a cyclic voltammetry experiment on [**XXI**]PF_6 in THF rather than CH_2Cl_2 or acetonitrile to assess the stability of neutral **XXI** and anionic **XXI**$^-$. In contrast to the results of Kölle and Gusev, we observed two overlapping reversible reduction processes at –1.99 and –2.10 V vs. Fc^+/Fc, which, at high scan rates, appear as one slightly broadened reduction wave (Figure 3.5). While the small separation between the two reductions indicates that neutral B may be unstable, which is in accord with Kölle's hypothesis, we concluded from the full reversibility of the second reduction that **XXI**$^-$ may in fact be isolable.

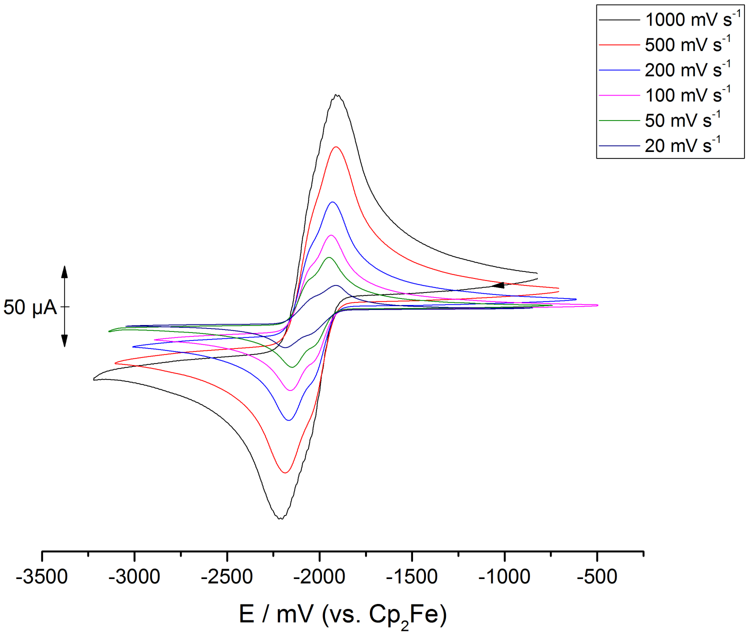

Figure 3.5. Cyclic voltammogram of [**XXI**]PF_6 in THF/NBu_4PF_6 at varying scan rates. Working electrode: Pt minidisk, counter electrode: Pt wire, pseudoreference electrode: Ag wire.

Encouraged by this result, we studied the chemical reduction of [**XXI**]PF_6 using a slight excess of the strong reducing agent potassium graphite (KC_8). Following the reaction of [**XXI**]PF_6 and KC_8 in DME at –35 °C we identified the desired low-valent ruthenate $[K\{Cp^*Ru(C_{10}H_8)\}]_n$ (**K1**) by X-ray crystallography (Figure 3.2).

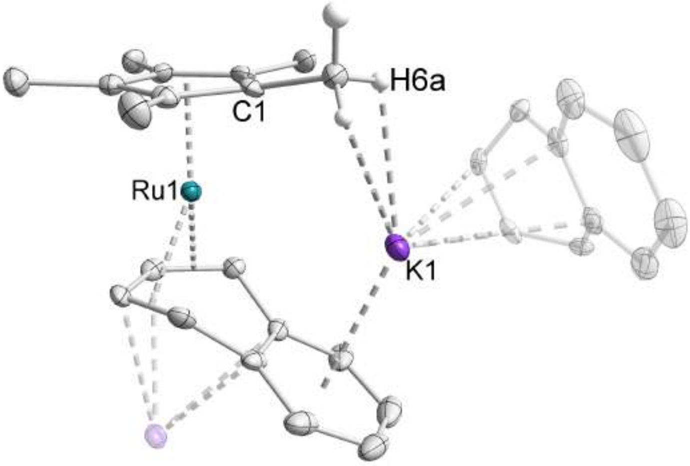

Figure 3.6. Solid state X-ray structure of **K1** (one formula unit of the coordination polymer with adjacent coordination partners; thermal ellipsoids at 50% probability; hydrogen atoms except H6a/b/c omitted for clarity).

K1 crystallized from *n*-hexane in the monoclinic space group $P2_1/c$ with four molecules in the unit cell. The crystal structure reveals that **K1** forms a polymer in the solid state in which the potassium counterion is stabilized by the naphthalene ligands of two adjacent $Cp^*Ru(C_{10}H_8)^-$ anions as well as one methyl group of the Cp* ligand. The ruthenium center is coordinated by the Cp* ligand in the expected η^5 mode as well as the naphthalene in an η^4 fashion. The naphthalene ligand is consequently folded along the C11–C14 vector by an angle of 38.8°, which is close to the fold angle observed in the analogous ferrate complex **XVII** (35.1°). The bonds between the ruthenium center and the C11 to C14 atoms are in the range of 2.11212(4) to 2.21647(5) Å while the distances to the bridgehead carbons C19 and C20, at 3.00936(5) and 3.01827(6) Å, are significantly longer, thus confirming the η^4 coordination of the naphthalene ligand. The C11–C12 (1.45271(4) Å), C12–C13 (1.41866(2) Å), and C13–C14 (1.46155(3) Å) bonds of the naphthalene ligand follow a long-short-long pattern, which is indicative of π back-bonding from the low-valent Ru(0) center.

Despite the fact that a single crystal of **K1** could be obtained, the compound only constitutes a minor byproduct of the reduction of [**XXI**]PF_6 and could not be isolated. Besides **K1** and a trace amount of **XXXVI**, the main product of the reaction is the dinuclear Ru(I) complex $[Cp^*Ru(\mu\text{-}\eta^4{:}\eta^4\text{-}C_{10}H_8)RuCp^*]$ (**2**, see section 3.4). We therefore shifted our attention to the preparation of the related diene complex $[K(dme)_2][Cp^*Ru(cod)]$ (**K3**).

3.3 Synthesis and Reactivity of [K(dme)$_2$][Cp*Ru(cod)] (K3)

In 1990 the group of Fagan reported the synthesis of a range of diene complexes of ruthenium, Cp*RuCl(diene) from [Cp*RuCl]$_4$ and their subsequent reduction to [Li(dme)][Cp*Ru(diene)] using lithium powder. While the chloride complexes, particularly [Cp*RuCl(cod)] (**XXIII**) received a great deal of attention for their catalytic properties, the low-valent ruthenates were hardly studied since their discovery. In light of the interesting properties of other metalates ligated by cod ligands, we decided to investigate the cod-stabilized ruthenate [Cp*Ru(cod)$^-$] (**3**$^-$). As attempts to replicate Fagan's synthesis were unsuccessful, the lithium powder used as reducing agent was exchanged for KC$_8$. Reacting **XXIII** with a slight excess of KC$_8$ in DME at –35 °C led to the formation of [K(dme)$_2$][Cp*Ru(cod)] (**K3**) which was isolated as a colorless powder in 43% yield (Scheme 3.6).

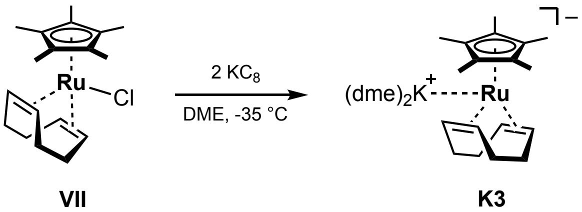

Scheme 3.6. Reduction of **XXIII** to yield the ruthenate **K3**.

X-ray quality crystals of **K3** were obtained by slow diffusion of diethyl ether into a DME solution. **K3** crystallizes in the orthorhombic space group *P*ca2$_1$. The unit cell contains two crystallographically independent molecules, one of which contains a disordered Cp* ligand. Figure 3.7 shows the molecule without the Cp* disorder, from which the relevant structural parameters were determined.

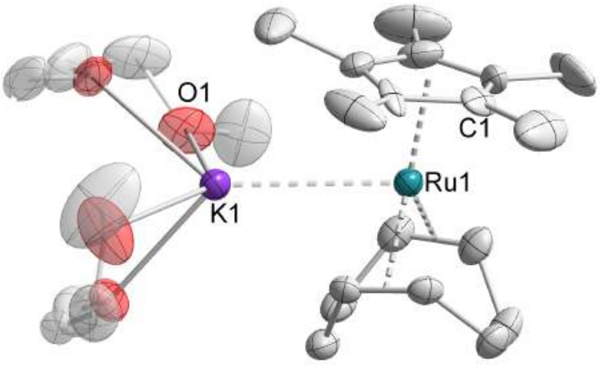

Figure 3.7. Solid state X-ray structure of **K3** (thermal ellipsoids at 50% probability, hydrogen atoms omitted for clarity).

K3 displays a half-sandwich structure with the Cp* ligand on one side of the ruthenium center and the cod ligand on the opposite side. The C–C double bonds of the cod ligand (1.431(6) and 1.443(6) Å) are slightly elongated with respect to non-coordinating double bonds due to backbonding from the ruthenium center. The distance of the potassium cation to the ruthenium center amounts to 3.3940(7) Å), which is slightly longer than a K–Ru single bond, indicating a weak interaction.

The ^{1}H NMR spectrum of **K3**, recorded in THF-d_8, is in good agreement with the data reported by Fagan for the analogous lithium salt. A singlet at 1.73 ppm corresponds to the protons of the Cp* ligand, while broadened signals at 1.54, 1.65, and 1.83 are assigned to the cod ligand. The coordinating dimethoxyethane resonates at 3.30 (OCH_3) and 3.46 ppm (OCH_2CH_2O). The integrals of the signals of 15:4:4:4:6:4, respectively, indicate that one of the dme ligands is lost upon drying *in vacuo*. This was confirmed by elemental analysis.

In order to assess the reactivity of **K3**, we chose the activation of white phosphorus (P_4) as a starting point. As reported by the group of Wolf, the reaction of ferrate **XVII** with P_4 yields a mixture of compounds, two of which were characterized crystallographically and by ^{31}P NMR spectroscopy (Scheme 3.7). The dianionic P_7 cluster **XXXVII** gives rise to a characteristic ^{31}P NMR spectrum with multiplets at –100.7, 6.3, and 151.2 ppm.

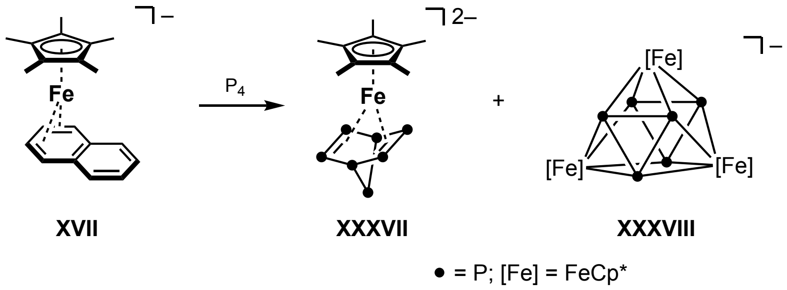

Scheme 3.7. Activation of white phosphorus by ferrate complex **XVII**.

We found that reacting **K3** with P_4 in toluene at low temperature yields a similar result. The ^{31}P NMR spectrum of the reaction mixture shows signals analogous to those of **XXXVII** at –95.0, 28.4, and and 160.8 ppm, along with a number of other signals (Figure 3.8). Despite numerous attempts, none of the products could be isolated, precluding a more detailed analysis.

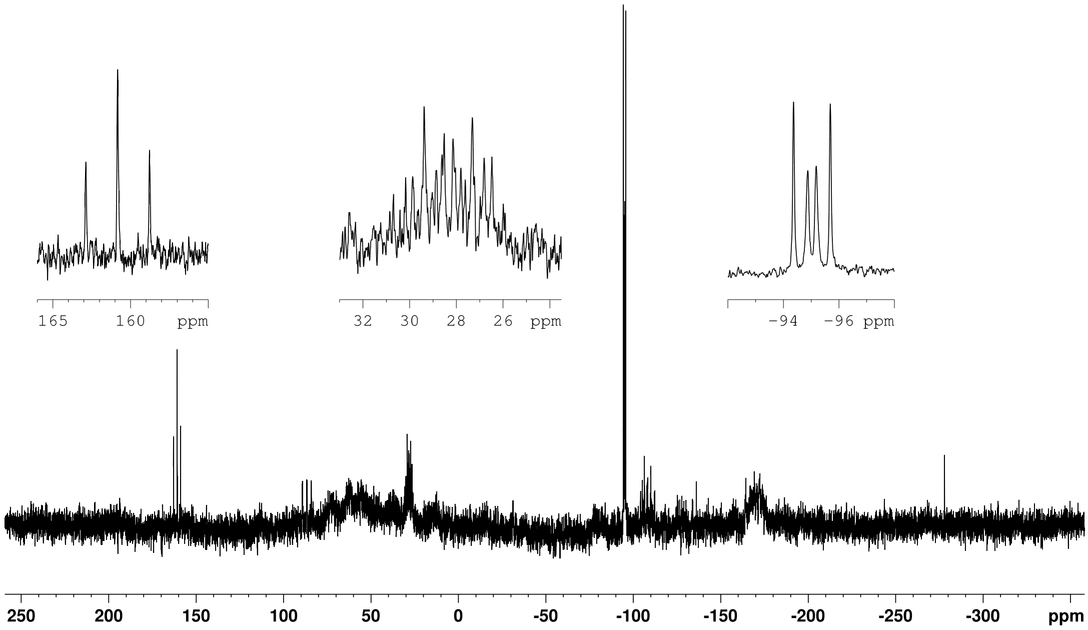

Figure 3.8. ^{31}P NMR spectrum of the reaction mixture of **K3** and P_4 in toluene. Insets show signals corresponding to P_7 cluster analogous to **XXXVII**.

3.4 Characterization of [Cp*Ru(μ-$C_{10}H_8$)RuCp*] (2)

In order to compare its properties with known polyarene-bridged transition metal complexes (*vide supra*, Figures 3.2 and 3.3), we investigated complex **2** in more detail. Under optimized reaction conditions (Scheme 3.8), **2** was isolated in a yield of 34% after recrystallization from a deep red toluene solution. Crystals of **2** appear either dark red or greenish, depending on the particle size.

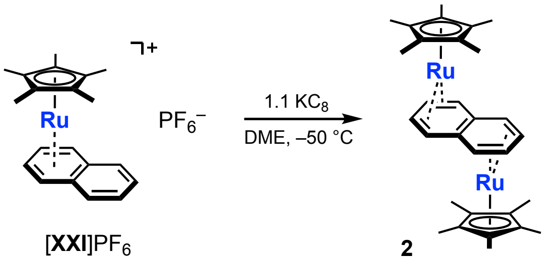

Scheme 3.8. Synthesis of dinuclear complex **2**.

3.4.1 Crystal Structure Analysis

2 crystallizes from toluene or *n*-hexane in the monoclinic space group $P2_1/n$ with two molecules in the unit cell. The solid-state molecular structure (Figure 3.9) is centrosymmetric and reveals an *anti*-facial configuration of the two Cp*Ru moieties binding to opposite faces of the bridging naphthalene ligand. The naphthalene ligand is η^4-coordinated to both Cp*Ru units with Ru–C distances from 2.161(7) to 2.229(8) Å (see Table 3.1), while the distances to the bridgehead carbons C15 and C15' (av. 2.588(8) Å) are substantially longer. In accord with this, the naphthalene ligand is folded by 14.4° along the C11–C14 vector. The C11–C12 (1.446(12) Å), C12–C13(1.414(13) Å) , and C13–C14 (1.416(13) Å) bond lengths of the naphthalene ligand do not show the short-long-short pattern observed in free naphthalene, but are very similar due to the back-bonding from the low-valent metal center.[23] The structural data of **2** are comparable to those of the analogous diiron and iron-ruthenium complexes of type **XVIII** and **XIX** (Figures 3.2 and 3.4), which display similar structures with an *anti*-facial configuration of the metal centers and essentially η^4-coordinated aromatic rings.

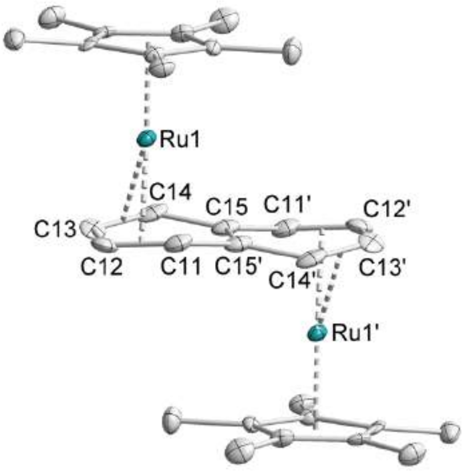

Figure 3.9. Solid state X-ray structure of **2** (thermal ellipsoids at 50% probability; hydrogen atoms omitted for clarity).

The molecular structure of **2** differs from that of the closely related *syn*-facial complex **XX** (Figure 3.3), which shows one of the ruthenium centers bound in an η^6 fashion to one of the naphthalene rings (Ru1–C 2.180(2)–2.336(2) Å; see Table 3.1 for detailed Ru–C bond distances), while the second ruthenium is coordinated in an η^4 fashion (Ru2–C 2.136(2)–2.190(2) Å). Long Ru–C distances are observed from this ruthenium atom to the bridgehead carbons atoms (Ru2–C19, C20 2.901(2) and 2.885(2) Å).[19d] A similar η^4:η^6-coordination mode is also found in the structure of **XIX'**. The η^4-coordinated aromatic ring displays a fold angle of 31.5°, which is similar to that of **XIX'** (25.2°) and anionic mononuclear complexes with η^4-coordinated naphthalene ligands, such as **XVII** (35.1°). This asymmetric coordination of the naphthalene ligand in the structure of **XX** is distinct from the symmetric structure of **2.** The presence of the η^4:η^6-naphthalene ligand in **XX** indicates a mixed-valent Ru^{II}Ru^0 electronic structure with the ruthenium atoms in d^6 and d^8 configurations, respectively. Chin et. al. reported that DFT calculations gave an energy difference of approximately 4.7 kcal mol^{-1} between the disfavored C_{2v} symmetric structure akin to **2** and the C$_s$ symmetric ground state.[19d]

Table 3.1. Selected bond lengths (Å) and angles (°) of complexes **2**, **XVIII**, **XIX**, **XIX'**, and **XX** determined by X-ray crystallography and *DFT* (DFT values given in italics). Numbering according to Fig. 3.10.

	2 ($M^1 = M^2 =$ Ru)	**XVIII** ($M^1 = M^2$ = Fe)	**XIX** (M^1 = Fe, M^2 = Ru)	**XIX'** * (M^1 = Fe, M^2 = Ru)	**XX** ** ($M^1 = M^2$ = Ru)
M1–C11	2.229(8) / *2.228*	2.101(2) / *2.102*	– / *2.101*	2.105(4) / *2.12*	2.190(2)
M1–C12	2.177(8) / *2.178*	2.016(3) / *2.025*	– / *2.028*	2.012(5) / *2.02*	2.136(2)
M1–C13	2.161(7) / *2.178*	2.031(3) / *2.025*	– / *2.028*	2.003(5) / *2.02*	2.136(2)
M1–C14	2.227(7) / *2.225*	2.100(3) / *2.102*	– / *2.100*	2.134(3) / *2.14*	2.177(2)
M1–C19	2.585(8) / *2.541*	2.441(2) / *2.427*	– / *2.424*	2.696(2) / *2.65*	2.901(2)
M1–C20	2.593(8) / *2.548*	2.435(2) / *2.427*	– / *2.419*	2.718(2) / *2.65*	2.885(2)
M1–C(Cp) (av.)	2.190(16)	2.068(9)		2.080(4) / *2.09*	2.195(3)
M2–C15	– / *2.230*	– / *2.097*	– / *2.223*	2.220(4) / *2.24*	2.249(2)
M2–C16	– / *2.155*	– / *2.022*	– / *2.168*	2.174(5) / *2.17*	2.180(2)
M2–C17	– / *2.156*	– / *2.022*	– / *2.168*	2.191(4) / *2.17*	2.193(2)
M2–C18	– / *2.225*	– / *2.097*	– / *2.225*	2.220(4) / *2.25*	2.252(2)
M2–C19	– / *2.655*	– / *2.464*	– / *2.611*	2.434(4) / *2.64*	2.317(2)
M2–C20	– / *2.649*	– / *2.464*	– / *2.609*	2.436(4) / *2.64*	2.336(2)
M2–C(Cp) (av.)	–	–		2.179(5) / *2.20*	2.205(27)
C11–C12	1.446(12) / *1.435*	1.431(4) / *1.431*	– / *1.431*	1.427(7) / *1.44*	1.450(2)
C12–C13	1.414(13) / *1.421*	1.406(4) / *1.420*	– / *1.420*	1.395(6) / *1.42*	1.407(3)
C13–C14	1.416(13) / *1.436*	1.420(4) / *1.431*	– / *1.431*	1.440(6) / *1.43*	1.442(3)
C15–C16	– / *1.441*	– / *1.433*	– / *1.438*	1.418(6) / *1.44*	1.421(3)
C16–C17	– / *1.421*	– / *1.420*	– / *1.422*	1.398(6) / *1.42*	1.409(3)
C17–C18	– / *1.440*	– / 1.433	– / *1.438*	1.418(7) / *1.44*	1.423(3)
C14–C20	1.442(12)	1.428(1)	–	1.440(6) / *1.44*	1.454(2)
C20–C15	1.422(13)	1.435(1)	–	1.427(6) / *1.44*	1.413(2)
C18–C19	–	–	–	1.417(6) / *1.44*	1.416(2)
C19–C11	–	–	–	1.457(6) / *1.44*	1.460(3)
Fold angles	14.4(6)[a] / *12.96*	12.4(2) [a] / *11.77*	–, – / *11.97, 15.93*	25.2(4)[a], 8.6(4)[b] / *11.2, 7.8*	31.5(1)[c]

[a] Dihedral angle C11–C12–C13–C14 / C14–C20–C19–C11. [b] Dihedral angle C15–C16–C17–C18 / C18–C19–C20–C15. [c] Dihedral angle C11–C12–C13–C14 / C14–C20–C15–C16–C17–C18–C19–C11. * Values taken from ref. 21c. ** Values taken from ref. 19d.

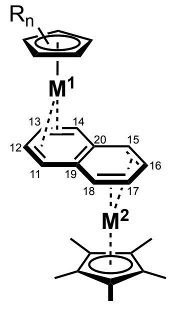

Figure 3.10. Numbering scheme for naphthalene bridged complexes.

3.4.2 NMR Spectroscopic Characterization

In accord with the symmetrical structure observed for **2** in the solid state, the ^{1}H NMR spectrum in C_6D_6 shows a single Cp* resonance at 1.84 ppm and two multiplets at 4.89 and 2.17 ppm which correspond to the hydrogen atoms of the coordinated naphthalene ligand. The naphthalene signals are notably shifted to lower frequency relative to free naphthalene. An even more pronounced chemical shift difference was observed for the related Cp*-substituted diiron and iron-ruthenium complexes **XVIII** and **XIX** (Table 3.2), which display dramatically shielded 1,4-hydrogen signals (1.11 ppm for **XVIII**, and 1.31 ppm for **XIX**).[21c] The diruthenium complex **2** shows a less pronounced low frequency shift for the 1,4-hydrogen atoms (H11 and H14) than **XVIII** and **XIX**, but the 2,3-hydrogen atoms (H12 and H13) are somewhat more shielded. The same trend is observed in the $^{13}C\{^{1}H\}$ NMR spectra of **2**, **XVIII**, and **XIX**. In all cases, the 1,4-carbon signals are shifted to lower field, as are the 2,3-carbon signals. While the difference to the spectrum of free naphthalene is striking, the $^{13}C\{^{1}H\}$ NMR spectra of **2**, **XVIII**, and **XIX** show only marginally different chemical shifts for the naphthalene carbon atoms.

Comparison of the ^{1}H NMR data of **2** with that of the *syn*-facial complex **XX** shows unexpected similarities. In C_6D_6 solution, **XX** is fluxional, resulting in a symmetric ^{1}H NMR spectrum. As a consequence, the ^{1}H NMR resonances for the naphthalene ligand are similar to those of **2** and appear at 3.71 and 4.88 ppm, respectively.[19d]

Table 3.2. Assignment of the ^{1}H and $^{13}C\{^{1}H\}$ NMR resonances of **2**, **XVIII**, **XIX**, **XX**, and free naphthalene. $^{13}C\{^{1}H\}$ resonances are given in parentheses. See Fig. 3.10 for the numbering scheme.

	2	**XVIII**	**XIX**	**XX**[a]	**Free $C_{10}H_8$**
$H_{11,14,15,18}$ ($C_{11,14,15,18}$)	2.17 (60.9)	1.11 (58.0)	1.31, 1.80 (58.8, 59.5)	3.71 –	7.63 (128.2)
$H_{12,13,16,17}$ ($C_{12,13,16,17}$)	4.89 (72.5)	5.72 (77.5)	5.10, 5.37 (72.0, 76.4)	4.88 –	7.24 (126.1)
$C_{19,20}$	(not obs.)	(110.1)	(110.8)	–	(134.0)
CH_3 of Cp*	1.84 (11.6)	1.49 (10.1)	1.64, 1.77 (10.3, 11.5)	–	–
quat. C of Cp*	(85.8)	(83.8)	(82.6, 85.1)	–	–

[a] No ^{13}C NMR data available.

3.4.3 Electrochemical Analysis

In order to gain insight into the redox properties of **2**, we recorded a cyclic voltammogram in THF/TBAH (Figure 3.11). The reduction potentials and peak-to-peak separations are summarized in Table 3.3 along with data for some related compounds. The CV of **2** shows two well-separated oxidation processes **2** → $\mathbf{2}^+$ (−1.47 V vs. Fc^+/Fc) and $\mathbf{2}^+$ → $\mathbf{2}^{2+}$ (−1.25 V vs. Fc^+/Fc), which are fully reversible under the experimental conditions. The redox potentials of the analogous diiron and iron-ruthenium complexes **XVIII** and **XIX** are in a similar range. The *syn*-facial dicyclopentadiene complex **XX** also shows a qualitatively similar cyclic voltammogram. The separation of the half-wave potentials $E_{1/2}$ ($\mathbf{2}/\mathbf{2}^+$) and $E_{1/2}$ ($\mathbf{2}^+/\mathbf{2}^{2+}$) amounts to $\Delta E_{1/2}$ = 220 mV. $\Delta E_{1/2}$ is similar for **XX** (180 mV), but substantially larger for **XVIII** (660 mV) and **XIX** (590 mV). The anthracene-bridged complex $\mathbf{XXX}^{2+}$ (Figure 3.3) displays two reductions at $E_{1/2}$ = −0.78 and −1.47 V with a separation of 690 mV, while the related complexes containing nonlinear polyarenes (phenanthrene, pyrene, and chrysene) as bridging ligands $[Cp^*Ru(\mu\text{-}L)RuCp^*]^{2+}$ ($\mathbf{XXXI}^{2+}$–$\mathbf{XXXIII}^{2+}$, Figure 3.3) feature two redox processes at substantially more negative potentials than **2** with $\Delta E_{1/2}$ separations ranging from 130 to 690 mV. Thus, it seems that the nature of the bridging ligand has a more profound influence on the redox potential than the metal or the cyclopentadienyl ligand.

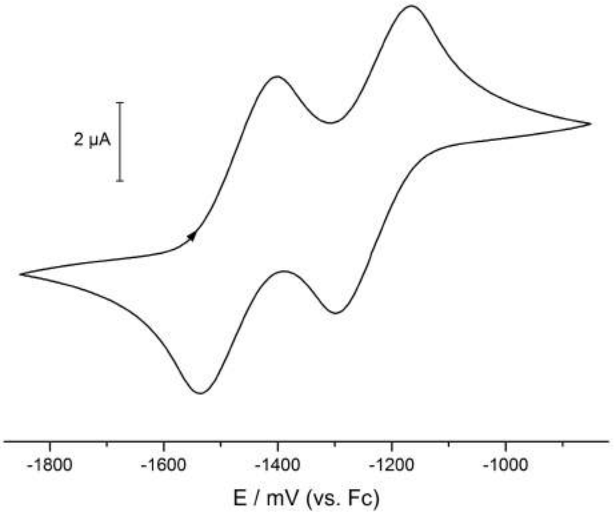

Figure 3.11. Cyclic voltammogram of **2**, recorded in THF / NBu_4PF_6 at v = 100 mV s^{-1}. Working electrode: Pt minidisk, counter electrode: Pt wire, pseudoreference electrode: Ag wire.

The $\Delta E_{1/2}$ value can be used to calculate the comproportionation constant K_C for **2** and $\mathbf{2}^{2+}$, which in turn is a potential indicator for the stability of the mixed-valence species $\mathbf{2}^+$.[24] The $\Delta E_{1/2}$ values of **XVIII** and **XIX** correspond to K_C values of $1.44 \cdot 10^{11}$ and $9.42 \cdot 10^{9}$, respectively. The K_C of **2**, at $5.73 \cdot 10^{3}$, is several orders of magnitude lower. A K_C of $1.12 \cdot 10^{3}$

was reported for **XX**. This led us to conclude that the mixed-valence species **2**$^+$ should be accessible by chemical oxidation of **2**.

Table 3.3. Reduction potentials ($E_{1/2}$ vs. Fc^+/Fc in V) and ΔE_P (in V) of some dinuclear polyarene-bridged complexes determined by cyclic voltammetry (THF / NBu_4PF_6, Pt disk working electrode unless noted otherwise); see Figures 3.2 and 3.3 for the molecular structures.

	1st oxidation **[M] → [M]$^+$**	ΔE_p	2nd oxidation **[M]$^+$ → [M]$^{2+}$**	ΔE_p	$\Delta E_{1/2}$
2	–1.47	0.11	–1.25	0.10	0.22
XVIII	–1.61	0.09	–0.95	0.09	0.66
XIX	–1.64	–	–1.05	–	0.59
XX[d]	–1.32	–	–1.14	–	0.18
XXX^{2+}[a]	–1.47	0.08	–0.78	0.09	0.69
XXXI^{2+}[a]	–1.96	0.15	–1.78	0.10	0.18
XXXII^{2+}[a]	–1.91	0.08	–1.68	0.07	0.13
XXXIII^{2+}[b]	–2.07[c]	0.21	–1.75[c]	0.06	–

[a] Ref. 19a; [b] Ref.19b; [c] E_{Pc} values instead of $E_{1/2}$; [d] measured in acetonitrile / NBu_4PF_6; ΔE_P not available.

3.4.4 Quantum Chemical Calculations

In order to gain more insight into the properties of **2**, we performed DFT calculations at the BP86/def2-TZVP level of theory as implemented in Gaussian. The structural parameters of **2** are in good agreement with the values from X-ray crystallography (Table 3.1), with the difference in bond lengths remaining below 0.07 Å. We next analyzed the frontier molecular orbitals of **2** (Figure 3.12) and compared them with those of the related complexes **XVIII** and **XIX**.

The HOMO is largely metal-centered with smaller contributions from the naphthalene and Cp* ligands, while the lower lying orbitals (HOMO-1 and HOMO-2) are essentially composed of d orbitals of the two ruthenium centers. HOMO-3 and HOMO-4 are largely associated with one metal center each, with small ligand contributions. By contrast, the LUMO displays larger contributions from the naphthalene ligand, as do the higher lying orbitals LUMO+1, LUMO+3, and LUMO+4. The LUMO+2 shows interactions of metal d orbitals and the Cp* ligands with only minor contributions from the naphthalene ligand. Comparison with the diiron complex **XVIII** and the iron-ruthenium complex **XIX** shows that the composition of the molecular orbitals is largely identical in the three complexes.

The UV/vis spectrum of **2** was calculated using TD-DFT at the B3LYP/def2-TZVP level of theory to shed light on nature of the electronic transitions. The only band in the visible region, at 477 nm, is composed of transitions from the HOMO-2 to the LUMO as well as from the HOMO to the LUMO+1. This result is in very good agreement with the experimental UV/vis spectrum which shows a band at 492 nm.

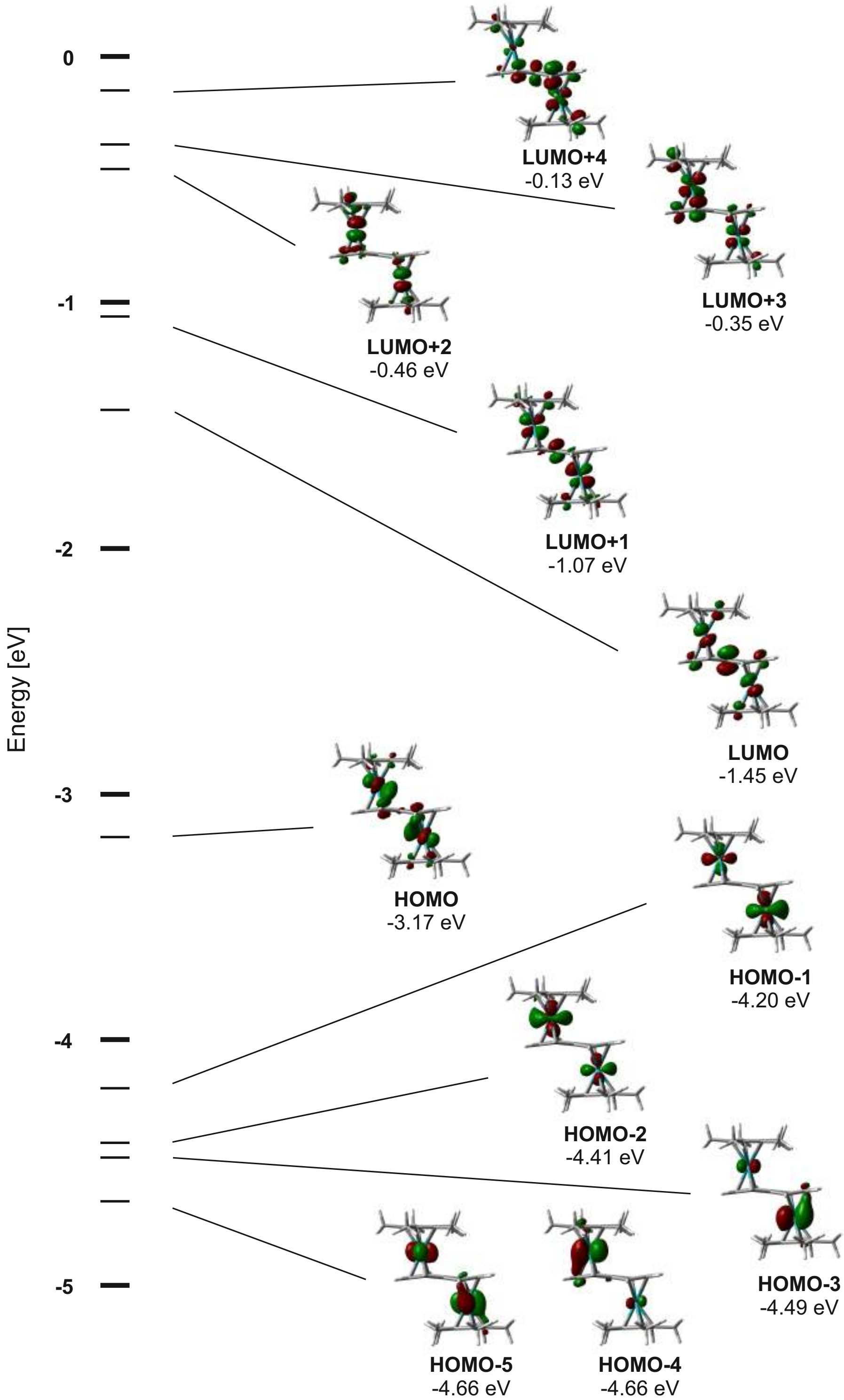

Figure 3.12. Frontier molecular orbitals of **2**, calculated with DFT at the BP86/def2-TZVP level of theory (molecular orbitals generated with GaussView 5.0).

3.4.5 UV-vis Spectroelectrochemistry

The changes in the electronic transitions upon oxidation of **2^0** to **2^+** and **2^{2+}** were monitored by UV-vis spectroelectrochemistry using an OTTLE cell. While both oxidation steps were found to be fully reversible at a scan rate of v = 100 mV s^{-1}, i.e. on a time scale of 1-2 minutes, the neutral species **2^0** could be only partially recovered after a CV measurement at v = 2 mV s^{-1} (74% of original amount). When performing the oxidation and back-reduction in rapid potential steps rather than a slow CV, 85% of the starting material were recovered.

The UV-vis spectrum of **2** shows a band in the visible region at 492 nm and three UV bands at 309, 274, and 240 nm. Upon oxidation to **2^+** (Figure 3.13a), these bands disappear and a new broad and weak band arises at 609 nm. Two additional bands at 467 and 250 nm become visible. When **2^+** is oxidized further to **2^{2+}** (Figure 3.13b), the bands in the visible range disappear and the original UV bands of **2** appear along with a new, relatively weak band at 365 nm. Upon back reduction, the spectrum of **2^+** and subsequently that of **2** is observed.

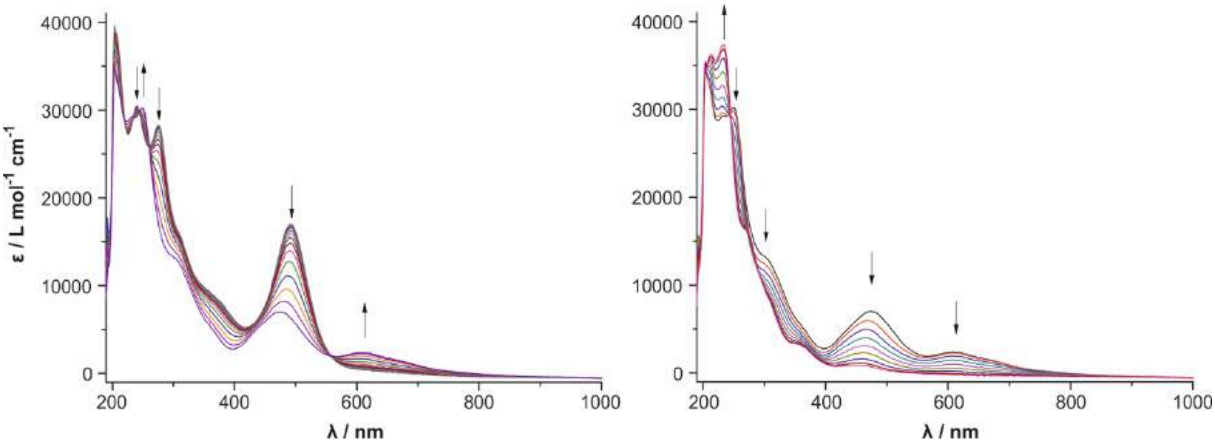

Figure 3.13. UV-vis spectral changes accompanying the processes **2** → **2^+** (left) and **2^+** → **2^{2+}** (right) on a Pt minigrid in THF / NBu_4PF_6 (v = 2 mV s^{-1}).

Comparing the UV-vis spectra of **XVIII**, **XIX**, and **2**, it is evident that replacing iron by ruthenium leads to a shift of the main visible band to higher energy, from 675 nm for **XVIII**[21b] to 599 nm for **XIX**[21c] to 492 nm for **2**. Complex **XX** gives a similar UV-vis spectrum with a maximum at 454 nm and a shoulder around 600 nm. Notably, although **XX** contains one Ru(0) and one Ru(II) center rather than two equivalent Ru(I) centers, which changes the nature of the frontier orbitals, Chin and co-workers reported that the visible bands are associated with the same transitions as those giving rise to the visible band of **2**. In all four complexes, oxidation to the mixed-valence species leads to the appearance of a new, very broad and weak band at lower energy (ca. 900 nm for **XVIII$^+$**, 796 nm for **XIX$^+$**, 854 nm for **XX$^+$**, and 609 nm for **2^+**). In **XVIII$^+$**, **XIX$^+$**, and **2^+**, another band appears at slightly higher energy relative to the visible absorption of the neutral complex (633 nm for **XVIII$^+$**, 591 nm for **XIX$^+$**, and 467 nm for **2^+**).

The oxidation to the dications **XVIII**$^{2+}$, **XIX**$^{2+}$, and **2**$^{2+}$ leads to the disappearance of all bands in the visible region. However, upon oxidation of **XX**$^{+}$ to **XX**$^{2+}$, the absorption at 454 nm reappears.

3.5 Chemical oxidation of [Cp*Ru(μ-$C_{10}H_8$)RuCp*]

3.5.1 Generation of Hydride Complexes

Since the electrochemical measurements indicated that the monocationic complex **2**$^{+}$ is stable, we attempted to synthesize it on a preparative scale. However, in contrast to **XVIII**$^{+}$ and **XIX'**$^{+}$, the oxidation of the neutral complex **2** with ferrocenium hexafluorophosphate in THF did not yield **2**$^{+}$. Instead, the cationic hydride complex [**2-H**]PF_6 was identified as one of the products by ^{1}H NMR spectroscopy and X-ray crystallography, presumably due to traces of residual moisture. To investigate **2-H**$^{+}$ in more detail, we developed a rational synthesis involving Brookhart's acid, $[H(OEt_2)_2]BAr^F_4$, as the hydrogen source (Scheme 3.9). After layering a concentrated diethyl ether solution with *n*-hexane, [**2-H**]BAr^F_4 was obtained as a colorless crystalline solid in 56% yield.

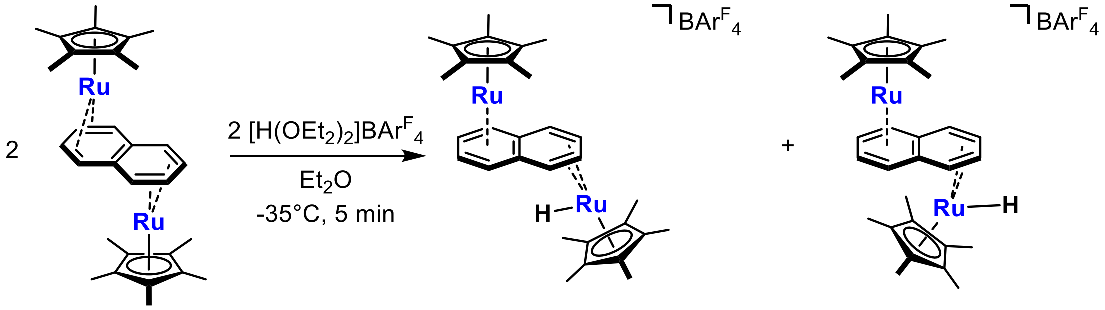

Scheme 3.9. Synthesis of **[2-H]**BAr^F_4.

Single crystals of **[2-H]**PF_6 suitable for X-ray diffraction were grown by layering a THF solution of the compound with *n*-hexane and storing at -30 °C. **[2-H]**PF_6 crystallizes in the triclinic space group *P*-1 with two molecules and one equivalent of THF in the unit cell. The molecular structure of **[2-H]**$^{+}$ (Figure 3.14) features two distinct Ru centers. While one ruthenium atom is coordinated by the naphthalene ligand in an η^6-fashion, the other ruthenium center is η^4-coordinated by naphthalene and bound by the hydride ligand, resulting in a 36 electron complex with both Ru centers in a formal oxidation state of +2. The asymmetric coordination of the naphthalene results in a significant folding along the C15/C18 vector by 36.5(1)°, which is in line with analogous η^4-naphthalene complexes (*vide supra*).

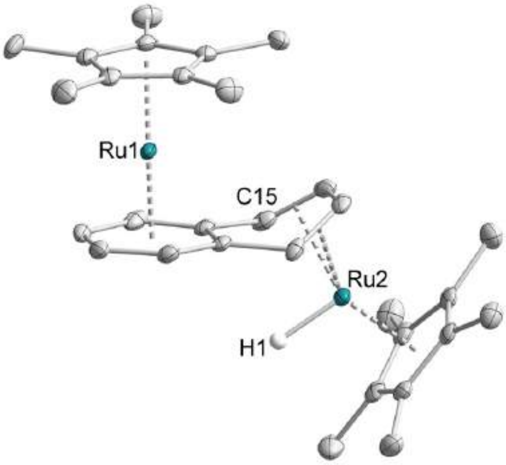

Figure 3.14. Solid state X-ray structure of **[2-H]**$^+$ (thermal ellipsoids at 50% probability; H atoms except H1 and counter anion omitted for clarity).

The diamagnetic complex gives rise to sharp signals in the ^{1}H NMR spectrum (recorded in C_6D_6). As for **2**, the signals of the naphthalene ligand are shifted to higher field with respect to free naphthalene. The H15/18 signal is shifted furthest upfield, at 2.82 ppm, while the remaining naphthalene signals are observed at 4.86 (H16/17), 4.14, and 3.78 ppm (H11-14). The signal of the hydride is found at -2.95 ppm. The two Cp* rings resonate at 1.41 and 1.17 ppm. The BAr^F_4 protons give rise to signals at 8.42 and 7.72 ppm. It is noteworthy that, when recording the spectrum very shortly after the reaction, a second set of signals can be observed shifted slightly upfield relative to the major product, with a hydride resonance at –3.09 ppm and signals for the naphthalene ligand at 2.68, 3.75, 4.04, and 4.69 ppm, respectively. The Cp* signals of the second species are observed at 1.28 and 1.07 ppm, and $BArF_4^-$ signals at 8.16 and 7.53 ppm. After leaving the sample overnight, only the major product is observed. Presumably, the minor species is an isomer of **[2-H]**BAr^F_4 in which the hydride atom is pointing away from the naphthalene ("*exo*-hydride"; Scheme 3.8). DFT calculations revealed that the main isomer ("*endo*-hydride") is more stable than the *exo*-hydride by 39.5 kJ mol^{-1}. Since the attack of the proton should proceed from the sterically least hindered position, the *exo*-hydride is assumed to be the kinetically favoured species which, upon storage overnight, is converted to the thermodynamically more stable *endo*-hydride.

The electrochemical analysis of **[2-H]**BAr^F_4 showed a reversible oxidation at E_{Pa} = 0.13 V vs. the ferrocenium/ferrocene couple as well as a strong, quasireversible reduction at –2.36 V (Figure 3.15). Notably, upon either of these nonreversible processes, the neutral complex **2** is formed along with a minor amount of the mononuclear cation **XXI**$^+$. The absence of redox waves corresponding to **2**^{x} at the start of the measurement confirms that **2** (or **2**$^{2+}$) is only formed upon electrochemical reduction or oxidation, respectively. This finding indicates that **2** may be an interesting candidate for the generation of H_2 by electrocatalytic proton reduction.

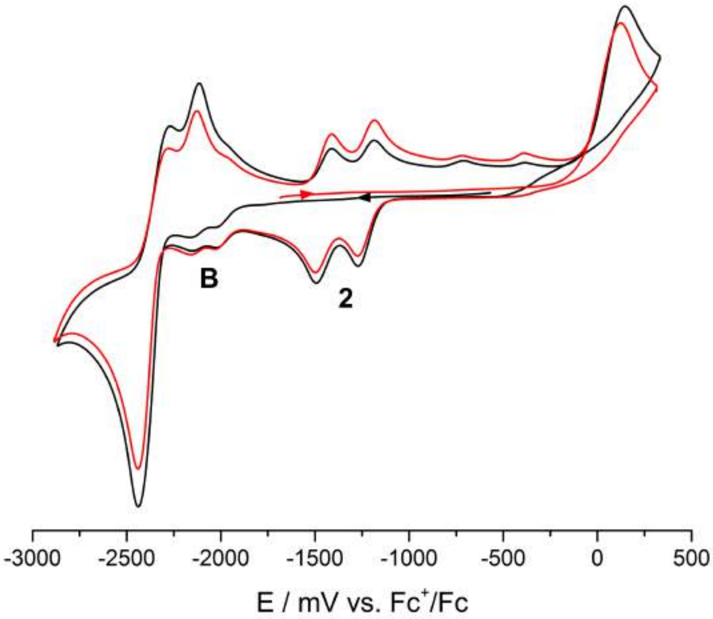

Figure 3.15. Cyclic voltammogram of **[2-H]**BAr^F_4 in THF/NBu_4PF_6 at v = 100 mV s^{-1}, starting with anodic oxidation (red) and cathodic reduction (black). Working electrode: Pt minidisk, counter electrode: Pt wire, pseudoreference electrode: Ag wire.

3.5.2 Preparation of [Cp*Ru($C_{10}H_8$)RuCp*]$^+$ (2^+)

Since the chemical oxidation of **2** using ferrocenium hexafluorophosphate in THF did not yield the expected product, we modified the procedure slightly, using $[Cp_2Fe]BAr^F_4$ instead of $[Cp_2Fe]PF_6$ as the oxidizing agent and diethyl ether rather than THF as the solvent. After removing the formed ferrocene and recrystallizing from diethyl ether, **[2]**BAr^F_4 was obtained in excellent yield as an olive-green crystalline solid.

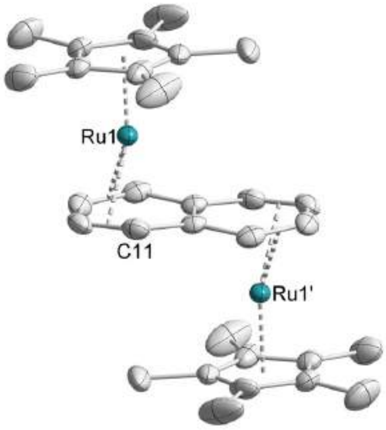

Figure 3.16. Solid state X-ray structure of $\mathbf{2^+}$ (thermal ellipsoids at 50% probability; hydrogen atoms and counterion omitted for clarity).

Table 3.4. Structural parameters of **2**$^+$, **XVIII**$^+$, **XIX**$^+$, and **XIX'**$^+$ obtained by X-ray crystallography and DFT calculations. DFT values given in italics. Numbering according to Figure 3.10.

	2$^+$ (M^1 = M^2 = Ru)	**XVIII**$^+$ [a] (M^1 = M^2 = Fe)	**XIX**$^+$ [b] (M^1 = Fe, M^2 = Ru)	**XIX'**$^+$ [c] (M^1 = Fe, M^2 = Ru)
M1–C11	2.220(3) / *2.223*	2.083(2) / *2.099*	– / *2.11*	2.100(3) / *2.12*
M1–C12	2.192(3) / *2.195*	2.052(3) / *2.063*	– / *2.00*	2.027(3) / *2.04*
M1–C13	2.200(3) / *2.196*	2.052(2) / *2.063*	– / *2.00*	2.030(3) / *2.04*
M1–C14	2.230(3) / *2.223*	2.084(2) / *2.099*	– / *2.11*	2.082(3) / *2.12*
M1–C19	2.416(3) / *2.425*	2.256(3) / *2.359*	– / *2.46*	2.690(3) / *2.63*
M1–C20	2.418(3) / *2.425*	2.253(3) / *2.359*	– / *2.46*	2.677(3) / *2.63*
M1–C(Cp) (av.)	2.183(2)	–	– / *2.10*	2.119(3) / *2.12*
M2–C15	–	–	– / *2.25*	2.227(3) / *2.24*
M2–C16	–	–	– / *2.16*	2.210(3) / *2.21*
M2–C17	–	–	– / *2.16*	2.211(3) / *2.21*
M2–C18	–	–	– / *2.25*	2.222(3) / *2.24*
M2–C19	–	–	– / *2.74*	2.277(3) / *2.38*
M2–C20	–	–	– / *2.74*	2.269(3) / *2.38*
M2–C(Cp) (av.)	–	–	– / *2.20*	2.178(3) / *2.20*
C11–C12	1.404(5) / *1.425*	1.403(4) / *1.430*	– / *1.43*	1.415(5) / *1.43*
C12–C13	1.417(6) / *1.423*	1.408(4) / *1.425*	– / *1.42*	1.396(5) / *1.42*
C13–C14	1.416(5) / *1.425*	1.414(4) / *1.430*	– / *1.43*	1.416(5) / *1.43*
C15–C16	–	–	– / *1.44*	1.412(5) / *1.42*
C16–C17	–	–	– / *1.43*	1.414(5) / *1.42*
C17–C18	–	–	– / *1.44*	1.415(5) / *1.42*
C14–C20	1.430(5)	1.428(4) / *1.445*	– / *1.43*	1.470(4) / *1.46*
C20–C15	–	–	– / *1.44*	1.422(5) / *1.43*
C18–C19	–	–	– / *1.44*	1.418(4) / *1.43*
C19–C11	1.437(5)	1.442(4) / *1.445*	– / *1.43*	1.469(5) / *1.46*
Fold angles	7.9(2)[d] / *8.35*	6.6(2) [d]	– , – / *13.9*[d], *21.1* [e]	28.7[d], 1.7[e] / *12.4*[d], *2.4*[e]

[a] X-ray and DFT values taken from ref. 21b; [b] DFT values taken from ref. 21c; [c] X-ray and DFT values taken from ref. 21c; [d] dihedral angle C11–C12–C13–C14 / C14–C20–C19–C11; [e] dihedral angle C15–C16–C17–C18 / C18–C19–C20–C15.

X-ray quality crystals were grown by slow evaporation of the solvent from a concentrated ether solution of [**2**]BAr$^{\mathrm{F}}_4$. The molecular structure of [**2**]BAr$^{\mathrm{F}}_4$ (Figure 3.16), which crystallizes in the triclinic space group *P*-1, shows a shift from an η^4 coordination to an intermediate between η^4 and η^6, as evidenced by the contraction of the Ru1–C15 and Ru1–C15' distances relative to those in complex **2** by 0.17 Å. This change in hapticity and the smaller fold angle of 7.9° are consistent with less electron-rich metal centers and a smaller degree of backbonding. Like **XVIII**$^+$, **2**$^+$ is centrosymmetric. Structural parameters obtained by DFT calculations at the BP86/def2-TZVP level of theory are in very good agreement with the values from X-ray crystallography. A list of relevant structural parameters is given in Table 3.4.

Due to the paramagnetic nature of **2**$^+$, no signals were observed in the ^{1}H NMR spectrum. The magnetic moment was determined by the Evans method. The observed value of $\mu_{eff} = 1.3(1)\ \mu_B$ is somewhat lower than the expected spin-only value of 1.73 μ_B for a complex featuring one unpaired electron.

The EPR spectrum of **[2]**BAr$^F{}_4$ reveals the presence of two species (Figure 3.17). The main species, representing ~97% of the total signal intensity, seems to correspond to the diruthenium complex **2**$^+$. The species reveals a rhombic spectrum with (poorly resolved) Ru hyperfine interactions (HFIs) along the g_y value (Figure 3.17, Table 3.5). The HFI seem to stem from a single ruthenium atom (coupling to ^{99}Ru and ^{101}Ru ~ 40 MHz, I = 5/2, 30% natural abundance). The minor species, representing only 3% of the total signal intensity, reveals an isotropic signal with g-values around 2.008. While the near isotropic nature of the signal is suggestive of the presence of an organic radical, the g-value perhaps deviates a bit too much from g_e to correspond to a pure organic radical like the naphthalene radical anion. As such, this minor signal probably stems from a second metal complex of unknown structure. Repeated experiments of several different samples of **[2]**BAr$^F{}_4$ in all cases revealed the presence of both components in similar ratios.

Table 3.5. Parameters used in the EPR simulations.

	Component 1	**Component 2**
g-tensor		
g_x	1.819	2.008
g_y	1.992	2.008
g_z	2.063	2.008
Hyperfine interactions (MHz)		
$A^{Ru}{}_x$	NR	-
$A^{Ru}{}_y$	40	-
$A^{Ru}{}_z$	NR	-

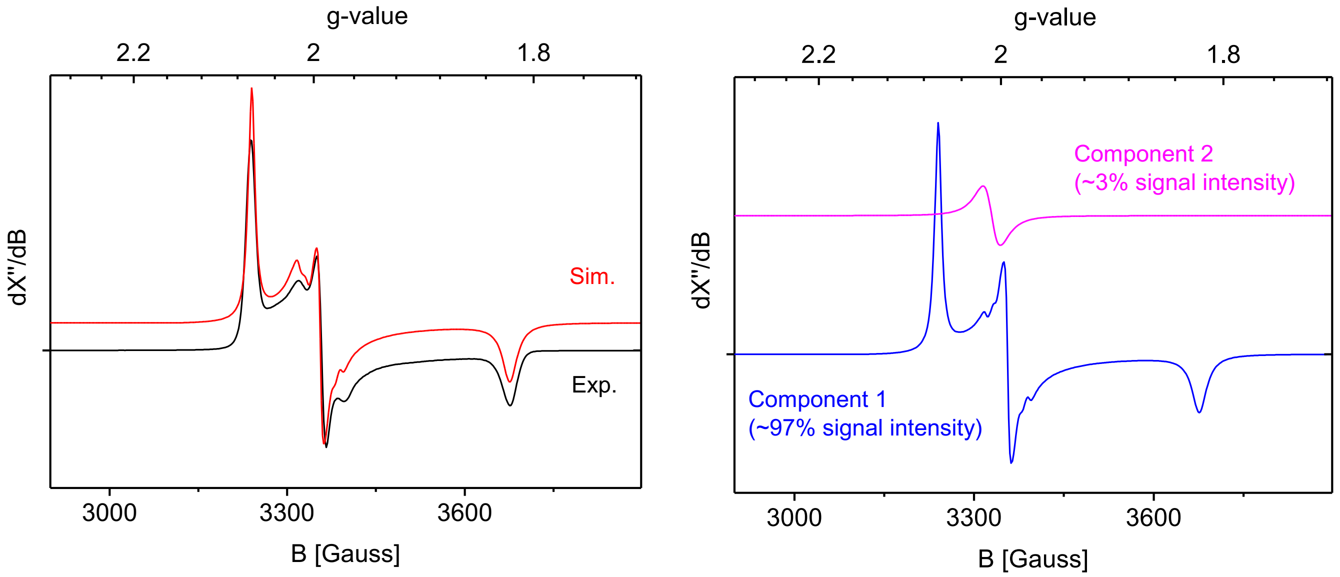

Figure 3.17. a) Experimental and simulated EPR spectra of compound **2**$^+$ measured in frozen THF at 20 K (NBu_4PF_6 added to obtain a better glass). Experimental parameters: Microwave frequency 9.363205 GHz, microwave power 0.632 mW, modulation amplitude 4 G. Simulation was obtained with the parameters shown in Table 3.5, assuming contribution of two species (b).

The UV/vis spectrum of **[2]**$BAr^F{}_4$ (recorded in THF) is in excellent agreement with the spectra obtained by the spectroelectrochemistry experiments (section 3.4.5), showing a weak band at 609 nm with a shoulder at 680 nm and a stronger band at 469 nm. The degree of electronic interaction between the two metal centers in a dinuclear complex can be estimated utilizing the theories of Hush and Brunschwig, Creutz, and Sutin, by analyzing the ratio of the theoretical half-height width of the intervalence transition band with the observed line width.[25] Unfortunately, a reliable analysis using Hush theory was not possible for [**2**]$BAr^F{}_4$ due to the severe overlap of the absorption bands at 609 and 680sh nm. Therefore, we investigated the electronic structure of **2**$^+$ by DFT calculations. The def2-TZVP basis set and various pure and hybrid functionals (BP86, B3LYP, CAM-B3LYP and BLYP35) were used.[26] The frontier molecular orbitals are displayed in Figure 3.18. Comparison with the MOs of the neutral complex **2** shows that the LUMOs are largely unchanged. The SOMO of **2**$^+$ shows some similarity with the HOMO of **2**, albeit with greater contributions from the Cp* and naphthalene ligands. Notably, the SOMO shows a high degree of symmetry with equal contributions from both metal centers. The lower-lying MOs are essentially d orbitals of the ruthenium centers and closely resemble the lower-lying occupied MOs of **2**.

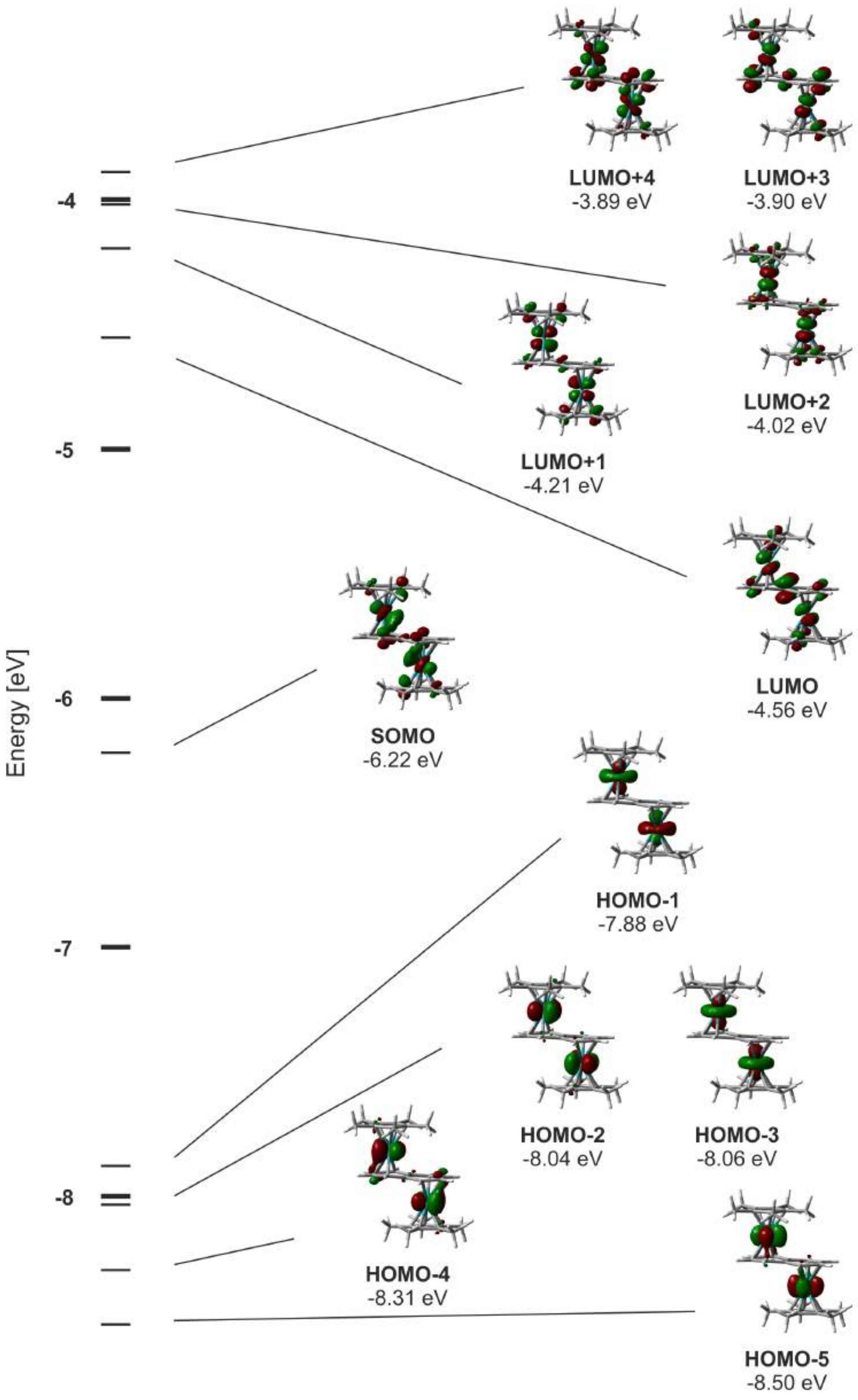

Figure 3.18. Frontier molecular orbitals of **2**$^+$ calculated by DFT at the BP86/def2-TZVP level of theory (molecular orbitals generated using GaussView 5.0).

The SOMO shows a high degree of symmetry with equal contributions from both metal centers. The spin density (Figure 3.19) is largely centered on the metal centers with minor contributions from the naphthalene and Cp* ligands. These calculations support the assignment of **2**$^+$ as a fully charge-delocalized class III species.[25] However, it should be noted that making a distinction between class III and borderline class II species is intricate even when several complementary spectroscopic techniques are applied.[26]

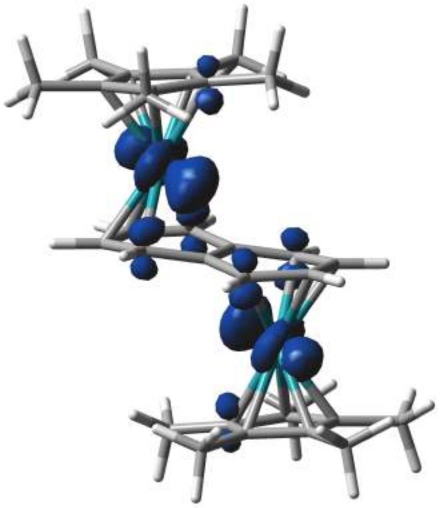

Figure 3.19. Spin density distribution of **2**$^+$ calculated at the BP86/def2-TZVP level of theory (spin density plot generated using GaussView 5.0).

3.6 References

[1] a) K. Jonas, *Angew. Chem.* **1985**, *97*, 292-307; b) K. Jonas, *Pure Appl. Chem.* **1990**, *62*, 1169-1174; c) J. E. Ellis, *Inorg. Chem.* **2006**, *45*, 3167-3186.

[2] a) M. Jang, J. E. Ellis, *Angew. Chem.* **1994**, *106*, 2036-2038; b) R. E. Jilek, M. Jang, E. D. Smolensky, J. D. Britton, J. E. Ellis, *Angew. Chem. Int. Ed.* **2008**, *47*, 8692-8695; c) E. Urnezius, W. W. Brennessel, C. J. Cramer, J. E. Ellis, P. v. R. Schleyer, *Science* **2002**, *295*, 832-834.

[3] W. W. Brennessel, V. G. Young Jr., J. E. Ellis, *Angew. Chem. Int. Ed.* **2002**, *41*, 1211-1215.

[4] a) R. Wolf, A. W. Ehlers, J. C. Slootweg, M. Lutz, D. Gudat, M. Hunger, A. L. Spek, K. Lammertsma, *Angew. Chem. Int. Ed.* **2008**, *47*, 4584-4587; b) R. Wolf, A. W. Ehlers, M. M. Khusniyarov, F. Hartl, B. de Bruin, G. J. Long, F. Grandjean, F. M. Schappacher, R. Pöttgen, J. C. Slootweg, M. Lutz, A. L. Spek, K. Lammertsma, *Chem. Eur. J.* **2010**, *16*, 14322-14334; c) J. Malberg, T. Wiegand, H. Eckert, M. Bodensteiner, R. Wolf, *Chem. Eur. J.* **2013**, *19*, 2356-2369; d) J. Malberg, T. Wiegand, H. Eckert, M. Bodensteiner, R. Wolf, *Eur. J. Inorg. Chem.* **2014**, 1638-1651; e) J. Malberg, M. Bodensteiner, D. Paul, T. Wiegand, H. Eckert, R. Wolf, *Angew. Chem. Int. Ed.* **2014**, *53*, 2771-2775; f) C. Rödl, R. Wolf, *Eur. J. Inorg. Chem.* **2016**, 736-742; g) D. Gärtner, A. Welther, B. Rezaei Rad, R. Wolf, A. Jacobi von Wangelin, *Angew. Chem. Int. Ed.* **2014**, *53*, 3722-3726; h) P. Büschelberger, D. Gärtner, E. Reyes-Rodriguez, F. Kreyenschmidt, K. Koszinowski, A. Jacobi von Wangelin, R. Wolf, *Chem. Eur. J.* **2017**, *23*, 3139-3151.

[5] a) K. Jonas, R. Mynott, C. Krüger, J. C. Sekutowski, Y.-H. Tsay, *Angew. Chem. Int. Ed. Engl.* **1976**, *15*, 767-768; b) K. Jonas, US Patent 4169845, **1979**.

[6] S. Pelties, T. Maier, D. Herrmann, B. de Bruin, C. Rebreyend, S. Gärtner, I. G. Shenderovich, R. Wolf, *Chem. Eur. J.* **2017**, *23*, 6094-6102.

[7] a) R. Wolf, E.-M. Schnöckelborg, *Chem. Commun.* **2010**, *46*, 2832-2834; b) E.-M. Schnöckelborg, J. J. Weigand, R. Wolf, *Angew. Chem.* **2011**, *123*, 6787-6790; *Angew. Chem. Int. Ed.* **2011**, *50*, 6657-6660; c) K. Weber, E.-M. Schnöckelborg, R. Wolf, *ChemCatChem* **2011**, *3*, 1572; d) B. Rezaei Rad, D. Herrmann, C. Lescop, R. Wolf, *Dalton Trans.* **2014**, *43*, 4247-4250; e) C. Hoidn, R. Wolf, *Dalton Trans.* **2016**, *45*, 8875-8884.

[8] a) A. M. McNair, K. R. Mann, *Inorg. Chem.* **1986**, *25*, 2519-2527; b) E. P. Kündig, F. R. Monnier, *Adv. Synth. Catal.* **2004**, *346*, 901-904.

[9] a) E. E. Karslyan, D. S. Perekalin, P. V. Petrovskii, K. A. Lyssenko, A. R. Kudinov, *Russ. Chem. Bull. Int. Ed.* **2008**, *57*, 2201-2203; b) E. E. Karslyan, D. S. Perekalin, P. V. Petrovskii, A. O. Borisova, A. R. Kudinov, *Russ. Chem. Bull. Int. Ed.* **2009**, *58*, 585-588; c) D. S. Perekalin, E. E. Karslyan, E. A. Trifonova, A. I. Konovalov, N. L. Loskutova, Y. V. Nelyubina, A. R. Kudinov, *Chem. Eur. J.* **2013**, 481-493; d) D. S. Perekalin, A. R. Kudinov, *Coord. Chem. Rev.* **2014**, *276*, 153-173.

[10] a) B. M. Trost, J. P. N. Papillon, T. Nussbaumer, *J. Am. Chem. Soc.* **2005**, *127*, 17921-17937; b) A. Labonne, T. Kribber, L. Hintermann, *Org. Lett.* **2006**, *25*, 5853-5856; c) L. Hintermann, L. Xiao, A.

Labonne, U. Englert, *Organometallics* **2009**, *28*, 5739-5748; d) F. Boeck, T. Kribber, L. Xiao, L. Hintermann, *J. Am. Chem. Soc.* **2011**, *133*, 8138-8141.

[11] P. J. Fagan, W. S. Mahoney, J. C. Calabrese, I. D. Williams, *Organometallics* **1990**, *9*, 1843-1852.

[12] a) S. A. Serron, L. Luo, C. Li, M. E. Cucullu, E. D. Stevens, S. P. Nolan, *Organometallics* **1995**, *14*, 5290-5297; b) C. Ernst, O. Walter, E. Dinjus, *J. Organomet. Chem.* **2001**, *627*, 249-254; c) J. Le Paih, S. Dérien, C. Bruneau, B. Demerseman, L. Toupet, P. H. Dixneuf, *Angew. Chem. Int. Ed.* **2001**, *40*, 2912-2915; d) J. Le Paih, S. Dérien, B. Demerseman, C. Bruneau, P. H. Dixneuf, L. Toupet, G. Dazinger, K. Kirchner, *Chem. Eur. J.* **2005**, *11*, 1312-1324; e) C. Fehr, I. Magpantay, M. Vuagnoux, P. Dupau, *Chem. Eur. J.* **2011**, *17*, 1257-1260; f) A. A. Birkbeck, X. Marquet, P. Millet, H. Pamingle, *Eur. J. Org. Chem.* **2014**, 7582-7585; g) K. Radkowski, B. Sundararaju, A. Fürstner, *Angew. Chem. Int. Ed.* **2013**, *52*, 355-360.

[13] a) D. Astruc, *Acc. Chem. Res.* **1997**, *30*, 383–391; b) T. Ren, *Organometallics* **2005**, *24*, 4854–4870; c) S. Szafert, J. A. Gladysz, *Chem. Rev.* **2003**, *103*, 4175–4206; d) F. Paul, C. Lapinte, *Coord. Chem. Rev.* **1998**, *178–180, Part 1*, 431–509.

[14] a) A. Ceccon, S. Santi, L. Orian, A. Bisello, *Coord. Chem. Rev.* **2004**, *248*, 683–724; b) P. Aguirre-Etcheverry, D. O'Hare, *Chem. Rev.* **2010**, *110*, 4839–4864; c) S. Barlow, D. O'Hare, *Chem. Rev.* **1997**, *97*, 637–670.

[15] a) M. N. Bochkarev, I. L. Fedushkin, H. Schumann, J. Loebel, *J. Organomet. Chem.* **1991**, *410*, 321-326; b) B. F. Bush, J. J. Lagowski, *J. Organomet. Chem.* **1990**, *386*, 37-50; c) S. Sun, C. A. Dullaghan, G. B. Carpenter, A. L. Rieger, P. H Rieger, D. A. Sweigart, *Angew. Chem. Int. Ed. Engl.* **1995**, *34*, 2540-2542.

[16] a) W. H. Morrison, E. Y. Ho, D. N. Hendrickson, *J. Am. Chem. Soc.* **1974**, *96*, 3603–3608; b) W. H. Morrison, Jr., E. Y. Ho, D. N. Hendrickson, *Inorg. Chem.* **1975**, *14*, 500-506.

[17] a) A. J. Frings, PhD dissertation, Ruhr-Universität Bochum, Germany, **1988**; b) P. Klusmann, PhD dissertation, Ruhr-Universität Bochum, Germany, **1993**.

[18] D. S. Perekalin, A. R. Kudinov, *Coord. Chem. Rev.* **2014**, *276*, 153-173.

[19] a) U. Koelle, M. H. Wang, *Organometallics* **1990**, *9*, 195-198; b) I. Chavez, A. Cisternas, M. Otero, E. Román, U. Müller, *Z. Naturforsch.* **1990**, *45b*, 658-666; c) I. Chavez, M. Otero, E. Román, U. Müller, *J. Organomet. Chem.* **1992**, *427,* 369-378; d) H. Salembier, J. Mauldin, T. Hammond, R. Wallace, E. Alqassab, M. B. Hall, L. M. Pérez, Y.-J. A. Chen, K. E. Turner, E. Bockoven, W. Brennessel, R. M. Chin, *Organometallics* **2012**, *31*, 4838-4848.

[20] M. A. Bennett, Z. Lu, X. Wang, M. Bown, D. C. R. Hockless, *J. Am. Chem. Soc.* **1998**, *120*, 10409-10415.

[21] a) E.-M. Schnöckelborg, PhD dissertation, University of Münster, Germany, **2011**; b) E.-M. Schnöckelborg, F. Hartl, T. Langer, R. Pöttgen, R. Wolf, *Eur. J. Inorg. Chem.* **2012**, *2012*, 1632–1638; c) J. Malberg, E. Lupton, E.-M. Schnöckelborg, B. de Bruin, J. Sutter, K. Meyer, F. Hartl, R. Wolf, *Organometallics* **2013**, *32*, 6040–6052.

[22] T. Hatanaka, Y. Ohki, T. Kamachi, T. Nakayama, K. Yoshizawa, M. Katada, K. Tatsumi, *Chem. Asian J.* **2012**, *7*, 1231-1242.

[23] E.-M. Schnöckelborg, M. M. Khusniyarov, B. de Bruin, F. Hartl, T. Langer, M. Eul, S. Schulz, R. Pöttgen, R. Wolf, *Inorg. Chem.* **2012**, *51*, 6719-6730.

[24] D. E. Richardson, H. Taube, *Inorg. Chem.* **1981**, *20*, 1278-1285.

[25] M. B. Robin, P. Day, *Adv. Inorg. Chem. Radiochem.* **1967**, *10*, 247-422.

[26] R. F. Winter, *Organometallics* **2014**, *33*, 4517-4536.

[27] a) M. Renz, K. Theilacker, C. Lambert, M. Kaupp, *J. Am. Chem. Soc.* **2009**, *131*, 16292–16302; b) M. Parthey, J. B. G. Gluyas, P. A. Schauer, D. S. Yufit, J. A. K. Howard, M. Kaupp, P. J. Low, *Chem. Eur. J.* **2013**, *19*, 9780–9784; c) M. Parthey, J. B. G. Gluyas, M. A. Fox, P. J. Low, M. Kaupp, *Chem. Eur. J.* **2014**, *20*, 6895–6908; d) M. Parthey, M. Kaupp, *Chem. Soc. Rev.* **2014**, *43*, 5067–5088; e) M. Kaupp, M. Renz, M. Parthey, M. Stolte, F. Werthner, C. Lambert, *Phys. Chem. Chem. Phys.* **2011**, *13*, 16973.

4. Synthesis of NHC Precursor Materials and NHC-Silver Complexes

4.1 Introduction

4.1.1 Preparation of *N*-heterocyclic Carbenes

Nearly 50 years ago, Wanzlick and Öfele were the first to report the preparation of transition metal complexes stabilized by *N*-heterocyclic carbenes (NHCs) by reacting imidazolium salts with basic metal precursors such as mercury acetate (Scheme 4.1, top left) or hydrido-pentakis(carbonyl)chromium(I) (Scheme 4.1, bottom left).[1] Shortly afterwards, the group of Lappert developed a synthetic approach starting from tetraazafulvalenes as NHC precursors which, for several decades, remained the most versatile method to generate NHC complexes (Scheme 4.1, right).[2]

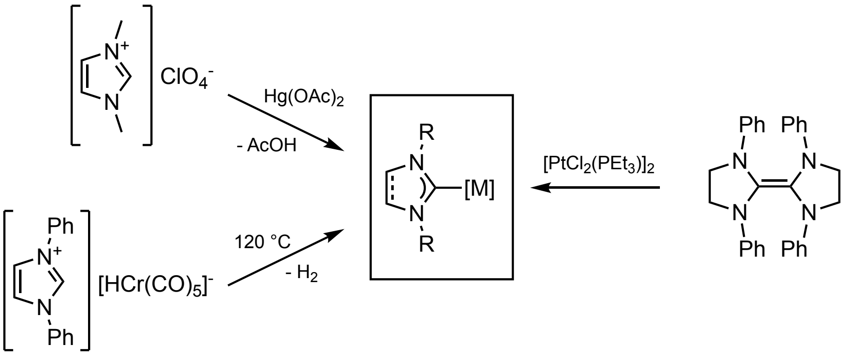

Scheme 4.1. Earliest examples of transition metal complexes containing NHC ligands.

It was not until Arduengo's landmark discovery of 1,3-diadamantylimidazolin-2-ylidene in 1991[3] that free NHCs became synthetically accessible. Since then, various synthetic routes have been developed to prepare free *N*-heterocyclic carbenes (Scheme 4.2). The applicability of these routes depends on a range of factors such as the nature of the *N*-substitutents, the backbone, or synthetic access to suitable precursor materials. Since detailed reviews on the preparation methods of *N*-heterocyclic carbenes are available,[4] they will only be briefly summarized here.

A popular method to generate free NHCs is by reduction of a cyclic thiourea (imidazolin-2-thione or imidazolidin-2-thione) with potassium metal (Scheme 4.2, route **A**) in refluxing THF.[5] While the reduction itself is straightforward, the preparation of suitable thiourea precursors poses a challenge and the route is limited to *N*-alkyl substituents.

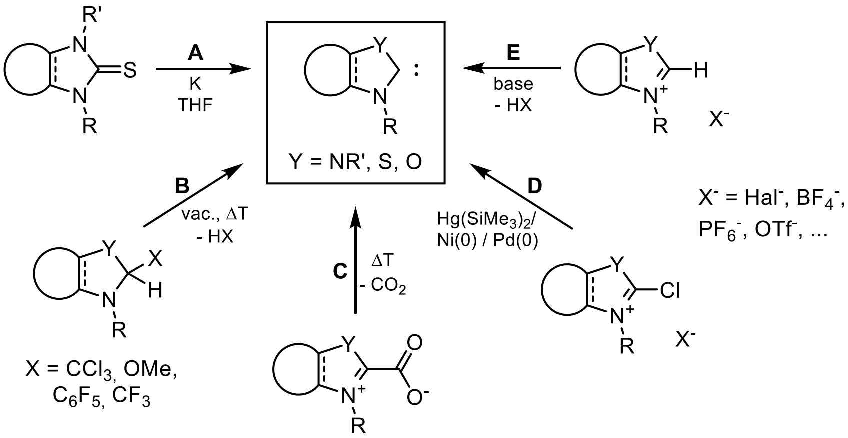

Scheme 4.2. Synthetic routes toward *N*-heterocyclic carbenes.

When Wanzlick postulated the existence of *N*-heterocyclic carbenes in 1961, he proposed that they can be accessed via the elimination of chloroform from trichloromethylimidazolidines (route **B**, X = CCl_3) by vacuum thermolysis (Scheme 4.2, route **B**).[6] While Wanzlick only obtained the dimers of his postulated carbenes, his synthesis method was later found to be effective for the formation of carbenes. In the CCl_3 adduct, chloroform can be considered a "protecting group" for the carbene carbon atom. Other carbene protecting groups, such as OMe, C_6F_5, or CF_3 are also effective.[7] Route **B** has become popular for generating carbenes *in situ* since the adducts are generally stable and much easier to handle and, unlike other routes to prepare carbenes, no additional reagents are required. However, drastic reaction conditions (vacuum, high temperature) are necessary.

The closely related route **C** employs CO_2 as a carbene protecting group, which is introduced by deprotonating an imidazolium salt in an atmosphere of carbon dioxide. The formed zwitterion dissociates upon heating, releasing CO_2 and the free carbene.[8]

More specialized methods have been developed, such as the use of 2-chloroazolium salts as carbene precursors (route **D**). 2-Chloroimidazolium salts can be converted to NHCs either by reduction using $Hg(SiMe_3)_2$ or by oxidative addition to low-valent Ni, Pd, or Pt complexes.[9]

The most popular method of generating NHCs, by far, is the deprotonation of azolium salts (route **E**). Wanzlick's and Öfele's early reports showed the possibility to generate NHCs this way,[1] and Arduengo prepared and isolated free 1,3-diadamantylimidazolin-2-ylidene (IAd) in 1991 by deprotonating 1,3-bis(adamantyl)imidazolium chloride with sodium hydride in THF in the presence of catalytic amounts of DMSO.[3] Route **E** is extremely versatile due to the well-established access to precursor salts, and a range of protocols have been developed employing different bases and reaction conditions.

4.1.2 Preparation of Azolium Salts as NHC Precursors

A large variety of synthetic procedures for the preparation of azolium salts have been developed over the last 25 years (Scheme 4.3).[4b] Apart from the straightforward *N*-substitution of imidazole or benzimidazole, symbolized by the arc at the backbone (route **1**), most syntheses involve a cyclization step, usually either introducing the precarbenic carbon atom as a C_1 building block into a preformed *N*,*N'*-disubstituted diamine or diimine (route **2**), or attaching the backbone to a formamidine carrying the *N*-substituents (route **3**). Varying the *N*-substituents and the backbone makes it possible to fine-tune the steric and electronic properties of the azolium salt and the carbene formed subsequently.

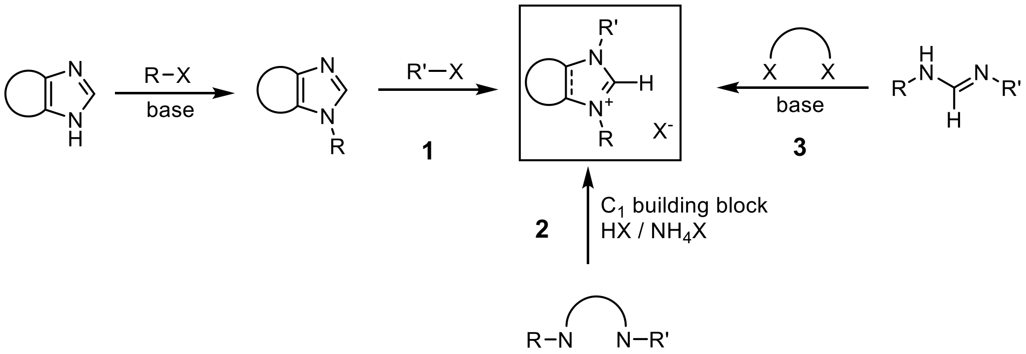

Scheme 4.3. Methods for the preparation of azolium salts.

The simplest, most straightforward way to prepare an imidazolium or benzimidazolium salt is the addition of alkyl halides RX to (benz-)imidazole (route **1**; Scheme 4.3, left). This route allows the synthesis of asymmetric imidazolium salts, i.e. with different substituents R and R' on the two nitrogen atoms when adding RX and R'X in consecutive steps. Dyson et. al. reported an improved procedure involving 1-(trimethylsilyl)imidazole which makes the addition of a base unnecessary.[10] The scope of route **1** is limited by several factors. Most importantly, it is limited to alkylated azolium salts; in order to introduce aryl substitutents, a Buchwald-Hartwig type amination using a Pd catalyst is necessary. Furthermore, azolium salts with α-chiral substitutents are not accessible since the stereoinformation on the α-carbon atom is lost in the S_N reaction.

Route **2** (Scheme 4.3, bottom) involves two consecutive steps. First, the "backbone" of the NHC ring, i.e. the end opposite the carbene carbon atom, is built up. Subsequently, cyclization with a suitable C_1 building block under acidic conditions leads to the formation of the desired azolium salt. The backbone part can either be a *N*,*N'*-disubstituted 1,2-diimine (for the preparation of imidazolium salts), a *N*,*N'*-disubstituted ethylenediamine (for the synthesis of imidazolinium, or 4,5-dihydroimidazolium salts), or a 1,2-phenylenediamine (for the preparation of benzimidazolium salts). The C_1 building block, later to become the carbene carbon, is either formaldehyde (for the reaction with 1,2-diimines) or an orthoformic acid ester such as triethyl orthoformate (in the reaction with 1,2-ethylenediamines or 1,2-phenylenediamines).

The synthesis of imidazolium salts following route **2** is an adaptation of the Debus-Radziszewski imidazole synthesis. In this classic heterocycle synthesis, glyoxal is reacted with ammonia to afford 1,4-diazabutadiene, followed by cyclization with formaldehyde. To obtain *N*,*N'*-disubstituted imidazolium salts, primary amines are used in the first step rather than NH_3. In the second step, the addition of an acid HX is necessary to afford the cyclization product (Scheme 4.4).

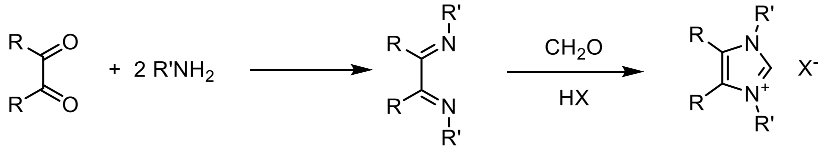

Scheme 4.4. Preparation of imidazolium salts via cyclization of α–diimines.

The imidazolium precursors for the most widely used *N*-heterocyclic carbenes, 1,3-bis(2,4,6-trimethylphenyl)imidazolin-2-ylidene (IMes) and 1,3-bis(2,6-diisopropylphenyl)imidazolin-2-ylidene (IDipp), are accessible via this route, and a highly optimized protocol was developed by Nolan et.al.[11] However, this procedure was found to give low yields or undesired byproducts when using other aryl- or alkylamines. Various modifications exist, such as Bildstein's synthesis of bis(ferrocenyl)imidazolium triflate, in which the intermediate 1,2-diimine is activated by $Zn(OTf)_2$. Replacement of glyoxal by a diketone allows the introduction of substituents on the backbone.

Imidazolinium salts, or 4,5-dihydroimidazolium salts, are accessible via the cyclization of an *N*,*N'*-disubstituted ethylenediamine with tryalkyl orthoformate under acidic conditions (Scheme 4.5). An ammonium salt NH_4X is commonly employed to introduce the counterion X^-. The right choice of X is important not only for the follow-up reactivity of the imidazolinium salt (e.g. in the preparation of silver complexes, *vide infra*), but also because it can determine the success of the reaction. Alexakis reported that procedures optimized for the synthesis of imidazolium tetrafluoroborates give very low yields when replacing BF_4^- by Cl^-.[12]

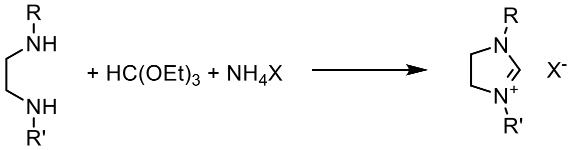

Scheme 4.5. Preparation of imidazolinium salts via cyclization of 1,2-ethylenediamines.

N,*N′*-disubstituted ethylenediamines can be prepared in a number of ways (Scheme 4.6), the easiest being the reaction of 1,2-dibromoethane with two equivalents of a primary amine. While straightforward, some complications can arise from this method (see section 4.2.4). Alternatively, *N*,*N′*-disubstituted ethylenediamines are accessible in two steps starting either from ethylenediamine and aldehydes or from primary amines and α-dicarbonyl compounds (e.g. glyoxal) followed by reduction with $NaBH_4$ or $LiAlH_4$. Asymmetrically substituted ethylenediamines are accessible via a three-step synthesis starting from 2-chloroacetyl chloride.

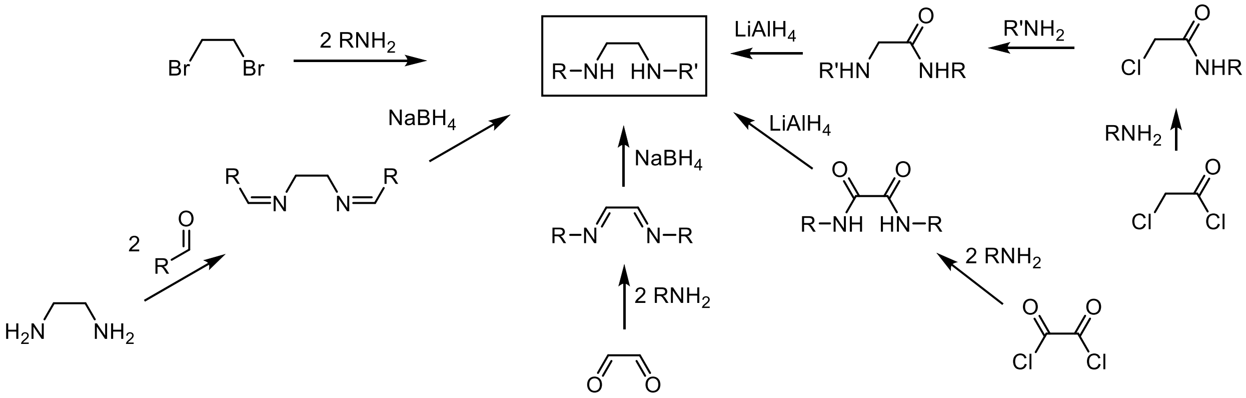

Scheme 4.6. Synthesis of *N*,*N′*-substituted 1,2-ethylenediamines.

Route **2** allows the introduction of virtually any *N*-substituent, the preparation of ring-expanded NHC precursor salts as well as the use of substituted or annulated backbones. It should be noted, however, that ethylenediamines can be somewhat air-sensitive and should be handled under inert conditions.

Route **3** avoids any air-sensitive intermediates by introducing the *N*-substituents into a formamidine, followed by cyclization to give the azolium salt (Scheme 4.7). The formamidine is obtained by condensation of a trialkyl orthoformate with a primary amine at elevated temperatures. To obtain an imidazolinium salt, the formamidine is deprotonated by a strong base, e.g. *n*-butyllithium, and reacted with 1,2-dibromoethane Scheme 4.7, top). The synthesis of imidazolium salts with substituted backbones proceeds via the condensation with an α-haloketone followed by an acetylation-elimination reaction (Scheme 4.7, middle). Glorius and co-workers prepared a library of azolium salts with various alkyl and aryl substitutents on the backbone as well as the nitrogen atoms this way. A related procedure was reported by Togni et. al., who prepared a bis(ferrocenyl)imidazolium salt featuring an unsubstituted, unsaturated backbone using 2-bromoacetaldehyde-diethyl acetal (Scheme 4.7, bottom).[13]

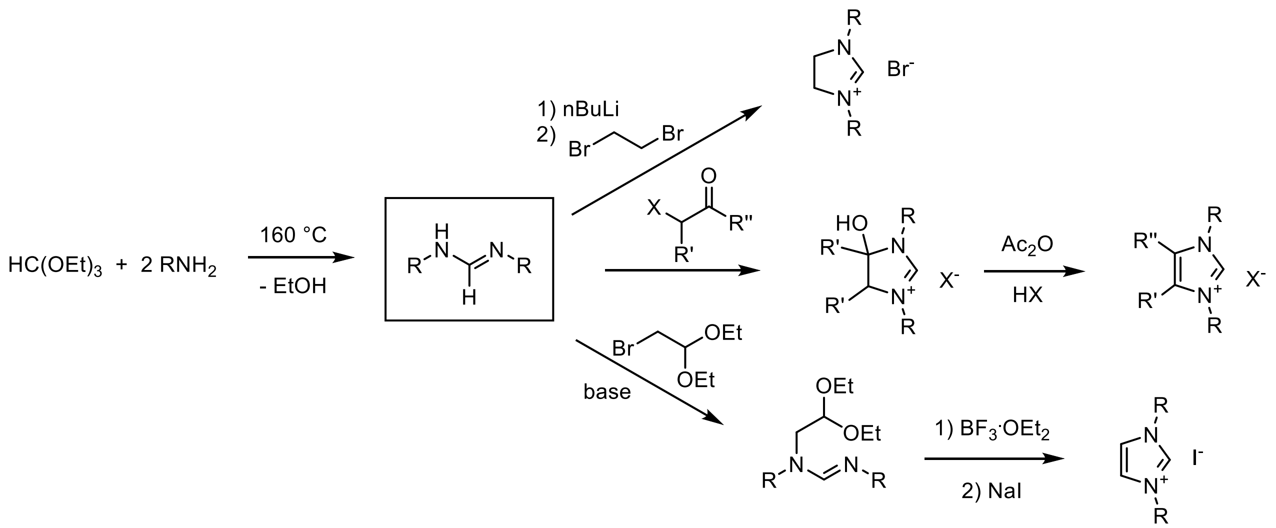

Scheme 4.7. Preparation of (4,5-dihydro)imidazolium salts via cyclization of a formamidine.

4.2 Synthesis of naphthyl-substituted imidazolium, imidazolinium, and benzimidazolium salts

Naphthyl substituents on *N*-heterocyclic carbenes have been used as stereodirecting groups in asymmetric catalysis,[14] and the synthesis of these ligands is described in the literature. While some procedures were reproduced for this thesis, others proved difficult to reproduce so that alternative routes had to be found.

NHC precursors with saturated backbones and 1-naphthylmethyl, the chiral (*R*)-1-(1-naphthyl)ethyl, and α-naphthyl substituents were prepared. Different backbones (saturated, unsaturated, and benzannulated) were used in carbene precursors with 1-naphthylmethyl substituents.

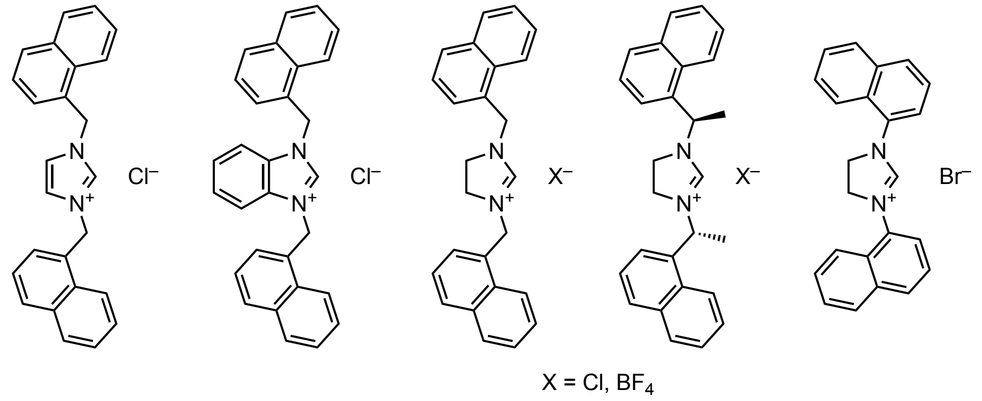

XXXIX **XL** **XLI** **XLII** (X = BF$_4$) **4** (X = Cl) **5**

Figure 4.1. Naphthyl-substituted azolium salts prepared following routes 1-3.

4.2.1 Synthesis of 1,3-Bis(1-naphthylmethyl)imidazolium chloride ([INpMeH]Cl, XXXIX)

Following a procedure by Dyson and co-workers,[10] 1,3-bis(1-naphthylmethyl)imidazolium chloride ([INpMeH]Cl, **XXXIX**) was prepared in a straightforward manner. In a modification of route 1, reaction of *N*-trimethylsilylimidazole with two equivalents of 1-chloromethylnaphthalene in THF at elevated temperature overnight yielded the product in 65% yield after recrystallization from CH_2Cl_2 / diethyl ether.

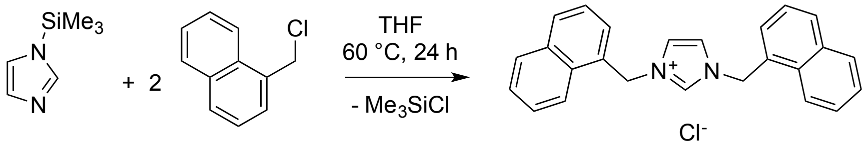

Scheme 4.8. Preparation of [INpMeH]Cl (**XXXIX**) from TMS-imidazole and 1-(chloromethyl)-naphthalene.

The ^1H NMR spectrum of **XXXIX**, recorded in $CDCl_3$, displays the expected signals corresponding to the protons of the naphthyl groups in the region of 7.41 to 8.05 ppm, the backbone at 6.89 ppm, and the methylene group of the *N*-substitutents at 6.03 ppm. The C_2 proton at the pre-carbenic carbon resonates at 11.47 ppm.

4.2.2 Synthesis of 1,3-Bis(1-naphthylmethyl)benzimidazolium chloride ([BNpMeH]Cl, XL)

The related 1,3-bis(1-naphthylmethyl)benzimidazolium chloride ([BNpMeH]Cl, **XL**) was also prepared following route 1. In the first step, following a modified procedure by Komarova and co-workers,[15] benzimidazole was reacted with an excess of KOH and one equivalent of 1-chloromethylnaphthalene, giving 1-(1-naphthylmethyl)benzimidazole as a colorless solid in 91% yield after aqueous workup. The second step was performed following a procedure by Özdemir and co-workers.[16] Reaction of 1-(1-naphthylmethyl)benzimidazole with a second equivalent of 1-chloromethylnaphthalene afforded **XL** as a colorless powder in 86% yield after filtration and washing with diethyl ether.

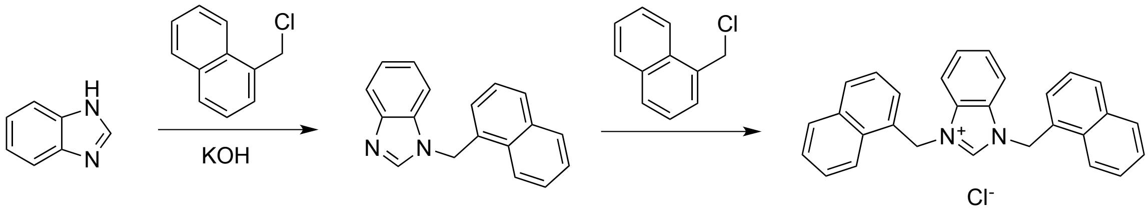

Scheme 4.9. Preparation of [BNpMeH]Cl (**XL**) from benzimidazole and 1-(chloromethyl)-naphthalene.

The ^{1}H NMR spectrum of **XL**, recorded in $CDCl_3$, is comparable to that of **XXXIX**, showing signals for the naphthyl groups and the aromatic backbone in the range 7.27-7.58 as well as 7.80 and 8.16 ppm. The methylene group resonates at 6.33 ppm and the azolium signal is found at 12.08 ppm.

4.2.3 Synthesis of 1,3-bis(1-naphthylmethyl)imidazolinium salts ([SINpMeH]X, XLI)

The synthesis of 1,3-bis(1-naphthylmethyl)imidazolinium chloride ([SINpMeH]Cl, **XLI**) was recently reported by Gök and co-workers following route 1, by reacting 1-(1-naphthylmethyl)imidazolin with 1-chloromethylnaphthalene.[17] The synthesis employed in this thesis, however, followed the procedure reported by Bruneau et. al. for related benzyl and (9-anthracenyl)methyl substituted imidazolinium salts.[18] Ethylenediamine was reacted with two equivalents of 1-naphthaldehyde to yield the 1,4-diimine, which was reduced to the 1,2-diamine using sodium borohydride. Reaction of the diamine with an excess of triethyl orthoformate and one equivalent of ammonium chloride yielded **XLI** as a light brown powder in 84% yield.

The corresponding tetrafluoroborate salt **XLI'** was prepared analogously, using ammonium tetrafluoroborate instead of ammonium chloride. **XLI'** was obtained as a colorless, crystalline solid after recrystallization from ethanol/diethyl ether.

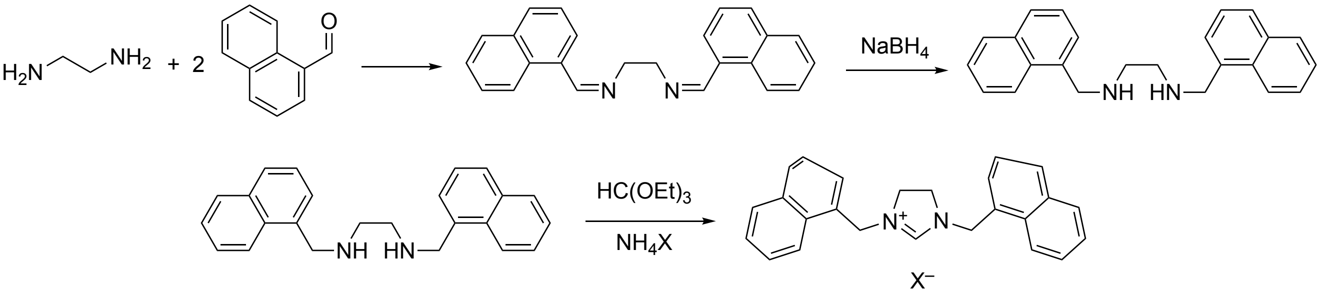

Scheme 4.10. Preparation of [SINpMeH]Cl (**XLI**) and [SINpMeH]BF_4 (**XLI'**).

In the ^{1}H NMR spectrum of **XLI**, recorded in $CDCl_3$, four signals are found that correspond to the naphthyl groups, at 7.40, 7.49-7.54, 7.59-7.65, and 8.18 ppm. The protons of the backbone are found at 3.59 ppm, which is in the expected range for an ethylenediamine. The CH_2 group resonates at 5.36 ppm, which is slightly more upfield than for **XXXIX** and **XL**. The azolium proton resonates at 11.10 ppm. The ^{1}H NMR spectrum of **XLI'** in $CDCl_3$ is almost identical to that of **XLI**, with the backbone protons at 3.70 ppm, the methylene group at 5.23 ppm, and the naphthyl groups at 7.42, 7.49-7.54, 7.60, 7.85, and 7.96 ppm. The key difference is the shift of the azolium proton, which resonates at 8.66 ppm, significantly upfield compared to **XLI** due to the lack of hydrogen bonding to the counterion.

4.2.4 Synthesis of *R,R*-1,3-Bis(1-(1-naphthyl)ethyl)imidazolinium tetrafluoroborate ([SINpEtH]BF_4, XLII)

The chiral imidazolinium salt (*R,R*)-1,3-bis(1-(1-naphthyl)ethyl)imidazolinium tetrafluoroborate ([SINpEtH]BF_4, **XLII**) was prepared following the procedure of Glorius and co-workers.[19] 1,2-Dibromoethane was reacted with two equivalents of (*R)*-1-(1-naphthyl)ethylamine to yield the disubstituted ethylenediamine, which, after alkaline workup, was reacted with stoichiometric amounts of triethyl orthoformate and ammonium tetrafluoroborate to give the imidazolinium salt in 47% yield as a crystalline, colorless solid after recrystallization from ethanol/diethyl ether.

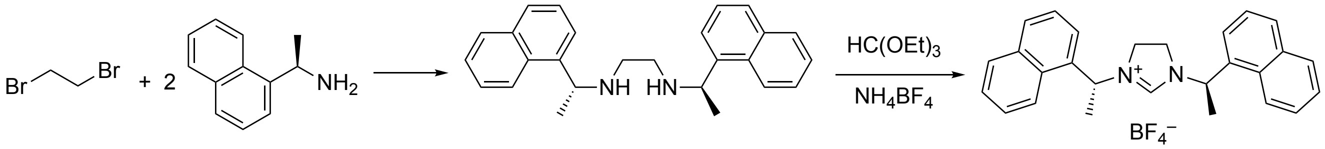

Scheme 4.11. Preparation of [SINpEtH]BF_4 (**XLII**).

The ^{1}H NMR spectrum of **XLII** shows similar signals to that of **XLI'**. Five signals in the range 7.43-8.02 ppm correspond to the naphthyl groups. A quartet at 5.83 ppm represents the protons at the alpha-carbon atoms which couple with the adjacent CH_3 group. This signal corresponding to this CH_3 group is a doublet at 1.94 ppm. The backbone protons couple with the chiral *N*-substituents and thus form a complex multiplet at 3.49-3.79 ppm. The azolium proton is found at 8.62 ppm.

The reason for the modest yield of **XLII** is likely the incomplete conversion of dibromoethane to the diamine. Attempts to increase the yield of diamine obtained from this reaction remained unsuccessful. When exchanging NH_4BF_4 by NH_4Cl, the desired imidazolinium chloride **4** could not be isolated in acceptable purity. Neither distillation nor column chromatography afforded the disubstituted diamine, so that the by-products remained in the reaction mixture for the cyclization step. While **XLII** crystallizes easily from solution, it can be isolated in good purity nonetheless, which is not the case for **4**. Consequently, only an oily crude product was obtained; attempts to purify the product failed.

However, pure *N,N'*-bis(1-(1-naphthyl)ethyl)ethylenediamine can be obtained via a different route. Following a modified procedure by Fiksdahl and co-workers[20], the condensation of oxalyl chloride with two equivalents of *R*-1-(1-naphthyl)ethylamine afforded the disubstituted 1,2-diamide in 87% yield. The diamide was subsequently reduced with an excess of lithium aluminum hydride. The 1,2-diamine thus obtained can be easily purified by column chromatography over silica using a 9:1 mixture of dichloromethane and methanol as the eluent, giving the product as a colorless oil in 80% yield. Reaction with triethyl orthoformate and ammonium chloride afforded the desired product **4** as a light brown solid in 73% yield, giving an overall yield of 51% (2.35 g) over three steps.

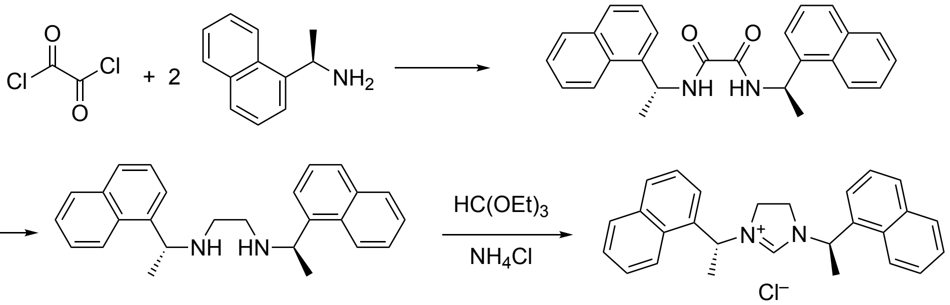

Scheme 4.12. Preparation of [SINpEtH]Cl (**4**) via the 1,2-oxalamide.

The ^{1}H NMR spectrum of **4** in $CDCl_3$ is largely identical to that of **XLII**. The naphthyl groups are found in the range 7.39-8.32 ppm, the protons at the *N*-adjacent stereocenters resonate at 6.19 ppm, the methyl groups at 2.02 ppm, and the backbone is identified as the multiplet at 3.23-3.62 ppm. As for the other azolium chlorides **XXXIX**, **XL**, and **XLI**, the signal of the C_2 proton is shifted far downfield to 11.28 ppm.

4.2.5 Synthesis of 1,3-Bis(1-naphthyl)imidazolinium bromide ([SINpH]Br, 5)

In the imidazolinium salt **5**, the 1-naphthyl substituents are bound directly to the N atoms of the central ring without an alkyl spacer, which has a pronounced effect on the properties of the salt and the derived carbene complexes. Dorta and co-workers reported the synthesis of analogous imidazolinium salts [SINp^{R}H]X (X = Cl, BF_4) via route 2 (*vide supra*, scheme 4.3), i.e. the preparation of an *N*,*N'*-disubstituted ethylenediamine and subsequent cyclization with triethyl orthoformate.[21] The diamines carrying naphthyl groups with various substituents were prepared from the respective 1-bromonaphthalenes and ethylenediamine via a Pd-catalyzed Buchwald-Hartwig amination. Related imidazolium salts [INp^{R}H]Cl were prepared via cyclization of a 1,2-bis(naphthyl)diimine (obtained from 1-naphthylamines and glyoxal) with paraformaldehyde.[22]

In our attempts, the reaction of 1-naphthylamine with glyoxal did not yield the desired 1,2-diimine, but resulted in an inseparable product mixture. In order to avoid the use of a palladium catalyst, we prepared **5** following route 3 (*vide supra*, Scheme 4.3), i.e. via a formamidine intermediate. In the first step, following a procedure by Glorius and co-workers,[23] 1-naphthylamine was reacted with triethyl orthoformate at elevated temperatures (140-160 °C) to yield the dinaphthylformamidine in near quantitative yield. For the subsequent cyclization step, we tested the conditions described by Fallis and co-workers[24] as well as Grubbs and co-workers,[25] who deprotonated the formamidine using K_2CO_3 or diisopropylamine, respectively, and subsequently reacted with 1,2-dichloroethane, 1,2-dibromoethane, or related dihaloalkanes. As these conditions did not give enable formation of the desired product, we turned to *n*-butyllithium as the base to generate the formimidinate. Drying *in vacuo* and subsequent reaction with an excess of 1,2-dibromoethane yielded **5** as an off-white powder in 67% yield.

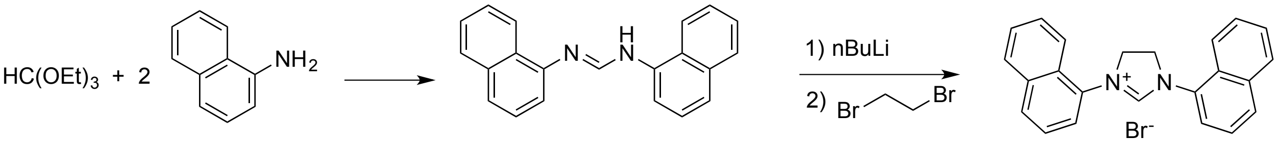

Scheme 4.13. Preparation of [SINpH]Br (**5**) via a formamidine.

The ^1H NMR spectrum of **5**, recorded in $CDCl_3$, displays a singlet at 4.80 ppm corresponding to the backbone protons, four multiplets that correspond to the naphthyl groups, and a singlet at 9.55 ppm which is attributed to the C_2 proton. The chemical shift of the C_2 proton indicates that the interaction with a Br^- counterion is significantly weaker than with a Cl^- ion, but stronger than with a weakly coordinating anion such as BF_4^-.

The azolium salts described here share the property that their respective NHCs cannot be isolated. The azolium salts **XXXIX**, **XL**, **XLI**, **XLI'**, **XLII**, and **4** contain (1-naphthyl)-methyl or 1-(1-naphthyl)ethyl substituents which feature protons in benzylic positions. The adjacent nitrogen atoms of the central azolium ring further increases the acidity of these protons. Therefore, reaction with a base of sufficient strength to deprotonate the C_2 position does not give the desired carbene, but leads to side reactions that result in the rapid dimerization of the initially formed carbene. A similar observation was reported for allyl-substituted imidazolium salts.[26] Investigations by Dorta and co-workers revealed that **5** dimerizes upon deprotonation.[21a]

4.3 Preparation and Applications of NHC-Silver Complexes

As discussed in section 4.1, *N*-heterocyclic carbenes can be utilized as ligands even when they are not isolable in their free form. The most common strategies to form NHC complexes from azolium salts are the addition of an external base to deprotonate the azolium salt *in situ* in the presence of the metal precursor, the use of a metal precursor featuring basic ligands, such as amides, alkoxides, or acetates, which effect the deprotonation, or the transfer of the carbene ligand from a labile NHC complex. In the last two decades, NHC-silver complexes have emerged as the preferred choice for NHC transmetalation reactions (Scheme 4.14).[27] Carbene transfer from silver has become a very popular method as it provides clean, robust access to a variety of NHC complexes. While there are few examples for transmetalation from silver to nickel,[28] the method is most suited for precious metals, particularly gold, copper, palladium, platinum, rhodium, iridium, and ruthenium.[27b]

The first NHC-silver complex was reported by Arduengo and co-workers in 1993, who reacted a free carbene with silver triflate in a 2:1 stoichiometry, yielding a cationic $[(NHC)_2Ag]^+$ complex.[29] In 1998, Lin and co-worker reported that NHC-silver complexes are easily accessible by reaction of an azolium salt with silver oxide.[27a] This route has since become the most widely applied way to prepare NHC-silver complexes since it neither requires inert conditions, dry solvents, nor the isolation of a free carbene. Wang and Lin were also the first to utilize NHC-silver complexes as carbene transfer agents.

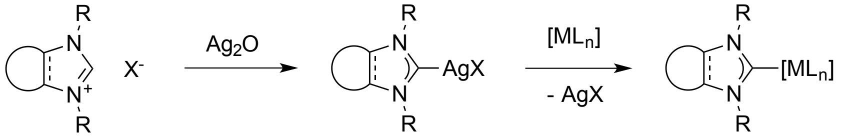

Scheme 4.14. Formation and Carbene Transfer of NHC-silver Complexes.

The reaction of an azolium salt with silver oxide can lead to a variety of structural motifs in the resulting complexes, which depend on the *N*-substituents, the counterion, and the solvent used for the reaction and crystallization. The most commonly observed structures are illustrated in Figure 4.2. Many NHC-silver complexes can actually be described as intermediates between types I and II, with a distorted linear coordination and weak intermolecular Ag–Cl interactions. Type III can be considered a special case of type IV, although III and IV are generally accessed via different syntheses. While III is accessible via the silver oxide route, complexes with structures of type IV are usually prepared from AgY (Y being a weakly coordinating anion) and a free carbene. The synthesis and structural variety of NHC-silver complexes have been reviewed in detail by Youngs and Lin.[27b,c]

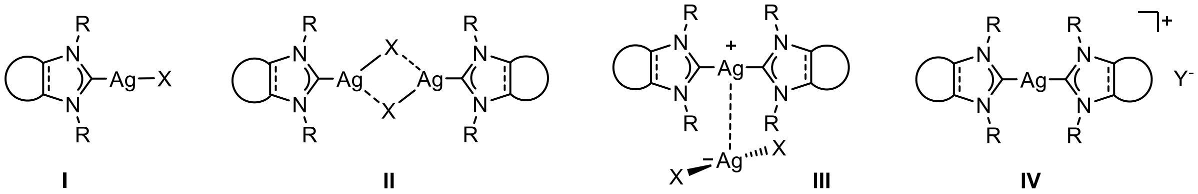

Figure 4.2. Common Structures of NHC-silver complexes (X = Cl, Br, I; Y^- = BF_4^-, PF_6^-, OTf^-, or other weakly coordinating anion).

Besides their use as carbene transfer agents, NHC-silver complexes have found further applications. In 2005, Peris and Fernandez reported the first catalytic application of an NHC-silver complex in the diboration of alkenes.[30] Since then, NHC-silver complexes have been used as catalysts for the ring-opening polymerization of lactides.[31] However, to date, NHC-silver catalysis remains a niche application.

Some groups reported the use of NHC-silver complexes for the synthesis of nanomaterials. Lin and co-workers discovered that mixtures of imidazolium salts and NHC-silver complexes carrying long alkyl chains as *N*-substituents form liquid crystals.[32] Son and co-workers prepared dendrimeric poly-imidazolium salts that formed spherical sub-micrometer particles which were transformed to poly(NHC-silver) and, subsequently, poly(NHC-palladium) and poly(NHC-copper) complexes.[33]

The use of silver compounds as antimicrobial and anticancer agents is a highly active and rapidly evolving field of research. It was discovered that NHC-silver complexes offer great advantages over simple silver compounds such as $AgNO_3$, which has been in use as a disinfectant and for the treatment of skin burns since the 19th century.[27b] The slow release of Ag^+ cations from the complexes in aqueous solution makes these complexes more effective as bactericides than a highly soluble Ag^+ source. More recent investigations found that NHC-silver complexes display cytotoxic activity towards several carcinogenic cell lines. [34]

For the present thesis, a series of silver complexes containing naphthyl-substituted *N*-heterocyclic carbenes were prepared following Lin's Ag_2O route. Regardless of the stoichiometry (an excess of Ag_2O was used), two-coordinate complexes with structure A were obtained.

4.3.1 Synthesis of (1,3-Bis(1-naphthylmethyl)imidazolin-2-ylidene)silver chloride, [(INpMe)AgCl] (6)

(1,3-Bis(1-naphthylmethyl)imidazolin-2-ylidene)silver chloride, [(INpMe)AgCl] (**6**), was synthesized by stirring [INpMeH]Cl (**XXXIX**) with a slight excess of Ag_2O in acetonitrile for 16 hours at room temperature under strict exclusion of light. Monitoring the reaction progress by ^1H NMR indicated full conversion of the imidazolium salt. After filtration and removal of the solvent *in vacuo*, the product was obtained as a colorless, crystalline solid in a modest yield of 26% after dissolving the crude product in CH_2Cl_2 and layering with *n*-hexane.

Complex **6** crystallizes in the triclinic space group *P*-1 with two molecules in the unit cell. The molecular structure (Figure 2) reveals a two-coordinate Ag atom with the carbene and chloride ligands forming an almost linear geometry. The C_1–Ag–Cl angle amounts to 177.41(7)°. This is noteworthy since in the closely related complexes (1,3-dibenzylimidazolin-2-ylidene)silver chloride, [(IBn)AgCl] (**XLIII**), and (1,3-bis(p-anisylmethyl)imidazolin-2-ylidene)silver chloride, [(IAnMe)AgCl] (**XLIV**), the C_1–Ag–Cl bond is distorted to 163.33° and 169.00°, respectively. The intermolecular Ag–Cl distances in **6**, **XLIII**, and **XLIV** are smaller than the sum of the van der Waals radii, indicating a weak interaction which is responsible for the distortion of the linear coordination. The C_1–Ag bond of **6** (2.079(2) Å) is in the usual range of NHC-silver complexes, albeit slightly shorter than those in **XLIII** and **XLIV**. The N_1–C_1–N_2 bond angle (104.799(2)°) as well as the N–C_1 bond lengths (1.340(3) and 1.353(3) Å) are comparable to the values of **XLIII** and **XLIV**. The relevant bond lengths and angles are summarized in Table 4.1.

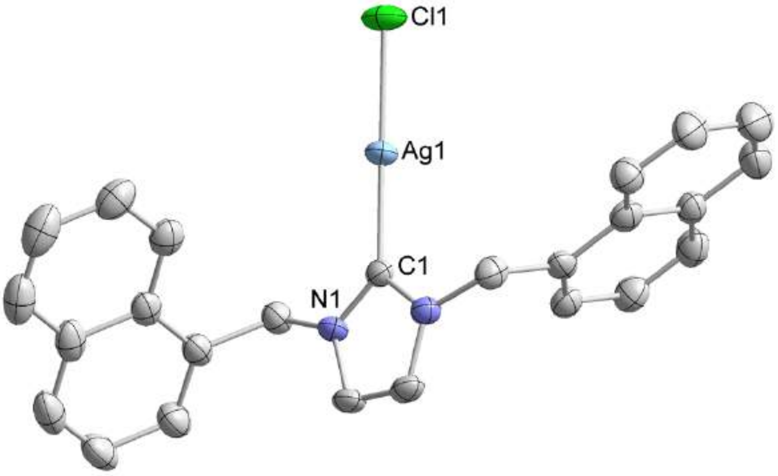

Figure 4.3. Molecular structure of [(INpMe)AgCl] (**6**) (thermal ellipsoids at 50% probability; hydrogen atoms omitted for clarity).

The ^{1}H NMR spectrum of **6**, recorded in $CDCl_3$, shows a singlet at 5.71 ppm corresponding to the protons of the $–CH_2–$ groups of the *N*-substitutents. While significant, this downfield shift of the methylene group is less pronounced than in the respective imidazolium salt **XXXIX** (6.89 ppm), which indicates a higher electron density in the neutral carbene species as opposed to the cationic precursor. The protons of the backbone resonate at 6.67 ppm. The multiplets in the range of 7.28 to 7.86 ppm can be assigned to the naphthyl subsitutents. The $^{13}C\{^1H\}$ NMR spectrum shows signals at 54.1 and 121.2, ppm which correspond to the methylene groups and the backbone, respectively. The carbon atoms of the naphthyl substituents give rise to signals in the range of 122.8 to 134.0 ppm. The carbene carbon signal was not observed in the $^{13}C\{^1H\}$ NMR spectrum; however, in the $^1H/^{13}C$ HMBC spectrum, an additional resonance was found at 180.8 ppm which is split into two concentric doublets. This signal corresponds to the carbene carbon. The multiplicity is caused by $^{13}C–^{107}Ag$ and $^{13}C–^{109}Ag$ coupling to the adjacent silver atom. The specific assignment of all ^{1}H and ^{13}C NMR signals was achieved by $^1H/^1H$ COSY, $^1H/^{13}C$ HSQC, and $^1H/^{13}C$ HMBC NMR experiments and is summarized in Table 4.2.

4.3.2 Synthesis of (1,3-Bis(1-naphthylmethyl)benzimidazolin-2-ylidene)silver chloride, [(BNpMe)AgCl] (7)

In analogy to complex **6**, (1,3-bis(1-naphthylmethyl)benzimidazolin-2-ylidene)silver chloride, [(BNpMe)AgCl] (**7**), is accessible by reacting the benzimidazolium chloride **XL** with a slight excess of silver oxide. In contrast to the preparation of **6**, dichloromethane was used as the reaction solvent rather than acetonitrile. After stirring overnight at room temperature, the mixture was filtered, the clear CH_2Cl_2 solution was concentrated to 50% of the volume and layered with *n*-hexane, whereupon **7** crystallized as colorless needles which were isolated by filtration and dried *in vacuo*, giving a colorless crystalline powder in 45% yield.

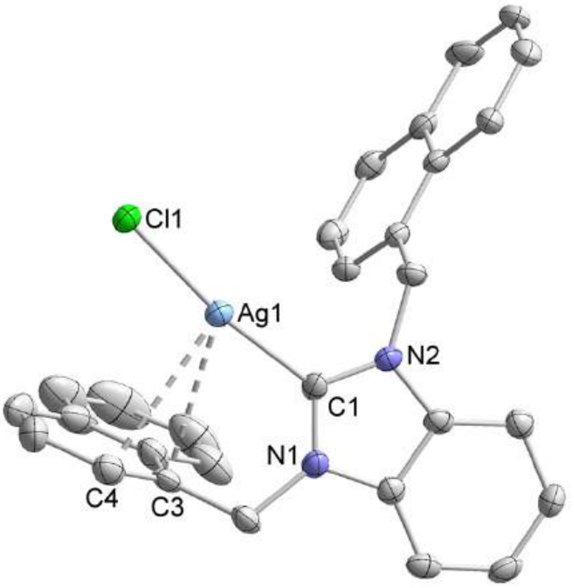

Figure 4.4. Molecular structure of [(BNpMe)AgCl] (**7**) (thermal ellipsoids at 50% probability; hydrogen atoms omitted for clarity).

Complex **7** crystallizes in the hexagonal space group $P6_1$ with six molecules in the unit cell. The molecular structure (Figure 4.4) closely resembles that of **6**, with the two-coordinate silver center in a distorted linear coordination geometry. The C_1–Ag–Cl angle, at 171.8(3)°, deviates significantly from the expected 180°. However, no van der Waals contacts, which might be a likely explanation for this distortion, were identified in the solid-state structure of **7**. In the closely related (1,3-dibenzylbenzimidazolin-2-ylidene)silver chloride, [(BBn)AgCl] (**XLV**), the respective angle was found to be slightly wider, amounting to 175.0(1)°. The C_1–Ag bond (2.097(9) Å) and the Ag–Cl bond (2.340(2) Å) differ only slightly from the values in **XLV**. The N_1–C_1–N_2 angle (107.1(8)°) is slightly larger than the one in **XLV** (105.9°) and the N–C_1 bond lengths are slightly shorter. In contrast to complex **6**, there is no intermolecular Ag–Cl or Cl–H interaction in the solid state. However, it is notable that the distances between the silver atom and two carbon atoms of one naphthyl group (C_3 and C_4, see Figures 4.4 and 4.6) are smaller than the sum of the van der Waals radii, indicating a weak interaction. This may be the cause of the slightly distorted linear coordination. All relevant bond lengths and angles are listed in Table 4.1.

The ^{1}H NMR spectrum of **7** in $CDCl_3$ closely resembles that of **6**. The $–CH_2–$ protons resonate at 6.14 ppm, which hints at the electron-deficient nature of the fused central ring system as opposed to an imidazole core. A rather complex signal around 7.26 ppm corresponds to the protons of the benzannulated backbone. The remaining signals in the range 7.03 to 8.02 ppm were assigned to the naphthyl moieties. Notably, while the solid-state structure displays an asymmetric geometry of the two naphthyl substituents, the ^{1}H NMR spectrum indicates that both substituents are equivalent in solution since only one set of signals is present. The same is true for the $^{13}C\{^{1}H\}$ NMR spectrum. Here, the signal of the methylene carbons is found at 51.6 ppm. The signals in the range 112.3 to 134.3 ppm were assigned to carbon atoms of the backbone and the naphthyl moieties. While no signal corresponding to the carbene carbon atom C_1 was identified, analysis of the HMBC spectrum revealed an additional resonance at 190.9 ppm which is split into two concentric doublets. This signal was assigned to C_1, the multiplicity being caused by $^{13}C–^{107}Ag$ and $^{13}C–^{109}Ag$ coupling. The detailed assignment of all signals was achieved using 2D NMR techniques ($^{1}H/^{1}H$ COSY, $^{1}H/^{13}C$ HSQC, $^{1}H/^{13}C$ HMBC). A list of all signals is given in Table 4.2.

4.3.3 Synthesis of (1,3-Bis(1-naphthylmethyl)imidazolidin-2-ylidene)silver chloride, [(SINpMe)AgCl] (8)

(1,3-Bis(1-naphthylmethyl)imidazolidin-2-ylidene)silver chloride, [(SINpMe)AgCl] (**8**), was prepared in a manner analogous to **6** and **7**, by reacting imidazolinium salt **XLI** with a slight excess of Ag_2O. After refluxing in dichloromethane overnight, the mixture was filtered, the filtrate was concentrated to half of the original volume and layered with diethyl ether to crystallize the product, which was isolated in 37% yield.

Complex **8** crystallizes in the monoclinic space group *I*2/a with 8 molecules in the asymmetric unit. In analogy to **6** and **7**, the silver atom in **8** is coordinated in a linear fashion by the carbene and chloride ligands. The $C_1–Ag–Cl$ angle amounts to 178.41(8)°. Unlike complexes **6** and **7**, neither intramolecular nor intermolecular van der Waals contacts are observed in the solid-state structure of **8**. The $C_1–Ag$ bond (2.08339(6) Å) is comparable to literature values of related complexes, as is the Ag–Cl bond (2.32348(7) Å). The $N_1–C_1–N_2$ angle (109.145(2)°) is slightly larger than those in **6** and **7**, and the N–C_1 bonds are slightly shorter (1.31875(4) and 1.32758(3) Å). All relevant bond lengths and angles are summarized in Table 4.1.

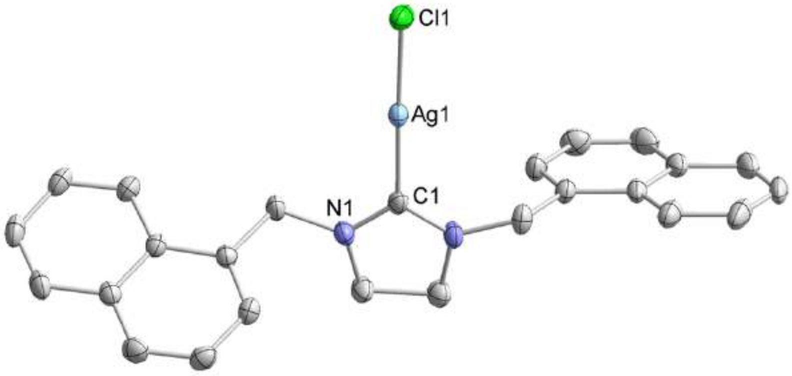

Figure 4.5. Molecular structure of [(SINpMe)AgCl] (**8**) (thermal ellipsoids at 50% probability; hydrogen atoms omitted for clarity).

The ^{1}H NMR spectrum is comparable to those of **6** and **7**. The $–CH_2–$ groups of the *N*-substituents resonate at 5.26 ppm. The protons NCH_2CH_2N are found at 3.40 ppm. The remaining signals between 7.45 and 8.16 ppm can be assigned to the naphthyl groups. The $^{13}C\{^1H\}$ NMR spectrum shows the expected set of signals, with the backbone resonating at 49.2 ppm, the methylene groups of the substituents at 53.9 ppm, and the naphthyl groups between 123.7 and 134.4 ppm. As in the spectra of **6** and **7**, the carbene carbon atom is not found in the $^{13}C\{^1H\}$ spectrum, but can be identified in the $^1H/^{13}C$ HMBC spectrum at 205.3 ppm. 2D NMR techniques were employed to achieve a detailed assignment of all signals, which are given in Table 4.2.

Table 4.1. Selected bond lengths and angles of NHC-silver complexes.

	6	**XLIII**	**XLIV**	**7**	**XLV**	**8**
C_1–Ag	2.079(2)	2.090(3)	2.093(3)	2.097(9)	2.082(2)	2.084(4)
Ag–Cl	2.3279(7)	2.3635(9)	2.3573(9)	2.340(2)	2.3324(5)	2.3235(7)
C_1–Ag–Cl	177.41(7)	163.33(8)	169.00(7)	171.8(2)	175.01(8)	178.41(8)
N–C_1–N	104.8(2)	104.3(2)	104.3(2)	107.1(8)	105.88(18)	109.2(3)
Ag–Cl*	3.4477(8)	3.0745(9)	3.269(11)	–	–	–
Cl–H*	2.7479(7)	2.8426(8)	2.8904(9)	–	–	–
Ag–C_3**	–	–	–	3.111(9)	2.989(2)	–
Ag–C_4**	–	–	–	3.174(10)	3.048(2)	–

* intermolecular distance; ** assignment: see below.

Table 4.2. ^{1}H and $^{13}C\{^{1}H\}$ NMR chemical shifts of complexes **6**, **7**, and **8**.

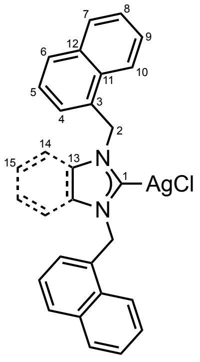

^{1}H / $^{13}C\{^{1}H\}$	[(INpMe)AgCl] (6)		[(BNpMe)AgCl] (7)		[(SINpMe)AgCl] (8)	
C_1	–	180.8	–	190.9	–	205.3
H_2 / C_2	5.71	54.1	6.14	51.6	5.26	53.9
C_3	–	134.0	–	133.9	–	134.4
H_4 / C_4	7.28	127.6	7.03	125.0	7.45	127.3
H_5 / C_5	7.41	125.4	7.37	125.4	7.49	125.8
H_6 / C_6	7.83	130.0	7.85	129.4	7.89	129.6
H_7 / C_7	7.86	122.8	7.92	129.3	7.93	129.3
H_8 / C_8	7.48	127.3	7.56	126.4	7.57	126.6
H_9 / C_9	7.48	126.4	7.56	127.1	7.61	127.2
H_{10} / C_{10}	7.84	129.1	8.02	122.4	8.16	123.7
C_{11}	–	131.0	–	130.6	–	131.8
C_{12}	–	130.4	–	130.1	–	131.1
H_{13} / C_{13}	6.67	121.2	–	134.3	3.40	49.2
H_{14} / C_{14}	–	–	7.26	112.3	–	–
H_{15} / C_{15}	–	–	7.26	124.6	–	–

Comparing the solid-state structures of **6**, **7**, and **8**, some slight differences can be noted. Complex **6** displays weak intermolecular Ag–Cl and Cl–H interactions. The Ag–Cl contact calls to mind the structural type **B** (Figure 4.2) featuring bridging chloride ligands. The interaction is weaker than in the related complexes **XLIII** and **XLIV**, which may be considered intermediates between the mononuclear, linear type I and the trigonal planar, dinuclear type **B**. Complex **7** does not feature these intermolecular interactions, but still exhibits a significant distortion of the C_1–Ag–Cl angle. The likely cause for this is a weak π interaction with one of the naphthyl substituents, which is also observed in similar complexes such as **XLV**. Complex **8** neither displays intermolecular Ag–Cl contacts nor an intramolecular interaction with the substituents. The C_1–Ag–Cl angle is less distorted than in **6** and **7**, and **8** is best described as a mononuclear type **A** complex.

The NMR spectra of **6**, **7**, and **8** each display one set of signals for the backbone and the *N*-substituents. This indicates that the asymmetries observed in the solid state as a consequence of weak interactions are not observed in solution. The chemical shifts of the 1-naphthylmethyl substituents are only marginally different in the three examined complexes. By contrast, the $^{13}C\{^{1}H\}$ chemical shift of the carbene carbon atom is markedly different, with complex **8** displaying the most extreme downfield shift ($\delta = 205$ ppm). The chemical shift of the carbene center is usually explained in terms of the σ donor and π acceptor ability of the NHC ligand. Since NHCs with saturated backbones generally display a lower degree of backbonding than NHCs with unsaturated or benzannulated backbones, the high chemical shift of C_1 in complex **8** is plausible.

For a more in-depth analysis of the backbonding ability of the employed carbene ligands, further experiments are necessary. Huynh and co-workers have developed a method to compare the donor abilities of different ligands (L) by $^{13}C\{^1H\}$ NMR spectroscopy using complexes of the type (NHC)$PdBr_2$(L) which correlates the chemical shift of C_1 of the NHC ligand with the donor strength of L.[35] In their original report, they compared the NHC ligands SIBn, IBn, and BBn (1,3-dibenzylimidazolidin-2-ylidene, -imidazolin-2-ylidene, and -benzimidazolin-2-ylidene), which are closely related to the ligands used in **6**, **7**, and **8**, and concluded that SIBn is the strongest donor and BBn the weakest. Since this trend is not directly observable from the NMR data of **6**, **7**, and **8**, a determination of the Huynh Electronic Parameter of INpMe, BNpMe, and SINpMe is advisable in order to gain deeper insight into the donor ability of these ligands.

4.3.4 Reactions of Imidazolinium Salts 4 and 5 with Ag_2O

Besides azolium salts **XXXIX**, **XL**, and **XLI** carrying 1-naphthylmethyl substitutents, the imidazolinium salts **4** and **5** with slightly modified *N*-substituents were also reacted with silver oxide in an analogous manner. Despite several attempts under different reaction conditions, no products could be isolated. ^1H NMR monitoring revealed mixtures of unidentified products which could not be separated. A possible by-product could be a bis(NHC) complex of the formula $[Ag(NHC)_2]Cl$ (Figure 4.2, **D**), formed by elimination of one equivalent of AgCl from two molecules of [(NHC)AgCl]. Racemization of the stereocenters of the chiral carbene *R,R*-SINpEt, leading to a *meso* form of the ligand, might be another, albeit unexpected side reaction. Some reports mention that an excess of silver oxide can lead to the formation of silver nanoparticles and undesired organic byproducts, indicated by a yellow discoloration of the reaction mixture.[27c] While this was not observed in the reactions with the azolium salts **XXXIX**, **XL**, and **XLI**, it might be another explanation for the complicated mixtures obtained using **4** and **5**. The presence of several products in the case of **5** may further be explained by the steric bulk of the α-naphthyl substitutents. Since the rotation of the naphthyl groups along the N_1–C_3 axis is hindered, three rotamers are conceivable (Figure 4.7). Increasing the selectivity of these reactions may be a matter of finding the right reaction conditions: in the case of **5**, for example, a higher reaction temperature may lead to the exclusive formation of the most stable isomer.

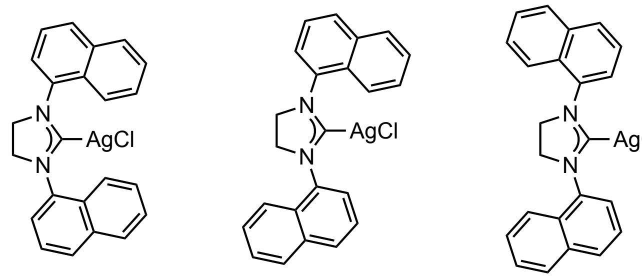

Figure 4.7. Possible rotamers from the reaction of [SINpH]Br (**5**) with Ag_2O.

4.4 References

[1] a) H.-W. Wanzlick, H.-J. Schönherr, *Angew. Chem.* **1968**, *80*, 154; *Angew. Chem. Int. Ed.* **1968**, *7*, 141-142; b) K. Öfele, *J. Organomet. Chem.* **1968**, *12*, P42-P43.

[2] D. J. Cardin, B. Çetinkaya, M. F. Lappert, L. Manojlovic-Muir, K. W. Muir, *Chem. Commun.* **1971**, 400-401.

[3] A. J. Arduengo III, R. L. Harlow, M. Kline, *J. Am. Chem. Soc.* **1991**, *113*, 361-363.

[4] Reviews: a) E. Peris, *Top. Organomet. Chem.* **2007**, *21*, 83-116; b) L. Benhamou, E. Chardon, G. Lavigne, S. Bellemin-Laponnaz, V. César, *Chem. Rev.* **2011**, *111*, 2705-2733.

[5] a) N. Kuhn, T. Kratz, *Synthesis* **1993**, 561-562; b) M. K. Denk, A. Hezarkhani, F.-L. Zheng, *Eur. J. Inorg. Chem.* **2007**, 3527-3534.

[6] H.-W. Wanzlick, E. Schikora, *Chem. Ber.* **1961**, *94*, 2389-2393.

[7] a) D. Enders, K. Breuer, G. Raabe, J. Runsink, J. H. Teles, J.-P. Melder, K. Ebel, S. Brode, *Angew. Chem.* **1995**, *107*, 1119-1122; *Angew. Chem. Int. Ed. Engl.* **1995**, *34*, 1021-1023; b) M. Scholl, S. Ding, C. W. Lee, R. H. Grubbs, *Org. Lett.* **1999**, *1*, 953-956; c) T. M. Trnka, J. P. Morgan, M. S. Sanford, T. E. Wilhelm, M. Scholl, T.-M. Choi, S. Ding, M. W. Day, R. H. Grubbs, *J. Am. Chem. Soc.* **2003**, *125*, 2546-2558; d) G. W. Nyce, S. Csihony, R. M. Waymouth, J. L. Hedrick, *Chem. Eur. J.* **2004**, *10*, 4073-4079.

[8] a) H. A. Duong, T. M. Tekavec, A. M. Arif, J. Louie, *Chem. Commun.* **2004**, 112-113; b) B. Bantu, G. M. Pawar, U. Decker, K. Wurst, A. M. Schmidt, M. R. Buchmeiser, *Chem. Eur. J.* **2009**, *15*, 3103-3109.

[9] a) M. Otto, S. Conejero, Y. Canac, V. D. Romanenko, V. Rudzevitch, G. Bertrand, *J. Am. Chem. Soc.* **2004**, *126*, 1016-1017; b) D. S. McGuinness, K. J. Cavell, B. F. Yates, B. W. Skelton, A. H. White, *J. Am. Chem. Soc.* **2001**, *123*, 8317-8328; c) D. Kremzow, G. Seidel, C. W. Lehmann, A. Fürstner, *Chem. Eur. J.* **2005**, *11*, 1833-1853.

[10] H. Song, N. Yan, Z. Fei, K. J. Kilpin, R. Scopelliti, X. Li, P. J. Dyson, *Catalysis Today* **2012**, *183*, 172-177.

[11] S. P. Nolan, *Synthesis of 1,3 Distributed Imidazolium Salts*, **2006**, 7109348.

[12] C. L. Winn, F. Guillen, J. Pytkowicz, S. Roland, P. Mangeney, A. Alexakis, *J. Organomet. Chem.* **2005**, *690*, 5672-5695.

[13] A. Bertogg, F. Camponovo, A. Togni, *Eur. J. Inorg. Chem.* **2005**, 347-356.

[14] W. A. Herrmann, L. J. Gooßen, C. Köcher, G. R. J. Artus, *Angew. Chem. Int. Ed. Engl.* **1996**, *35*, 2805-2807.

[15] O. V. Starikova, G. V. Dolgushin, L. I. Larina, P. E. Ushakov, T. N. Komarova, V. A. Lopyrev, *Russ. J. Org. Chem.* **2003**, *39*, 1467-1470.

[16] Y. Gök, N. Gürbüz, I. Özdemir, B. Cetinkaya, E. Cetinkaya, *Appl. Organometal. Chem.* **2005**, *19*, 870-874.

[17] A. Aktas, S. Akkoç, Y. Gök, *J. Coord. Chem.* **2013**, *66*, 2901-2909.

[18] S. Yasar, I. Özdemir, B. Cetinkaya, J.-L. Renaud, C. Bruneau, *Eur. J. Org. Chem.* **2008**, 2142-2149.

[19] S. Urban, N. Ortega, F. Glorius, *Angew. Chem. Int. Ed.* **2011**, *50*, 3803-3806.

[20] R. B. Strand, T. Helgerud, T. Solvang, C. A. Sperger, A. Fiksdahl, *Tetrahedron: Asymmetry* **2011**, *22*, 1994-2006.

[21] a) X. Luan, R. Mariz, M. Gatti, C. Costabile, A. Poater, L. Cavallo, A. Linden, R. Dorta, *J. Am. Chem. Soc.* **2008**, *130*, 6848-6858; b) L. Vieille-Petit, X. Luan, R. Mariz, S. Blumentritt, A. Linden, R. Dorta, *Eur. J. Inorg. Chem.* **2009**, 1861-1870.

[22] L. Wu, E. Drinkel, F. Gaggia, S. Capolicchio, A. Linden, L. Falivene, L. Cavallo, R. Dorta, *Chem. Eur. J.* **2011**, *17*, 12886-12890.

[23] K. Hirano, S. Urban, C. Wang, F. Glorius, *Org. Lett.* **2009**, *11*, 1019-1022.

[24] M. Iglesias, D. J. Beetstra, J. C. Knight, L.-L. Ooi, A. Stasch, S. Coles, L. Male, M. B. Hursthouse, K. J. Cavell, A. Dervisi, I. A. Fallis, *Organometallics* **2008**, *27*, 3279-3289.

[25] K. M. Kuhn, R. H. Grubbs, *Org. Lett.* **2008**, *10*, 2075-2077.

[26] a) C. Holtgrewe, C. Diedrich, T. Pape, S. Grimme, F. E. Hahn, *Eur. J. Org. Chem.* **2005**, 3116-3124; b) F. E. Hahn, B. Heidrich, A. Hepp, T. Pape, *J. Organomet. Chem.* **2007**, *692*, 4630-4638.

[27] a) H. M. J. Wang, I. J. B. Lin, *Organometallics* **1998**, *17*, 972-975; b) J. C. Garrison, W. J. Youngs, *Chem. Rev.* **2005**, *105*, 3978-4008; c) J. C. Y. Lin, R. T. W. Huang, C. S. Lee, A. Bhattacharyya, W. S. Hwang, I. J. B. Lin, *Chem. Rev.* **2009**, *109*, 3561-3598.

[28] S. Hameury, P. de Frémont, P.-A. R. Breuil, H. Olivier-Bourbigou, P. Braunstein, *Dalton Trans.* **2014**, *43*, 4700-4710.

[29] A. J. Arduengo III, H. V. R. Dias, J. C. Calabrese, F. Davidson, *Organometallics* **1993**, *12*, 3405-3409.

[30] J. Ramírez, R. Corberán, M. Sanaú, E. Peris, E. Fernandez, *Chem. Commun.* **2005**, 3056-3058.

[31] M. K. Samantaray, V. Katiyar, K. Pang, H. Nanavati, P. Ghosh, *J. Organomet. Chem.* **2007**, *692*, 1672-1682.

[32] C. K. Lee, C. Sekhar Vasam, T. W. Huang, H. M. J. Wang, R. Y. Yang, C. S. Lee, I. J. B. Lin, *Organometallics* **2006**, *25*, 3768-3775.

[33] K. H. Park, I. Ku, H. J. Kim, S. U. Son, *Chem. Mater.* **2008**, *20*, 1673-1675.

[34] a) A. Kascatan-Nebioglu, M. J. Panzner, C. A. Tessier, C. L. Cannon, W. J. Youngs, *Coord. Chem. Rev.* **2007**, *251*, 884-895; b) W. J. Youngs, p. 151-172, in: *"N-Heterocyclic Carbenes. Effective Tools for Organometallic Synthesis",* ed. S. P. Nolan, **2014**, Wiley-VCH.

[35] a) H. V. Huynh, Y. Han, R. Jothibasu, J. A. Yang, *Organometallics* **2009**, *28*, 5395-5404; b) Q. Teng, H. V. Huynh, *Dalton Trans.* **2017**, *46*, 614-627.

5. NHC Complexes of Gold, Rhodium, and Ruthenium*

5.1 Introduction

5.1.1 Synthesis and Applications of NHC-Gold Complexes

The synthesis of the first gold complex with an NHC ligand was reported by Lappert and co-workers in 1973, starting from a tetraazafulvalene as the NHC precursor (Scheme 5.1, **A**).[1] After a period of inactivity, the field of NHC-gold complexes was revived in the late 1980s and early 1990s following reports by Bonati, Burini, and co-workers, and Raubenheimer and co-workers (Scheme 5.1, **B**).[2] In 1999, Lin and co-workers prepared NHC-gold complexes by carbene transfer from NHC-silver complexes in a straightforward manner (Scheme 5.1, **C**).[3] In 2013, Nolan and co-workers reported an even more convenient, high-yielding procedure which involves deprotonation in situ of an azolium salt with a mild base such as K_2CO_3 in technical grade solvents (Scheme 5.1, **D**).[4] Since the early 2000s, gold-NHC complexes have found broad application in catalysis, materials chemistry and medicinal chemistry.[5,6]

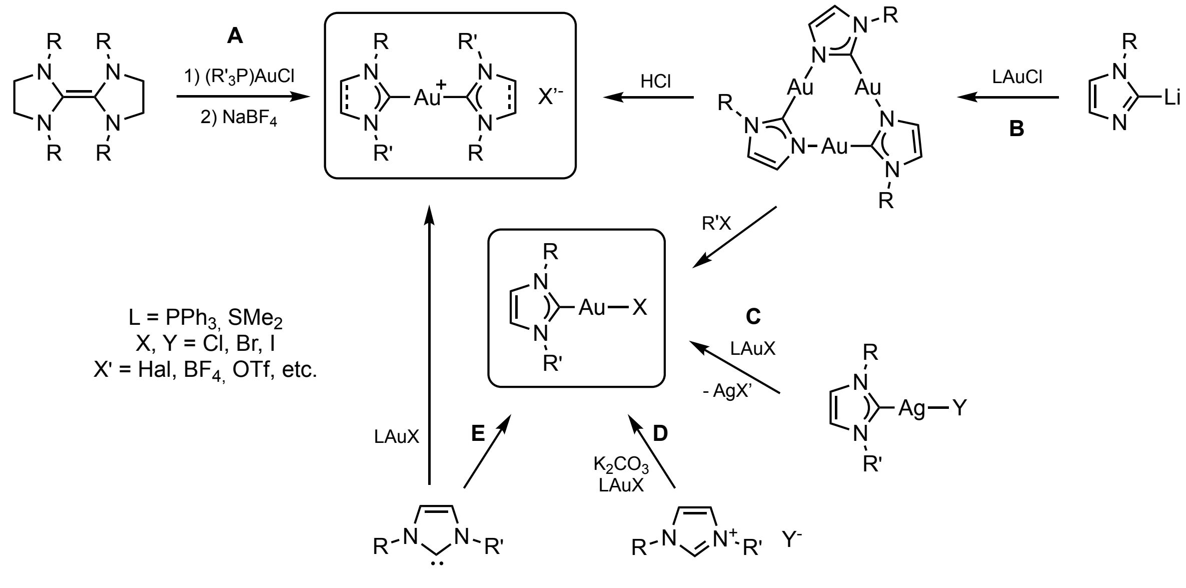

Scheme 5.1. Early examples of NHC-Au Complexes and Their Preparation.

In 2003, Herrmann and co-workers reported the first use of gold-carbene complexes [(NHC)AuCl] and [(NHC)Au(OAc)] in the hydration of alkynes to generate ketones (Scheme 5.2).[7] Since then, NHC complexes have found broad application in the rapidly evolving field of gold catalysis. The groups of Hashmi and Kündig made use of the high affinity of gold for alkenes and alkynes in the cyclo-isomerization of enynes (Scheme 5.3).[5e, 8] The

---

* The experiments on catalytic hydrogenations using NHC-rhodium complexes (section 5.3.5) were performed and analysed by Dr. Daniel Paul (group of Prof. Dr. F. Glorius, WWU Münster).

rearrangement of propargylic esters to enones, allenes, indenes, and heterocyclic compounds (Scheme 5.4) follows a similar mechanism.[5a, 9] Detailed studies examined the scope and mechanism of this reaction type and found that in many cases both π coordination to the alkyne and σ bonding to deprotonated alkynyl groups play significant roles.[5e] The use of chiral NHC ligands has enabled the development of enantioselective cyclizations.[8]

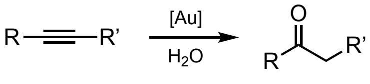

Scheme 5.2. Hydration of alkynes catalyzed by NHC-gold complexes.[7]

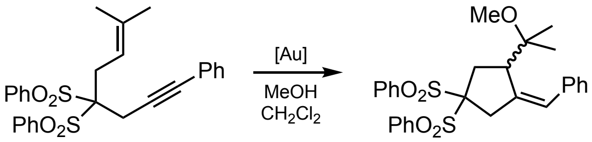

Scheme 5.3. Asymmetric cycloisomerization of enynes.[8]

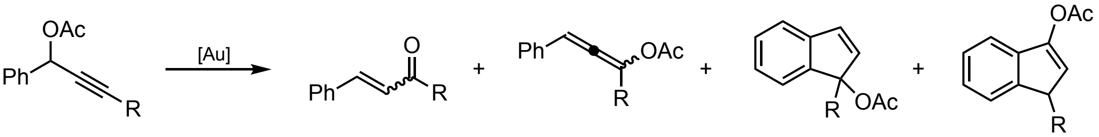

Scheme 5.4. Rearrangement of propargylic esters yielding enones, allenes, and indenes.[5a, 9]

A common feature is the activation of the [(NHC)AuX] precatalyst by a halide abstractor such as $AgSbF_6$ or $AgNTf_2$, generating a highly electrophilic $[(NHC)Au]^+$ fragment. Using silver salts of chiral anions as halide abstractors is a promising strategy to generate chiral ion pairs for enantioselective catalysis.[5f-h, 10] The group of Nolan introduced a class of highly basic and nucleophilic complexes [(NHC)Au(OH)] with an estimated pK_a of 29 to 31.[5d, 11] The ability to deprotonate alkynes and electron-deficient aromatic compounds makes [(NHC)Au(OH)] complexes excellent catalysts for the carboxylation of aromatic carbo- and heterocycles.[12] The recent development of a range of gold-catalyzed reactions including, but not limited to, hydroalkynylation, hydroarylation, polymerization, and multicomponent reactions demonstrate the potential of NHC-gold complexes for catalysis.[13]

A recent report by Lammertsma and co-workers demonstrated the use of an electrophilic $[(NHC)Au]^+$ fragment for the activation of white phosphorus, resulting in the gold fragment binding to an edge of the P_4 molecule in an η^2 fashion (Scheme 5.5).[14] Analogous As_4 and, more recently, P_4 adducts were described by the group of Scheer using a gold-phosphane complex.[15]

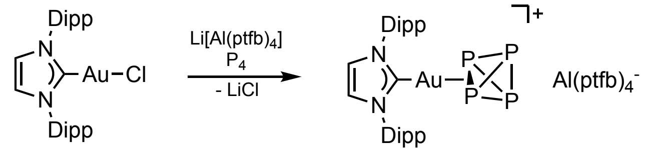

Scheme 5.5. Activation of P_4 with an electrophilic $[(NHC)Au]^+$ fragment.[14]

NHC-gold complexes have received considerable attention regarding their medicinal properties in the treatment of arthritis, malaria, HIV, and some forms of cancer.[6, 16] NHC-gold complexes are highly attractive alternatives to gold-phosphane and gold-thiol complexes commonly used as pharmaceuticals (e.g. Auranof as they show fewer side-effects. The group of Berners-Price developed mono- and dinuclear gold-carbene complexes that are selectively cytotoxic for tumor cells (Figure 5.1, right and second-to-right).

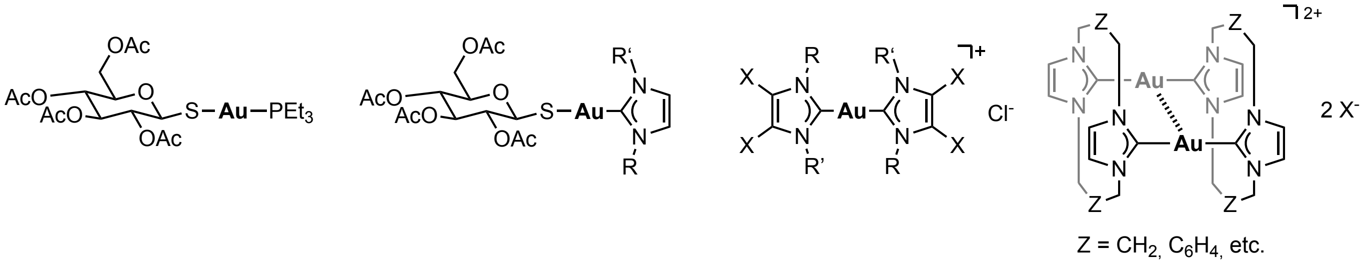

Figure 5.1. Auranofin (left) and biologically active NHC-Au complexes.

The advent of *N*-heterocyclic carbenes has brought progress to other areas of gold chemistry as well. In materials chemistry and nanoscience, gold surfaces and particles are generally stabilized by thiol ligands. The use of NHCs instead of thiols led to a significant improvement of the thermal, oxidative, and acid-base stability of gold nanoparticles and surfaces.[17] Compounds showing aurophilic interactions as well as gold clusters stabilized by NHC ligands show luminescence in the visible region,[3, 18] which, combined with their biological activity, may bring about the development of biocompatible and bioactive luminescent diagnostic and therapeutic agents.

5.1.2 Synthesis and Applications of NHC-Rhodium Complexes

In 1972, Lappert and co-workers first observed NHC-rhodium complexes $[Rh(CO)(PPh_3)Cl(NHC)]$ (**A**) and $[Rh(PPh_3)_2Cl(NHC)]$ (**B**) in reactions of tetraazafulvalenes with $[Rh(PPh_3)_3Cl]$ (commonly referred to as Wilkinson's catalyst) and $[Rh(CO)(PPh_3)_2Cl]$ (Scheme 5.6).[19] Crudden and co-workers later found that air-sensitive complexes **B** can be converted to the stable carbonyl complexes **A** by addition of CO.[20] In 1977 the group of Nile reported the synthesis of cyclooctadiene complexes [(cod)RhCl(NHC)] (**C**) from tetraazafulvalenes and $[RhCl(cod)]_2$.[21] In 1996, Herrmann and co-workers prepared NHC-rhodium complexes by reacting $[RhCl(cod)]_2$ with free carbenes generated *in situ*.[22] They later introduced a simplified procedure, first converting $[RhCl(cod)]_2$ to $[RhCl(\mu\text{-}OEt)]_2$ with NaOEt and subsequently adding an imidazolium salt as the carbene precursor.[23] In 2003, the groups of Crabtree and Youngs reported the preparation of NHC-rhodium complexes by transmetalation from NHC-silver precursors.[24] A variety of other structural motifs and more specialized syntheses have been reviewed by Crudden and co-workers as well as Nolan and co-workers.[25]

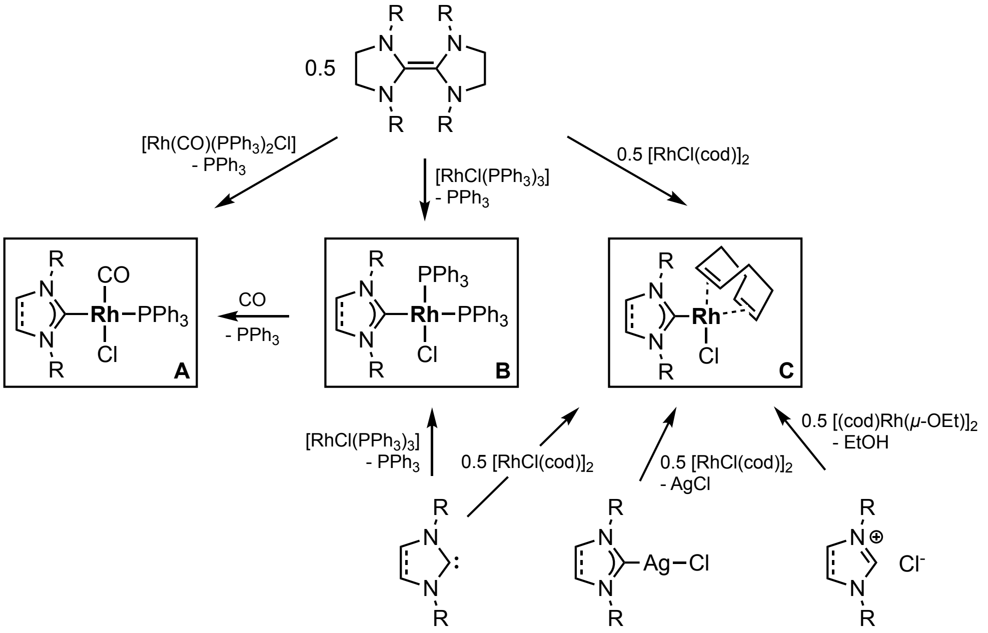

Scheme 5.6. Synthetic access to NHC-rhodium complexes.

Inspired by the excellent catalytic performance of the Wilkinson catalyst, the groups of Nile and Lappert explored catalytic applications of NHC-rhodium complexes in the hydrosilylation of ketones, alkenes, and alkynes.[21,26] In 1996, Herrmann and co-workers prepared the chiral Rh complex [(INpEt)RhCl(cod)] (**XLVI**) with *R*,*R*-1,3-bis-(1-(1-naphthyl)ethyl)imidazolin-2-ylidene (INpEt), which enabled the asymmetric hydrosilylation of ketones even at low catalyst loadings of 0.1 to 1%, albeit with moderate ee values of 32% or less (Scheme 5.7). Gade and co-workers used NHCs with chiral oxazoline side-arms, which had previously been reported by the group of Burgess, [27] in the rhodium-catalyzed hydrosilylation of ketones with excellent asymmetric induction, reaching ee values of up to 99% (Scheme 5.7).[28]

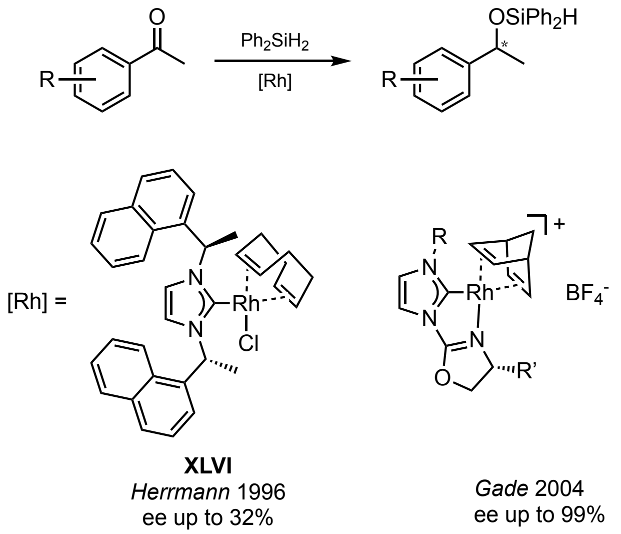

Scheme 5.7. Asymmetric rhodium-catalyzed hydrosilylation of acetophenone.[22]

The hydrosilylation of alkynes and alkenes using NHC-rhodium catalysts was reported by the group of Peris as well as the groups of Jiménez and Oro.[29] In both cases chelating ligands were utilized: While Peris and co-workers used bis(imidazolin-2-ylidene) ligands, Jiménez, Oro, and co-workers employed hemilabile aminoalkyl-substituted NHC ligands.

Alkene hydrogenation catalyzed by NHC-rhodium complexes was reported by several groups, but none of the used catalysts displayed an activity greater than that of the Wilkinson catalyst.[30, 25b] More recently, Zeng and co-workers found that, when using rhodium complexes containing cyclic (alkyl)(amino)carbenes (cAACs) rather than imidazolin-2-ylidenes, an unusual reactivity is observed in the hydrogenation of aromatic ketones and phenols: Rather than the carbonyl group, the arene is hydrogenated (Scheme 5.8).[31]

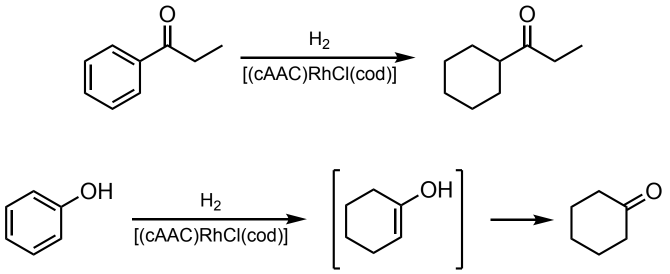

Scheme 5.8. Hydrogenation of aromatic ketones and phenols catalyzed by [(cAAC)RhCl(cod)].

The most industrially relevant process involving rhodium catalysis is the hydroformylation of alkenes (Scheme 5.9). [20] While rhodium-carbene adducts were used early on in hydrosilylation reactions, their application in hydroformylation was not reported until the year 2000. Crudden and co-workers described the use of complexes $[(NHC)RhCl(PPh_3)L]$ (L = CO, PPh_3; Scheme 5.6, motifs **A** and **B**) in the hydroformylation of styrenes with higher activity than carbene-free analogues and with high selectivity for the branched products.[20,32,25a]

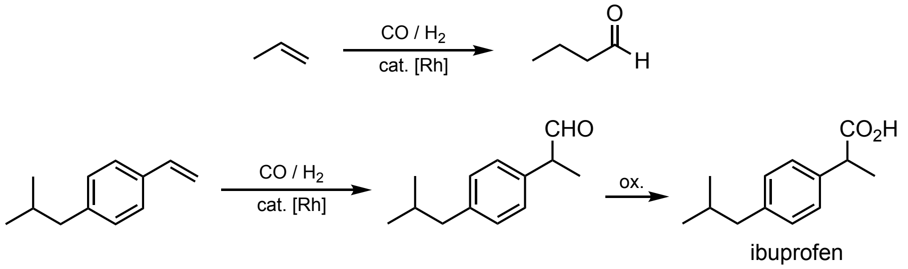

Scheme 5.9. Hydroformylation of alkenes.

While chelating NHC ligands have been used successfully in Rh-catalyzed hydrogenations and hydrosilylations, there are only few examples in which π-acceptors were used as chelating groups, such as the allyl-NHC complex **III** reported by Lai, Li, and co-workers (Figure 5.2, left).[33] Analogous iridium complexes stabilized by chelating allyl-substituted NHCs were prepared by the groups of Hahn and Oro[34] as well as the group of Mata (Figure 5.2, **IV**).[35] Activation of **IV** with $AgBF_4$ yielded **V** in which the Ir center is bound by two allyl moieties. **IV** and **V** catalyze the transfer hydrogenation of ketones and the hydrosilylation of alkynes.

Very recently, Dorta and co-workers reported the unusual complex **XVI** with a coordinating naphthyl moiety.[36] They showed that **XVI** catalyzes the intramolecular hydroamination of aminoalkenes with excellent results, reasoning that the involvement of the naphthyl group is crucial since complexes with other NHC ligands showed no catalytic activity for this reaction type.

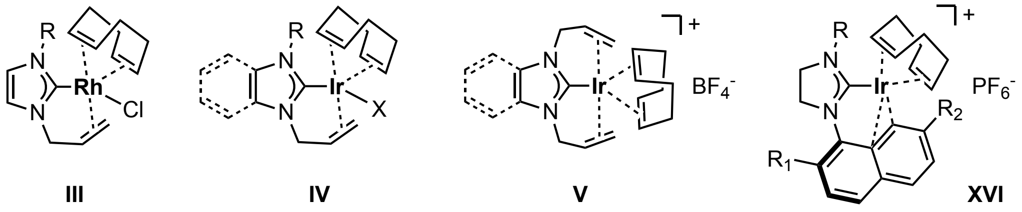

Figure 5.2. Rh and Ir carbene complexes with π-acceptor side arms.

5.1.3 Synthesis and Applications of NHC-Ruthenium Complexes

As with most other transition metals, the first reports of NHC complexes of ruthenium came from the group of Lappert in the 1970s.[37] Reaction of tetraazafulvalenes with $[RuCl_2(PPh_3)_3]$ resulted in the formation of tetrakis(carbene) complexes (Scheme 5.10, top). They observed that *N*-arylated NHC ligands can undergo spontaneous C–H activation to form metallacycles in the presence of PEt_3. NHC-ruthenium complexes received little attention until 1996, when the groups of Herrmann, Dixneuf, and Çetinkaya reported the synthesis of half-sandwich complexes of the type [(NHC)$RuCl_2$(arene)] (Scheme 5.10, bottom).[38]

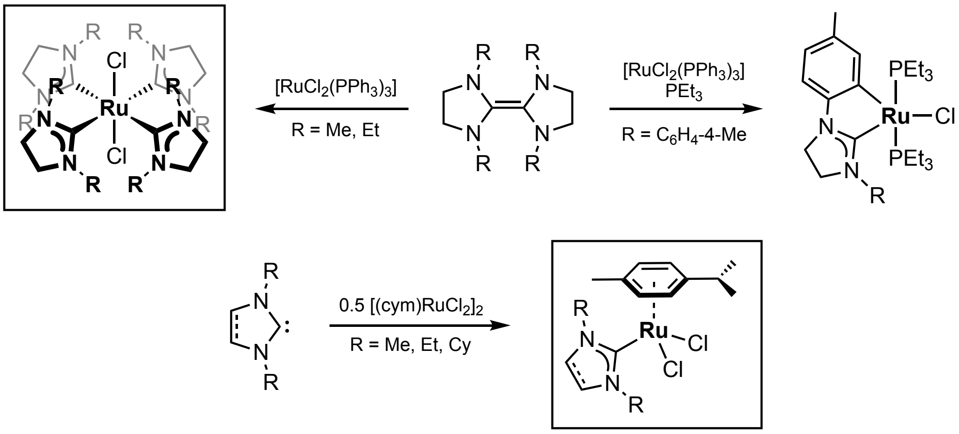

Scheme 5.10. Early examples of NHC-ruthenium complexes (cym = *p*-cymene).

Following a report by Herrmann and co-workers in 1998, [39a] many researchers became interested in NHC-ruthenium complexes due to their excellent activity in olefin metathesis; reports by the groups of Grubbs, Fürstner, and Nolan followed in 1999,[39b-e] starting a flurry of research activity. The area of olefin metathesis has since developed into a research field in its own right, and reviews on all relevant aspects are available in the literature.[40] In the course of this development, Grubbs and co-workers reported the generation of NHCs *in situ* from 2-alkoxyimidazolines, which release the corresponding alcohol upon heating; this was used for the preparation of the Grubbs II catalyst under mild conditions (Scheme 5.11).[39b]

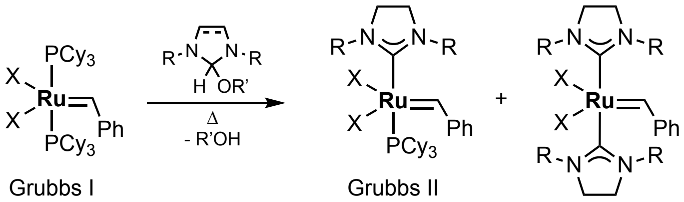

Scheme 5.11. Ruthenium-based olefin metathesis catalysts.

The transfer of NHC ligands from silver to ruthenium was first reported in 2004 by the groups of Arnold and Joó.[41] Çetinkaya, Dixneuf, and co-workers prepared half-sandwich NHC-ruthenium complexes via deprotonation of azolium salts *in situ*.[42] The groups of Çetinkaya, Dixneuf, and Özdemir observed that sterically encumbered benzyl substitutents on the NHC ligands can displace the arene ligand, thus forming η^1:η^6-chelate complexes such as **VII** (Figure 5.3, left) which display catalytic activity in olefin metathesis,[43] transfer hydrogenation of ketones,[44] and amine alkylation reactions.[45] Albrecht and co-workers employed similar complexes featuring chelating allyl *N*-substituents, such as **VI** (Figure 5.3, right), in the catalytic transfer hydrogenation of alkenes using alcohols as the hydrogen source.[46] Further catalytic applications include *N*-alkylation of amines,[47] amination and amidation of alcohols,[48] arylation of arylpyridines,[49] and dehydrogenation of alcohols.[50]

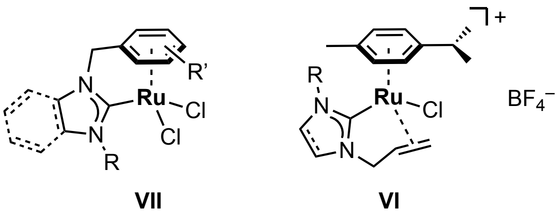

Figure 5.3. Ruthenium complexes featuring chelating NHC ligands.

Similar to Lappert's report of spontaneous C–H activation of the *N*-substituent (*vide supra*, Scheme 5.10), Whittlesey and co-workers observed that, upon reaction of $[Ru(PPh_3)_3(CO)H_2]$ with 1,3-bis(2,4,6-trimethylphenyl)imidazolin-2-ylidene (IMes), a C–C bond of one of the mesityl groups was cleaved, leading to the elimination of CH_4. Reaction of the intermediate $[Ru(IMes)(PPh_3)_2(CO)H_2]$ (**XLVII**) with trimethylvinylsilane led to the reversible C–H activation of a ligand methyl group (Scheme 5.12).[51] The related reaction of $[Ru(PPh_3)_3(CO)HCl]$ with 1,3-diisopropyl-4,5-dimethylimidazolin-2-ylidene ($I^iPr_2Me_2$) led to C–H activation and even the cleavage of a ligand C–N bond (Scheme 5.13, top).[52]

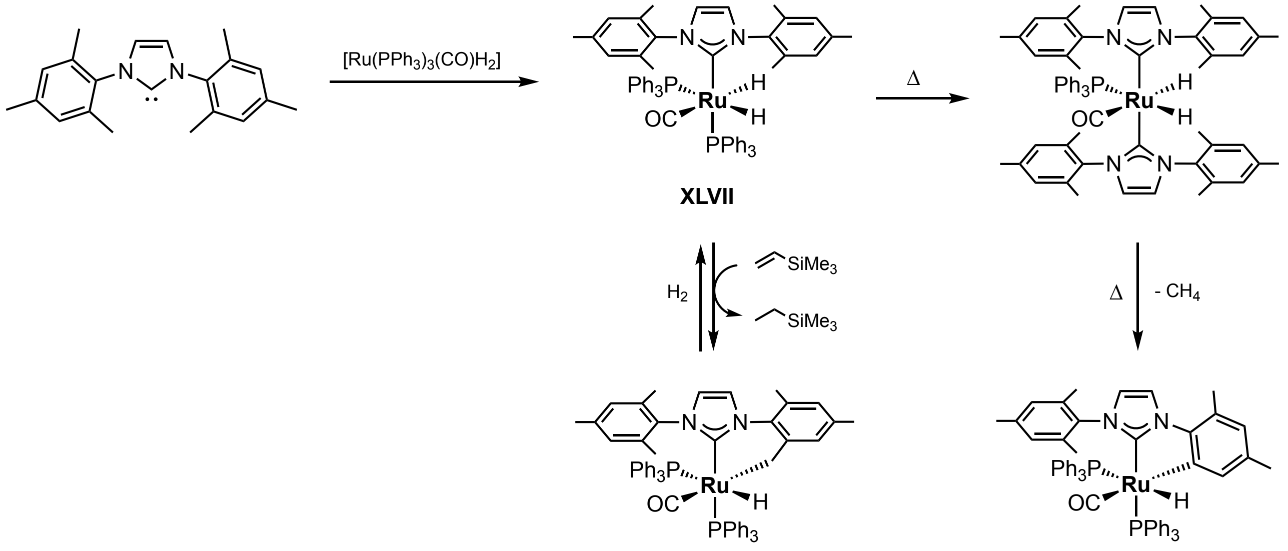

Scheme 5.12. Synthesis and subsequent C–H and C–C activation of Ru-NHC hydride complexes.

Wolf and co-workers observed ligand C–H activation In Ru-NHC complexes when they investigated the nature of the catalyst in the dehydrogenative amide synthesis reported by the group of Madsen.[53] Reaction of $[(cod)RuCl_2]_x$, 1,3-diisopropylimidazolium chloride ($[I^iPrH]Cl$), KO^tBu, and either PCy_3 or PPh_3 afforded C–H-activated alkyl and alkenyl NHC complexes (Scheme 5.13, bottom). However, these complexes displayed no catalytic activity in the Madsen amide synthesis and may constitute degradation products of the actual catalyst.[54]

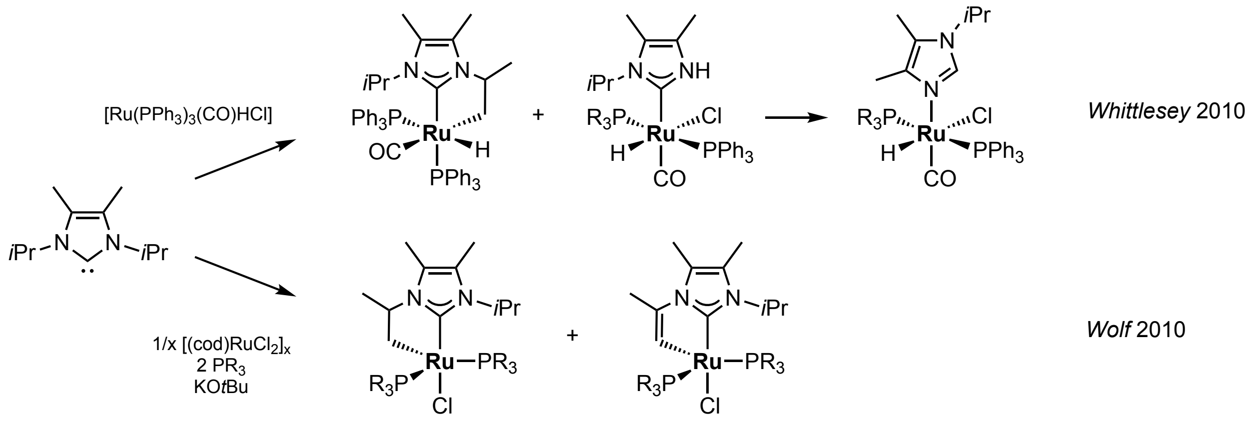

Scheme 5.13. C–H and C–N activation of NHC ligands on ruthenium.

The utility of cyclometalated Ru-NHC complexes was demonstrated impressively by the group of Glorius. Reaction of the axially chiral carbene *R*,*R*-SINpEt (1,3-bis(1-(1-naphthyl)ethyl)-imidazolidin-2-ylidene), generated *in situ* from the imidazolinium salt **XLII** and KO*t*Bu, with [Ru(cod)(2-methylallyl)$_2$] (Scheme 5.14) afforded a complex that proved highly active in the asymmetric hydrogenation of a wide range of (hetero)arenes.[55] Detailed joint investigations by the groups of Wolf and Glorius revealed the structure of the precatalyst **XV**, which contains a doubly C–H-activated NHC ligand and is further stabilized by coordination of a naphthyl group of the second NHC ligand.[56] Mechanistic studies indicated that the cleavage of Ru–C bonds under an H$_2$ atmosphere and partial hydrogenation of the naphthyl groups are key factors for catalytic activity. The outstanding reactivity of **XV** is evidence for the utility of C–H-activated chelating ligands as well as the on-off chelation by naphthyl-substituted NHC ligands.

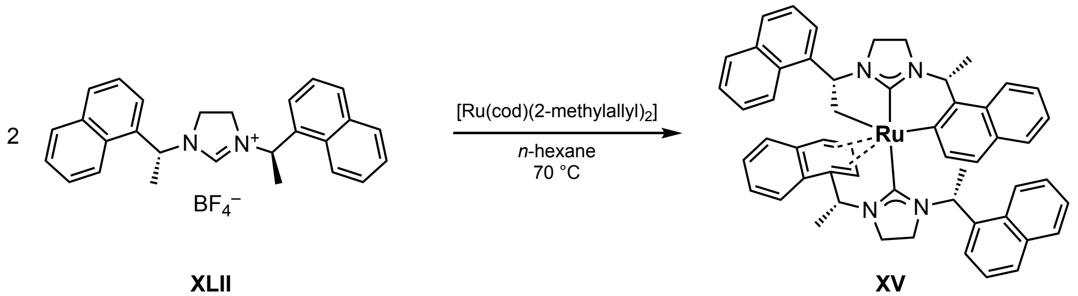

XLII **XV**

Scheme 5.14. [Ru(SINpEt'')(SINpEt)] (**XV**), precatalyst for asymmetric hydrogenations.

5.2 Synthesis and Follow-up Reactivity of Naphthyl-NHC Gold Complexes

The carbene transfer route developed by Lin and co-workers provides easy access to NHC complexes of all precious metals and has become the most popular way to prepare NHC-gold complexes. It was therefore applied for the synthesis of the naphthyl-substituted NHC-gold complexes reported here. Other methods were tested as well, but were found to be less effective than carbene transfer from silver (see section 5.2.1). As described in section 4.3, the isolated yields of NHC-silver complexes were generally lower than 50%, but ^{1}H NMR monitoring revealed full conversion of the used azolium salts. For this reason, the syntheses of NHC-gold complexes were not performed using isolated silver complexes, but rather in a one-pot procedure using stoichiometric amounts of an azolium salt, silver oxide, and (tetrahydrothiophene)gold(I) chloride.

5.2.1 Synthesis of (1,3-Bis(1-naphthylmethyl)imidazolidin-2-ylidene)gold(I) Chloride, [(SINpMe)AuCl] (9)

Complex **9** was prepared by transferring the carbene ligand from silver complex **8**, which was generated *in situ* from imidazolinium salt **XLI** and silver oxide, to [(tht)AuCl] (Scheme 5.15). After stirring in dichloromethane overnight, filtering the mixture and layering the filtrate with *n*-hexane, **9** was isolated as a colorless solid in 46% yield.

Nolan's procedure for the preparation of gold complexes[4] was tested as an alternative in order to avoid the use of silver oxide. **XLI** was reacted with an excess of K_2CO_3 to generate the carbene [SINpMe] *in situ* in the presence of [(tht)AuCl], affording **9** as an off-white solid in 20% yield. The ^{1}H NMR spectrum of the crude product, recorded in $CDCl_3$, revealed the presence of significant amounts of by-products.

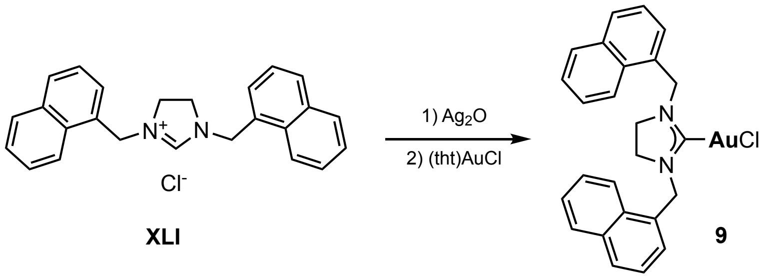

Scheme 5.15. Synthesis of [(SINpMe)AuCl] (**9**).

A further attempt was made to replace silver oxide by a more inexpensive base. Reaction of **XLI** with KO^{t}Bu in the presence of [(tht)AuCl] yielded an off-white crude product that was analysed by ^{1}H NMR spectroscopy in $CDCl_3$, revealing a mixture of 63% **9** and 37% **XLI**. Pure **9** was isolated in 46% yield from this mixture by column chromatography.

From these results we concluded that Lin's silver route is the preferred method due to its straightforward work-up und good yield of the desired product.

The ^{1}H NMR spectrum of **9** recorded in $CDCl_3$ is almost identical to that of the analogous silver complex **8**. The methylene protons resonate at 5.40 ppm (**8**: 5.25 ppm). A singlet at 3.28 ppm corresponds to the backbone (8: 3.39 ppm). The remaining signals between 7.43 and 8.28 ppm were assigned to the naphthyl groups.

The $^{13}C\{^1H\}$ NMR spectrum of **9** is closely related to that of **8**. The methylene carbon atoms resonate at 53.2 ppm (**8**: 53.9) and the backbone carbon atoms at 48.0 ppm (**8**: 49.2). The naphthyl groups are found between 123.5 and 133.9 ppm. The signal of the carbene carbon atom was not observed in the $^{13}C\{^1H\}$ NMR spectrum, but was detected at 194.0 ppm in the $^1H/^{13}C$ HMBC spectrum. The full assignment is given in Table 5.1.

X-ray quality crystals of **9** were obtained by slow diffusion of diethyl ether into a concentrated CH_2Cl_2 solution. **9** crystallizes in the monoclinic space-group *I*2/*a* with four molecules in the asymmetric unit. The gold center is ligated by the carbene ligand and the chloride in a linear coordination arrangement (C1–Au1–Cl1 angle 178.8(1)°). The C1–Au1 bond length (1.987(4)A) is in the typical range for gold complexes of imidazolidin-2-ylidenes. The N1–C1–N2 angle amounts to 109.2(3)°, which is identical to the N1–C1–N2 angle in the corresponding silver complex **8**.

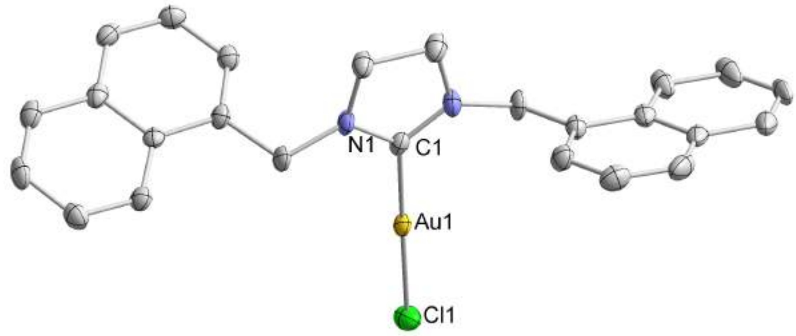

Figure 5.4. Solid state X-ray structure of [(SINpMe)AuCl] (**9**) (thermal ellipsoids at 50% probability; hydrogen atoms omitted for clarity).

5.2.2 Synthesis and Characterization of (1,3-bis(1-naphthylmethyl)benzimidazolin-2-ylidene)gold(I) chloride, [(BNpMe)AuCl] (10)

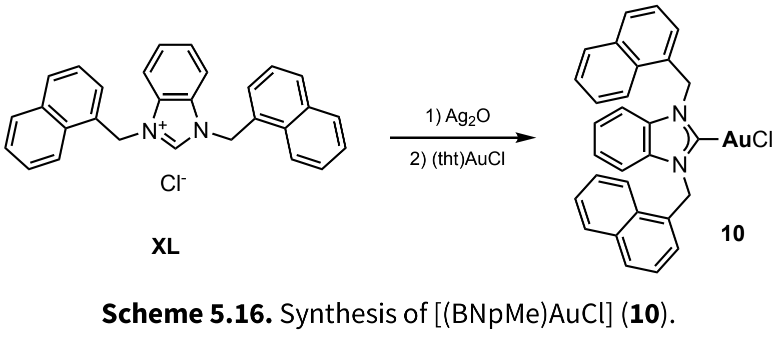

Scheme 5.16. Synthesis of [(BNpMe)AuCl] (**10**).

Complex **10** was prepared the same way as **9** by carbene transfer from the corresponding Ag-NHC complex **7**, generated *in situ* from **XL** and Ag_2O, to [(tht)AuCl] (Scheme 5.16). Following an analogous workup procedure as described above, **10** was isolated as a colorless solid in 42% yield. Several attempts to grow X-ray quality crystals resulted only in the formation of very thin needles that were unsuitable for X-ray diffraction.

The ^{1}H NMR spectrum of **10** recorded in $CDCl_3$ is similar to that of the anaologous silver complex **7**, with the signals of the methylene protons at 6.32 ppm the benzannulated backbone at 7.17 ppm, and the naphthyl groups in the range of 7.06 to 8.19 ppm. In the $^{13}C\{^1H\}$ NMR spectrum, the methylene carbons resonate at 51.2 ppm, and the backbone carbons at 112.5, 124.9, and 133.9 ppm. Signals from 122.6, to 133.9 ppm are assigned to the naphthyl carbons. The carbene carbon atom gives rise to a signal at 181.0 ppm. The shift of the carbene signal of ~10 ppm upfield with respect to the $^{13}C\{^1H\}$ NMR spectrum of **7** (190.9 ppm) is consistent with the trend observed for Ag and Au complexes **8** and **9** (205.3 and 194.0 ppm, respectively). See Table 5.1 for a list of all ^{1}H and ^{13}C NMR signals.

Table 5.1. ^{1}H and ^{13}C NMR signals of **9** and **10**, recorded in $CDCl_3$.

^{1}H / ^{13}C	**[(SINpMe)AuCl] (9)**		**[(BNpMe)AuCl] (10)**	
C_1	–	194.0	–	181.0
H_2 / C_2	5.40	53.2	6.29	51.2
C_3	–	130.2	–	133.7
H_4 / C_4	7.44	127.4	7.06	124.8
H_5 / C_5	7.43	125.3	7.37	125.3
H_6 / C_6	7.84	129.5	7.84	129.3
H_7 / C_7	7.90	129.0	7.92	129.2
H_8 / C_8	7.55	126.3	7.56	126.4
H_9 / C_9	7.61	127.1	7.61	126.7
H_{10} / C_{10}	8.28	123.5	8.19	122.6
C_{11}	–	131.5	–	129.8
C_{12}	–	134.0	–	133.9
H_{13} / C_{13}	3.28	48.0	–	133.9
$H_{14/15}$ / $C_{14/15}$	–	–	7.17	112.5/ 124.9

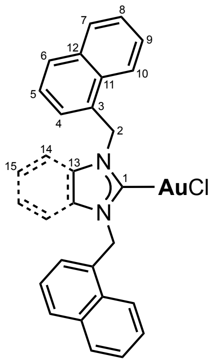

5.2.3 Reactions of 9 with NaBAr$^F{}_4$ and AgBF$_4$

In gold catalysis, the catalytically active species is usually generated from a gold(I) halide complex by abstracting the halide ligand with a silver salt of a weakly coordinating anion. Since the resulting gold(I) fragments show a high affinity for alkynes and alkenes, and polyarenes are known to possess diene-like ligand properties, it seemed plausible that a species could be generated in which the metal center is chelated by a naphthyl-substituted carbene (Figure 5.2). Complex **9** was therefore reacted with two well-established chloride abstracting agents, sodium tetrakis(3,5-bis(trifluoromethyl)phenyl)borate (NaBAr$^F{}_4$) and silver tetrafluoroborate (Scheme 5.17).

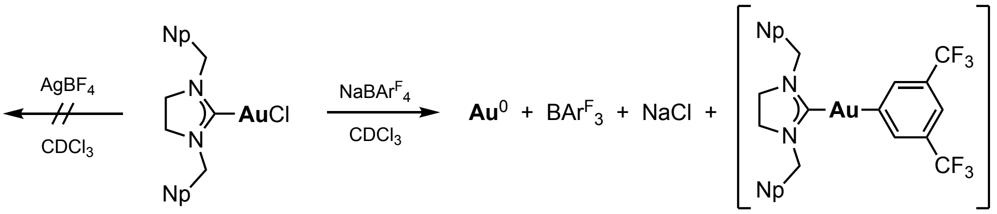

Scheme 5.17. Reaction of **9** with chloride abstracting agents. Proposed product is shown in brackets.

Mixing **9** with AgBF$_4$ in CDCl$_3$ at room temperature did not lead to any observable reaction. In the ^{1}H NMR spectrum of the reaction mixture, only starting material was identified. This was somewhat unexpected given the popularity of AgBF$_4$ as a chloride abstracting agent in gold catalysis. By contrast, NaBAr$^F{}_4$ reacted readily with **9** in CDCl$_3$, leading to an immediate color change to dark purple and the formation of a dark precipitate. This indicated the reduction of the gold(I) species to elemental gold (known as "purple of Cassius"). The highly electrophilic gold cation which is generated upon chloride abstraction likely undergoes a reaction with the BAr$^F{}_4{}^-$ anion.

Straub and Nolan have reported similar observations when reacting NHC-gold(I) complexes with NaBAr$^F{}_4$ (Scheme 5.18).[57] Their results differ, however, in the obtained gold species (Figure 5.6). Nolan and co-workers attempted to generate a gold species stabilized by a chelating alkenyl-NHC ligand, but they did not investigate the fate of the borate anion and isolated a cationic dicarbene species [(NHC)$_2$Au]$^+$BAr$^F{}_4{}^-$ (Scheme 5.18, right). Straub and co-workers were able to observe a cationic species via ^{1}H NMR spectroscopy, in which the gold center was stabilized by coordination to one aryl ring of the BAr$^F{}_4{}^-$ anion. After several days, the electrophilic gold center cleaved the BAr$^F{}_4{}^-$ counterion and a carbene-gold(I)-(3,5-

bis(trifluoromethyl)phenyl complex as well as tris(3,5-bis(trifluoromethyl)phenyl)borane resulted as the final products (Scheme 5.18, left).

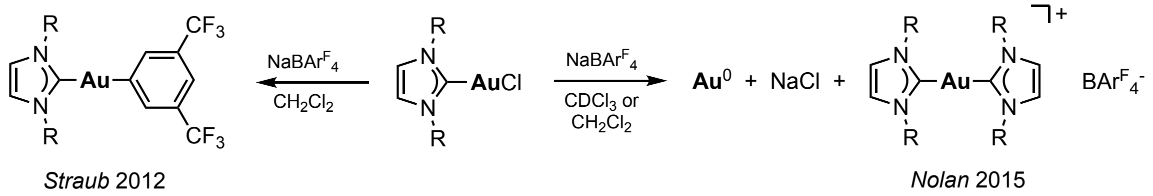

Scheme 5.18. Reactions of NHC-gold complexes with $NaBAr^F{}_4$.

The ^{1}H and ^{19}F NMR spectra indicate that, of the two possible products, the monocarbene-gold-aryl complex is more likely to have formed. In the ^{1}H NMR spectrum, no signals corresponding to an intact $BAr^F{}_4^-$ anion are observed. Instead, four signals in the range of 7.77 to 8.03 ppm with an integral ratio of 6:3:1:2 indicate that $BAr^F{}_4^-$ was cleaved into $BAr^F{}_3$ and an aryl moiety which may be bound to a gold fragment. This is corroborated by the ^{19}F NMR spectrum which shows two main signals at –63.31 and –63.38 ppm with an integral ratio of roughly 3:1, with a weaker signal at –62.87 ppm. However, the remaining signals in the ^{1}H NMR spectrum could not be assigned unambiguously, hence the identity of the obtained gold complex remains unclear. Given the immediate decomposition when mixing **9** and $NaBAr^F{}_4$ at room temperature, the slow addition of $NaBAr^F{}_4$ at low temperature may lead to a more controlled reaction and possibly the formation of the desired chelating complex.

5.3 Synthesis, Characterization, and Reactivity of Naphthyl-NHC Rhodium Complexes

Encouraged by the straightforward preparation of NHC-gold complexes by carbene transfer from silver, the same procedure was used for the synthesis of NHC-rhodium complexes. The high stability of these compounds towards air and water allowed the work-up to be performed under ambient conditions.

5.3.1 Synthesis of (1,3-Bis(1-naphthylmethyl)imidazolidin-2-ylidene)(1,5-cyclooctadiene)rhodium(I) Chloride, [(SINpMe)RhCl(cod)] (11)

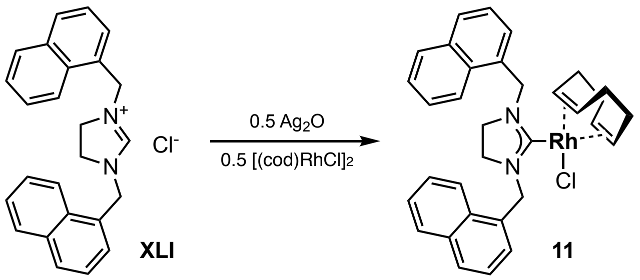

Scheme 5.19. Synthesis of [(SINpMe)RhCl(cod)] (**11**).

Complex **11** was prepared by carbene transfer from **8**, which was generated in situ from **XLI** and a slight excess of Ag_2O, in the presence of $[(cod)RhCl]_2$ (Scheme 5.19). Due to the high stability of the product, impurities could be removed by column chromatography. Pure **11** was obtained as a bright yellow solid in 73% yield. X-ray quality crystals were obtained by layering a toluene solution of **11** with *n*-hexane.

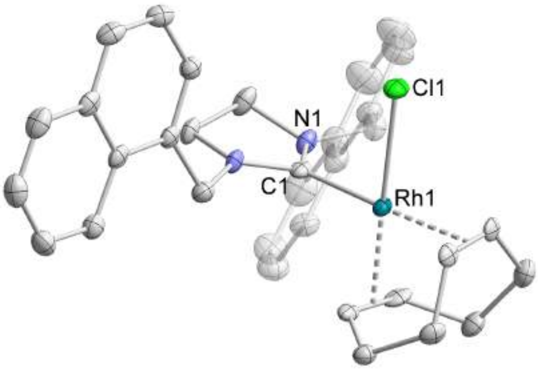

Figure 5.5. Solid-state X-ray structure of **11** (thermal ellipsoids at 50% probability; hydrogen atoms and solvent removed for clarity).

Complex **11** crystallizes in the monoclinic space group $P2_1/c$ with four molecules in the unit cell, as well as a disordered toluene molecule. The molecular structure (Figure 5.5) reveals a rhodium center coordinated in a square planar geometry by the carbene ligand, the chloride, and the cyclooctadiene ligand, as is expected for a d^8 metal center. The C1–Rh1 bond (2.01305(3) Å) is within the range of carbene-rhodium bonds in structurally related imidazolidin-2-ylidene rhodium(I) complexes.[58] The angles around the rhodium center are between 85 and 94°, with the sum of angles amounting to 350°. This confirms the slightly distorted square planar coordination. The N–C1 bond lengths (1.33880(1) and 1.35018(1) Å) and the N1–C1–N2 bond angle (108.091(1)°) are in the typical range of imidazolidin-2-ylidene ligands.

The ^1H NMR spectrum of **11** in $CDCl_3$ shows the expected signals of the SINpMe ligand and the cyclooctadiene ligand. Broadened doublets at 1.89 and 2.26 ppm correspond to the CH_2 groups of the cod, with the CH=CH protons resonating at 3.67 and 5.11 ppm. The resonance of the NHC backbone protons is split into a complex multiplet at 3.14-3.39 ppm. The signal corresponding to the CH_2 groups of the *N*-substituents is found at 5.92 ppm and the signals between 7.49 and 8.45 ppm were assigned to the naphthyl groups. Recording the ^1H NMR spectrum in CD_2Cl_2 rather than $CDCl_3$ leads to a notable change: The singlet at 5.92 is split into two doublets at 5.67 and 6.13 ppm with a coupling constant of 15.0 Hz, while none of the other signals are affected. This may indicate that the rotation of the naphthyl groups around the H_2C–C_{Np} bond is slow on the NMR time scale in CD_2Cl_2 solution, but significantly faster in $CDCl_3$.

In the $^{13}C\{^1H\}$ NMR spectrum, the signals at 28.6 and 32.9 ppm were assigned to the CH_2 groups of the cod ligand. The CH=CH carbon atoms are found at 68.6 and 99.7 ppm as doublets with $^1J_{C-Rh}$ coupling constants of 14.6 and 6.2 Hz, respectively. The NHC backbone carbons resonate at 48.6 ppm, the CH_2 groups substituents at 52.6 ppm, and the naphthyl C*H* carbons between 123.8 and 133.8 ppm. While no signal corresponding to the carbene carbon atom was observed in the $^{13}C\{^1H\}$ NMR spectrum, a $^1H/^{13}C$ HMBC experiment revealed an additional resonance at 214.1 ppm due to coupling of the carbene carbon to the CH_2 groups of the carbene ligand. The chemical shift is consistent with related imidazolidin-2-ylidene rhodium(I) complexes.[58] A list of all ^1H and $^{13}C\{^1H\}$ NMR signals of **11** is given in Table 5.2.

5.3.2 Synthesis of (1,3-Bis(1-(1-naphthyl)ethyl)imidazolidin-2-ylidene)(1,5-cycloocta-diene)rhodium(I) Chloride, (SINpEt)(cod)RhCl (12)

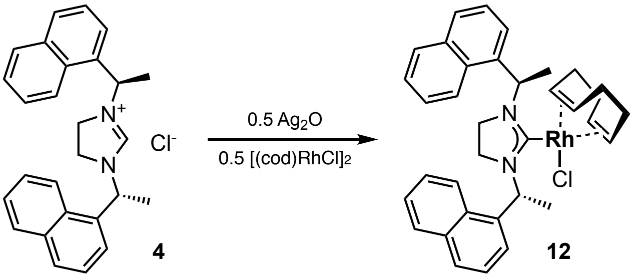

Scheme 5.20. Synthesis of [(SINpEt)RhCl(cod)] (**12**).

While the reaction of silver oxide with the chiral imidazolinium salt **4** produced a mixture of compounds, the synthesis of the corresponding rhodium complex [(SINpEt)RhCl(cod)] (**12**) using the silver carbene transfer route was successful (Scheme 5.20). **12** was prepared in the same manner as **11**. After purification by column chromatography, **12** was obtained as a light yellow powder in 61% yield. Several attempts to obtain X-ray quality crystals remained unsuccessful. However, the NMR spectra indicate that the structure of **12** is analogous to that of **11**.

Due to the lower symmetry of the SINpEt ligand in **12** as compared to SINpMe in **11**, the ^1H NMR spectrum of **12** recorded in $CDCl_3$ is more complex since all hydrogen atoms are now magnetically inequivalent. The methylene protons of the cod ligand give rise to broad multiplets in the range of 0.82 to 2.33 ppm, while the olefinic protons of cod resonate at 2.91, 3.51, 5.00, and 5.09 ppm. Multiplets corresponding to the NHC backbone are observed at 3.40, 3.69, and 3.89 ppm. The CH_3 groups bound to the chiral centers give rise to doublets at 1.89 and 1.69 with $^3J_{HH}$ coupling constants of 7.0 and 7.1 Hz, respectively. The protons bound to the neighboring carbon atoms, which are stereocenters, are observed at 7.04 and 7.85 ppm. While the signal at 7.04 ppm is split into a quartet with $^3J_{HH} = 7.1$ Hz, the signal at 7.85 overlaps with a signal assigned to the naphthyl substituents. The naphthyl groups resonate in the range of 7.33 to 9.24 ppm.

In accord with the ^{1}H NMR spectrum of **12**, the reduced symmetry with respect to **11** leads to a fairly complex $^{13}C\{^1H\}$ NMR spectrum. Whereas in **11**, the two “sides” of the NHC ligand as well as the cod ligand were magnetically equivalent, every carbon in **12** gives rise to a signal of its own. The chemical shifts of the signals corresponding to the same positions, however, are almost identical for **11** and **12**. The cod ligand gives rise to signals between 27.3 and 32.6 ppm (CH_2 carbons) and between 66.7 and 99.4 ppm ($CH{=}CH$ carbons). The NHC backbone resonates at 44.4 and 46.4 ppm. The CH_3 groups are observed at 20.5 and 20.0 ppm, and the chiral carbons at 53.8 and 56.2 ppm. Fourteen signals between 121.4 and 128.9 ppm correspond to the *C*H carbons of the naphthyl groups while the quaternary naphthyl carbons give rise to six signals between 130.3 and 142.0 ppm. The resonance of the carbene carbon was observed at 213.0 ppm in a $^1H/^{13}C$ HMBC spectrum. This chemical shift is nearly identical to the corresponding signal of complex **11**. The full assignment is given in Table 5.2.

5.3.3 Synthesis of (1,3-Bis(1-naphthylmethyl)benzimidazolin-2-ylidene)(1,5-cycloocta-diene)rhodium(I) Chloride, [(BNpMe)(cod)RhCl] (13)

The preparation of **13** followed the same procedure as **11** and **12**. Stirring benzimidazolium salt **XL** with a slight excess of Ag_2O in the presence of $[(cod)RhCl]_2$ (Scheme 5.21) and subsequent purification of the crude product by column chromatography gave **13** as a bright yellow powder in a yield of 67%. Rather than by column chromatography, pure **13** can also be obtained by recrystallizing the crude product from toluene.

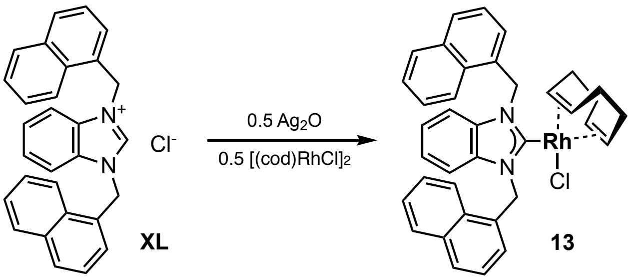

Scheme 5.21. Synthesis of [(BNpMe)RhCl(cod)] (**13**).

X-ray quality crystals were obtained by layering a toluene solution of **13** with *n*-hexane. **13** crystallizes in the triclinic space group *P*-1 with two molecules in the unit cell. The molecular structure of **13** (Figure 5.6) is analogous to that of **11**, with a square planar coordination geometry at the rhodium center. The L1–Rh1–L2 angles (L = ligand) are in the range of 87.6 to 93.8° with a sum of angles of 360°. The Rh1–C1 bond, at 2.017(2) Å, is comparable to related complexes [(NHC)RhCl(cod)] containing benzimidazolin-2-ylidene ligands.[59] The N–C1 bond lengths (1.357(3) and 1.361(3) Å) and N1–C1–N2 angle (105.9(2)°) are almost identical to those in the related complex [(BMe)RhCl(cod)] (BMe = 1,3-dimethylbenzimidazolin-2-ylidene).[59a]

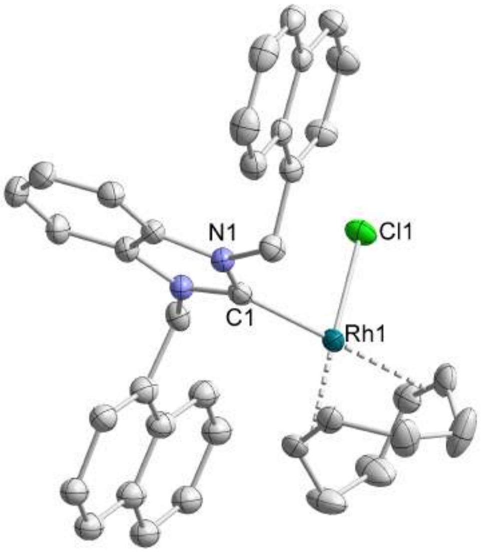

Figure 5.6. Solid-state X-ray structure of **13** (thermal ellipsoids at 50% probability; H atoms omitted for clarity).

The ^{1}H NMR spectrum of **13** recorded in $CDCl_3$ is very similar to that of **11** with the addition of resonances of the backbone protons. The largest differences are observed for one of the olefinic cod signals, which is observed at 3.31 ppm (**11**: 3.67 ppm) and the CH_2 groups of the *N*-substituents, which give rise to two doublets at 6.32 and 7.28 ppm with a coupling constant of 16.7 Hz. The remaining resonances are only marginally shifted with respect to the spectrum of **11**. The splitting of the methylene signals into two doublets was observed for **11** in CD_2Cl_2 solution and indicates that the rotation of the naphthyl groups around the C7–C8 axis is hindered.

In the $^{13}C\{^1H\}$ NMR spectrum of **13**, most signals are identical to those of **11**. The only major difference is the chemical shift of the resonance of the carbene carbon. For **13**, a doublet at 199.1 ppm with a $^1J_{C–Rh}$ coupling constant of 51.2 Hz was assigned to the carbene (11: 214.0 ppm). Due to coupling with rhodium, the carbene signal is split into a doublet with a coupling constant of 51.2 Hz. See Table 5.2 for a full list of ^{1}H and $^{13}C\{^1H\}$ NMR signals.

Table 5.2. ^{1}H and ^{13}C NMR chemical shifts of complexes **11**, **12**, and **13** (assignment: see Figure 5.7).

^{1}H / ^{13}C	[(SINpMe)RhCl(cod)] (11)		[(SINpEt)RhCl(cod)] (12)		[(BNpMe)RhCl(cod)] (13)	
C_1	–	214.1	–	213.0	–	199.1
H_2 / C_2	5.92	52.6	7.04/7.85	53.8/56.2	6.32/7.28	50.2
H_3 / C_3	–	–	1.89/1.69	20.5/20.0	–	–
C_4	–	132.1	–	135.9/142.0	–	131.9
H_5 / C_5	7.54	126.1	7.54/7.33	124.0/121.4	6.97-7.03	123.6
H_6 / C_6	7.48	125.4	7.49/7.45	125.3/124.6	7.36	125.4
H_7 / C_7	7.84	128.6	7.84/7.80	128.7/127.5	7.85	128.2
H_8 / C_8	7.90	128.7	7.90/7.84	128.9/128.3	7.98	129.0
H_9 / C_9	7.56	126.1	7.56/7.54	126.1/126.2	7.61-7.67	126.3
H_{10} / C_{10}	7.64	126.7	7.68/7.73	126.4/127.0	7.74	126.9
H_{11} / C_{11}	8.45	123.9	8.53/9.24	124.0/126.0	8.42	122.8
C_{12}	–	131.7	–	131.5/130.4	–	130.6
C_{13}	–	133.8	–	134.0/134.1	–	133.7
H_{14} / C_{14}	3.19/3.35	48.6	3.40/3.69/3.89	44.4/46.4	–	135.4
H_{15} / C_{15}	–	–	–	–	6.97-7.03	111.0
H_{16} / C_{16}	–	–	–	–	7.04-7.09	122.8
CH (cod)	3.66/5.11	68.6/99.7	2.91/3.51/5.00/5.09	70.0/66.7/99.4/98.2	3.31/5.07	69.3/100.5
CH_2 (cod)	1.89/2.26	28.6/32.9	0.82/1.17/1.43/1.66/1.66/2.25/1.83/2.33	32.6/27.3/32.1/29.4	1.47-2.06	28.3/32.6

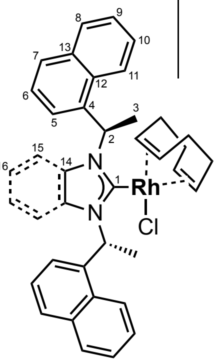

Figure 5.7. Assignment scheme for rhodium complexes **11**, **12**, and **13**.

5.3.4 Reaction of NHC-Rhodium Complexes with Chloride Abstracting Agents

In analogy to the work of Dorta and co-workers on iridium complexes of naphthyl-substituted NHC ligands,[36] we attempted to prepare a chelating NHC-rhodium complex in which a naphthyl substituent coordinates to the metal center by removing the chloride ligand. Sodium tetrakis(3,5-bis(trifluoromethyl)phenyl)borate ($NaBAr^F_4$) and silver tetrafluoroborate were employed as chloride abstracting agents. The reactions were performed in $CDCl_3$ to allow monitoring by NMR spectroscopy.

Reacting complex **11** with one equivalent of NaBAr$^F{}_4$ (Scheme 5.22) led to a color change from light yellow to orange within less than a minute. A colorless precipitate formed which was removed by filtration. Due to broadening of the NMR signals, no conclusive determination of the structure of the formed complex was possible. Attempts to crystallize the formed ionic species were unsuccessful, so that only a tentative suggestion as to the structure of the product **14a** can be made.

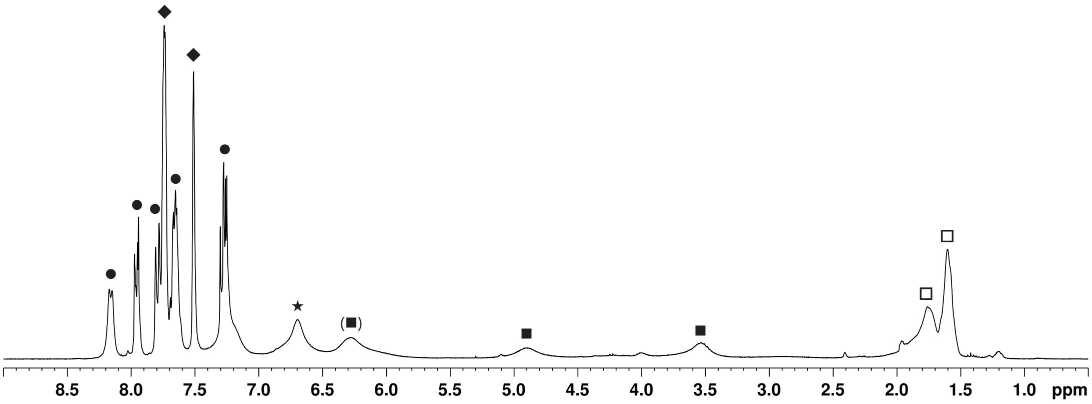

Figure 5.8. ^{1}H NMR spectrum of **14a** (reaction mixture in CDCl$_3$). ◆: BAr$^F{}_4{}^-$, ●: naphthyl groups, □: CH$_{2\,cod}$, ■: CH$_{cod}$, ★: NCH$_2$Ar.

In contrast to the reaction of NaBAr$^F{}_4$ with NHC-gold complexes, the BAr$^F{}_4{}^-$ anion did not undergo a reaction with the cationic NHC-Rh complex formed upon chloride abstraction. This is evident from the ^{19}F NMR spectrum, which displays only a singlet at –62.8 ppm, corresponding to the CF$_3$ groups of BAr$^F{}_4{}^-$ as well as two signals in the ^{1}H NMR spectrum at 7.74 and 7.51 ppm which correspond to an intact BAr$^F{}_4{}^-$ anion (Figure 5.8, marked with ◆). The ^{1}H NMR signals of the naphthyl groups (●) as well as the CH$_2$ groups of the cod ligand (□) remain relatively unchanged with respect to **12**, but the signals of the olefinic protons of cod (■) and the CH$_2$ groups of the *N*-substituents (★) are broadened substantially. For this reason the integrals of the signals could not be determined beyond doubt. However, since only one set of naphthyl signals was observed, a symmetric complex [(BNpMe)Rh(cod)$^+$] (**14a**) with no chelation of a naphthyl group seems most plausible.

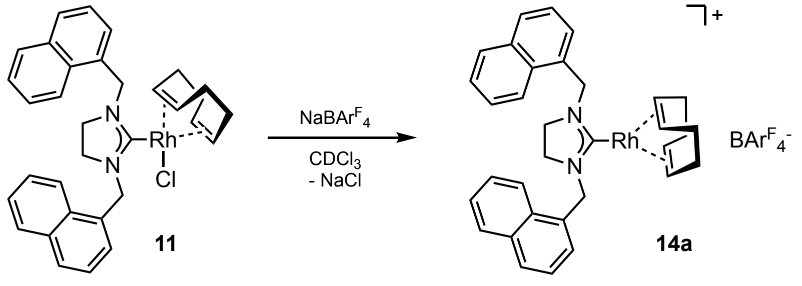

Scheme 5.22. Reaction of **11** with NaBAr$^F{}_4$.

The reaction of complex **13** with $AgBF_4$ (Scheme 5.23) did not lead to a visible change in color, but the formation of a colorless precipitate was observed which was again removed by filtration. Since no X-ray quality crystals could be obtained, the suggested product structure is based on the NMR spectrum of the reaction mixture (Figure 5.9).

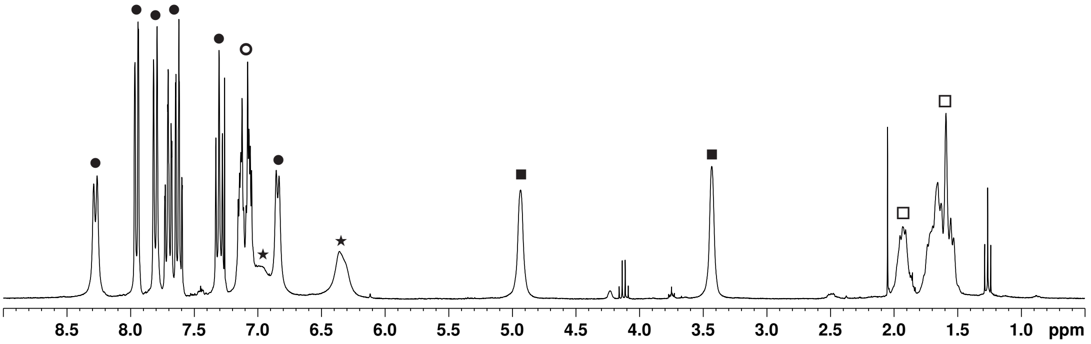

Figure 5.9. ^{1}H NMR spectrum of **14b** (reaction mixture in $CDCl_3$). ●: naphthyl groups, ○: backbone, □: $CH_{2\,cod}$, ■: CH_{cod}, ★: NCH_2Ar.

The spectrum is quite similar to that of the above reaction in that the signals of the naphthyl groups (●), the benzannulated backbone (○), and the cod CH_2 groups (□) are relatively unchanged. The olefinic protons (■) give rise to slightly broadened signals at 3.43 and 4.93 ppm (shifted from 3.31 and 5.07 ppm for complex **13**, respectively). The signals corresponding to the CH_2 groups of the (1-naphthylmethyl) substituents (★) are broadened significantly. Rather than the doublets at 6.32 and 7.28 ppm found in the spectrum of **13**, broad signals at 6.35 and 6.98 ppm are observed. Overall, the ^{1}H NMR spectrum indicates that the product, **14b**, is structurally analogous to **14a**, with the naphthyl groups giving rise to only one set of signals and marginal changes in the chemical shifts of the signals of the cod ligand.

Further investigations by mass spectrometry and continued efforts to obtain X-ray quality crystals will hopefully shed more light on the molecular structures of **14a** and **14b**.

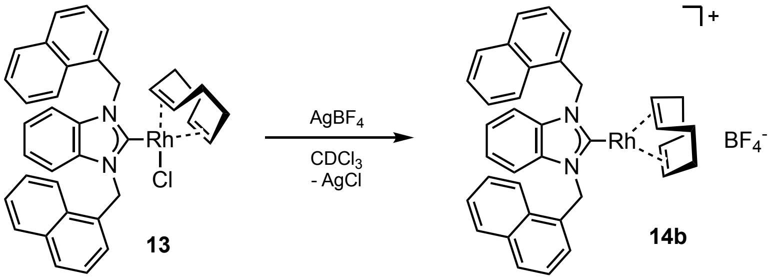

Scheme 5.23. Reaction of **13** with $AgBF_4$.

5.3.5 Catalytic Hydrogenations with 11, 12, and 13

The ability of the NHC-rhodium **11**, **12**, and **13** complexes to catalyze hydrogenation reactions was assessed by the group of Glorius at the University of Münster. Acetophenone, stilbene, and 2-phenylbenzofuran were selected as benchmark substrates to study the reduction of C=O double bonds, C=C double bonds, and heterocyclic compounds. Being prochiral substrates, acetophenone and 2-phenylbenzofuran further allowed the investigation of the degree of asymmetric induction when using the chiral rhodium complex **12**.

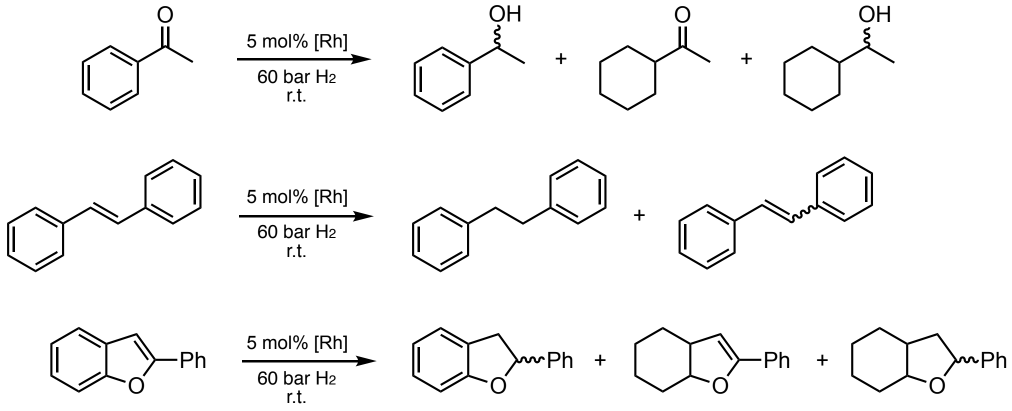

Scheme 5.24. Rhodium-catalyzed hydrogenation of acetophenone, stilbene, and 2-phenylbenzofuran.[60]

The reactions were performed in THF at room temperature at a hydrogen pressure of 60 bar and a catalyst loading of 5 mol%. Analysis of the product mixtures by GC-MS showed that the starting material reacted quantitatively, but the reactions were unselective as mixtures of several products were observed. The aryl groups in some of the products were partially hydrogenated in addition to the C=C and C=O bonds (Scheme 5.24). Furthermore, no asymmetric induction was observed when using **12** as the catalyst. The obtained product mixtures indicate a heterogeneous mechanism, which is supported by the formation of a black powder and a colorless supernatant from the yellow solution of precatalyst and substrate. It can be assumed that the NHC-rhodium complexes decompose under hydrogen pressure, leading to the formation of metallic rhodium particles which are catalytically active, but of limited use due to the lack of selectivity. Under lower hydrogen pressure, the starting material was only partially converted with no increase in selectivity.[60]

5.4 Synthesis of NHC-Ruthenium Complexes

5.4.1 Synthesis of (1,3-Bis(1-naphthylmethyl)benzimidazolin-2-ylidene)(cymene)-ruthenium(II) Dichloride, [(BNpMe)RuCl$_2$(cym)] (15)

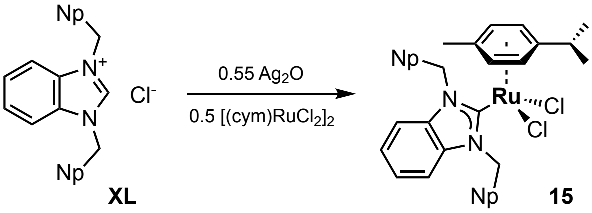

Scheme 5.25. Synthesis of [(BNpMe)RuCl$_2$(cym)] (**15**).

Complex **15** was prepared following the widely established method of carbene transfer from silver. In a first microscale experiment, 0.5 equivalents of [(cym)RuCl$_2$]$_2$ were reacted with [(BNpMe)AgCl] (**7**) in acetonitrile, yielding the desired compound (Scheme 5.25). **15** was obtained as deep red crystals upon diffusion of diethyl ether into a dichloromethane solution. In subsequent experiments it was found that generating **7** *in situ* from Ag$_2$O and **XL** and exchanging acetonitrile for dichloromethane led to superior results, circumventing the low-yielding isolation of complex **7**. Using this method, **15** was obtained in an excellent yield of 94% by simply filtering off the formed silver chloride and removing the solvent *in vacuo*. ^{1}H NMR and elemental analysis showed the product to be pure without recrystallization or column chromatography.

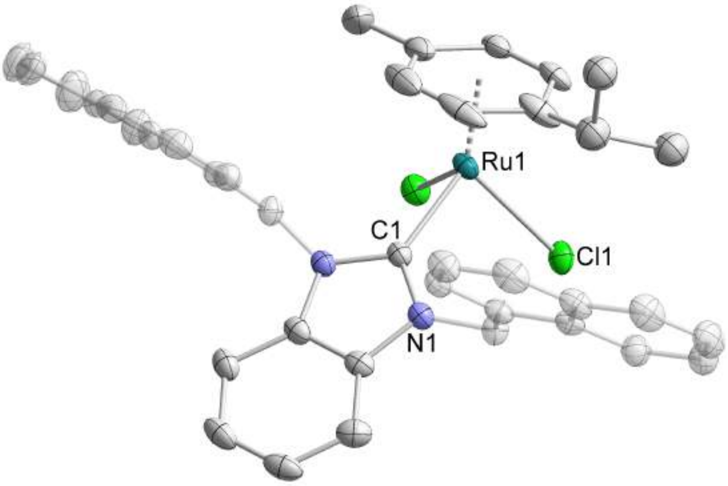

Figure 5.10. Solid-state X-ray structure of **15** (thermal ellipsoids at 50% probability; H atoms and solvent molecules omitted for clarity).

15 crystallizes from CH$_2$Cl$_2$ / Et$_2$O in the monoclinic space group $P2_1/n$ with four molecules in the unit cell. The molecular structure (Figure 5.10) features a half-sandwich motif commonly described as a “piano stool”, with the ruthenium center η^6-coordinated by the cymene ligand, with two chlorides and the NHC ligand forming the three “legs”. The C1–Ru1 distance

(2.074(3) Å) is in the expected range for a NHC-ruthenium complex. The N–C1 bonds (1.364(4) and 1.366(4) Å) and N1–C1–N2 angle (105.0(3)°) are unremarkable, as is the distance of the ruthenium center to the centroid of the arene ligand (1.7011(3) Å). The unit cell further contains one molecule of dichloromethane and one molecule of diethyl ether.

The ^{1}H NMR spectrum recorded in $CDCl_3$ displays the expected signals of the cymene and NHC ligands. The alkyl signals of cymene are shifted significantly upfield by 0.5 to 0.8 ppm with respect to $[(cym)RuCl_2]_2$. The methyl group gives rise to a singlet at 1.50 ppm ($[(cym)RuCl_2]_2$: 2.11 ppm), and the isopropyl group resonates at 0.76 ppm (doublet, $CH(CH_3)_2$; 1.23 ppm for $[(cym)RuCl_2]_2$), and 2.09 ppm (heptet, $CH(CH_3)_2$; 2.87 ppm for $[(cym)RuCl_2]_2$). The aromatic cymene signals are shifted slightly from 5.30 and 5.43 ppm for $[(cym)RuCl_2]_2$ to 4.94 and 5.17 ppm (d, $3J_{HH}$ = 5.9 Hz). The methylene groups of the *N*-substituents give rise to two broadened doublets at 6.00 and 7.53 ppm. The naphthyl groups resonate in the range of 6.72 to 8.29 ppm, with the backbone signals observed at 7.16 ppm.

In the $^{13}C\{^1H\}$ NMR spectrum, the alkyl groups of the cymene ligand are observed at 17.8 ppm (CH_3), 22.3 ($CH(CH_3)_2$), and 30.5 ppm ($CH(CH_3)_2$). The arene *C*H carbons resonate at 84.9 and 85.6 ppm; the quaternary cymene carbons were identified at 96.6 and 105.5 ppm in a $^1H/^{13}C$ HMBC experiment. The NCH_2Np methylene carbons resonate at 50.6 ppm. The backbone *C*H carbons are observed at 111.0 and 123.6 ppm, with the quaternary carbon of the backbone at 136.0 ppm. The naphthyl groups are observed between 121.5 and 133.8 ppm. The carbene carbon resonance is observed at 192.6 ppm, which is in good agreement with the related complex $[(BBn)RuCl_2(cym)]$ (BBn = 1,3-dibenzylbenzimidazolin-2-ylidene).[61] A summary of all ^{1}H and $^{13}C\{^1H\}$ NMR signals is given in Table 5.3.

5.4.2 Synthesis of (1,3-Bis(1-naphthylmethyl)imidazolidin-2-ylidene)(cymene)-ruthenium(II) Dichloride, [(SINpMe)RuCl₂(cym)] (16)

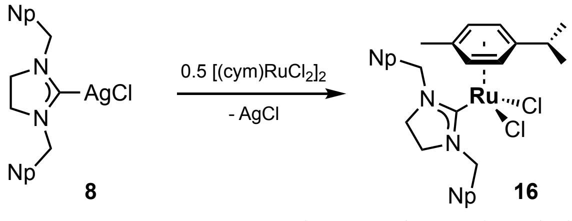

Scheme 5.26. Synthesis of $[(SINpMe)RuCl_2(cym)]$ (**16**).

Complex **16** was prepared in a microscale experiment (~20 mg) analogous to that described in section 5.4.1. Stirring **8** with 0.5 equivalents of $[(cym)RuCl_2]_2$ in acetonitrile at room temperature overnight resulted in the formation of a grey precipitate and a red solution (Scheme 5.26). Recrystallization of the residue from CH_2Cl_2 / Et_2O gave red crystals of **16**.

Table 5.3. ^{1}H and ^{13}C NMR chemical shifts of complex **15**.

^{1}H / ^{13}C	[(BNpMe)$RuCl_2$(cym)] (15)	
C_1	–	192.6
H_2 / C_2	6.00/7.53	50.6
C_3	–	133.4
H_4 / C_4	6.73	121.5
H_5 / C_5	7.42	125.1
H_6 / C_6	7.85	128.1
H_7 / C_7	7.97	128.9
H_8 / C_8	7.64	126.7
H_9 / C_9	7.70	127.2
H_{10} / C_{10}	8.29	123.1
C_{11}	–	130.5
C_{12}	–	133.8
C_{13}	–	136.0
$H_{14/15}$ / $C_{14/15}$	7.16	111.0/123.6
H_{16} / C_{16}	1.51	17.8
H_{17} / C_{17}	2.10	30.5
H_{18} / C_{18}	0.76	22.3
H_{19} / C_{19}	5.17	84.9
H_{20} / C_{20}	4.94	85.6
C_{21}	–	105.5
C_{22}	–	96.6

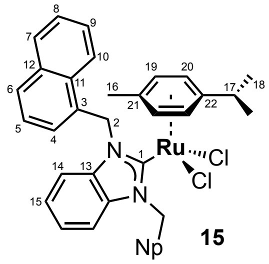

15

16 crystallizes in the orthorhombic space group *P*cba with eight molecules in the unit cell. The molecular structure (Figure 5.11) is similar to that of **15**, with the cymene ligand binding to the ruthenium center in an η^6-fashion and two chlorides as well as the carbene ligand. The C1–Ru1 distance amounts to 2.083(3) Å and is in good agreement with analogous complexes; so are the C1–N bonds (1.345(4) and 1. 355(4) Å) and the N1–C1–N2 angle (107.6(3)°) as well as the distance of Ru1 to the centroid of the arene ligand (1.6991(2) Å).

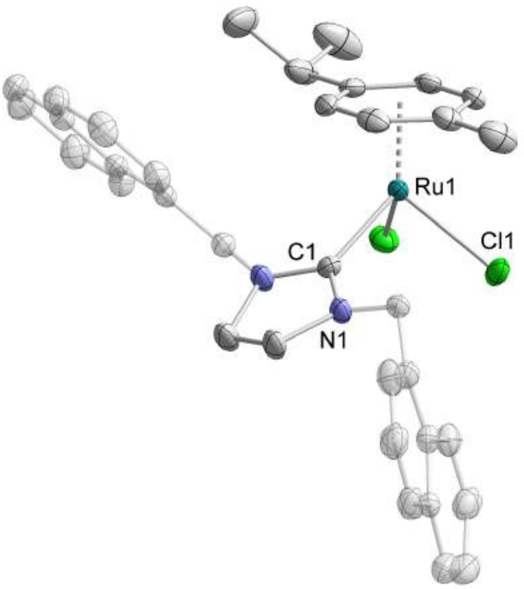

Figure 5.11. Solid-state X-ray structure of **16** (thermal ellipsoids at 50% probability; H atoms omitted for clarity).

The ^{1}H NMR spectrum of **16** recorded in $CDCl_3$ resembles that of **15**. The signals arising from the cymene ligand are shifted upfield by 0.2 to 0.4 ppm with respect to $[(cym)RuCl_2]_2$, which is a less pronounced shift than that observed for **15**. The singlet at 1.84 as well as the doublet at 0.99 and the septet at 2.46 ppm with a $^3J_{HH}$ coupling constant of 6.9 Hz correspond to the methyl and the isopropyl group of cymene. Two doublets at 5.10 and 5.31 ppm with a $^3J_{HH}$ coupling constant of 6.0 Hz correspond to the aromatic cymene protons. The backbone of the NHC ligand gives rise to multiplets at 3.63 and 3.95 ppm. The methylene groups of the *N*-substituents give rise to two slightly broadened doublets at 5.39 and 6.15 ppm with a coupling constant of 16.5 Hz. The remaining signals at 7.53 to 8.16 ppm correspond to the naphthyl protons.

5.4.3 Synthesis of (1,3-Bis(1-naphthylmethyl)imidazolin-2-ylidene)(cymene)-ruthenium(II) Dichloride, [(INpMe)RuCl$_2$(cym)] (17)

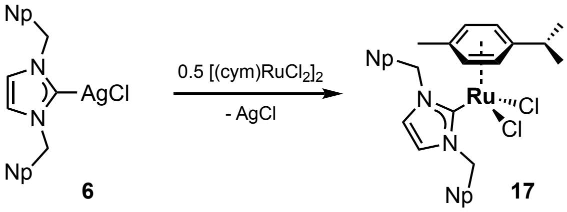

Scheme 5.27. Synthesis of [(INpMe)RuCl$_2$(cym)] (**17**).

In analogy to the microscale preparations of **15** and **16**, complex **17** was synthesized by stirring 0.5 equivalents of $[(cym)RuCl_2]_2$ with one equivalent of the NHC-silver complex **6** in acetonitrile at room temperature overnight (Scheme 5.27). The product was isolated by layering a CH_2Cl_2 solution with diethyl ether, however, no X-ray quality crystals were obtained.

However, the resemblance of the ^{1}H NMR spectrum of **17** to those of **15** and **16** indicates that the molecular structure is essentially identical.

In the ^{1}H NMR spectrum of **17** recorded in $CDCl_3$, the chemical shifts of the cymene protons (0.96, 1.75, 2.45 ppm for the methyl and isopropyl group; 4.96 and 5.21 ppm for the aromatic protons) are almost identical to those observed for **16**. The signals arising from the NHC ligand are changed somewhat with respect to the silver complex **6**. The backbone signal is observed at 6.98 ppm (**6**: 6.67 ppm); the CH_2 groups of the *N*-substituents give rise to very broad signals at 6.03 and 6.68 ppm (**6**: sharp singlet at 5.71 ppm). The naphthyl moieties give rise to well-resolved multiplets between 7.18 and 8.15 ppm (**6**: multiplets from 7.28 to 7.86 ppm).

5.4.4 Reactivity of [(BNpMe)RuCl$_2$(cym)] (15) towards NaBAr^F$_4$, KC$_8$, and Grignard reagents

Özdemir and co-workers reported that the reaction of $[(cym)RuCl_2]_2$ with a benzyl-substituted azolium salt in the presence of a base in refluxing toluene led, in some cases, to the displacement of the cymene ligand and the formation of a chelate complex with one of the benzyl substituents binding to the ruthenium center.[44] Attempts to replicate this type of reactivity with naphthyl-substituted azolium salts did not yield the desired products; in fact, no reaction was observed at all and only the starting materials were detected by ^{1}H NMR spectroscopy.

With the aim of obtaining a chelate complex, the next method of choice was the reaction with a chloride abstracting agent. The strong chloride scavenger $NaBAr^F{}_4$ was reacted with complex **15** in THF overnight, but no defined product could be isolated. The ^{1}H NMR spectrum of the reaction mixture showed a range of broadened signals, suggesting the formation of several products. A large amount of $BAr^F{}_4{}^-$ compared to the remaining signals indicates that some of the starting ruthenium complex has decomposed.

As an alternative to a ruthenium(II) complex, we next attempted to prepare a low-valent ruthenium(0) complex which would be stabilized by the π-accepting properties of the naphthyl substituents. However, the reaction of **15** with the strong reducing agent potassium graphite turned out to be unselective as well. At least two products are discernible in the ^{1}H NMR spectrum of the reaction mixture after removing all volatiles *in vacuo* and redissolving the dark red residue in C_6D_6. The spectrum reveals two sets of signals corresponding to cymene and a large number of signals in the aromatic region, corresponding to the naphthyl substituents. Attempts to separate the products by fractional crystallization remained unsuccessful and no molecular structure could be deduced from the NMR spectrum.

We next utilized Grignard reagents for the replacement of the chloride ligands of **15**. Reacting a suspension of **15** in THF with two equivalents of (trimethylsilyl)methylmagnesium chloride at low temperature led to the formation of a clear, dark red solution. The initial product—a tentative structure is displayed in Scheme 5.28—decomposes rapidly upon warming to room temperature, yielding a light yellow solid which is insoluble in THF. By storing a THF solution of the product at –80°C the decomposition can be slowed down, but the formation of a yellow powder is still observed. The reaction was repeated as a low-temperature NMR experiment. While the initial ^{1}H NMR spectrum displayed signals around 0 ppm corresponding to a silyl moiety, these signals were not observed in the ^{1}H NMR spectrum of the isolated yellow solid. This indicates the loss of any silyl groups. A possible explanation would be the formation of $SiMe_4$ with concomitant deprotonation of the side arms of the carbene ligand. Since no X-ray quality crystals could be obtained, this assumption remains to be confirmed by further analysis of the product.

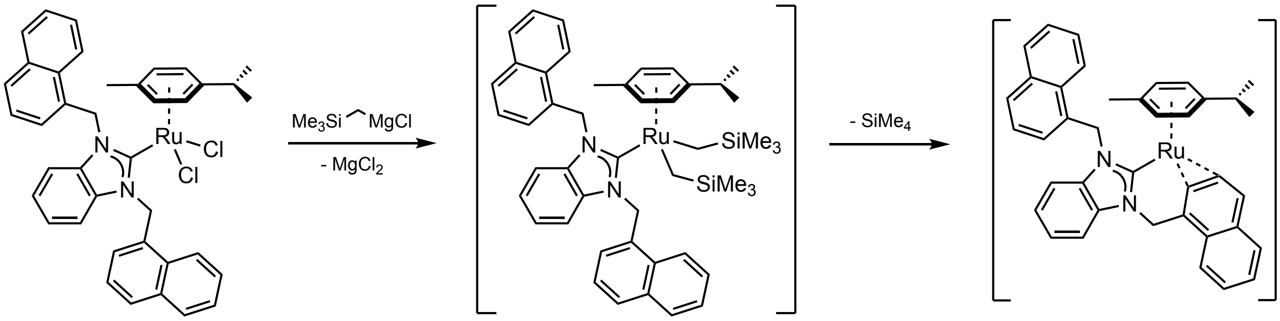

Scheme 5.28. Reaction of **15** with (trimethylsilyl)methylmagnesium chloride. Proposed products given in brackets.

The reaction of **15** with two equivalents of phenylmagnesium chloride (Scheme 5.29) led to an unexpected product. While we expected the chloride ligands to be replaced by phenyl groups, we also observed the displacement of the cymene ligand. One of the naphthyl moieties of the carbene ligand coordinates to the ruthenium center.

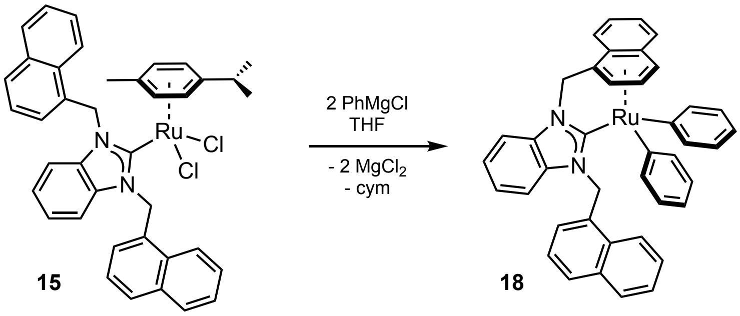

Scheme 5.29. Synthesis of [(η^6:η^1-BNpMe)$RuPh_2$] (**18**) from **15**.

The reaction proceeds rapidly at room temperature in either THF or toluene, yielding a deep red solution from which complex **18** was isolated in 56% yield by first removing $MgCl_2$ by filtration and subsequently removing the solvent *in vacuo*. X-ray quality crystals of **18** were obtained by slow solvent evaporation from a saturated toluene solution.

18 crystallizes in the monoclinic space group $P2_1/c$ with four molecules in the unit cell. The molecular structure (Figure 5.12) can be described as a distorted piano-stool. The ruthenium center is coordinated in an η^6-fashion by one of the naphthyl groups of the carbene ligand, with the three remaining coordination sites filled by the carbene and two phenyl groups. The distances between the ruthenium atom and the carbon atoms of the coordinating naphthyl group are in the range of 2.1535(17) to 2.3349(17) Å for C20-C23; the bonds to the bridgehead carbons C28 and C29 are slightly elongated, at 2.4211(15) and 2.4690(15) Å, respectively. The naphthyl moiety is slightly bent with a fold angle of 10.24(13)°, which overall confirms the η^6 coordination mode. The C1–N bond lengths (1.367(2) and 1.383(2) Å) and N1–C1–N2 bond angle of the NHC ligand (104.31(14)°) are close to those in complex **15**. The chelation of one of the *N*-substituents causes a slight distortion at the carbene carbon, the central ring of the NHC being slightly tilted with respect to the C1–Ru1 bond with a tilt angle of about 11.9°.

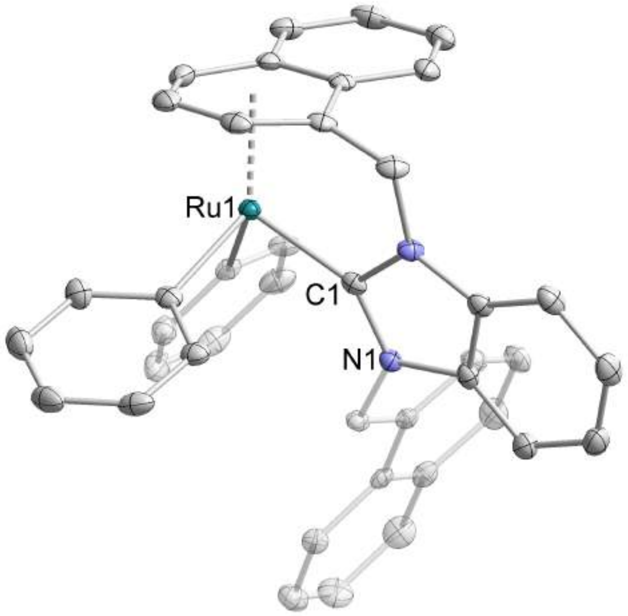

Figure 5.12. Molecular structure of **18** (thermal ellipsoids at 50% probability; hydrogen atoms omitted for clarity).

The ^{1}H NMR spectrum of **18** in C_6D_6 is in accord with the observation from the crystal structure that the two *N*-substituents are no longer equivalent. Two doublets at 3.79 and 4.88 ppm with a coupling constant of 12.5 Hz are assigned to the methylene protons of one of the *N*-substituents. The methylene group of the other N-substituent is observed as two doublets at 5.26 and 5.56 ppm with a coupling constant of 17.1 Hz. A group of three coupled signals at 5.10 (d), 5.68 (dd), and 5.49 ppm (d) with coupling constants of 5.3 and 6.6 Hz likely corresponds to the part of one naphthyl group that coordinates to the ruthenium center; the downfield shift of the arene signals is indicative of metal coordination. Due to the lack of magnetic equivalence of the substituents and the presence of two phenyl ligands, the remainder of the spectrum is very complex, so that no complete assignment is possible. A multitude of signals is observed in the range of 6.31 to 7.57 ppm corresponding to the remaining naphthyl H atoms, phenyl groups, and the benzannulated backbone.

Even in a concentrated solution, the $^{13}C\{^{1}H\}$ NMR spectrum only shows very weak signals. However, using 2D techniques such as $^{1}H/^{13}C$ HSQC and HMBC, some carbon resonances could be identified. The methylene carbon signals of the two *N*-substituents are observed at 47.7 and 49.7 ppm, respectively. The coordinating part of the naphthyl group gives rise to signals at 84.8, 81.3, and 105.7 ppm, with an additional quaternary carbon resonance at 95.0 ppm that shows an interaction with the coordinating group in the $^{1}H/^{13}C$ HMBC spectrum. The remaining signals between 108.1 and 144.8 ppm arise from the remaining naphthyl group, the phenyl ligands, and the backbone, but no detailed assignment could be made.

5.4.5 Catalytic Hydrosilylation of Alkenes with 15 and 18

The studies of Albrecht, Özdemir, and Glorius on the application of ruthenium complexes of NHC ligands with chelating π-acceptor side chains encouraged us to evaluate the catalytic activity of complex **18**. We chose the hydrosilylation of alkenes as a model reaction (Scheme 5.30). Complex **15** was tested as well to compare the activity of both complexes.

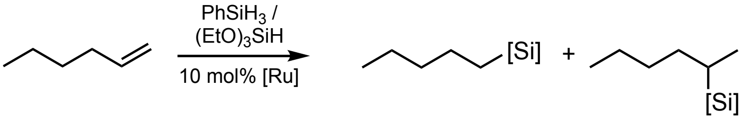

Scheme 5.30. Attempted catalytic alkene hydrosilylation.

Equimolar amounts of 1-hexene and either triethoxysilane or phenylsilane were dissolved in toluene and stirred at room temperature for 15 hours with 10 mol% catalyst. After the reaction the catalyst was quenched by adding aqueous $NaHCO_3$ and removed by filtration over a pad of alumina. Monitoring by GC-FID and comparison with the expected product revealed that the employed complexes displayed no catalytic activity as only the starting material was observed. In light of this result, and considering the high reactivity of **18**, other reaction types should be considered to better evaluate the potential of **18** in catalysis.

5.5 References

[1] a) B. Çetinkaya, P. Dixneuf, M. F. Lappert, *J. Chem. Soc., Chem. Commun.* **1973**, 206; b) B. Çetinkaya, P. Dixneuf, M. F. Lappert, *J. Chem. Soc., Dalton Trans.* **1974**, 1827-1833.

[2] a) F. Bonati, A. Burini, B. R. Pietroni, B. Bovio, *J. Organomet. Chem.* **1989**, *375*, 147-160; b) F. Bonati, A. Burini, B. R. Pietroni, B. Bovio, *J. Organomet. Chem.* **1991**, *408*, 271-280; c) B. Bovio, A. Burini, B. R. Pietroni, *J. Organomet. Chem.* **1993**, *452*, 287-291; d) H. G. Raubenheimer, L. Lindeque, S. Cronje, *J. Organomet. Chem.* **1996**, *511*, 177-184.

[3] a) H. M. J. Wang, I. J. B. Lin, *Organometallics* **1998**, *17*, 972-975; b) H. M. J. Wang, C. Y. L. Chen, I. J. B. Lin, *Organometallics* **1999**, *18*, 1216-1223.

[4] A. Collado, A. Gómez-Suárez, A. R. Martin, A. M. Z. Slawin, S. P. Nolan, *Chem. Commun.* **2013**, *49*, 5541.

[5] Reviews on NHC-gold catalysis: a) N. Marion, S. P. Nolan, *Chem. Soc. Rev.* **2008**, *37*, 1776-1782; b) S. Diéz-González, S. P. Nolan, *Acc. Chem. Res.* **2008**, *41*, 349-358; c) S. P. Nolan, *Acc. Chem. Res.* **2011**, *44*, 91-100; d) S. Gaillard, C. S. J. Cazin, S. P. Nolan, *Acc. Chem. Res.* **2012**, *45*, 778-787; e) A. S. K. Hashmi, *Acc. Chem. Res.* **2014**, *47*, 864-876; f) Y.-M. Wang, A. D. Lackner, F. D. Toste, *Acc. Chem. Res.* **2014**, *47*, 889-901; g) P. Gu, Q. Xu, M. Shi, *Tet. Lett.* **2014**, *55*, 577-584; h) M. Jia, M. Bandini, *ACS Catal.* **2015**, *5*, 1638-1652; i) B. Ranieri, I. Escofet, A. M. Echavarren, *Org. Biomol. Chem.* **2015**, *13*, 7103-7118.

[6] Reviews on medicinal applications of NHC-gold complexes: a) P. J. Barnard, S. J. Berners-Price, *Coord. Chem. Rev.* **2007**, *251*, 1889-1902; b) I. Ott, *Coord. Chem. Rev.* **2009**, *253*, 1670-1681; c) M.-L. Teyssot, A.-S. Jarousse, M. Manin, A. Chevry, S. Roche, F. Norre, C. Beaudoin, L. Morel, D. Boyer, R. Mahiou, A. Gautier, *Dalton Trans.* **2009**, 6894-6902; d) S. J. Berners-Price, A. Filipovska, *Metallomics* **2011**, *3*, 863-873.

[7] S. K. Schneider, W. A. Herrmann, E. Herdtweck, *Z. Anorg. Allg. Chem.* **2003**, *629*, 2363-2370.

[8] a) D. Banerjee, A. K. Buzas, C. Besnard, E. P. Kündig, *Organometallics* **2012**, *31*, 8348-8354; b) P. Gu, Q. Xu, M. Shi, *Tet. Lett.* **2014**, *55*, 577-584.

[9] A. Gómez-Suárez, R. S. Ramón, O. Songis, A. M. Z. Slawin, C. S. J. Cazin, S. P. Nolan, *Organometallics* **2011**, *30*, 5463-5470.

[10] G. L. Hamilton, E. J. Kang, M. Mba, F. D. Toste, *Science* **2007**, *317*, 496-499.

[11] a) S. Gaillard, A. M. Z. Slawin, S. P. Nolan, *Chem. Commun.* **2010**, *46*, 2742-2744; b) F. Nahra, S. R. Patrick, A. Collado, S. P. Nolan, *Polyhedron* **2014**, *84*, 59-62.

[12] I. I. F. Boogaerts, S. P. Nolan, *J. Am. Chem. Soc.* **2010**, *132*, 8858-8859.

[13] S. Díez-González, N. Marion, S. P. Nolan, *Chem. Rev.* **2009**, *109*, 3612-3676.

[14] J. E. Borger, M. S. Bakker, A. W. Ehlers, M. Lutz, J. C. Slootweg, K. Lammertsma, *Chem. Commun.* **2016**, *52*, 3284-3287.

[15] a) C. Schwarzmaier, M. Sierka, M. Scheer, *Angew. Chem. Int. Ed.* **2013**, *52*, 858-861; b) A. E. Seitz, Dissertation, Universität Regensburg, **2017**.

[16] C. F. Shaw III, *Chem. Rev.* **1999**, *99*, 2589-2600.

[17] S. Engel, E.-C. Fritz, B. J. Ravoo, *Chem. Soc. Rev.* **2017**, *46*, 2057-2075.

[18] L. Mercs, M. Albrecht, *Chem. Soc. Rev.* **2010**, *39*, 1903-1912.

[19] D. J. Cardin, M. J. Doyle, M. F. Lappert, *J. Chem. Soc., Chem. Comm.* **1972**, 927-928.

[20] A. C. Chen, L. Ren, A. Decken, C. M. Crudden, *Organometallics* **2000**, *19*, 3459-3461.

[21] J. E. Hill, T. A. Nile, *J. Organomet. Chem.* **1977**, *137*, 293-300.

[22] a) W. A. Herrmann, L. J. Goossen, C. Köcher, G. R. J. Artus, *Angew. Chem. Int. Ed. Engl.* **1996**, *35*, 2805-2807; b) W. A. Herrmann, L. J. Goossen, G. R. J. Artus, C. Köcher, *Organometallics* **1997**, *16*, 2472-2477.

[23] C. Köcher, W. A. Herrmann, *J. Organomet. Chem.* **1997**, *532*, 261-265.

[24] a) A. R. Chianese, X. Li, M. C. Janzen, J. W. Faller, R. W. Crabtree, *Organometallics* **2003**, *22*, 1663-1667; b) R. S. Simons, P. Custer, C. A. Tessier, W. J. Youngs, *Organometallics* **2003**, *22*, 1979-1982.

[25] a) J. M. Praetorius, C. M. Crudden, *Dalton Trans.* **2008**, 4079-4094; b) S. Díez-González, N. Marion, S. P. Nolan, *Chem. Rev.* **2009**, *109*, 3612-3676.

[26] a); b) M. F. Lappert, R. K. Maskell, *J. Organomet. Chem.* **1984**, *264*, 217-228.

[27] M. T. Powell, D.-R. Hou, M. C. Perry, X. Cui, K. Burgess, *J. Am. Chem. Soc.* **2001**, *123*, 8878-8879.

[28] L. H. Gade, V. César, S. Bellemin-Laponnaz, *Angew. Chem. Int. Ed.* **2004**, *43*, 1014-1017.

[29] a) M. Poyatos, E. Mas-Marzá, J. A. Mata, M. Sanaú, E. Peris, *Eur. J. Inorg. Chem.* **2003**, 1215-1221; b) M. V. Jiménez, J. J. Pérez-Torrente, M. I. Bartolomé, V. Gierz, F. J. Lahoz, L. A. Oro, *Organometallics* **2008**, *27*, 224-234.

[30] a) G. A. Grasa, Z. Moore, K. L. Martin, E. D. Stevens, S. P. Nolan, V. Paquet, H. Lebel, *J. Organomet. Chem.* **2002**, *658*, 126-131; b) W. A. Herrmann, G. D. Frey, E. Herdtweck, M. Steinbeck, *Adv. Synth. Catal.* **2007**, *349*, 1677-1691; c) X.-Y. Yu, H. Sun, B. O. Patrick, B. R. James, *Eur. J. Inorg. Chem.* **2009**, 1752-1758.

[31] Y. Wei, B. Rao, X. Cong, X. Zeng, *J. Am. Chem. Soc.* **2015**, *137*, 9250-9253.

[32] A. C. Chen, D. P. Allen, C. M. Crudden, R. Wang, A. Decken, *Can. J. Chem.* **2005**, *83*, 943-957.

[33] J. Li, J. Peng, Y. Bai, G. Lai, X. Li, *J. Organomet. Chem.* **2011**, *696*, 2116-2121.

[34] F. E. Hahn, C. Holtgrewe, T. Pape, M. Martin, E. Sola, L. A. Oro, *Organometallics* **2005**, *24*, 2203-2209.

[35] A. Zanardi, E. Peris, J. A. Mata, *New J. Chem.* **2008**, *32*, 120-126.

[36] G. Sipos, A. Ou, B. W. Skelton, L. Falivene, L. Cavallo, R. Dorta, *Chem. Eur. J.* **2016**, *22*, 6939-6946.

[37] a) P. B. Hitchcock, M. F. Lappert, P. L. Pye, *J. Chem. Soc., Chem. Comm.* **1976**, 644-646; b) P. B. Hitchcock, M. F. Lappert, P. L. Pye, *J. Chem. Soc., Chem. Comm.* **1977**, 196-198.

[38] a) W. A. Herrmann, M. Elison, J. Fischer, C. Köcher, G. R. J. Artus, *Chem. Eur. J.* **1996**, *2*, 772-780; b) W. A. Herrmann, C. Köcher, L. J. Gooßen, G. R. J. Artus, *Chem. Eur. J.* **1996**, *2*, 1627-1636; c) H. Kücükbay, B. Çetinkaya, S. Guesmi, P. H. Dixneuf, *Organometallics* **1996**, *15*, 2434-2439.

[39] a) T. Weskamp, W. C. Schattenmann, M. Spiegler, W. A. Herrmann, *Angew. Chem. Int. Ed.* **1998**, *37*, 2490-2493; b) M. Scholl, S. Ding, C. W. Lee, R. H. Grubbs, *Org. Lett.* **1999**, *1*, 953-956; c) M. Scholl, T. M. Trnka, J. P. Morgan, R. H. Grubbs, *Tet. Lett.* **1999**, *40*, 2247-2250; d) L. Ackermann, A. Fürstner, T. Weskamp, F. J. Kohl, W. A. Herrmann, *Tet. Lett.* **1999**, *40*, 4787-4790; e) J. Huang, E. D. Stevens, S. P. Nolan, J. L. Petersen, *J. Am. Chem. Soc.* **1999**, *121*, 2674-2678.

[40] Reviews and textbooks on olefin metathesis: a) E. Despagnet-Ayoub, T. Ritter, *Top. Organomet. Chem.* **2007**, *21*, 193-218; b) C. Samojłowicz, M. Bieniek, K. Grela, *Chem. Rev.* **2009**, *109*, 3708-3742; c) G. C. Vougioukalakis, R. H. Grubbs, *Chem. Rev.* **2010**, *110*, 1746-1787; d) *Olefin Metathesis: Theory and Practice* (Ed. K. Grela), Wiley-VCH, Weinheim, **2014**; e) S. Mavila, N. G. Lemcoff in *N-Heterocyclic Carbenes: Effective Tools in Organometallic Synthesis* (Ed. S. P. Nolan), Wiley-VCH, Weinheim, **2014**, 307-340.

[41] a) P. L. Arnold, A. C. Scarisbrick, *Organometallics* **2004**, *23*, 2519-2521; b) P. Csabai, F. Joó, *Organometallics* **2004**, *23*, 5640-5643.

[42] B. Çetinkaya, S. Demir, İ. Özdemir, L. Toupet, D. Sémeril, C. Bruneau, P. H. Dixneuf, *Chem. Eur. J.* **2003**, *9*, 2323-2330.

[43] a) B. Çetinkaya, S. Demir, İ. Özdemir, L. Toupet, D. Sémeril, C. Bruneau, P. H. Dixneuf, *New J. Chem.* **2001**, *25*, 519-521; b) İ. Özdemir, S. Demir, B. Çetinkaya, L. Toupet, R. Castarlenas, C. Fischmeister, P. H. Dixneuf, *Eur. J. Inorg. Chem.* **2007**, 2862-2869.

[44] Selected references: a) M. Yiğit, B. Yiğit, İ. Özdemir, E. Çetinkaya, B. Çetinkaya, *Appl. Organomet. Chem.* **2006**, *20*, 322-327; b) N. Gürbüz, S. Yaşar, E. Özcan, İ. Özdemir, B. Çetinkaya, *Eur. J. Inorg. Chem.* **2010**, 3051-3056; c) N. Gürbüz, E. Özcan, İ. Özdemir, B. Çetinkaya, O. Şahin, O. Büyükgüngör, *Dalton Trans.* **2012**, *41*, 2330-2339.

[45] Z. Şahin, N. Gürbüz, İ. Özdemir, O. Şahin, O. Büyükgüngör, M. Achard, C. Bruneau, *Organometallics* **2015**, *34*, 2296-2304.

[46] a) C. Gandolfi, M. Heckenroth, A. Neels, G. Laurenczy, M. Albrecht, *Organometallics* **2009**, *28*, 5112-5121; b) S. Horn, M. Albrecht, *Chem. Commun.* **2011**, *47*, 8802-8804; c) S. Horn, C. Gandolfi, M. Albrecht, *Eur. J. Inorg. Chem.* **2011**, 2863-2868.

[47] S. P. Shan, X. Xiaoke, B. Gnanaprakasam, T. T. Dang, B. Ramalingam, H. V. Huynh, A. M. Seayad, *RSC Adv.* **2015**, *5*, 4434-4442.

[48] X. Xioke, H. V. Huynh, *ACS Catal.* **2015**, *5*, 4143-4151.

[49] A. Prades, M. Poyatos, E. Peris, *Adv. Synth. Catal.* **2010**, *352*, 1155-1162.

[50] S. Sabater, J. A. Mata, E. Peris, *ACS Catal.* **2014**, *4*, 2038-2047.

[51] a) R. F. R. Jazzar, S. A. Macgregor, M. F. Mahon, S. F. Richards, M. K. Whittlesey, *J. Am. Chem. Soc.* **2002**, *124*, 4944-4945; b) M. J. Chilvers, R. F. R. Jazzar, M. F. Mahon, M. K. Whittlesey, *Adv. Synth. Catal.* **2003**, *345*, 1111-1114.

[52] L. J. L. Häller, M. J. Page, S. Erhardt, S. A: Macgregor, M. F. Mahon, A. Naser, A. Velez, M. K. Whittlesey, *J. Am. Chem. Soc.* **2010**, *132*, 18408-18416.

[53] a) L. U. Nordstrøm, H. Vogt, R. Madsen, *J. Am. Chem. Soc.* **2008**, *130*, 17672-17673; b) J. H. Dam, G. Osztrovszky, L. U. Nordstrøm, R. Madsen, *Chem. Eur. J.* **2010**, *16*, 6820-6827.

[54] a) R. Wolf, M. Plois, *Eur. J. Inorg. Chem.* **2010**, 4419-4422; b) M. Plois, Dissertation, WWU Münster **2012**.

[55] a) S. Urban, N. Ortega, F. Glorius, *Angew. Chem. Int. Ed.* **2011**, *50*, 3803-3806; b) N. Ortega, S. Urban, B. Beiring, F. Glorius, *Angew. Chem. Int. Ed.* **2012**, *51*, 1710-1713; c) S. Urban, B. Beiring, N. Ortega, D. Paul, F. Glorius, *J. Am. Chem. Soc.* **2012**, *134*, 15241-15244; d) N. Ortega, D.-T. D. Tang, S. Urban, D. Zhao, F. Glorius, *Angew. Chem. Int. Ed.* **2013**, *52*, 9500-9503; e) D. Zhao, B. Beiring, F. Glorius, *Angew. Chem. Int. Ed.* **2013**, *52*, 8454-8458; f) J. Wysocki, N. Ortega, F. Glorius, *Angew. Chem. Int. Ed.* **2014**, *53*, 8751-8755; g) J. Wysocki, C. Schlepphorst, F. Glorius, *Synlett* **2015**, *26*, 1557-1562; h) W. Li, C. Schlepphorst, C. Daniliuc, F. Glorius, *Angew. Chem. Int. Ed.* **2016**, *55*, 3300-3303.

[56] D. Paul, B. Beiring, M. Plois, N. Ortega, S. Kock, D. Schlüns, J. Neugebauer, R. Wolf, F. Glorius, *Organometallics* **2016**, *35*, 3641-3646.

[57] a) S. G. Weber, D. Zahner, F. Rominger, B. F. Straub, *Chem. Commun.* **2012**, *48*, 11325-11327; b) M. Brill, A. Collado, D. B. Cordes, A. M. Z. Slawin, M. Vogt, H. Grützmacher, S. P. Nolan, *Organometallics* **2015**, *34*, 263-274.

[58] A. P. Blum, T. Ritter, R. H. Grubbs, *Organometallics* **2007**, *26*, 2122-2124.

[59] a) M. V. Baker, S. K. Brayshaw, B. W. Skelton, A. H. White, *Inorg. Chim. Acta* **2004**, *357*, 2841-2849; Y. Borguet, G. Zaragoza, A. Demonceau, L. Delaude, *Dalton Trans.* **2013**, *42*, 7287-7296; c) S. Ruiz-Botella, G. Guisado-Barrios, J. A. Mata, E. Peris, *Organometallics* **2013**, *32*, 6613-6619.

[60] D. Paul, Dissertation, WWU Münster **2016**.

[61] L. Oehninger, M. Stefanopoulou, H. Alborzinia, J. Schnur, S. Ludewig, K. Namikawa, A. Muñoz-Castro, R. W. Köster, K. Baumann, S. Wölfl, W. S. Sheldrick, I. Ott, *Dalton Trans.* **2013**, *42*, 1657-1666.

6 Iron and Cobalt Complexes of Naphthyl-substituted *N*-heterocyclic Carbenes*

6.1 Introduction

Most processes in organic chemistry rely on catalysts derived from precious metals such as palladium, rhodium, or ruthenium. Due to their scarcity and high cost, there is a strong interest in replacing them with cheaper alternatives containing lighter transition metals such as iron or cobalt.

For a long time, the only industrially relevant catalytic applications of iron were the Haber-Bosch process and the Fischer-Tropsch synthesis, both using heterogeneous catalysts. However, the prevalence and variety of iron-containing biomolecules and their broad range of functions demonstrates the great potential of homogeneous iron catalysis. Much like iron, cobalt has found its most prominent industrial application as a heterogeneous catalyst in the Fischer-Tropsch process. The most important application of a homogeneous cobalt catalyst is the hydroformylation reaction, where $[HCo(CO)_4]$ was found to be the active species.

The development of new ligand classes such as *N*-heterocyclic carbenes have led to an upsurge in research on catalytically active transition metal complexes, and the last two decades have seen a rapid evolution of the field of iron and cobalt catalysis. As the chemistry and catalytic applications of NHC-Fe complexes have been reviewed in detail by Herrmann, Kühn, and co-workers,[1] only some representative examples will be given here.

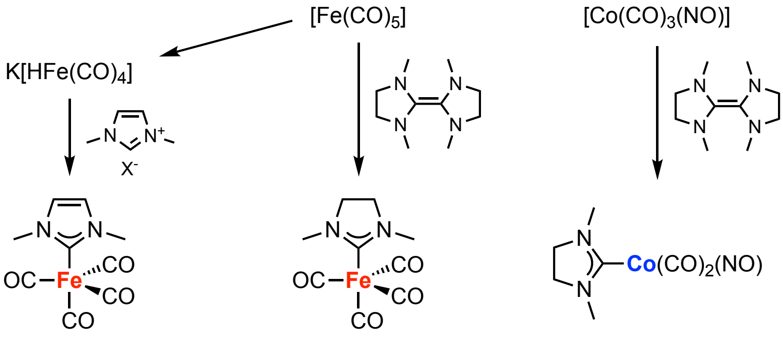

Scheme 6.1. Early examples of Fe- and Co-NHC complexes as reported by Öfele and Lappert.

---

* The SQUID measurements and analyses of NHC-cobalt complexes (section 6.3) were performed by Jan Gerkens (group of Prof. Dr. Sven Schneider, University of Göttingen), who also created Figure 6.8. The catalytic hydrogenation reactions using NHC-iron complexes (section 6.6) were performed by Dr. Tim Gieshoff (group of Prof. Dr. Axel Jacobi von Wangelin, University of Regensburg, now University of Hamburg). Data in Table 6.4 was reproduced from ref. 31 with permission from the author.

In 1969, the first NHC-Fe complex was mentioned in a note by Öfele, who reported the reaction of imidazolium salts with the low-valent carbonyl complex K[HFe(CO)$_4$] (Scheme 6.1, left).[2] In 1973, the group of Lappert reported the reaction of tetraazafulvalenes with transition metal sources such as Fe(CO)$_5$ (Scheme 6.1, center).[3] Several years later, the first NHC-Co complex was reported by Lappert and co-workers following the same method (Scheme 6.1, right).[4] After almost two decades of low activity, Fehlhammer and co-workers were the first to utilize isolated free carbenes for the synthesis of an NHC-Fe complex (Scheme 6.2, top).[5] Five years later, Butenschön and co-workers reported the first synthesis of a NHC-Co complex using a free carbene (Scheme 6.2, bottom).[6]

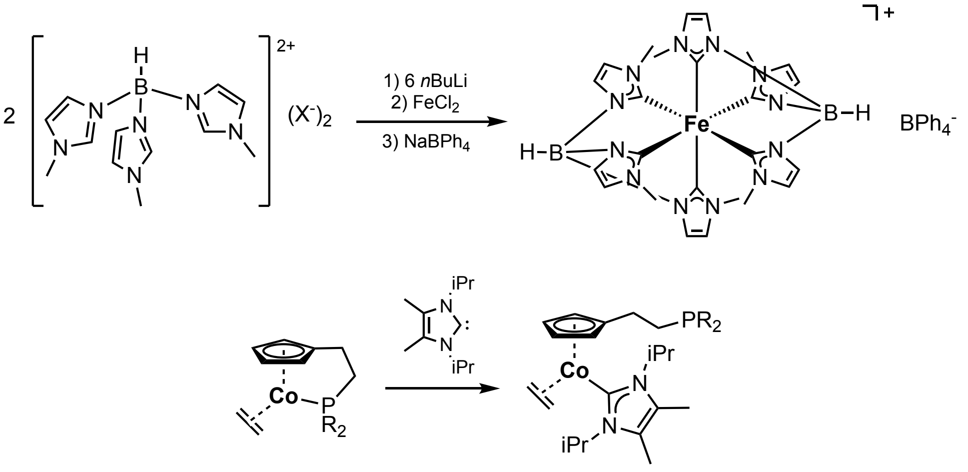

Scheme 6.2. Syntheses of NHC-Fe and NHC-Co complexes using free carbenes.

The first iron halide NHC complexes were introduced in 2000 by Grubbs and co-workers, who reacted free carbenes with iron(II) halide salts (Scheme 6.3, left).[7] They demonstrated that (NHC)$_2$FeX$_2$ complexes catalyze the atom-transfer radical polymerization of styrene and methyl methacrylate, which was first catalytic application of an NHC-Fe complex. Following the same route, the groups of Tonzetich and Danopoulos prepared dinuclear NHC iron complexes [(NHC)FeX(μ-X)]$_2$ from FeX$_2$ and free NHCs (Scheme 6.3, center).[8] Danopoulos and co-workers also reported a route towards (NHC)$_2$FeX$_2$ complexes using imidazolium salts and [Fe{N(SiMe$_3$)$_2$}$_2$] in a 2:1 stoichiometry. The amide ligands act as an internal base, deprotonating the azolium salt. A big advantage of this route is the possibility to introduce NHC ligands that cannot be isolated in their free form. When adjusting the stoichiometry to 1:1, they obtained trigonal planar complexes of the structure [(NHC)FeX{N(SiMe$_3$)$_2$}] (Scheme 6.3, right).[9] The analogous cobalt complexes were first reported by the group of Matsubara in 2012[10] and the group of Tonzetich in 2013, who also applied these complexes in catalytic cross-coupling reactions.[11]

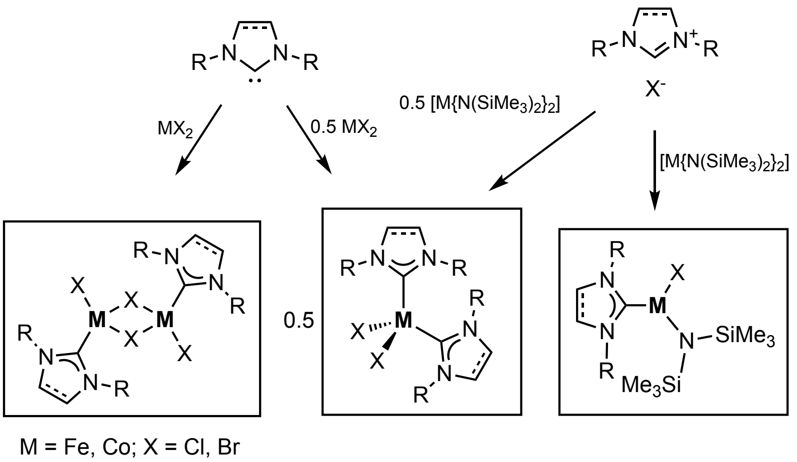

Scheme 6.3. Syntheses of NHC-Fe and NHC-Co halide complexes.

Since their discovery, the reactivity and catalytic applications of NHC-halide complexes of iron and cobalt have been the subject of extensive reactivity studies. Deng and co-workers reacted $(NHC)_2FeX_2$ complexes with alkylating agents such as MeLi or Me_3SiCH_2MgCl as well as the arylating agent MesMgBr to yield complexes of the type $(NHC)_2FeR_2$, while reaction with PhLi led to a transformation of the carbene ligands.[12] They subsequently studied the reactivity of the alkyl and aryl complexes towards unsaturated organic compounds, amines, and alkyl and aryl halides (Scheme 6.4). The high reactivity towards the latter demonstrated the potential of these complexes for catalytic cross-couplings, even with alkyl fluorides.[13] The groups of Tatsumi and Glorius also alkylated $(NHC)_2FeX_2$ complexes and used the resulting compounds in catalytic hydrosilylations and transfer hydrogenations of ketones.[14]

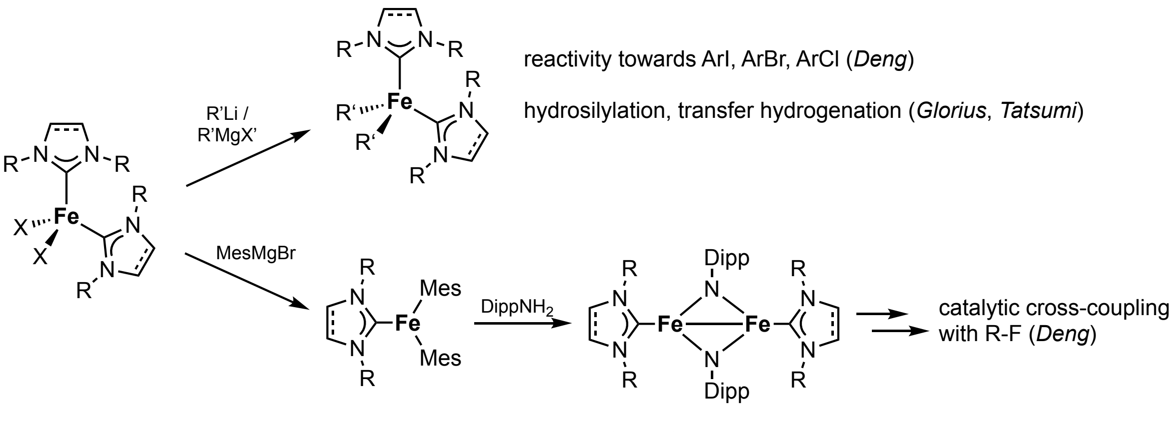

Scheme 6.4. Reactivity of $(NHC)_2FeX_2$ complexes.

Besides their catalytic application, NHC-Fe halide complexes are precursors for low-valent Fe(I) and Fe(0) NHC complexes. Tatsumi and co-workers reported that chemical reduction of an $(NHC)FeCl_3$ complex (generated in situ from $FeCl_3$ and the free NHC) with potassium graphite yielded dinuclear Fe(0) complexes, in which each of the iron centers is stabilized by an aryl substituent of the NHC ligand bound to the other iron center (Scheme 6.5).[15]

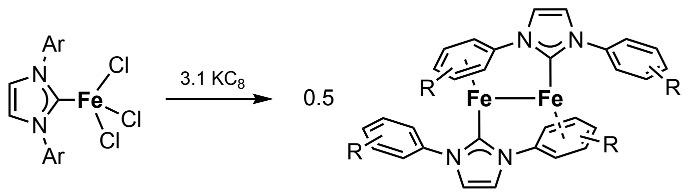

Scheme 6.5. Synthesis of NHC-Fe(0) complexes.

Deng and co-workers prepared and characterized a series of low-coordinate Fe(I) carbene complexes with coordination numbers 2, 3, and 4 by reduction of the respective halide complexes with potassium graphite.[16] Following a different route, Tatsumi and co-workers also prepared three- and four-coordinate Fe(I) NHC complexes.[17]

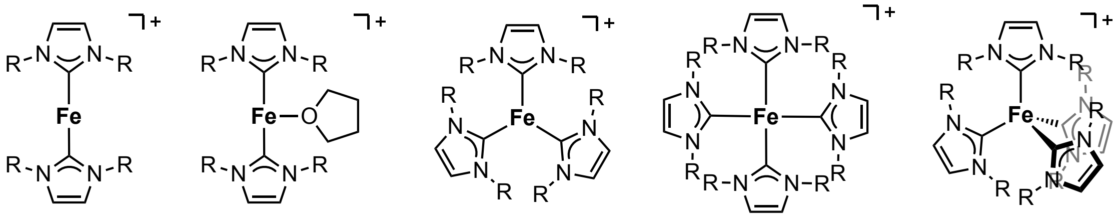

Figure 6.1. Two-, three- and four-coordinate Fe(I) NHC complexes.

Reactivity studies by Deng and co-workers on the low-valent NHC-Co(I) chloride complex [$(IMes)_2CoCl$] and the related [$(IMes)_2Co$]BPh_4 showed that chemical reduction does not yield the expected Co(0) complex, but rather results in a cyclometalation of the mesityl substituents.[18] Subsequent reaction with a silane resulted in the dehydrogenative insertion of a silyl group into the Co–C bond, demonstrating its high reactivity.[19]

Heteroleptic, three-coordinate Co complexes such as [(IDipp)CoCl{$N(SiMe_3)_2$}] were shown to be versatile starting materials by Hansen and Hillhouse.[20] The $N(SiMe_3)_2^-$ ligand was easily replaced by other ligands such as phenolates or anilides. Reaction with a very bulky terphenyl amine resulted in [(IDipp)CoCl(NHAr)], which exhibits an interaction of the cobalt center with one of the phenyl rings of the terphenyl system.

In 2011, the group of Layfield reported the synthesis of trigonal planar NHC-iron complexes [(NHC)Fe{$N(SiMe_3)_2$}$_2$] from free NHCs and [Fe{$N(SiMe_3)_2$}$_2$] (Scheme 6.6, left).[21] Subsequently, the analogous Co complexes were prepared by the same group.[22] DFT calculations by Layfield and Bickelhaupt on the Fe amide complexes showed that, while bonds between carbenes and transition metals are generally considered to be strong, this is not necessarily true for the Fe–C bond.[23] Their computations further showed that the Fe–C bond energy decreases with increasing steric bulk of the *N*-substituents of the carbene ligand. Both the Fe and the Co complexes undergo rearrangements upon heating, forming abnormal carbene complexes (Scheme 6.6, right).[22,23]

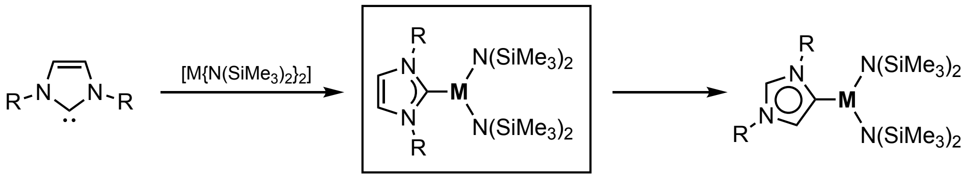

Scheme 6.6. Synthesis and rearrangement of NHC-Fe and NHC-Co amide complexes.

A reactivity study by Danopoulos and Braunstein demonstrated that the $N(SiMe_3)_2^-$ ligands are displaced upon reaction with primary amines.[24] Recently, the same researchers reported on the preparation of two-coordinate low-valent Fe and Co complexes by reduction of the bis(amide) complexes with KC_8 (Scheme 6.7).[25]

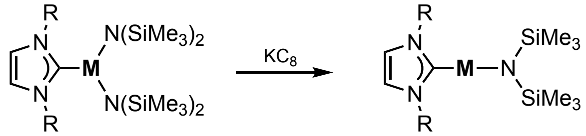

Scheme 6.7. Chemical reduction of $[(NHC)M\{N(SiMe_3)_2\}_2]$ (M = Fe, Co) to two-coordinate M(I) complexes.

Deng and co-workers recently showed that complexes of the type $[(NHC)Co\{N(SiMe_3)_2\}_2]$ are promising precatalysts for the hydrosilylation of olefins. Their mechanistic study indicated that low-coordinate Co(I) species formed by reaction with a tertiary silane may be the catalytically active species. Tilley and co-workers successfully used the analogous Fe(I) complex $[(IDipp)Fe\{N(SiMe_3)_2\}]$ (IDipp = 1,3-bis(2,6-diisopropylphenyl)imidazolin-2-ylidene) for the catalytic cyclotrimerization of alkynes, further demonstrating the versatility of hexamethyldisilazide ligands in low-valent NHC-iron complexes.[26]

6.2 Synthetic Approaches Towards Fe and Co NHC Complexes

6.2.1 Initial Reactions of Azolium Salts with Bis(amido) Complexes

The three-coordinate heteroleptic complexes $[(NHC)MX\{N(SiMe_3)_2\}]$ (M = Fe, Co; Scheme 6.2, right) introduced by Danopoulos, Braunstein, and co-workers are highly interesting because both the halide and the $N(SiMe_3)_2^-$ ligand can be replaced independently of each other.[9] This should allow the synthesis of a variety of functionalized complexes in a straightforward manner.

We therefore followed the reported protocol and reacted the imidazolinium salt [SINpH]Br (**5**) with $[M\{N(SiMe_3)_2\}_2]$ (M = Fe, Co) in a 1:1 ratio. However, the expected heteroleptic complexes could not be obtained. Instead, several mono- and dinuclear iron and cobalt complexes were identified by X-ray crystallography.

Reaction of **5** with [Fe{N(SiMe$_3$)$_2$}$_2$] in toluene gave a clear yellow solution within five minutes at room temperature. After removing the solvent and formed HN(SiMe$_3$)$_2$ *in vacuo*, fractional extraction of the residue with *n*-hexane, diethyl ether, and toluene led to the formation of yellow crystals in the ether extract and brown crystals in the toluene extract. X-ray crystallography revealed the dinuclear complexes **19** and **20** (Scheme 6.8).

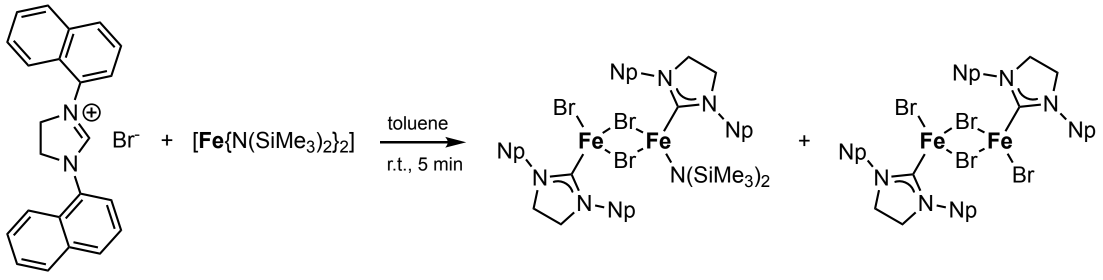

5 **19** **20**

Scheme 6.8. Reaction of [SINpH]Br (**5**) with [Fe{N(SiMe$_3$)$_2$}$_2$].

19 crystallizes in the monoclinic space group $P2_1/c$ with four molecules in the unit cell. The molecular structure (Figure 6.2, left) features a central four-membered Fe$_2$Br$_2$ ring with bridging bromide ligands and a fold angle of 6.01(6)° along the Br2–Br3 axis. Each of the iron centers is in a tetrahedral coordination environment made up of a carbene ligand, the two bridging bromides, and the terminal bromide for Fe1 or terminal N(SiMe$_3$)$_2^-$ for Fe2, respectively. The tetrahedral coordination of the Fe centers is slightly distorted, with Br2–Fe–Br3 angles of 97.47(4) and 90.95(4)°. All relevant bond lengths and angles are summarized in Table 6.1.

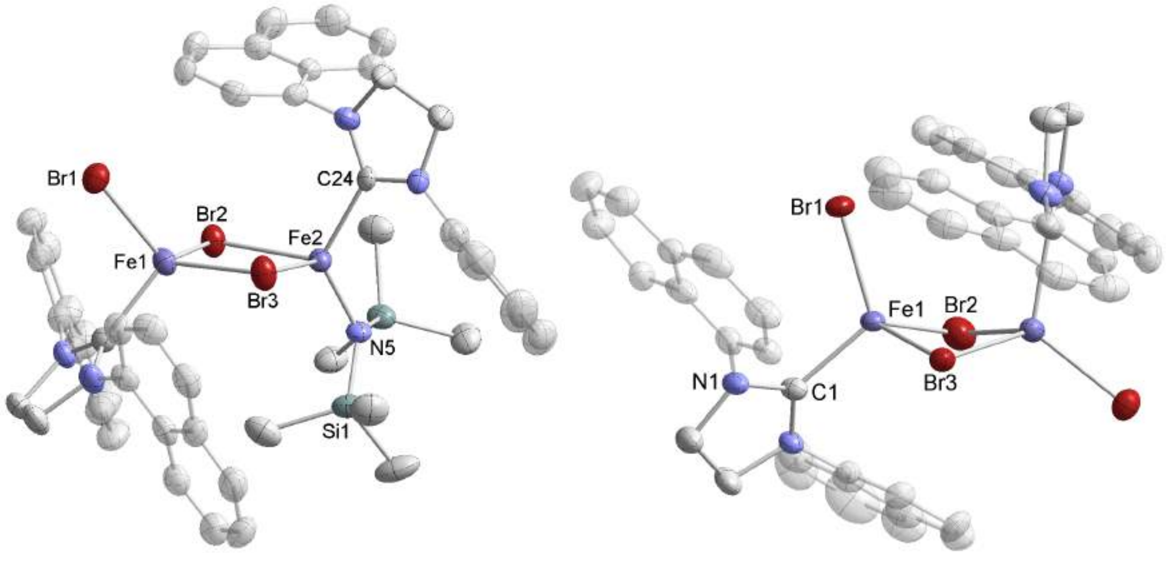

Figure 6.2. Solid-state X-ray structures of **19** (left) and **20** (right; thermal ellipsoids at 50% probability, hydrogen atoms omitted for clarity).

Complex **20** crystallizes in the monoclinic space group $P2_1/n$ with four molecules in the unit cell. The molecular structure (Figure 6.2, right) is similar to that of **19**, with a central four-membered Fe_2Br_2 ring. However, while this moiety is almost planar in **19**, it is significantly folded along the Br2–Br3 axis in **20** with a fold angle of 29.47(7)°. Both iron centers are in tetrahedral coordination environments comprising a carbene ligand, two bridging bromides, and a terminal bromide. All relevant structural parameters are given in Table 6.1.

In analogy to the reaction with $[Fe\{N(SiMe_3)_2\}_2]$, **5** was reacted with $[Co\{N(SiMe_3)_2\}_2]$ in toluene. Within five minutes, a clear green solution had formed from the gray-green suspension of the starting material. Fractional extraction with *n*-hexane, diethyl ether, and toluene led to the crystallization of the mononuclear diamide complex **21** from the hexane fraction as olive-green blocks. Bright green crystals of **21** were obtained from the ether extract. Repeating the reaction in THF under otherwise identical conditions and applying the same work-up procedure led to the crystallization of the dinuclear complex **22** from the toluene fraction. (Scheme 6.9).

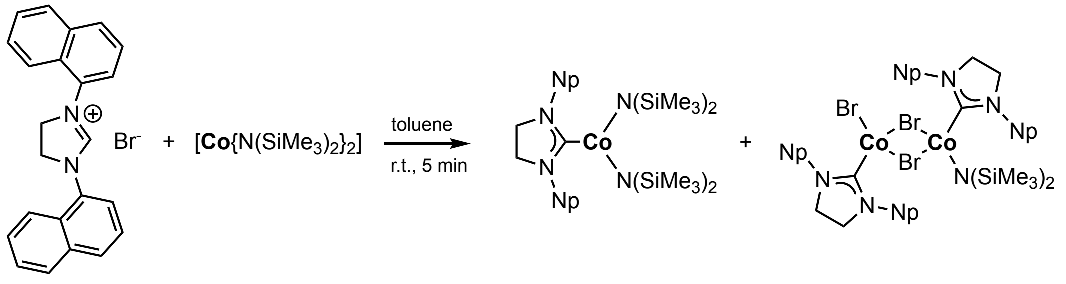

5 **21** **22**

Scheme 6.9. Reaction of **5** with $[Co\{N(SiMe_3)_2\}_2]$.

Complex **21** crystallizes from *n*-hexane in the triclinic space group P–1 . Besides two molecules of **21**, one molecule of *n*-hexane is present in the unit cell. The molecular structure of **21** (Figure 6.3, left) reveals a cobalt center in a trigonal planar coordination environment. The N3–Co–N4 angle is slightly widened to 130.75(5)° due to the steric demand of the $N(SiMe_3)_2^-$ ligands, and the C1–Co–N angles deviate accordingly from the expected value of 120° to 113.98(5) and 115.27(5)°. The C1–Co1 bond length, at 2.0856(14) Å, is in the expected range of imidazolidin-2-ylidene cobalt(II) complexes. Crystals of **21** obtained from diethyl ether, rather than *n*-hexane, have the monoclinic space group C2/*c* with four molecules of **21** and no solvent in the unit cell. The structural parameters are essentially identical to those obtained from the crystals from *n*-hexane. All relevant bond lengths and angles are given in Table 6.2.

The dinuclear complex **22** crystallizes from toluene in the monoclinic space group $P2_1/c$ with four molecules in the unit cell. The molecular structure (Figure 6.3, right) is essentially identical to that of the diiron complex **19**, with a planar central four-membered Co_2Br_2 ring and tetrahedrally coordinated Co(II) centers. The central ring shows minimal folding along the Br2–

Br3 axis by an angle of 2.81(2)°. The cobalt–carbene bonds (Co1–C1: 2.037(3) Å; Co2–C24: 2.065(3) Å) are in the normal range of NHC-Co(II) complexes. The bond angles around the cobalt centers are nearly identical to those around iron in complex **19**. All relevant structural parameters are given in Table 6.1.

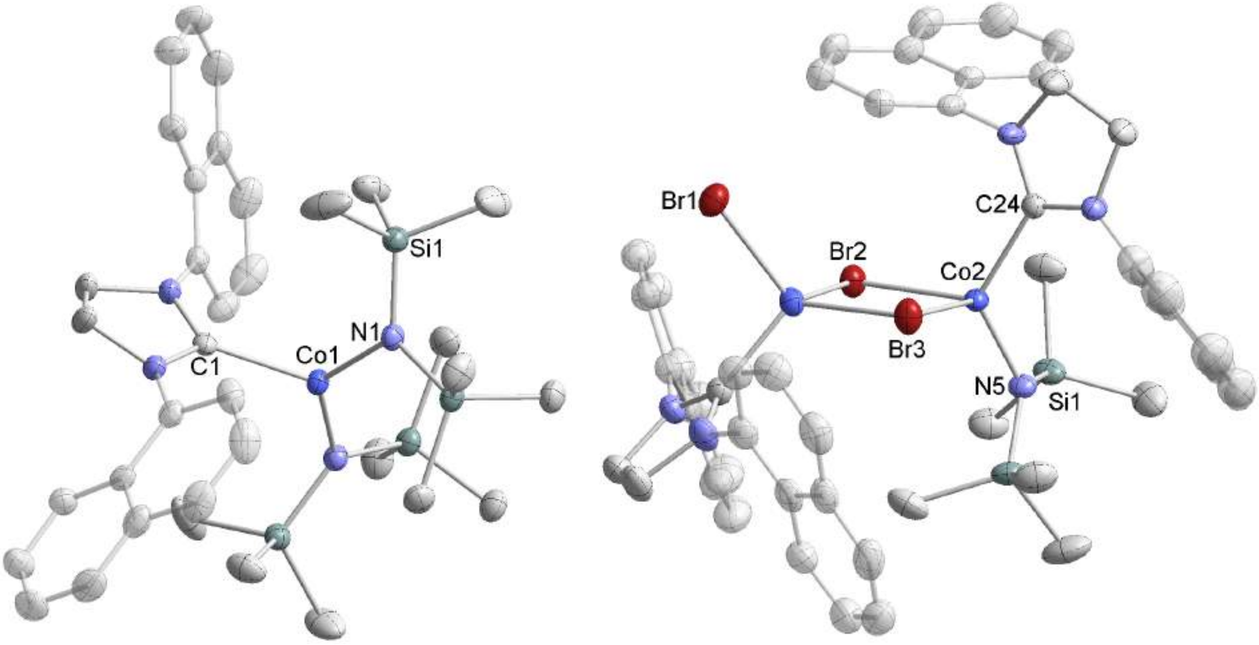

Figure 6.3. Solid-state X-ray structures of complexes **21** (left) and **22** (right; thermal ellipsoids at 50% probability, hydrogen atoms and solvent molecules omitted for clarity).

The formation of **19-22** was somewhat unexpected, given the results reported by Danopoulos, Braunstein, and co-workers (Scheme 6.3, right). We presume that the initial formation of a heteroleptic, three-coordinate complex $[(\mathrm{NHC})\mathrm{MX}\{\mathrm{N}(\mathrm{SiMe}_3)_2\}]$ is followed by either the transfer of an NHC ligand to $[\mathrm{M}\{\mathrm{N}(\mathrm{SiMe}_3)_2\}_2]$ or a dismutation to give bis(amido) complexes $[(\mathrm{NHC})\mathrm{M}\{\mathrm{N}(\mathrm{SiMe}_3)_2\}]$ and bromide complexes $[(\mathrm{NHC})\mathrm{MBr}_2]_2$. It appears that **19** and **22**, which contain both Br^- and $\mathrm{N}(\mathrm{SiMe}_3)_2^-$ ligands, are products of an incomplete dismutation. Not all of the products expected from the dismutation could be identified ($[(\mathrm{SINp})\mathrm{Fe}\{\mathrm{N}(\mathrm{SiMe}_3)_2\}_2]$ and $[(\mathrm{SINp})\mathrm{CoBr}_2]_2$ were not observed).

Bis(bis(trimethylsilyl)amido) NHC complexes, such as **21**, as well as NHC-stabilized dihalides of iron and cobalt represent highly interesting compound classes due to their potential application in catalysis and their magnetic properties. We therefore decided to investigate these substances in more detail. However, complexes **19** and **20** as well as **21** and **22** crystallize as inseparable mixtures due to their similar solubilities. We therefore developed procedures that allowed us to isolate the target complexes $[(\mathrm{NHC})\mathrm{MX}_2]_2$ and $[(\mathrm{NHC})\mathrm{M}\{\mathrm{N}(\mathrm{SiMe}_3)_2\}]$.

6.2.2 Synthesis of NHC-stabilized Iron(II) and Cobalt(II) Halide Complexes

NHC-stabilized iron and cobalt halide complexes are usually accessed by reaction of MX_2 with a free *N*-heterocyclic carbene. The scope of this route is limited by the fact that the NHC needs to be stable in its free form. A method that allows the use of non-isolable carbenes to generate complexes $[(NHC)FeX_2]_n$ (n = 1, 2) was introduced in 2012 by the groups of Lavoie and Byers.[27, 28] Mixing $[Fe\{N(SiMe_3)_2\}_2]$ and FeX_2 in THF led to the formation of an "$FeX\{N(SiMe_3)_2\}$" species, which was reacted *in situ* with an imidazolium salt. We successfully adapted this procedure for the synthesis of iron and cobalt complexes stabilized by the non-isolable NHC SINpMe (1,3-bis(1-naphthylmethyl)imidazolidin-2-ylidene).

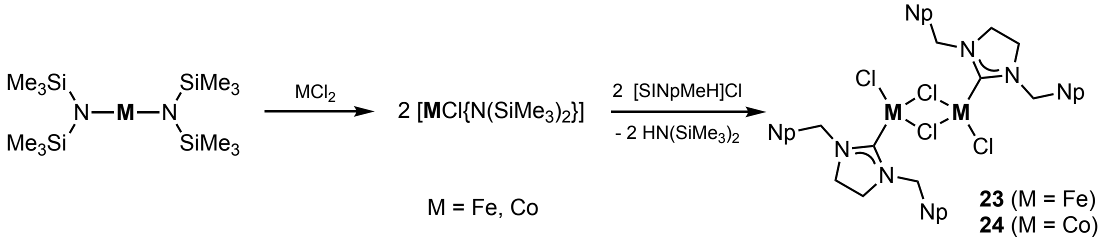

Scheme 6.10. Synthesis of complexes $[(SINpMe)MCl_2]_2$ (M = Fe (**23**), Co (**24**)).

The synthesis of **23** and **24** is based on the formation of a putative "$[MCl\{N(SiMe_3)_2\}]$" intermediate, which was generated by mixing MCl_2 and $[M\{N(SiMe_3)_2\}_2]$ in THF. Adding the imidazolinium salt **XLI** to a solution of $FeCl_2(thf)_{1.5}$ and $[Fe\{N(SiMe_3)_2\}_2]$ or $CoCl_2$ and $[Co\{N(SiMe_3)_2\}_2]$ led to the rapid formation of **23** and **24**, respectively. Quickly removing the solvent *in vacuo* and extracting the residue with toluene enabled us to isolate **23** as light yellow crystals in 41% yield and **24** as blue crystals in a yield of 15%.

23 crystallizes in the monoclinic space group $P2_1/c$ and contains one molecule of toluene per formula unit. Unlike the similar complex **20**, **23** has an inversion center. The molecular structure of **23** (Figure 6.4, left) is reminiscent of **19** with a central Fe_2Cl_2 ring. Whereas the central Fe_2Br_2 ring in **20** is folded by 29.47(7)°, the Fe_2Cl_2 ring in **23** is perfectly planar. The four-coordinate iron(II) centers are in a slightly distorted tetrahedral environment with a Cl2–Cl3 angle of 91.26(2)°. The C1–Fe1 bond, at 2.099(2) Å, is in the typical range of iron(II) NHC complexes.

The crystallographic analysis of the cobalt complex **24** revealed a close resemblance to the analogous iron complex **23**. **24** crystallizes in the same monoclinic space group $P2_1/c$ with one equivalent of toluene. The molecular structure (Figure 6.4, right) is essentially the same as that of **23**, with a planar central Co_2Cl_2 ring and tetrahedrally coordinated cobalt(II) centers. The deviation from a perfectly tetrahedral environment is slightly less pronounced than in 23, with a Cl2–Co–Cl3 angle of 93.58(6)°. The C1–Co1 bond length amounts to 2.049(5) Å, which is within the range of cobalt(II) NHC complexes. All relevant structural parameters of **23** and **24** are given in Table 6.1.

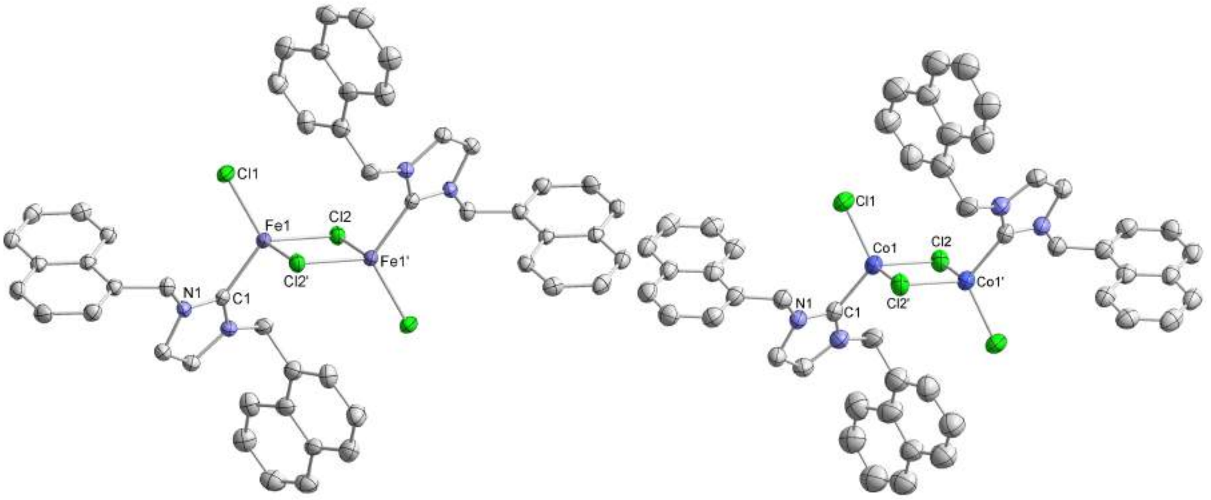

Figure 6.4. Crystal structures of **23** (left) and **24** (right; thermal ellipsoids at 50% probability, hydrogen atoms omitted for clarity).

Table 6.1. Selected bond lengths (Å) and angles (°) of **19**, **20**, **21**, **23**, and **24**.

	19[a]	**20**[a]	**22**[a]	**23**	**24**
M–C	2.086(6) / 2.122(6)	2.077(7) / 2.099(7)	2.037(3) / 2.065(3)	2.099(2)	2.049(5)
M–X$_{\mathrm{term}}$	2.4420(12) / 1.945(5)	2.3963(16) / 2.3887(14)	2.4048(5) / 1.930(2)	2.2486(7)	2.2313(15)
M–X$_{\mathrm{br}}$(1)	2.4666(11) / 2.5602(11)	2.4544(16) / 2.5305(13)	2.4297(5) / 2.5013(5)	2.4372(7)	2.3386(17)
M–X$_{\mathrm{br}}$(2)	2.4688(12) / 2.6423(12)	2.5423(13) / 2.5027(17)	2.4335(5) / 2.5688(5)	2.3392(6)	2.3247(14)
C–M–X$_{\mathrm{term}}$	102.72(17) / 127.1(2)	115.06(19) / 118.7(2)	102.78(8) / 125.17(10)	116.32(6)	114.62(14)
C–M–X$_{\mathrm{br}}$(1)	111.02(18) / 115.97(16)	113.83(19) / 105.2(2)	112.97(8) / 118.43(7)	103.27(6)	107.53(16)
C–M–X$_{\mathrm{br}}$(2)	117.59(18) / 91.35(15)	106.3(2) / 102.9(2)	117.11(8) / 92.05(7)	117.21(6)	117.54(16)
X$_{\mathrm{term}}$–M–X$_{\mathrm{br}}$(1)	115.85(4) / 106.44(15)	111.58(5) / 113.72(5)	115.45(2) / 105.74(7)	104.72(3)	109.41(7)
X$_{\mathrm{term}}$–M–X$_{\mathrm{br}}$(2)	112.88(4) / 121.73(15)	110.45(5) / 116.40(6)	113.51(2) / 119.41(7)	118.00(3)	111.75(7)
X$_{\mathrm{br}}$(1)–M–X$_{\mathrm{br}}$(2)	97.47(4) / 90.95(4)	98.09(5) / 97.15(5)	95.707(17) / 90.653(15)	91.26(2)	93.58(6)
M–X$_{\mathrm{br}}$ –M'	86.55(4) / 84.73(4)	80.21(5) / 78.03(4)	87.582(16) / 85.994(15)	88.74(2)	86.42(6)
Fold angle	6.01(6)	29.47(7)	2.81(2)	0	0

[a] First value corresponds to M1, second value to M2 (see Figure 6.3 and Figure 6.4, right).

In the synthesis of complexes **23** and **24**, short reaction times were essential to obtain the target compounds. When the THF solutions were stirred for one hour, the desired products could not be obtained. Instead, we identified the dicarbene complexes [(SINpMe)$_2$FeCl$_2$] and [(SINpMe)$_2$CoCl$_2$] as well as MCl$_2$(thf)$_{1.5}$ by X-ray crystallography. Thus, it appears that **23** and **24**, while stable in toluene solution, undergo dismutation in THF. The low solubility of the starting materials prevented us from using toluene as the reaction solvent. Further efforts to optimize the synthesis of **23**, **24**, and related complexes should involve other solvents such as dichloromethane.

6.2.3 Synthesis of Iron(II) and Cobalt(II) Amide Complexes

Iron and cobalt NHC complexes [(NHC)M{N(SiMe$_3$)$_2$}] are usually prepared by reacting the bis(bis(trimethylsilyl)amido)metal precursor with a free carbene.[1,21,22,23,29] In order to be able to use non-isolable NHCs as ligands in such complexes, we devised a synthetic route in which the carbene ligand is generated *in situ*. Rather than adding an external base to deprotonate the azolium salt, we used metal precursors that provided the necessary equivalent of base. Our approach was inspired by the Danopoulos/Braunstein route, in which a silylamide ligand of [M{N(SiMe$_3$)$_2$}$_2$] acts as the base and is replaced by the formed carbene and the counterion X of the azolium salt to give [(NHC)MX{N(SiMe$_3$)$_2$}] (*vide supra*, Scheme 6.3, right, and section 6.2.1). Rather than neutral bis(amido)iron(II) and -cobalt(II) precursors, we used homoleptic tris(amido)ferrate(II) and -cobaltate(II) M'[M{N(SiMe$_3$)$_2$}$_3$] (M' = Li, Na). Here, one of the three silylamide ligands acts as the base that deprotonates the azolium salt, while the other two amide ligands remain attached to the metal center. In fact, the isolation of the tris(amido)metalate is not necessary, allowing the synthesis to proceed in a straightforward one-pot reaction. Stirring [M{N(SiMe$_3$)$_2$}$_2$] with one equivalent of LiN(SiMe$_3$)$_2$ or NaN(SiMe$_3$)$_2$ and subsequent addition of the NHC precursor salt afforded the target complex [(NHC)M{N(SiMe$_3$)$_2$}$_2$] within minutes (Scheme 6.11). This procedure proved effective for the synthesis of iron and cobalt complexes of the five NHC precursors described in chapter 4.

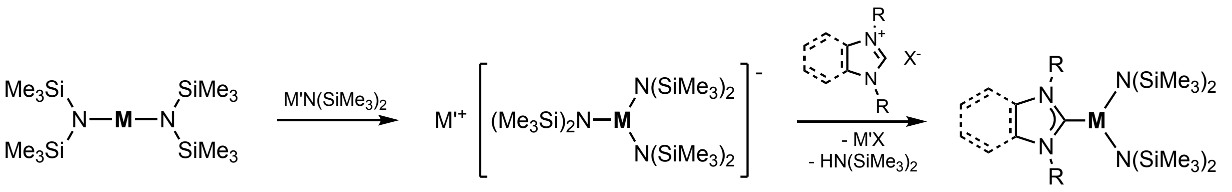

M = Fe, Co
M' = Li, Na
X = Cl, Br
R = Np, CH$_2$Np, CH(Me)Np

25 [(SINp)Fe{N(SiMe$_3$)$_2$}$_2$]
26 [(BNpMe)Fe{N(SiMe$_3$)$_2$}$_2$]
27 [(SINpMe)Fe{N(SiMe$_3$)$_2$}$_2$]
28 [(SINpEt)Fe{N(SiMe$_3$)$_2$}$_2$]

21 [(SINp)Co{N(SiMe$_3$)$_2$}$_2$]
29 [(INpMe)Co{N(SiMe$_3$)$_2$}$_2$]
30 [(BNpMe)Co{N(SiMe$_3$)$_2$}$_2$]
31 [(SINpMe)Co{N(SiMe$_3$)$_2$}$_2$]
32 [(SINpEt)Co{N(SiMe$_3$)$_2$}$_2$]

Scheme 6.11. Synthesis of complexes ([(NHC)M{N(SiMe$_3$)$_2$}$_2$].

The cobalt complex **21**, which was identified as one of the products in the reaction of **5** with $[\mathrm{Co}\{\mathrm{N(SiMe_3)_2}\}_2]$ (see section 6.2.1), can be prepared following the tris(amido)metalate route. Stirring $[\mathrm{Co}\{\mathrm{N(SiMe_3)_2}\}_2]$ and $\mathrm{NaN(SiMe_3)_2}$ in diethyl ether for two minutes and subsequent addition of **5** gave **21** in 19 % yield after work-up. In the same manner, the analogous iron complex $[\mathrm{(SINp)Fe}\{\mathrm{N(SiMe_3)_2}\}_2]$ (**25**) was isolated in 29% yield. Reaction of the azolium salts **XXXIX**, **XL**, **XLI**, and **4** with the tris(amido)metalates afforded the desired products $[\mathrm{(BNpMe)Fe}\{\mathrm{N(SiMe_3)_2}\}_2]$ (**26**), $[\mathrm{(SINpMe)Fe}\{\mathrm{N(SiMe_3)_2}\}_2]$ (**27**), $[\mathrm{(SINpEt)Fe}\{\mathrm{N(SiMe_3)_2}\}_2]$ (**28**), $[\mathrm{(INpMe)Co}\{\mathrm{N(SiMe_3)_2}\}_2]$ (**29**), $[\mathrm{(BNpMe)Co}\{\mathrm{N(SiMe_3)_2}\}_2]$ (**30**), $[\mathrm{(SINpMe)Co}\{\mathrm{N(SiMe_3)_2}\}_2]$ (**31**), and $[\mathrm{(SINpEt)Co}\{\mathrm{N(SiMe_3)_2}\}_2]$ (**32**) in yields of 62 to 80%.

X-ray quality crystals of **25**, **26**, **27**, **29**, **30**, **31**, and **32** were obtained from diethyl ether. The molecular structures (Figures 6.5 and 6.6) are very similar and resemble that of **21** (section 6.2.1). In each complex, the metal center is in a trigonal planar coordination environment with a slightly enlarged N–M–N' angle of 125.5 to 132.39(7)°. The relevant bond lengths and angles are summarized in Table 6.2. Notably, the crystallographic analysis of **32** revealed four crystallographically independent molecules in the unit cell, and the parameters given in Table 6.2 represent average values.

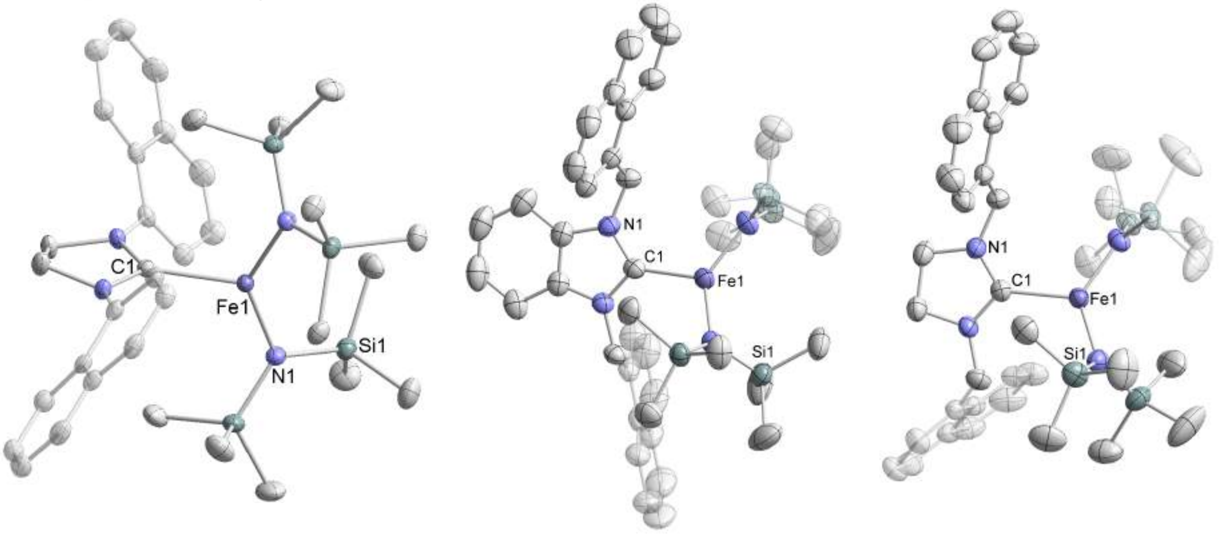

Figure 6.5. Crystal structures of NHC-Fe complexes **25**, **26**, and **27** (thermal ellipsoids at 50% probability, hydrogen atoms and solvent molecules omitted for clarity).

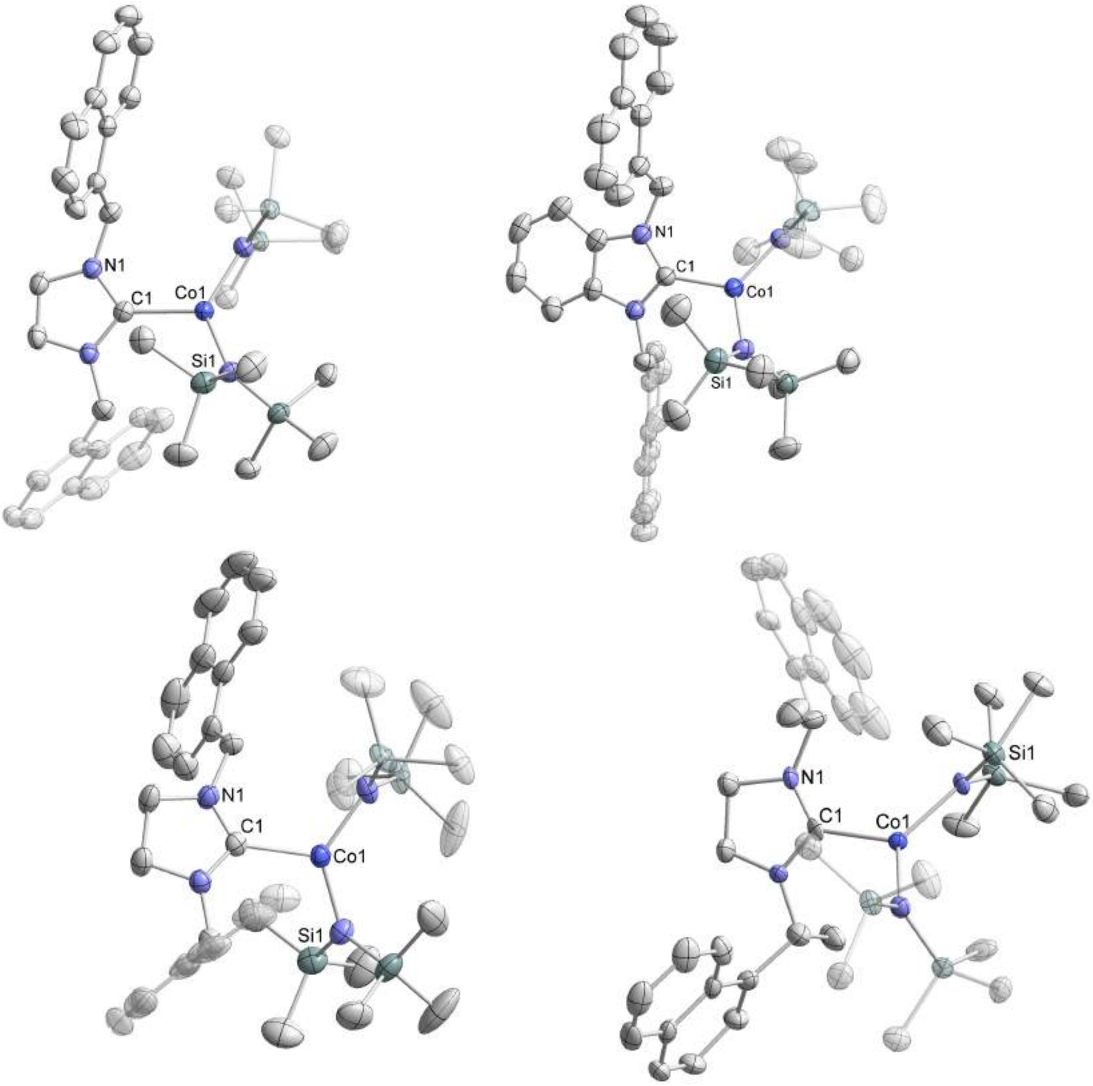

Figure 6.6. Crystal structures of NHC-Co complexes **29**, **30**, **31**, and **32** (thermal ellipsoids at 50% probability, hydrogen atoms and solvent molecules omitted for clarity).

Table 6.2. Selected bond lengths (Å) and angles (°) of [(NHC)M{N(SiMe$_3$)$_2$}$_2$] complexes.

	21	**25**	**26**	**27**	**29**	**30**	**31**	**32** (avg.)
Space group	*C*2/*c*	*P*-1	*P*-1	$P2_12_12_1$	$P2_12_12_1$	*P*-1	$P2_12_12_1$	$P2_1$
M–C	2.0922(17)	2.1576(18)	2.128(2)	2.161(3)	2.081(4)	2.059(3)	2.082(5)	2.088
M–N	1.9322(10)	1.9566(16)	1.9484(19)	1.945(3)	1.938(3)	1.922(2)	1.927(5)	1.939
M–N'		1.9517(15)	1.933(2)	1.951(3)	1.936(6)	1.930(2)	1.936(4)	
C–M–N	116.34(3)	115.14(7)	113.62(8)	114.56(11)	115.09(14)	115.85(10)	115.4(2)	117.2
C–M–N'		112.44(7)	115.18(9)	115.53(12)	116.58(14)	114.42(10)	117.0(2)	
N–M–N'	127.32(7)	132.39(7)	130.90(8)	129.88(12)	128.29(14)	129.53(9)	127.4(2)	125.5

Due to the paramagnetic nature of the prepared compounds, the signals in the ^{1}H NMR spectra cannot be assigned to specific hydrogen atoms. Still, the spectra are characteristic for each complex and can be used to identify the isolated substances. The spectra and a summary of the chemical shifts are given in Appendix B.

6.3 Magnetic Properties of NHC-stabilized Iron and Cobalt Amide Complexes

The magnetic moments of complexes **21**, **25**, **26**, **27**, **30**, and **31** in C_6D_6 solution were determined using the Evans method. The effective magnetic moments of the iron complexes **25**, **26**, and **27** amount to 4.8(1), 4.7(1), and 4.4(1) μ_B, respectively, which is in agreement with the expected spin-only value for a complex with four unpaired electrons (calculated value: 4.90 μ_B). This is in accord with the results of Layfield and co-workers who determined quintet ground states for analogous $[(NHC)Fe\{N(SiMe_3)_2\}_2]$ complexes by SQUID measurements.[21] The magnetic moments of the cobalt complexes **21** (5.0(1) μ_B), **30** (4.3(1) μ_B), and **31** (4.7(1) μ_B) were found to be slightly higher than expected for high-spin Co(II) complexes which would have three unpaired electrons (calculated spin-only value: 3.87 μ_B). Similar observations were reported for related $[(NHC)Co\{N(SiMe_3)_2\}_2]$ complexes.[22,29]

A more detailed analysis of the magnetic properties of the cobalt complexes **21** and **30** was carried out in collaboration with the group of Sven Schneider (University of Göttingen). Temperature-dependent magnetic susceptibility measurements using a SQUID gave effective magnetic moments μ_{eff} = 5.3(1) μ_B for **21** and 5.1(1) μ_B for **30** at 210 K. Variable-temperature/variable-field (VTVH) measurements revealed large negative zero-field splitting parameters D of -87.4 cm^{-1} ($E/D = 0$, $g_x = g_y = 2.567$, $g_z = 2.989$) for **21** and $D = -95.2$ cm^{-1} ($E/D = 0$, $g_x = g_y = 2.404$, $g_z = 955$) for **30**, assuming a $S = 3/2$ spin state. Alternating current magnetic susceptibility measurements in the presence of a direct current magnetic field (AC/DC) revealed temperature-dependent maxima of the out-of-phase magnetic susceptibility χ'' (Figure 6.7). Analysis of the temperature-dependent χ'' data gave energy barriers $U_{eff} = 9.8$ cm^{-1} for **21** and 16.9 cm^{-1} for **30** with relaxation times $\tau_0 = 4.29 \cdot 10^{-6}$ s (**21**) and $1.74 \cdot 10^{-6}$ s (**30**). These parameters indicate that **21** and **30** show significant magnetic anisotropy.

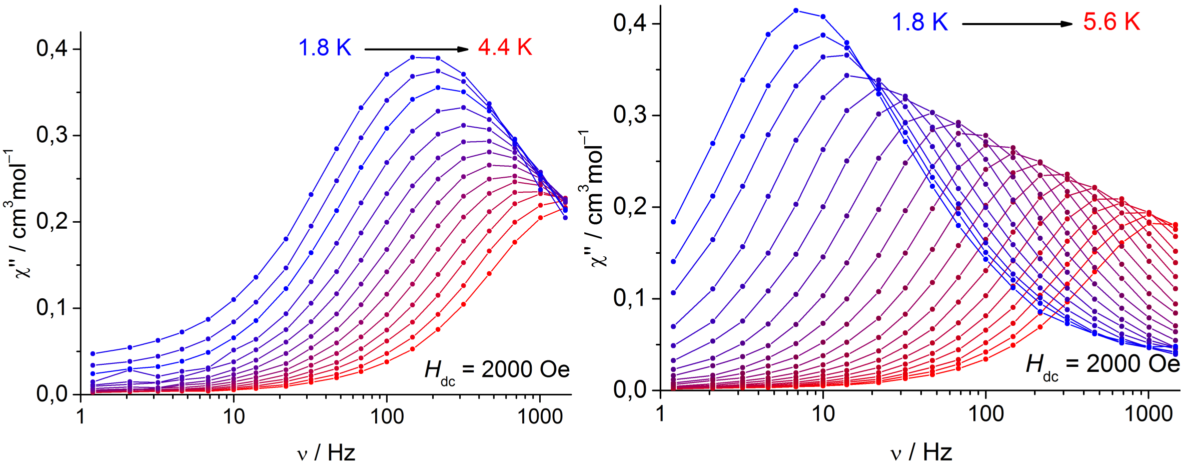

Figure 6.7. Out-of-phase magnetic susceptibility of **21** (left) and **30** (right). Measurements and data analysis were performed by Jan Gerkens (group of Sven Schneider, University of Göttingen).

6.4 UV-vis Spectroscopic Characterization of Iron and Cobalt NHC Complexes

The UV-vis spectroscopic analysis of **21**, **25-28**, and **30-32** revealed great similarities between all studied complexes (Figure 6.8). The spectra were recorded in diethyl ether. All spectra show a strong, narrow band around 225 nm ($\varepsilon = 8.52 \cdot 10^4$ L mol^{-1} cm^{-1} for **25**; $1.53 \cdot 10^5$ to $1.87 \cdot 10^5$ L mol^{-1} cm^{-1} for the other compounds) and a band between 281 and 294 nm ($\varepsilon = 2.63 \cdot 10^4$ to $7.21 \cdot 10^4$ L mol^{-1} cm^{-1}). Complex **26** shows very broad, relatively weak band at 412 nm ($\varepsilon = 5.32 \cdot 10^3$ L mol^{-1} cm^{-1}); for complex **27**, a weak shoulder is observed around 347 nm. For the other iron complexes, no bands are discernible in the visible region. In addition to the UV bands, the cobalt complexes **21** and **30-32** give rise to three very weak bands in the visible region between 606 and 718 nm with $\varepsilon = 62$ to 171 L mol^{-1} cm^{-1} (Figure 6.8 bottom, inset) in line with the green color of the isolated substances.

The observation of very similar spectra indicates that the nature of the NHC backbone has hardly any influence on the electronics of the complexes. The presence of aryl *N*-substituents in **21** and **25**, as opposed to the benzylic substituents in **26-28** and **30-32**, causes a very slight shift of the observed bands to lower energy by about 10 nm. The transitions in the UV region are basically identical in all studied complexes and are therefore presumed to be centered on the naphthyl groups. The weak bands observed in the visible region for the cobalt complexes likely correspond to metal-centered d-d transitions.

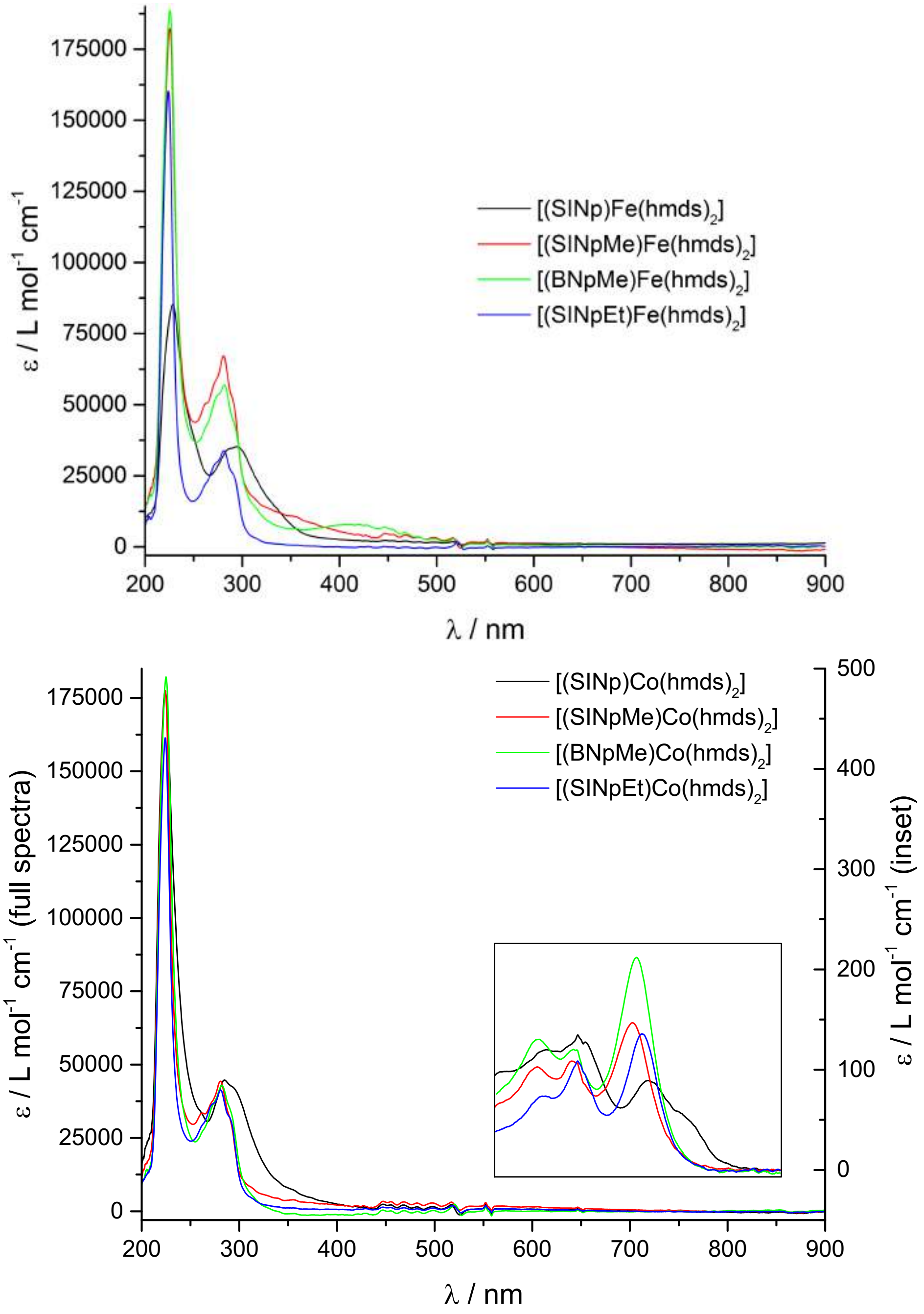

Figure 6.8. UV-Vis spectra of NHC-iron complexes **25**-**28** (top); NHC-cobalt complexes **21** and **30**-**32** (bottom) recorded in diethyl ether. The inset in the right graph shows a blown-up section of the spectra at high wavelength (550-850 nm); the vertical scale on the right refers to the blown-up spectrum.

6.5 Electrochemical Analysis of Iron and Cobalt NHC Complexes

With the aim of utilizing the silylamide compounds as precursors for the synthesis of low-valent iron and cobalt complexes, their redox properties were investigated by cyclic voltammetry. Besides allowing us to judge the feasibility of chemical reduction, comparison of the reduction potentials provide insight into the influence of the ligand and the metal center on the redox properties. All measurements were performed under identical conditions in a glovebox (see Section 8.1) on 1,2-difluorobenzene solutions of each complex. Potentials are referenced versus the ferrocenium/ferrocene couple. The cyclic voltammograms are displayed in Figures 6.9 and 6.10 and reduction potentials are summarized in Table 6.3.

Complex **25** (Figure 6.9, black curve) shows an oxidation at $E_{1/2} = +0.08$ V and a reduction at $E_{1/2} = –2.52$ V. While the reduction wave is fully reversible at scan rates of $v > 50$ mV s^{-1}, the back oxidation is weakened significantly at slower scan rates. At $v = 10$ mV s^{-1}, the back oxidation disappears entirely. By contrast, the oxidation at 0.08 V is fully reversible even at very slow scan rates.

The redox behavior of **26**, **27**, and **28** is in stark contrast to that of **25**. In the cyclic voltammogram of **26** (Figure 6.9, dark blue curve), a quasireversible oxidation is observed at $E_{1/2} = 0.21$ V. At scan rates of $v < 200$ mV s^{-1}, the back reduction disappears almost entirely. An irreversible oxidation is observed at $E_{Pa} = 1.00$ to 1.15 V. A quasireversible reduction is found at $E_{1/2} = –2.56$ V; the back oxidation is only visible at scan rates of $v > 100$ mV s^{-1}. Complex **27** (Figure 6.9, blue curve) exhibits a quasireversible oxidation at $E_{Pa} = +0.15$ V and an irreversible oxidation at $E_{Pa} = +0.86$ V. The weak back reduction of the quasireversible process is visible when stopping the measurement at a potential of $E = +0.5$ V, but disappears upon overoxidation. An irreversible reduction wave is observed at $E_{p,red} = –2.87$ V. Complex **28** (Figure 6.9, light blue curve) behaves similarly, with a quasireversible oxidation found at $E_{1/2} = +0.15$ V when measuring in a potential window of –1 to +1 V. The separation of the oxidation and reduction peaks of this process amounts to $\Delta E = 0.32$ V (at $v = 50$ mV s^{-1}) to 0.49 V ($v = 2000$ mV s^{-1}). For a perfectly reversible process $\Delta E_{theor} = 0.059$ V; a large ΔE value may indicate a kinetically hindered redox process. Extending the potential window leads to a drastic change of the cyclic voltammogram: the quasireversible process disappears and is replaced by two irreversible oxidation waves at $E_{Pa} = –0.15$ and +0.41 to +0.68 V. The peak of the second oxidation wave is shifted to higher potential at faster scan rates; the peak of the first reduction wave is shifted to lower potential. Two irreversible reduction processes are observed at $E_{Pc} = –1.66$ ($v = 50$ mV s^{-1}) to –1.84 V ($v = 2000$ mV s^{-1}) and –2.52 V.

The cyclic voltammogram of the cobalt complex **21** (Figure 6.10, black curve) is very similar to that of the analogous iron complex **25**. A reversible oxidation is observed at $E_{1/2} = +0.26$ V and a reversible reduction at –2.22 V. At slow scan rates of $v < 100$ mV s^{-1}, the back reduction of the oxidation wave is weakened very slightly. The back oxidation of the reduction wave is weakened substantially at slow scan rates.

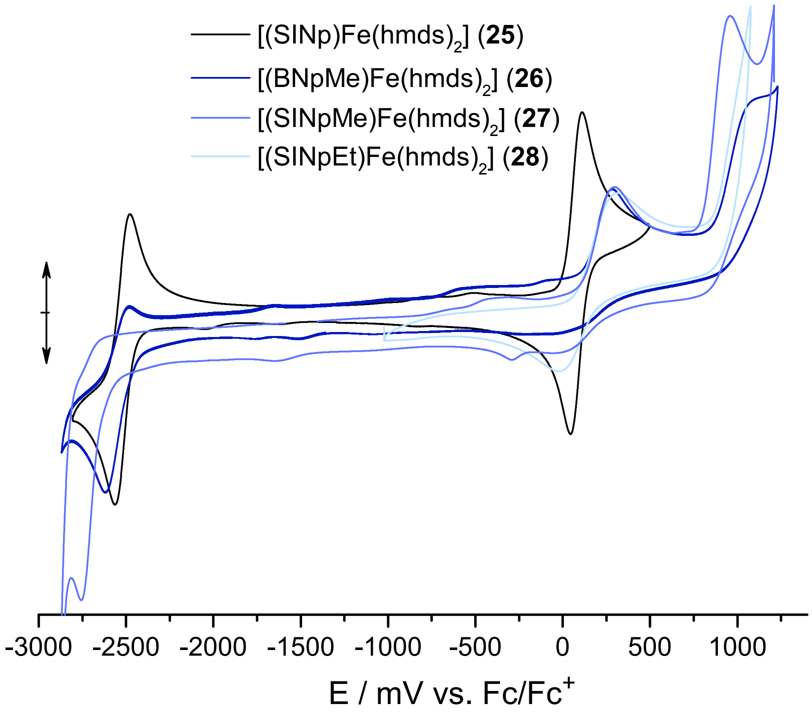

Figure 6.9. Cyclic voltammograms of **25**-**28**, recorded in DFB/NBu$_4$PF$_6$ at a Pt disk working electrode using a Pt wire counter electrode and an Ag wire as the pseudoreference electrode. Decamethylferrocene was used as an internal reference and a constant of –0.48 V was subtracted to obtain values referenced versus the ferrocenium/ferrocene redox couple.

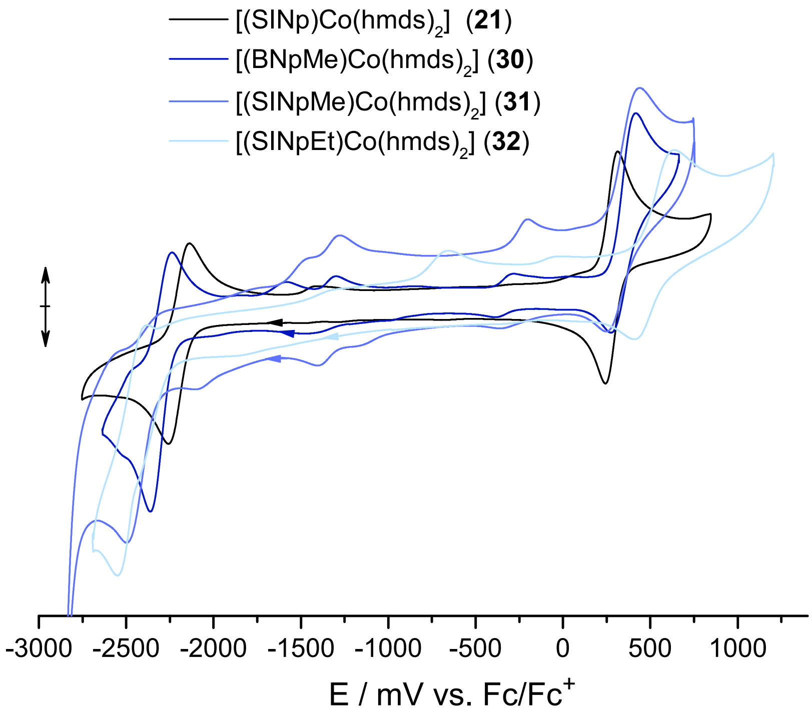

Figure 6.10. Cyclic voltammograms of **21** and **30**-**32**, recorded in DFB/NBu$_4$PF$_6$ at a Pt disk working electrode using a Pt wire counter electrode and an Ag wire as the pseudoreference electrode. Ferrocene was used as an internal reference.

As was observed for the iron complexes, the cobalt complexes with (1-naphthyl)alkyl substituents are less well-behaved. The cyclic voltammogram of **30** (Figure 6.10, dark blue curve) shows a quasireversible oxidation at $E_{1/2}$ = +0.35 V and a quasireversible reduction at $E_{1/2}$ = –2.30 V. Additional weak waves around –1.00 to –1.50 V likely correspond to degradation products due to partial overoxidation and/or overreduction. Complex **31** (Figure 6.10, blue curve) undergoes a quasireversible oxidation at $E_{1/2}$ = 0.34 V. While the oxidation appears reversible at very high scan rates of $v > 1000$ mV s^{-1}, the back reduction disappears entirely at scan rates of $v < 100$ mV s^{-1}. An irreversible reduction is observed at E_{Pc} = -2.50 V. After the first cycle, several small waves appear which likely correspond to degradation products from overoxidation or overreduction. The cyclic voltammogram of **32** (Figure 6.10, light blue curve) shows a quasireversible oxidation at $E_{1/2}$ = 0.52 V which appears almost fully reversible at scan rates of $v > 500$ mV s^{-1}. An irreversible reduction at E_{Pc} = –2.56 V leads to the degradation of **32**. The degradation product subsequently gives rise to an irreversible oxidation wave at E_{Pa} = –0.66 V which is not observed during the first cycle.

Table 6.3. Reduction potentials of **21**, **25**-**28**, and **30**-**32** (V vs. Fc/Fc$^+$). Values printed in bold represent reversible or quasireversible processes.

Process	**25**	**26**	**27**	**28**	**21**	**30**	**31**	**32**
Ox. 1	**0.08**	0.21	**0.15**	0.15	**0.26**	**0.35**	**0.34**	–0.66
Ox. 2		1.08 (av.)	0.86	0.55 (av.)				**0.52**
Red. 1	**–2.52**	–2.56	–2.87	–1.75 (av.)	**–2.22**	**–2.30**	–2.50	–2.56
Red. 2				–2.52				

Comparing the cyclic voltammetry results, it is evident that the complexes **27**, **28**, **31**, and **32**, which contain SINpMe and SINpEt ligands, undergo rapid degradation upon reduction under the applied conditions. The electrochemical oxidations are quasireversible, indicating that the oxidized species are stable at least for a short time. This observation is consistent with the strongly σ-donating character of the imidazolidin-2-ylidene ligands, which are able to stabilize high-valent metal centers. The BNpMe complexes **26** and **30** are able to undergo quasireversible oxidation and reduction processes at high scan rates. This indicates that the reduced species may be somewhat stable, although they quickly decompose under the conditions of the CV measurement. The SINp complexes **21** and **25** undergo reversible reductions and oxidations, although the oxidation product of **25** seems to decompose partly at slow scan rates. The reduction products might thus be stable enough to be isolated following chemical reduction. The behavior of **21**, **25**, **26**, and **30** is in accord with a weakened σ-donating character due to the –I effect of the benzannulated backbone in the BNpMe ligand and of the aryl *N*-substituents of SINp.

6.6 Catalytic Olefin Hydrogenation using NHC-Iron Complexes

The group of Jacobi von Wangelin recently found an efficient method for the hydrogenation of olefins using $[Fe\{N(SiMe_3)_2\}_2]$ as the precatalyst.[30] After reduction with iBu$_2$AlH (Dibal-H), the formed active species enabled the hydrogenation of a broad range of olefins under mild conditions. We therefore became interested in studying whether the presence of a NHC ligand on the iron center might have a stabilizing effect on the catalytically active species. We envisaged that utilizing the chiral SINpEt ligand might result in some degree of stereoinduction, allowing Jacobi von Wangelin's system to be adapted for asymmetric hydrogenations. In collaboration with Dr. Tim Gieshoff from the group of Jacobi von Wangelin, the performance of $[(BNpMe)Fe\{N(SiMe_3)_2\}_2]$ (**26**) and $[(SINpEt)Fe\{N(SiMe_3)_2\}_2]$ (**28**) in the hydrogenation of alkenes was investigated.[31] The addition of Dibal-H was necessary to transform **26** and **28** into catalytically active species. While **28** reacted quickly with Dibal-H, the reaction of **26** was slow and did not reach full conversion; after stirring **26** and Dibal-H in toluene for 24 hours, the starting material was identified by X-ray crystallography. Work-up of the reaction mixtures was performed nonetheless. The hydrogenation of 1-phenylcyclohexene reached completion within 18 hours under 10 bar H_2 pressure with 5 mol% **26** and 10 mol% Dibal-H. At 4 bar H_2 with otherwise unchanged conditions, a yield of 95% was observed. Using $[Fe\{N(SiMe_3)_2\}_2]$ instead of **26**, 1-phenylcyclohexene is fully hydrogenated at 1.3 bar H_2 within 30 minutes. The slow and incomplete reaction of **26** with Dibal-H and the low catalytic activity are indications that the presence of the BNpMe ligand prevents the formation of the catalytically active species.

Complex **28** showed a higher reactivity towards Dibal-H and displayed high catalytic activity in the hydrogenation of prochiral styrene derivatives. At an H_2 pressure of 1.9 bar and a catalyst loading of 5 mol% (10 mol% Dibal-H), full conversion was reached in 4 hours, which is comparable to the results obtained with $[Fe\{N(SiMe_3)_2\}_2]$. However, no enantiomeric excess was observed, which may result from dissociation of the carbene ligand from the iron center.

Table 6.4. Catalytic hydrogenation of 1-phenylcyclohexene (performed by Dr. Tim Gieshoff, group of Axel Jacobi von Wangelin; results from ref. 31).

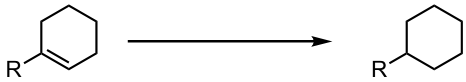

Entry	[Fe]	Conditions	Yield (Conversion) in %[a]
1	[Fe{N(SiMe$_3$)$_2$}$_2$]	1.3 bar H$_2$, r.t., 0.5 h	>99 (>99)
2	**26**	10 bar H$_2$, r.t., 18 h	>99 (>99)
3	**26**	4 bar H$_2$, r.t., 18 h	95 (95)
4	**26**	1.9 bar H$_2$, r.t., 0.5 h	<1 (<1)
5	**26**	1.9 bar H$_2$, r.t., 0.5 h[b]	<1 (<1)
6	**26**	No Dibal-H, 50 bar H$_2$, r.t., 18 h	<1 (<1)
7	**28**	10 bar H$_2$, r.t., 18 h	>99 (>99)

Conditions unless mentioned otherwise: 5 mol% [Fe], 10 mol% Dibal-H; R = Ph; [a] quantitative GC-FID vs. *n*-pentadecane as internal reference; [b] catalyst preparation 18 hours prior to reaction.

6.7 Chemical Reduction of NHC-stabilized Iron and Cobalt Complexes

6.7.1 Reduction of Silylamide Complexes

Following the electrochemical analysis, we investigated whether low-valent iron and cobalt species are accessible by chemical reduction of the amide complexes. Potassium graphite, sodium amalgam, lithium triethylborohydride ("superhydride"), and potassium tri-*sec*-butylborohydride ("K-selectride") were used as reducing agents, and the reactions were performed in a 1:1 and 1:2 stoichiometry of metal complex to reducing agent in THF solution at room temperature. Instantaneous color changes were observed from yellow to dark brown for the iron complexes and from light green to dark olive green for the cobalt complexes. The reaction mixtures were concentrated to dryness *in vacuo* and subsequently fractionally extracted with *n*-hexane, diethyl ether, toluene, and THF.

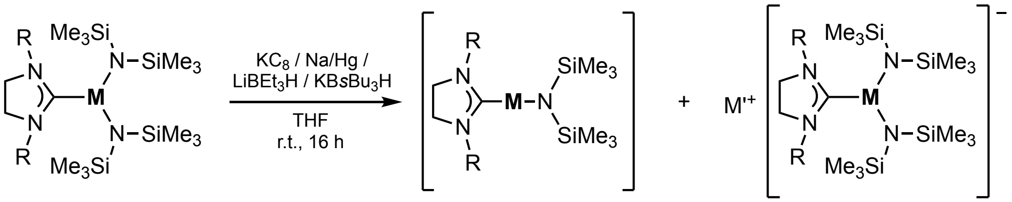

25 [(SINp)Fe{N(SiMe$_3$)$_2$}$_2$]
27 [(SINpMe)Fe{N(SiMe$_3$)$_2$}$_2$]
21 [(SINp)Co{N(SiMe$_3$)$_2$}$_2$]
31 [(SINpMe)Co{N(SiMe$_3$)$_2$}$_2$]

Scheme 6.12. Chemical reduction of **21**, **25**, **27**, and **31**. Postulated target compounds given in brackets.

Since the expected target complexes are presumed to be paramagnetic, reaction monitoring by NMR was unpractical and we relied on X-ray crystallography for an unambiguous identification of the obtained products. X-ray quality crystals were obtained in three cases. From the reaction of $[(SINpMe)Fe\{N(SiMe_3)_2\}_2]$ (**27**) with two equivalents of KC_8, yellow crystals were obtained, which, upon crystallographic analysis, were identified as the starting complex **27**. The reaction of $[(SINp)Fe\{N(SiMe_3)_2\}_2]$ (**25**) with two equivalents of $LiBEt_3H$ gave brownish-yellow, crystalline blocks upon slow evaporation of the diethyl ether fraction. X-ray crystallography revealed the formation of the metal-free compound **33** (Figure 6.11, left). This compound formally results from a transfer of two ethyl groups to the carbene carbon atom and an insertion of the resulting borylene into a C–N bond of the free carbene. This type of ring expansion with boranes, silanes, and other main group compounds has been studied in detail by the group of Radius.[32] No iron-containing products were isolated from this reaction.

The analogous reaction of **27** with two equivalents of $LiBEt_3H$ gave yellow, crystalline blocks from the diethyl ether extract. The iron-free compound **34** (Figure 6.11, right) was identified by X-ray crystallography. Unlike the reaction of **25** with $LiBEt_3H$, no ring expansion occurs, but one of the *N*-substituents is displaced and a dimeric compound is formed in which two imidazole moieties bind to two Li(thf) fragments. The carbene carbons are bound to BEt_3. The fate of the iron fragment remains unclear as no iron-containing products were identified.

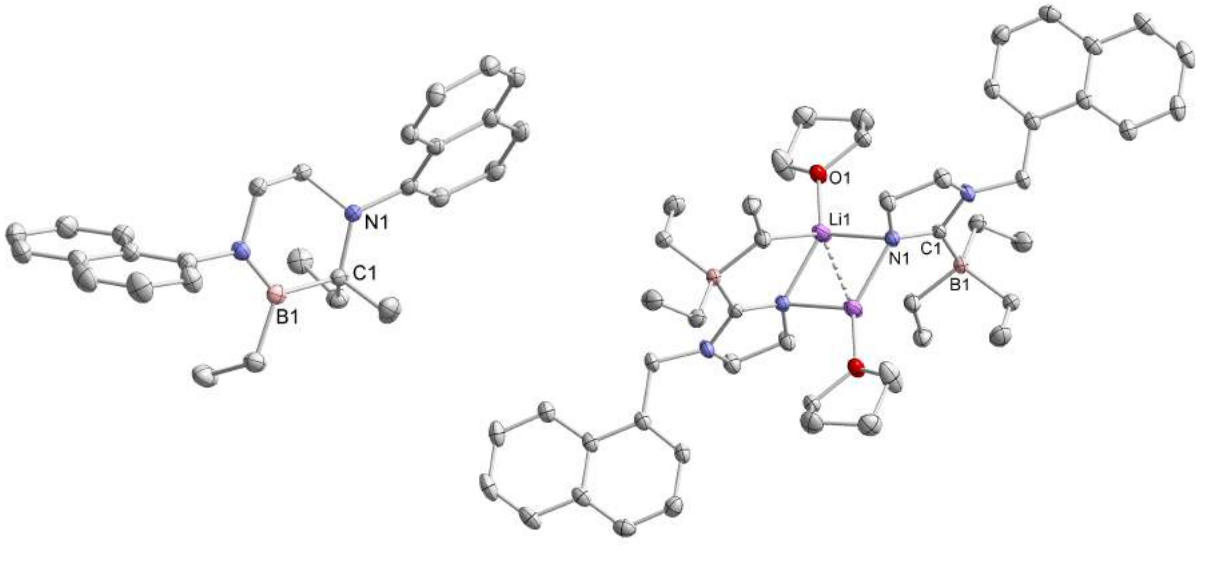

Figure 6.11. Solid state X-ray structures of NHC degradation products **33** (left) and **34** (right) (thermal ellipsoids at 50% probability; H atoms omitted for clarity).

X-ray quality crystals could not be obtained from the reductions of the analogous cobalt complexes **21** and **31**. These initial attempts to identify low-valent iron and cobalt complexes were unsuccessful. Analysis of the reaction mixtures by other means such as mass spectrometry may be useful to gain more insight into the nature of the formed products and potentially identify some of the target compounds.

From the present results, it appears that the strongly σ-donating NHC ligands are incompatible with metal centers that are too electron-rich, leading to the cleavage of the carbene-metal bond. An alternative synthetic approach might start with the formation of a chelating Fe or Co complex by abstraction of the $N(SiMe_3)_2^-$ ligands, e.g. by reaction with Brookhart's acid, $[H(OEt_2)_2]BAr^F_4$, or a slightly acidic salt of a weakly coordinating anion, such as $NH_4BAr^F_4$. Subsequent reaction with a reducing agent might then lead to a low-valent species that is stabilized by the π-accepting property of the naphthyl groups.

6.7.2 Reduction of Halide Complexes

The halide complexes **23** and **24** were reacted with potassium graphite in an attempt to synthesize low-valent complexes. Reacting **24** with KC_8 in THF in the presence of 18-crown-6 resulted in a color change from blue to olive green within several minutes. From fractional extraction of the residue with *n*-hexane, diethyl ether, and toluene it appeared that several products had formed, since the ether extract was olive green while the toluene fraction showed a turquoise color. Crystals obtained by slow evaporation of the toluene fraction revealed the formation of an ion-paired species $[K(18\text{-crown-}6)][(SINpMe)CoCl_3]$ (**35**, Figure 6.12).

35 crystallizes in the orthorhombic space group $P2_12_12_1$ with four molecules in the unit cell. The cobalt center is coordinated in a tetrahedral geometry by a carbene ligand and three chlorides. The Co1–C1 bond length of 2.047(5) Å is in accord with an oxidation state of +II on the cobalt center. The anionic $[(SINpMe)CoCl_3]^-$ fragment forms an ion pair with $[K(18\text{-crown-}6)]^+$. The potassium cation sits 0.914(2) Å above the plane defined by the oxygen atoms of the crown ether and is bound to the three chlorides of the cobaltate fragment.

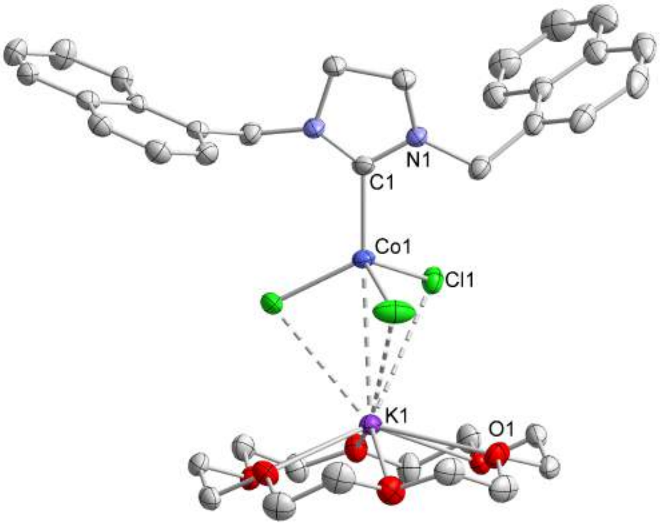

Figure 6.12. Molecular structure of complex **35** (thermal ellipsoids at 50% probability, hydrogen atoms omitted for clarity).

The fate of the remaining [(SINpMe)CoCl]$^+$ fragment is unclear thus far. The olive-green color of the ether extract may indicate by the presence of a reduced species. However, no X-ray quality crystals could be obtained. Further attempts to crystallize the product dissolved in the ether extract and analysis by mass spectrometry could give a more detailed understanding of this reaction.

6.8 References

[1] K. Riener, S. Haslinger, A. Raba, M. P. Högerl, M. Cokoja, W. A. Herrmann, F. E. Kühn, *Chem. Rev.* **2014**, *114*, 5215-5272.

[2] a) K. Öfele, *Angew. Chem. Int. Ed. Engl.* **1969**, *8*, 916-917; b) K. Öfele, C. G. Kreiter, *Chem. Ber.* **1972**, *105*, 529-540.

[3] B. Cetinkaya, P. Dixneuf, M. F. Lappert, *J. Chem. Soc., Chem. Comm.* **1973**, 206.

[4] M. F. Lappert, P. Pye, *J. Chem. Soc., Dalton Trans.* **1977**, 2172-2180.

[5] U. Kernbach, M. Ramm, P. Luger, W. P. Fehlhammer, *Angew. Chem. Int. Ed. Engl.* **1996**, *35*, 310-312.

[6] J. Foerstner, A. Kakoschke, R. Goddard, J. Rust, R. Wartchow, H. Butenschön, *J. Organomet. Chem.* **2001**, *617-618*, 412-422.

[7] J. Louie, R. H. Grubbs, *Chem. Commun.* **2000**, 1479-1480.

[8] a) J. A. Przyojski, H. D. Arman, Z. J. Tonzetich, *Organometallics* **2012**, *31*, 3264-3271; b) A. A. Danopoulos, P. Braunstein, M. Wesolek, K. Y. Monakhov, P. Rabu, V. Robert, *Organometallics* **2012**, *31*, 4102-4105.

[9] A. A. Danopoulos, P. Braunstein, M. Stylianides, M. Wesolek, *Organometallics* **2011**, *30*, 6514-6517.

[10] K. Matsubara, T. Sueyasu, M. Esaki, A. Kumamoto, S. Nagao, H. Yamamoto, Y. Koga, S. Kawata, T. Matsumoto, *Eur. J. Inorg. Chem.* **2012**, 3079-3086.

[11] J. A. Przyojski, H. D. Arman, Z. J. Tonzetich, *Organometallics* **2013**, *32*, 723-732.

[12] L. Xiang, J. Xiao. L. Deng, *Organometallics* **2011**, *30*, 2018-2025.

[13] a) Q. Zhang, L. Xiang, L. Deng, *Organometallics* **2012**, *31*, 4537-4543; b) Z. Mo, Q. Zhang, L. Deng, *Organometallics* **2012**, *31*, 6518-6521.

[14] T. Hashimoto, S. Urban, R. Hoshino, Y. Ohki, K. Tatsumi, F. Glorius, *Organometallics* **2012**, *31*, 4474-4479.

[15] T. Hashimoto, R. Hoshino, T. Hatanaka, Y. Ohki, K. Tatsumi, *Organometallics* **2014**, *33*, 921-929.

[16] a) Z. Mo, Z. Ouyang, L. Wang, K. L. Fillman, M. L. Neidig, L. Deng, *Org. Chem. Front.* **2014**, *1*, 1040-1044; b) Z. Ouyang, J. Du, L. Wang, J. L. Kneebone, M. L. Neidig, L. Deng, *Inorg. Chem.* **2015**, *54*, 8808-8816; c) Z. Ouyang, Y. Meng, J. Cheng, J. Xiao, S. Gao, L. Deng, *Organometallics* **2016**, *35*, 1361-1367.

[17] Y. Ohki, R. Hoshino, K. Tatsumi, *Organometallics* **2016**, *35*, 1368-1375.

[18] Z. Mo, D. Chen, X. Leng, L. Deng, *Organometallics* **2012**, *31*, 7040-7043.

[19] Z. Mo, Y. Liu, L. Deng, *Angew. Chem. Int. Ed.* **2013**, *52*, 10845-10849.

[20] C. B. Hansen, R. F. Jordan, G. L. Hillhouse, *Inorg. Chem*. **2015**, *54*, 4603-4610.

[21] R. A. Layfield, J. J. W. McDouall, M. Scheer, C. Schwarzmaier, F. Tuna, *Chem. Commun.* **2011**, *47*, 10623-10625.

[22] B. M. Day, K. Pal, T. Pugh, J. Tuck, R. A. Layfield, *Inorg. Chem.* **2014**, *53*, 10578-10584

[23] B. M. Day, T. Pugh, D. Hendriks, C. F. Guerra, D. J. Evans, F. M. Bickelhaupt, R. A. Layfield, *J. Am. Chem. Soc.* **2013**, *135*, 13338-13341.

[24] A. A. Danopoulos, P. Braunstein, K. Y. Monakhov, J. van Leusen, P. Kögerler, M. Clémancey, J.-M. Latour, A. Benayad, M. Tromp, E. Rezabal, G. Frison, *Dalton Trans.* **2017**, *46*, 1163-1171.

[25] Y. Liu, L. Deng, *J. Am. Chem. Soc.* **2017**, *139*, 1798-1801.

[26] M. I. Lipschutz, T. Chantarojsiri, Y. Dong, T. D. Tilley, *J. Am. Chem. Soc.* **2015**, *137*, 6366-6372.

[27] a) J. Al Thagfi, G. G. Lavoie, *Organometallics* **2012**, *31*, 2463-2469; b) H. Z. Kaplan, B. Li, J. A. Byers, *Organometallics* **2012**, *31*, 7343-7350; c) J. Al Thagfi, G. G. Lavoie, *Organometallics* **2012**, *31*, 7351-7358.

[28] Q. Liang, T. Janes, X. Gjergji, D. Song, *Dalton Trans.* **2016**, *45*, 13872-13880.

[29] A. Massard, P. Braunstein, A. A. Danopoulos, S. Choua, P. Rabu, *Organometallics* **2015**, *34*, 2429-2438.

[30] T. Gieshoff, U. Chakraborty, M. Villa, A. Jacobi von Wangelin, *Angew. Chem. Int. Ed.* **2017**, *56*, 3585-3589.

[31] T. Gieshoff, Dissertation, Universität Regensburg **2016**.

[32] a) S. Pietsch, U. Paul, I. A. Cade, M. J. Ingleson, U. Radius, T. B. Marder, *Chem. Eur. J.* **2015**, *21*, 9018-9021; b) S. Würtemberger-Pietsch, U. Radius, T. B. Marder, *Dalton Trans.* **2016**, *45*, 5880-5895; c) S. Würtemberger-Pietsch, H. Schneider, T. B. Marder, U. Radius, *Chem. Eur. J.* **2016**, *22*, 13032-13036.

7. Summary and Outlook

The first part of this thesis described the synthesis of low-valent ruthenium complexes stabilized by the π acceptor ligands 1,5-cyclooctadiene and naphthalene from readily available Ru(II) precursors. The anionic cod complex [K(dme)$_2$][Cp*Ru(cod)] (**K3**) was obtained by reduction of [Cp*RuCl(cod)] with KC$_8$ in DME (Scheme 7.1) and characterized spectroscopically and crystallographically. Reaction with P$_4$ revealed a mixture of products in the ^{31}P NMR spectrum that is reminiscent of the analogous reaction of the complex [K(18-crown-6){Cp*Fe(C$_{10}$H$_8$)}].

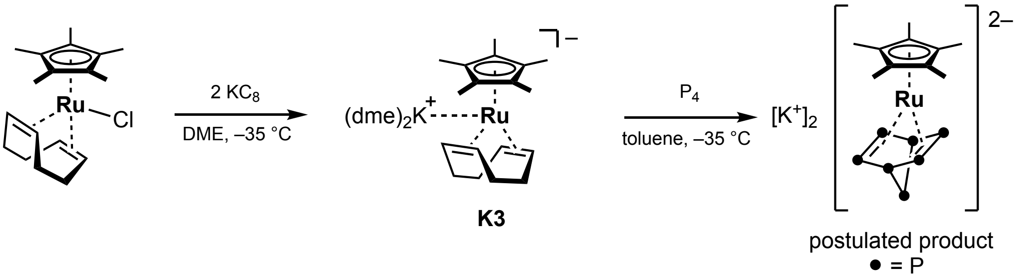

Scheme 7.1. Synthesis of **K3** from [Cp*RuCl(cod)] and subsequent reaction with P$_4$.

Cyclic voltammetry of [Cp*Ru(C$_{10}$H$_8$)]PF$_6$ ([**XXI**]PF$_6$) in THF showed two overlapping reversible reductions. Chemical reduction of [**XXI**]PF$_6$ with a slight excess of KC$_8$ gave the dinuclear complex [Cp*Ru(μ-C$_{10}$H$_8$)RuCp*] (**2**; Scheme 7.2, left). Complex **2** is highly interesting as it represents an extension of the series of dinuclear naphthalene-bridged group 8 metal complexes and, at the same time, the series of diruthenium complexes with bridging polyarene ligands. NMR spectroscopy and X-ray crystallography revealed a symmetric molecular structure with two η^4-coordinated Ru(I) centers, akin to the related iron and iron-ruthenium complexes. Cyclic voltammetry showed that **2** can be reversibly oxidized, and chemical oxidation with [Cp$_2$Fe]BAr$^F{}_4$ (Scheme 7.2, top right) gave the monocation [**2**]BAr$^F{}_4$, which was characterized crystallographically, spectroscopically, and by computational methods. DFT calculations suggest that, in analogy to the related iron complexes, **2**$^+$ is a class III complex with full charge delocalization.

Reaction of **2** with Brookhart's acid, [H(OEt$_2$)$_2$]BAr$^F{}_4$ (Scheme 7.2, bottom right), gave the hydrido complex [**2-H**]BAr$^F{}_4$ ([Cp*Ru(μ-C$_{10}$H$_8$)Ru(H)Cp*]BAr$^F{}_4$). This metal-centered reactivity is notable since the Ru(II) precursor [**XXI**]PF$_6$ was reported to show ligand-centered reactivity towards protons upon reduction.[1] ^{1}H NMR monitoring revealed that the initially formed *exo*-isomer (Scheme 7.2, far right), which is assumed to be kinetically favoured, is converted into the thermodynamically more stable *endo*-isomer (Scheme 7.2) at room temperature. Cyclic voltammetry showed that, upon either reduction or oxidation, [**2-H**]BAr$^F{}_4$

reverts back to the neutral compound **2**. This observation suggests that **2** may be used as a catalyst for the electrocatalytic reduction of protons to generate H_2. Future research efforts should explore the feasibility of using **2** as an electrocatalyst.

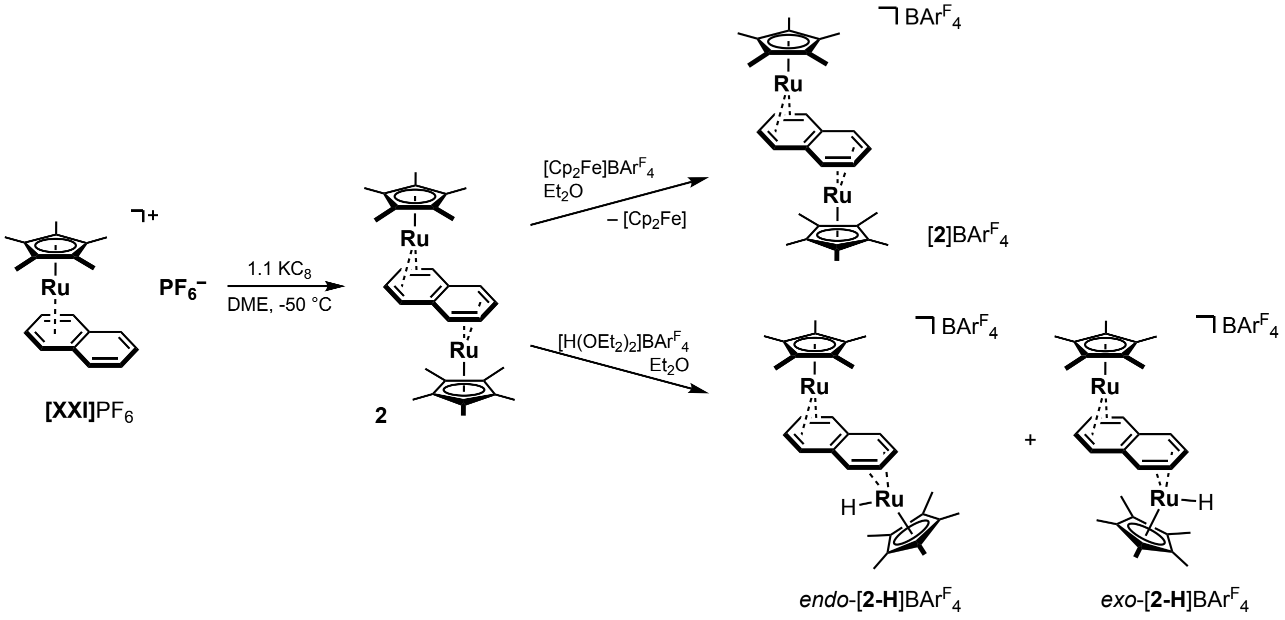

Scheme 7.2. Synthesis of [Cp*Ru(μ-$C_{10}H_8$)RuCp*] (**2**) from [Cp*Ru($C_{10}H_8$)]PF_6.

In the second part of this thesis, polyarene moieties were integrated into *N*-heterocyclic carbenes (NHCs) in order to obtain multidentate ligands with strongly binding σ-donating and labile π-accepting binding sites. Previous research by the groups of Glorius and Wolf as well as the group of Dorta had demonstrated the feasibility and the great potential of using naphthyl-NHCs as hemilabile chelating ligands (see section 1.3).[2] Several NHC precursors with different backbone structures, three different *N*-substitution patterns, and different counterions, were selected as viable candidates (Figure 7.1). Imidazolium salts **XXXIX** and **XLII** were prepared following literature methods; for **XL** and **XLI**, known procedures for similar

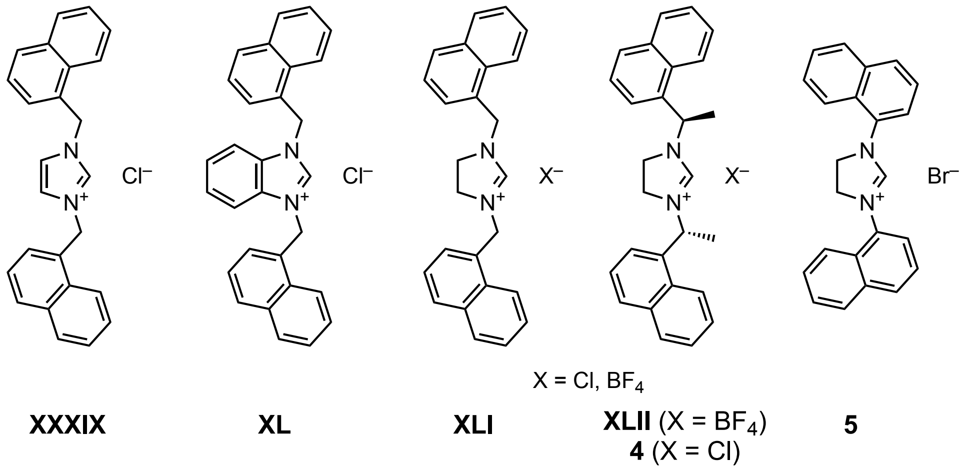

Figure 7.1. Precursor salts of *N*-heterocyclic carbenes with naphthyl substituents.

compounds and intermediates were adapted; for **4** and **5**, new synthetic procedures were developed that were loosely based on other azolium salt syntheses with substantial modifications (see section 4.2).

Since none of the selected NHCs can be isolated in their free form, the preparation of transition metal complexes stabilized by these ligands relied on two strategies: Reaction with a basic metal precursor and carbene transfer from a silver-carbene complex.

NHC-silver complexes **6**, **7**, and **8** were prepared by reaction of the respective azolium salt with Ag_2O (Scheme 7.3, left). While ^1H NMR monitoring indicated quantitative conversion of the NHC precursor, the isolated yields of **6**, **7**, and **8** were only moderate. X-ray crystallography revealed mononuclear, two-coordinate complexes with linear or slightly bent coordination of the silver center.

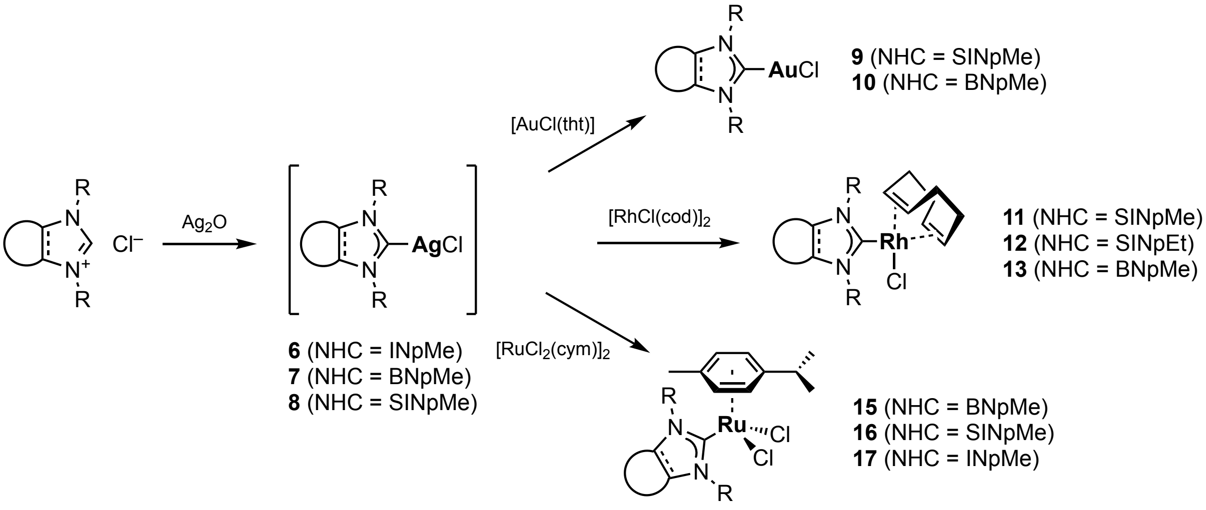

Scheme 7.3. Synthesis of NHC complexes of silver, gold, rhodium, and ruthenium.

The silver complexes were used to prepare complexes of gold, rhodium, and ruthenium (Scheme 7.3, right). While the isolated silver compounds were employed in initial tests, it was found that generating the NHC–Ag species *in situ* gave the same results and thus better overall yields as the poor-yielding isolation of the silver complexes was no longer necessary.

The solid-state molecular structure of the gold complex [(SINpMe)AuCl] (**9**) is analogous to that of **8**, with a linear coordination of the Au center. **9** was reacted with chloride abstraction agents $AgBF_4$ and $NaBAr^F{}_4$ with the goal of generating a cationic complex $[(NHC)Au]^+X^-$, possibly stabilized by chelation by one or both naphthyl substituents. While no reaction was observed with $AgBF_4$, the reaction with $NaBAr^F{}_4$ led to degradation, probably via cleavage of a C–B bond of the tetraarylborate, giving $[(SINpMe)Au(C_6H_3(CF_3)_2)]$ (observed via ^1H NMR spectroscopy) and, eventually, colloidal gold particles.

The rhodium complexes [(NHC)RhCl(cod)] (NHC = SINpMe (**11**), SINpEt (**12**), BNpMe (**13**)) were prepared via carbene transfer from silver. Remarkably, **12** could be obtained smoothly by reacting [SINpEtH]Cl (**4**) with Ag_2O and $[RhCl(cod)]_2$, even though the reaction of **4** and Ag_2O without $[(cod)RhCl]_2$ did not afford the corresponding silver complex [(SINpEt)AgCl]. A possible explanation is that several mono- and dinuclear silver-NHC complexes formed in the reaction of **4** and Ag_2O, which could not be separated, but all of these silver-NHC species acted as carbene transfer agents to rhodium.

In analogy to gold complex **9**, **11** and **13** were reacted with chloride scavengers $NaBAr^F{}_4$ and $AgBF_4$, respectively, in order to generate naphthyl-NHC chelate complexes (Scheme 7.4). The ^{1}H NMR spectra of the resulting mixtures each showed only one set of naphthyl signals which was only slightly shifted with respect to the spectra of **11** and **13**, which indicates that no naphthyl coordination occurred. No measurable crystals could be obtained, so that a definitive structural analysis was not possible.

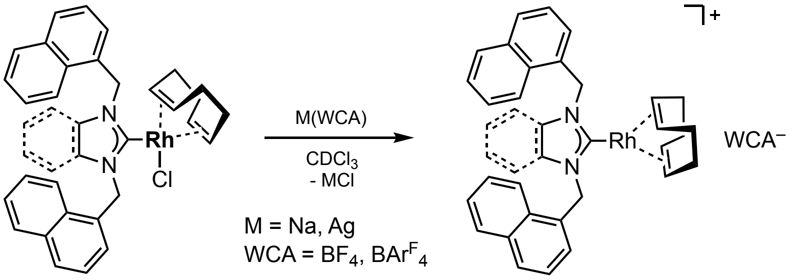

11 (NHC = SINpMe)
13 (NHC = BNpMe)

14a (WCA = $BAr^F{}_4$)
14b (WCA = BF_4)

Scheme 7.4. Chloride abstraction from **11** and **13** with $NaBAr^F{}_4$ and $AgBF_4$, respectively.

11, **12**, and **13** were used as catalysts in the hydrogenation of ketones and heterocyclic arenes in a collaboration with the group of Glorius at WWU Münster. GC analysis of the reaction mixtures showed that for each of the tested substrates, several products had formed in which either the carbonyl group, the arene, or both were hydrogenated. This lack of selectivity is indicative of a heterogeneous reaction pathway; the observation of a black precipitate after applying hydrogen pressure supports this hypothesis.

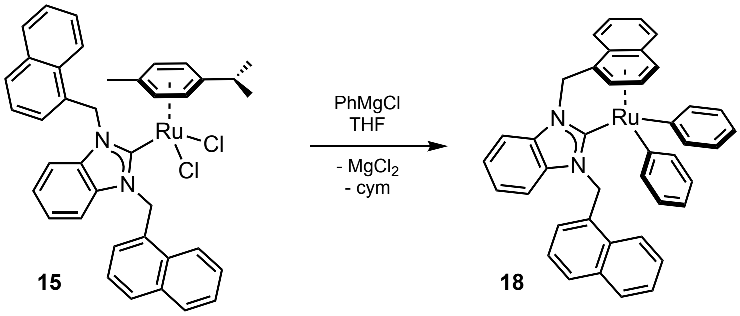

15

18

Scheme 7.5. Synthesis of chelate complex **18** from **15** and PhMgCl.

The ruthenium complexes $[(NHC)RuCl_2(cym)]$ (NHC = BNpMe (**15**), INpMe (**16**), and SINpMe (**17**)) were prepared via the silver route (Scheme 7.3, bottom right) and subsequently reacted with Grignard reagents to replace the chloride ligands by alkyl or aryl groups. Unexpectedly, the reaction of **15** with PhMgCl not only led to the replacement of the chlorides by phenyl groups, but to the dissociation of the cymene ligand and chelation by one of the naphthyl substituents of the carbene (Scheme 7.5). This chelate complex **18** is a rare example of chelation of a polyarene substituent of an NHC. Related complexes with phenyl substituents chelating to ruthenium are known from the work of Özdemir and Çetinkaya as well as Dyson.[3] However, the synthetic approaches reported by these researchers did not give the desired chelate complexes with the ligands used in this project. The reactions with other Grignard reagents only gave mixtures of different products, none of which could be isolated. Complexes **15** and **18** were tested as catalysts in the hydrosilylation of 1-hexene, but no conversion was observed.

Iron- and cobalt-NHC complexes were prepared from basic metal precursors. Initial reactions of the NHC precursor salts with $[\mathrm{Fe\{N(SiMe_3)_2\}_2}]$ and $[\mathrm{Co\{N(SiMe_3)_2\}_2}]$ gave mixtures of mono- and dinuclear complexes **21-24**, which were identified by X-ray crystallography, but could not be isolated as pure compounds. In order to obtain diamide complexes amide complexes $[\mathrm{(NHC)M\{N(SiMe_3)_2\}_2}]$, a modified synthesis was developed (Scheme 7.6): By adding one equivalent of $\mathrm{M^I[N(SiMe_3)_2]}$ ($\mathrm{M^I}$ = Li, Na) to $[\mathrm{M\{N(SiMe_3)_2\}_2}]$ (M = Fe, Co), the tris(amido)metalate $\mathrm{M^I[M\{N(SiMe_3)_2\}_3]}$ was generated and subsequently reacted *in situ* with the respective azolium salt. The reactions proceeded smoothly and within minutes at room temperature and allowed us to isolate amide complexes **21** and **25-32** with straightforward work-up. Similarly, reacting $[\mathrm{M\{N(SiMe_3)_2\}_2}]$ with an equimolar amount of $\mathrm{MX_2}$ (X = Cl, Br) gave an intermediate species of the general formula “$[\mathrm{MX\{N(SiMe_3)_2\}}]$”. Addition of an azolium salt gave the halide complexes $[\mathrm{(NHC)MX_2}]_2$ (Scheme 7.7). The work-up of the halide complexes proved challenging since the compounds tend to dismutate into $[\mathrm{(NHC)_2MX_2}]$ and $[\mathrm{MX_2(thf)_{1.5}}]$ upon standing in THF solution.

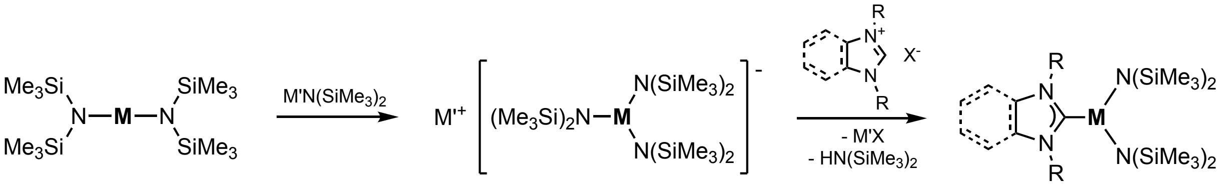

M = Fe, Co
M' = Li, Na
X = Cl, Br
R = Np, $\mathrm{CH_2Np}$, CH(Me)Np

25 $[\mathrm{(SINp)Fe\{N(SiMe_3)_2\}_2}]$
26 $[\mathrm{(BNpMe)Fe\{N(SiMe_3)_2\}_2}]$
27 $[\mathrm{(SINpMe)Fe\{N(SiMe_3)_2\}_2}]$
28 $[\mathrm{(SINpEt)Fe\{N(SiMe_3)_2\}_2}]$

21 $[\mathrm{(SINp)Co\{N(SiMe_3)_2\}_2}]$
29 $[\mathrm{(INpMe)Co\{N(SiMe_3)_2\}_2}]$
30 $[\mathrm{(BNpMe)Co\{N(SiMe_3)_2\}_2}]$
31 $[\mathrm{(SINpMe)Co\{N(SiMe_3)_2\}_2}]$
32 $[\mathrm{(SINpEt)Co\{N(SiMe_3)_2\}_2}]$

Scheme 7.6. Synthesis of silylamide NHC complexes of iron and cobalt.

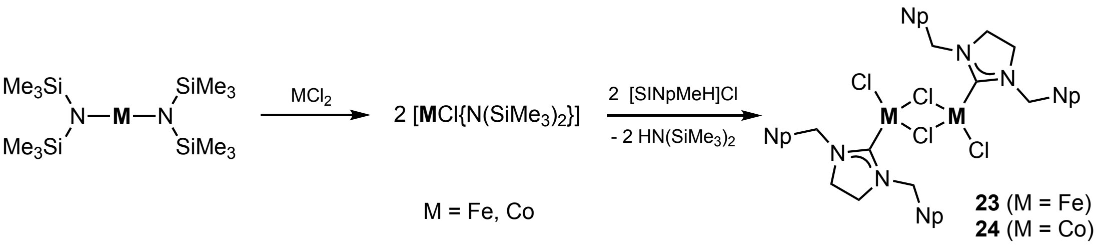

Scheme 7.7. Synthesis of iron- and cobalt-NHC halide complexes.

Both silylamide and halide complexes of iron and cobalt were reported to be highly attractive compounds due to their catalytic activity, the facile ligand exchange and consequently their utility as organometallic building blocks, and because of their interesting magnetic properties. In a cooperation with the group of Sven Schneider at the University of Göttingen, the magnetism of the [(NHC)Co{N(SiMe$_3$)$_2$}$_2$] complexes **21** and **30** was investigated. The magnetic measurements showed that these complexes feature a negative zero-field splitting of $D = –87.4$ cm^{-1} for **21** and –95.2 cm^{-1} for **30** and substantial energy barriers $U_{eff} = 9.8$ cm^{-1} for **21** and 16.9 cm^{-1} for **30** with relaxation times $\tau_0 = 4.29\cdot10^{-6}$ s (**21**) and $1.74\cdot10^{-6}$ s (**30**).

The application of [(NHC)Fe{N(SiMe$_3$)$_2$}$_2$] in catalytic hydrogenations was tested in cooperation with the group of Axel Jacobi von Wangelin at the University of Regensburg (now University of Hamburg). The results showed a performance identical to that of the carbene-free precursor [Fe{N(SiMe$_3$)$_2$}$_2$] and no asymmetric induction from the chiral carbene SINpEt.

Co and Fe amide complexes were reacted with different reducing agents, but no low-valent products could be identified. The reactions of [(SINp)Fe{N(SiMe$_3$)$_2$}$_2$] (**25**) with KC$_8$ gave iron-free NHC degradation products (Figure 7.2). **33** was formed by cleavage of a C–N bond and insertion of triethylborane. In dimeric **34**, Fe is replaced by triethylboarne and one naphthylmethyl group of each carbene is lost; the resulting imidazolates are bound to two bridging Li(thf) fragments. The reaction of the chloride complex **24** with KC$_8$ (Scheme 7.8) gave the trichlorocobaltate(II) complex **35**; no low-valent transition metal products were identified.

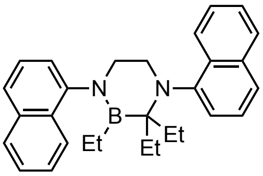

33

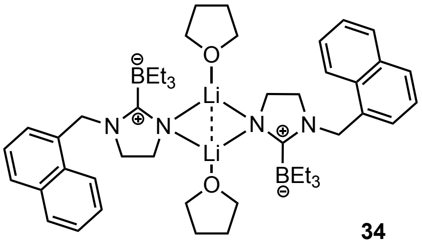

34

Figure 7.2. Ring-expansion product **33** and borane-imidazolate **34** obtained from the reaction of **25** with KC$_8$.

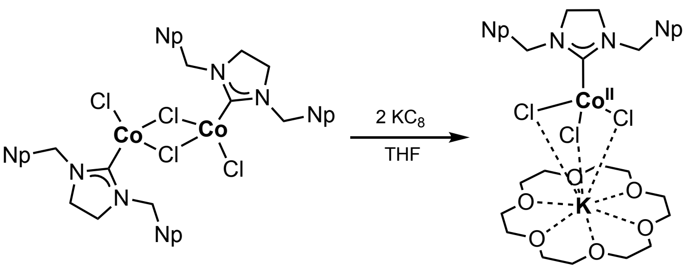

24 **35**

Scheme 7.8. Formation of trichlorocobaltate **35** from **24** by reaction with KC_8.

Many of the challenges of preparing naphthyl-substituted NHC precursors and the respective transition metal complexes were mastered, and robust synthetic procedures were developed for the compounds reported here. The recent literature on NHC complexes gives evidence of the great relevance of transition metal complexes of the types reported here in diverse fields ranging from catalysis and materials research to medical applications. The follow-up chemistry of the reported compounds, however, leaves room for further investigations. There are several avenues of future research that could elucidate the reactivity and properties of the reported compounds and the general concept of chelate complexes with NHC and polyarene binding sites.

The used NHC precursor compounds can be modified; this may lead to isolable NHCs, which would greatly simplify the subsequent synthesis of metal complexes. Some examples are given in Figure 7.3.

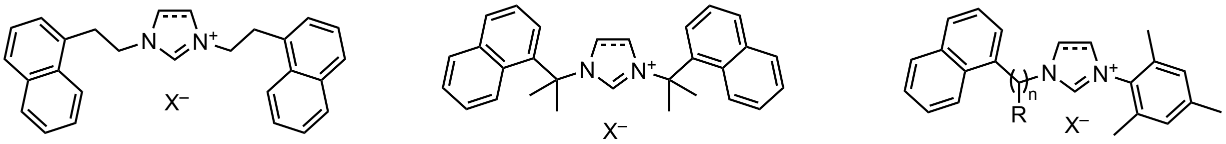

Figure 7.3. Suggested NHC precursors featuring naphthyl moieties.

Finding a suitable chloride scavenger for the NHC-gold complexes **9** and **10** (see section 5.2) might enable the isolation of cationic species; chelation by one or both naphthyl substituents may stabilize the electrophilic Au(I) center. The cationic rhodium complexes obtained by chloride abstraction (see section 5.3) should be characterized in more detail by mass spectrometry and X-ray crystallography; using different chloride scavengers might help in obtaining a crystalline material. The reactivity of the ruthenium chloride complexes towards Grignard reagents should be investigated in order to identify and isolate the formed products. Using organolithium reagents may be an alternative to Grignard reagents. The chelate compound **18** is likely to show some interesting follow-up chemistry, as the chelating naphthyl group should be easily displaced by other ligands.

The iron and cobalt complexes offer several interesting aspects. Cyclic voltammetry indicated that chemical reduction should be feasible, and the variation of reducing agents, solvent, and reaction temperature are just some of the factors that might lead to success here. Reaction of the halide complexes with halide abstractors such as $NaBAr^F_4$ may give interesting and highly reactive low-coordinate complexes. The silylamide ligands were reported to be easily replaced by other less basic ligands in what is basically an acid-base reaction.[4] Reaction with bulky, acidic compounds such as Brookhart's acid, $[H(OEt_2)_2]BAr^F_4$, may therefore be a way to remove an amide without replacing it by another ligand, giving rise to a low-coordinate complex or chelation by a naphthyl group from the NHC ligand. Subsequent chemical reduction should enable the isolation of low-valent iron and cobalt compounds.

References

[1] O. G. Gusev, M. A. Ievlev, M. G. Peterleitner, S. M. Peregudova, L. I. Denisovich, P. V. Petrovskii, N. A. Ustynyuk, *J. Organomet. Chem.* **1997**, *534*, 57-66.

[2] See references 22, 23 in chapter 1.

[3] a) S. Demir, I. Özdemir, B. Çetinkaya, *J. Organomet. Chem.* **2009**, *694*, 4025-4031; b) T. J. Geldbach, G. Laurenczy, R. Scopelliti, P. J. Dyson, *Organometallics* **2006**, *25*, 733-742.

[4] a) A. Massard, P. Braunstein, A. A. Danopoulos, S. Choua, P. Rabu, *Organometallics* **2015**, *34*, 2429-2438; b) C. B. Hansen, R. F. Jordan, G. L. Hillhouse, *Inorg. Chem.* **2015**, *54*, 4603-4610.

8. Experimental Section

8.1 General Remarks

Unless stated otherwise, all reactions were performed under an inert atmosphere of purified argon (Argon 4.6, trace oxygen removed by a BTS catalyst, trace moisture removed by P_2O_5) using standard Schlenk techniques or in a MBraun UniLab glovebox filled with an atmosphere of purified argon.

Solvents were dried using the following procedures: *n*-Hexane, diethyl ether, toluene, and dichloromethane were dried in a MBraun SPS800 solvent purification system and stored over potassium mirror (*n*-hexane) or molecular sieve (diethyl ether, toluene, dichloromethane). *n*-Pentane was distilled over sodium and stored over a potassium mirror. Tetrahydrofuran and 1,2-dimethoxyethane were distilled over sodium/benzophenone and stored over molecular sieve. Acetonitrile was distilled over calcium hydride and stored over molecular sieve. Deuterated solvents were dried by stirring with sodium or potassium (THF-d_8, C_6D_6) or molecular sieve ($CDCl_3$, CD_2Cl_2).

NMR spectra were recorded on Bruker Avance 300 and Avance 400 spectrometers and referenced internally to residual solvent signals (^{1}H, ^{13}C) or externally (^{31}P with H_3PO_4, ^{19}F with CF_3SO_2H). Unless noted otherwise, the spectra were recorded at 300 K.

Elemental analyses were determined with Vario ELIII CHNS and Elementar Micro Vario Cube instruments.

Cyclic voltammetry measurements were performed using Metrohm Autolab PGSTAT 101, Metrohm Autolab 302N and CH Instruments CHI 600c potentiostats using a Pt disk working electrode which was polished with a 25 µm diamond paste and 5 µm corundum paste, a Pt wire counter electrode, and Ag wire pseudoreference electrode. The supporting electrolyte, tetrabutylammonium hexafluorophosphate, was dried *in vacuo* at 100 °C overnight and stored in a glove-box under an Ar atmosphere. The voltammograms were referenced against the ferrocenium/ferrocene redox couple by adding ferrocene to the analyte solution or, for substances that showed redox waves overlapping with ferrocene, by adding decamethylferrocene or cobaltocene and subtracting a correction value of $\Delta E = 480$ mV (Cp^*_2Fe) or 1350 mV (Cp_2Co), respectively.

UV-vis spectroelectrochemistry measurements were performed using an OTTLE cell with a Pt grid as the working electrode, Pt wire counter electrode, and Ag wire pseudoreference electrode. UV-vis spectra were recorded during the electrolysis with an Ocean Optics Flame-S spectrometer equipped with a deuterium/tungsten-halogen light source, the sample holder being located inside a glove-box under a nitrogen atmosphere. Conventional UV-vis spectra were recorded on this instrument or on a Cary 50 spectrometer.

X-ray diffraction experiments were performed on a Rigaku Oxford Diffraction SuperNova or a Rigaku Oxford Diffraction Gemini R Ultra Diffractometer. Either semiempirical multiscan absorption correction[1] or analytical corrections[2] were applied to the data. The structures were solved with SHELXT[3] and least-squares refinements on F^2 were carried out with SHELXL.[4]

Density functional theory. The calculations were performed by Christian Rödl, M.Sc., University of Regensburg, using the Gaussian09 program package (Revision E.01).[5] The BP86 density functional and the Ahlrichs def2-TZVP basis set were employed for all atoms.[6,7] Atom-pairwise dispersion correction to the DFT energy with Becke-Johnson damping (d3bj) were applied.[8] The nature of stationary point was verified by a numerical frequency analysis. The calculation of UV-vis spectra was performed with the B3LYP hybrid functional,[9] and the TZVP basis set for all atoms. Tetrahydrofuran solvent effects were implied using the self-consistent reaction field (SCRF), as implemented in Gaussian.[10] Molecular orbitals and spin density plots were visualized with GaussView5.[11] The isosurface value is set to 0.05 for all figures.

EPR spectra were recorded by Prof. Dr. Bas de Bruin, University of Amsterdam, Van't Hoff Institute for Molecular Sciences, and details are given in section 3.5.2.

CHN analyses were performed by the analytics department of the Faculty of Chemistry and Pharmacy at the University of Regensburg, using an Elementar Micro Vario Cube. Samples of air-sensitive compounds were sealed in tin ampoules under an argon atmosphere prior to analysis.

8.2 Synthesis of Starting Materials

8.2.1 Synthesis of Potassium Graphite, KC_8

$$\mathrm{K} + 8\,\mathrm{C} \xrightarrow{\Delta} \mathrm{KC_8}$$

Potassium (1.000 g, 25.58 mmol) was cut into small chunks and added to a Schlenk flask containing graphite powder (2.458 g, 204.64 mmol). The flask was evacuated and heated to 160 °C in an oil bath until a homogeneous, bronze-colored powder had formed.

Yield: 3.390 g (98%).

8.2.2 Synthesis of Potassium Bis(trimethylsilyl)amide, K[N(SiMe$_3$)$_2$]

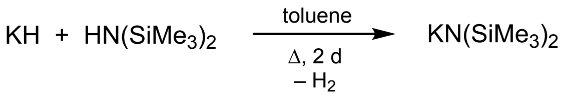

$$KH + HN(SiMe_3)_2 \xrightarrow[\Delta,\ 2\ d \\ -\ H_2]{toluene} KN(SiMe_3)_2$$

Potassium hydride (4.011 g, 100.0 mmol) was added to a three-neck round-bottomed flask and toluene (100 mL) was added via a dropping funnel. A solution of bis(trimethylsilyl)amine (23.0 mL, 110 mmol, 1.10 equiv.) in toluene (75 mL) was subsequently added to the KH suspension. Following the addition, the mixture was heated to reflux for two days. After filtering the resulting gray suspension and washing with toluene (3x20 mL), all volatile components of the filtrate were removed *in vacuo*, yielding the product as a colorless solid.

Yield: 18.934 g (95%).

^{1}H NMR (300.13 MHz, 300 K, C_6D_6): δ (ppm) = 0.14 (s, Si(CH_3)$_3$).

8.2.3 Synthesis of Sodium Tetrakis(3,5-bis(trifluoromethyl)phenyl)borate, NaBAr$^F_4$

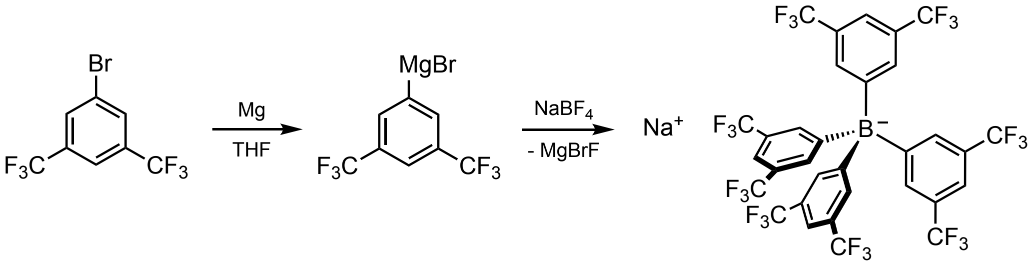

Magnesium turnings (10.02 g, 412 mmol, 6.9 equiv.) were placed in a round-bottom Schlenk flask and suspended in THF (100 mL). A solution of 2-chloropropane (35.5 mL, 338 mmol, 5.6 equiv.) in THF (50 mL) was added dropwise and the mixture was heated to reflux for one hour following completion of the addition. Subsequently, a mixture of 1-bromo-3,5-bis(trifluoromethyl)benzene (102.83 g, 473 mmol, 7.9 equiv.) and THF (50 mL) was added dropwise at such a rate that the reaction mixture remained at reflux. After the addition was completed, the mixture was refluxed for another hour.

After cooling to room temperature, $NaBF_4$ (6.596 g, 60.00 mmol, 1.0 equiv.) was added and the mixture was stirred at room temperature for 48 hours. The resulting suspension was poured into an aqueous solution of $NaHCO_3$ (60 g) and Na_2CO_3 (66 g), leading to the formation of a colorless precipitate. The mixture was extracted with diethyl ether (5x200 mL) and the combined organic phases were dried over Na_2SO_4 and filtered. The filtrate was concentrated to dryness, yielding a colorless solid. The crude product was dissolved in CH_2Cl_2. After filtration, the solvent was removed *in vacuo* and the product was dried overnight.

Yield: 30.014 g (33.868 mmol, 56%).

^{1}H NMR (400.13 MHz, 300 K, $CDCl_3$): δ (ppm) = 7.52 (s, 4H), 7.68 (s, 8H).

8.2.4 Synthesis of Brookhart's Acid, $[H(OEt_2)_2]BAr^F_4$

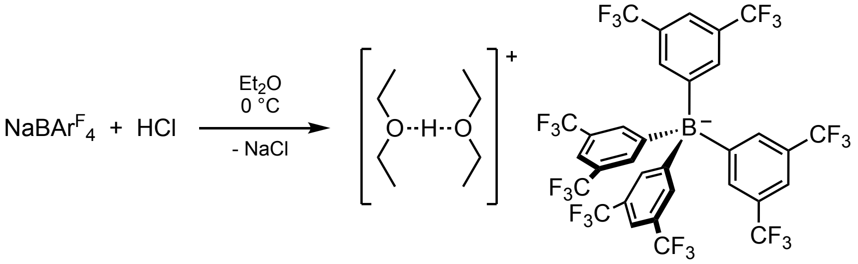

Brookhart's acid was prepared following a modified procedure by Volpe, Grant, and Brookhart. It is important to note that $[H(OEt_2)_2]BAr^F{}_4$ slowly decomposes in solution at room temperature and therefore must be handled and stored below 0 °C.

HCl in diethyl ether (c = 1.96 mol L^{-1}, 3.5 mL, 6.86 mmol, 2.0 equiv.) was added to a solution of $NaBAr^F{}_4$ (2.98 g, 3.36 mmol, 1.0 equiv.) in diethyl ether (100 mL) at 0 °C. The formed suspension was stirred for 15 minutes and filtered. The solid residue was washed with diethyl ether (3x20 mL) and, after adding the extract to the filtrate, the solution was concentrated *in vacuo* to 10 mL under cooling in an ice bath, layered with 20 mL of *n*-pentane and stored at –25 °C overnight, during which time the product precipitated. The suspension was filtered at 0 °C and the remaining solid washed with cold *n*-pentane and dried *in vacuo*.

Yield: 3.06 g (3.02 mmol, 90%).

^1H NMR (400.13 MHz, 300 K, CD_2Cl_2): δ (ppm) = 1.37 (t, $^3J_{HH}$ = 7 Hz, 12H, CH_3), 3.97 (q, $^3J_{HH}$ = 7 Hz, 8H, $–CH_2–$), 7.57 (s, 4H, *para-H*$_{Ar}$), 7.72 (t, $^3J_{BH}$ = 2 Hz, 8H, *ortho-H*$_{Ar}$), 13-18 (br, 1H, H^+).

8.2.5 Synthesis of 1,2,3,4,5-Pentamethylcyclopentadiene (Cp*H)

1,2,3,4,5-Pentamethylcyclopentadiene was prepared following a procedure by Bergman et. al.[12]

a) Synthesis of 3,4,5-Trimethylhepta-2,5-dien-4-ol

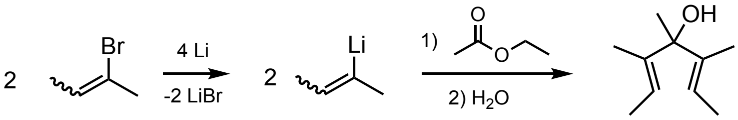

In a 2 L three-neck round-bottomed flask equipped with a dropping funnel and a reflux condenser, lithium granules (14.94 g (2.153 mol, 4.05 equiv.) were suspended in diethyl ether (75 mL). 2-Bromo-2-butene (108.0 mL, 1.062 mol, 2.00 equiv.) was transferred into a dropping funnel and 3 mL were added to the reaction flask to activate the lithium granules. The mixture was diluted by adding diethyl ether (500 mL) and the remaining 2-bromo-2-butene was added dropwise at a rate such that the mixture remained at reflux. Following the addition, the mixture was stirred for one hour at room temperature. Subsequently, freshly distilled ethyl acetate

(53.0 mL, 0.537 mol, 1.01 equiv.) was added dropwise, yielding a yellowish suspension. After stirring for one hour at room temperature, the mixture was carefully poured into a 5L round-bottomed flask containing 1.5 L of a saturated aqueous NH_4Cl solution. The phases were separated and the aqueous phase was brought to a pH of 9 with diluted HCl. The aqueous phase was extracted with 3x100 mL of diethyl ether and the combined organic phases were dried over $MgSO_4$, filtered, and concentrated to about 100 mL.

b) Synthesis of 1,2,3,4,5-Pentamethylcyclopentadiene

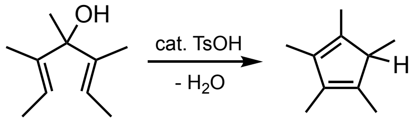

In a three-neck round-bottomed flask equipped with a dropping funnel and a reflux condenser, *p*-toluenesulfonic acid-monohydrate (9.250 g, 48.63 mmol, 0.09 equiv.) was suspended in diethyl ether (150 mL). The concentrate from step a) was added dropwise at a rate such that the mixture remained at reflux. After stirring for one hour, 200 mL of a saturated aqueous $NaHCO_3$ solution was added and the phases were separated. The organic phase was washed with 50 mL of the $NaHCO_3$ solution. The combined aqueous phases were subsequently extracted with diethyl ether (3x100 mL). The combined organic phases were then dried over $MgSO_4$, filtered, and the solvent removed *in vacuo*. The resulting orange oil was distilled under reduced pressure (10^{-1} mbar, 55-65 °C) to yield the product as a light yellow oil.

Yield: 51.35 g (376.9 mmol, 71%).

^{1}H NMR (300.13 MHz, 300 K, $CDCl_3$): δ (ppm) = 1.01 (d, $^3J_{HH}$ = 7.6 Hz, 3H), 1.80 (d, $^4J_{HH}$ = 18.2 Hz, 12H), 2.50 (m, 1H).

8.2.6 Synthesis of 1,3-Bis(1-naphthylmethyl)imidazolium Chloride, [INpMeH]Cl (XXXIX)

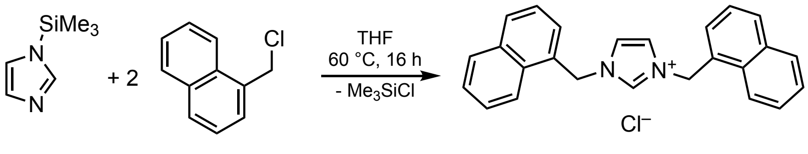

XXXIX

XXXIX was synthesized following a procedure by Dyson and co-workers.[13]

1-(Chloromethyl)naphthalene (31.4 mL, 210 mmol) and *N*-trimethylsilylimidazole (14.7 mL, 100 mmol) were dissolved in dry THF (50 mL) and stirred at 60 °C overnight. A voluminous, colorless solid formed, which was isolated by filtration, washed with diethyl ether (100 mL), and dried *in vacuo*. The crude product was dissolved in hot CH_2Cl_2 (600 mL), cooled in an ice bath and precipitated by adding diethyl ether (600 mL). After storage at –30 °C overnight, the mixture was filtered, washed with diethyl ether (400 mL), and dried *in vacuo*, yielding a colorless powder.

Yield: 25.0 g (65.0 mmol, 65%).

^{1}H NMR (300.13 MHz, 300 K, CDCl$_3$): δ (ppm) = 6.03 (s, 4H, NCH_2Np), 6.89 (d, J_{HH} = 1.6 Hz, 2H, NCHCHN), 7.41-7.61 (m, 8H, CH_{naph}), 7.85-7.93 (m, 4H, CH_{naph}), 8.05 (d, J_{HH} = 8.3 Hz, 2H, CH_{naph}), 11.47 (s, 1H, NCHN).

8.2.7 Synthesis of 1,3-Bis(1-naphthylmethyl)benzimidazolium Chloride, [BNpMeH]Cl (XL)

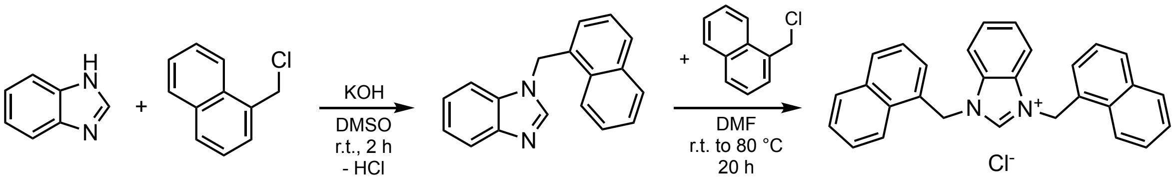

XL

XL was prepared following modified procedures reported by Komarova and co-workers (a) and Gök and co-workers (b).[14]

a) Synthesis of 1-(1-Naphthylmethyl)benzimidazole

Benzimidazole (1.181 g, 10.00 mmol) was dissolved in dimethylsulfoxide (20 mL) and KOH (0.842 g, 15.00 mmol) was added. After stirring at room temperature for 30 minutes, 1-(chloromethyl)naphthalene (1.766 g, 10.00 mmol) was added and the mixture was stirred for another two hours. The resulting mixture was then poured into water (200 mL). The cloudy suspension was extracted with chloroform (6x25 mL). The chloroform phases were combined and dried with magnesium sulfate. After filtration and removal of the solvent *in vacuo*, the crude product was purified by column chromatography over silica gel using dichloromethane / methanol (20:1) as the eluent.

Yield: 2.352 g (9.110 mmol, 91%).

^{1}H NMR (300.13 MHz, 300 K, CDCl$_3$): δ (ppm) = 5.70 (s, 2H, NCH_2Np), 7.02 (dd, J_{HH} = 7.1 Hz, 1.1 Hz, 1H), 7.22-7.36 (m, 4H, CH_{Ar}), 7.51 (m, 2H, CH_{naph}), 7.80-7.91 (m, 5H, CH_{naph} and NCHN).

b) Synthesis of 1,3-Bis(1-naphthylmethyl)benzimidazolium Chloride (XL)

1-(1-Naphthylmethyl)benzimidazole (2.352 g, 9.110 mmol) and 1-(chloromethyl)naphthalene (1.609 g, 9.110 mmol) were dissolved in *N*,*N*-dimethylformamide (5 mL) and stirred at room temperature for four hours and subsequently at 80 °C overnight, whereupon a voluminous, colorless precipitate formed. The product was precipitated quantitatively by adding diethyl ether (10 mL). The product was isolated by filtration, washed with diethyl ether (20 mL), and dried *in vacuo*.

Yield: 3.408 g (7.835 mmol, 86%).

^{1}H NMR (300.13 MHz, 300 K, CDCl$_3$): δ (ppm) = 6.38 (s, 4H, NCH_2Np), 7.41 (m, 8H, CH_{Ar} and CH_{naph}), 7.53 (m, 2H, CH_{naph}), 7.61 (m, 2H, CH_{naph}), 7.87 (m, 4H, CH_{naph}), 8.21 (d, J_{HH} = 8.3 Hz, 2H, CH_{naph}), 12.24 (s, 1H, NCHN).

8.2.8 Synthesis of 4,5-Dihydro-1,3-bis(1-naphthylmethyl)imidazolium Chloride, [SINpMeH]Cl (XLI), and Tetrafluoroborate, [SINpMeH]BF$_4$ (XLI')

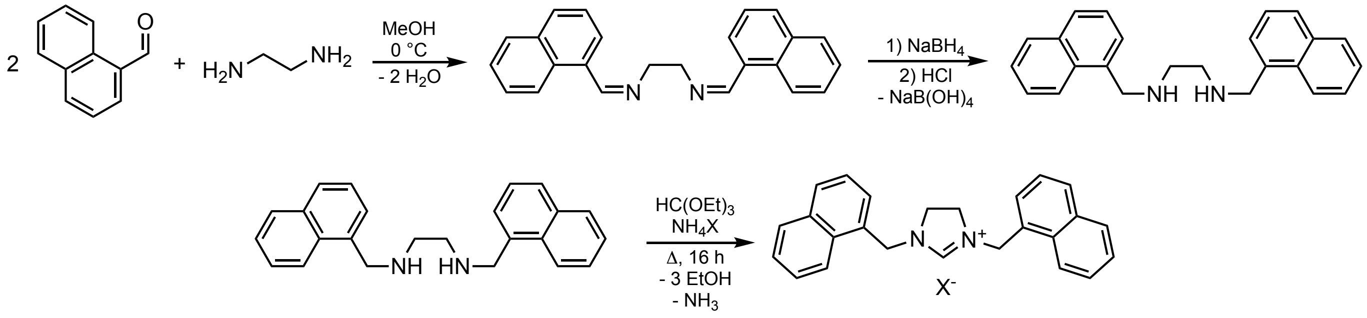

XLI (X = Cl)
XLI' (X = BF$_4$)

XLI was synthesized following a procedure by Özdemir and co-workers.[15]

a) Synthesis of N,N'-4-Bis(1-naphthylmethyl) Ethylenediamine

1-Naphthaldehyde (24.968 g, 159.87 mmol, 2.0 equiv.) was dissolved in methanol (120 mL) and cooled in an ice bath. Ethylenediamine (5.338 mL, 79.93 mmol, 1.0 equiv.) was added via an Eppendorf pipette. After stirring for two minutes, a colorless solid precipitated. The reaction was completed by stirring at room temperature for two hours. Subsequently, sodium borohydride (9.0716 g, 239.8 mmol, 3.0 equiv.) was carefully added in small portions to the suspension of the diimine, leading to a substantial gas evolution and the formation of a clear, pale yellow solution. After stirring for one hour at room temperature, excess sodium borohydride was quenched by adding HCl (3 mol L^{-1}, 15 mL). The mixture was neutralized by adding Na$_2$CO$_3$ in small portions until gas evolution ceased, yielding a colorless precipitate and a pale yellow solution. The mixture was extracted with CH$_2$Cl$_2$ (3x150 mL). The combined organic phases were dried over MgSO$_4$. After filtration and removal of all volatiles *in vacuo*, the disubstituted diamine was obtained as a yellowish oil which solidified overnight. The product was washed with *n*-hexane and dried *in vacuo*.

Yield: 20.862 g (61.274 mmol, 77%).

b) Synthesis of 4,5-Dihydro-1,3-bis(1-naphthylmethyl)imidazolium Chloride (**XLI**)

Triethyl orthoformate (70 mL, 421 mmol, 6.9 equiv.) and finely powdered ammonium chloride (3.2776 g, 61.274 mmol, 1.0 equiv.) were added to the solid bis(1-naphthylmethyl)ethylenediamine. The mixture was stirred at room temperature for two hours and refluxed overnight. All volatiles were removed *in vacuo*, yielding a light brown solid, which was purified by dissolving in hot ethanol, cooling in an ice bath and precipitating with diethyl ether. The obtained off-white solid was isolated by filtration, washed with diethyl ether, and dried *in vacuo*.

Yield: 19.903 g (51.440 mmol, 84%).

^{1}H NMR (300 K, 300.13 MHz, $CDCl_3$): δ (ppm) = 3.59 (s, 4H, NCH_2CH_2N), 5.36 (s, 4H, NCH_2Np), 7.40 (dd, J = 7.1 Hz, 8.1 Hz, 2H, CH_{naph}), 7.49-7.54 (m, 4H, CH_{naph}), 7.59-7.65 (m, 2H, CH_{naph}), 7.84 (m, 4H, CH_{naph}), 8.18 (d, J = 8.4 Hz, 2H, CH_{naph}), 11.10 (s, 1H, NC*H*N).

$^{13}C\{^1H\}$ NMR (300 K, 75.47 MHz, $CDCl_3$): δ (ppm) = 47.6 (NCH_2CH_2N), 50.1 (NCH_2Np), 122.9 (CH_{naph}), 125.3 (CH_{naph}), 126.5 (aryl-*C*H), 127.7 (CH_{naph}), 127.9 ($C_{quart,\ naph}$), 128.6 (CH_{naph}), 129.0 (CH_{naph}), 130.2 (CH_{naph}), 131.2 ($C_{quart,\ naph}$), 133.9 ($C_{quart,\ naph}$), 159.2 (N*C*HN).

c) Synthesis of 4,5-Dihydro-1,3-bis(1-naphthylmethyl)imidazolium Tetrafluoroborate (**XLI'**)

Triethyl orthoformate (14 mL, 10 equiv.) and ammonium tetrafluoroborate (0.8837 g, 8.430 mmol, 1.0 equiv.) were added to the solid bis(1-naphthylmethyl)ethylenediamine (2.870 g, 8.430 mmol, 1.0 equiv.). The mixture was stirred at 120 °C overnight. All volatiles were removed *in vacuo*. After washing with *n*-hexane and diethyl ether, the product was dissolved in hot ethanol and precipitated by layering with diethyl ether.

Yield: 3.294 g (7.516 mmol, 89%).

^{1}H NMR (300 K, 300.13 MHz, $CDCl_3$): δ (ppm) = 3.59 (s, 4H, NCH_2CH_2N), 5.36 (s, 4H, NCH_2Np), 7.40 (dd, J = 7.1 Hz, 8.1 Hz, 2H, CH_{naph}), 7.49-7.54 (m, 4H, CH_{naph}), 7.59-7.65 (m, 2H, CH_{naph}), 7.84 (m, 4H, CH_{naph}), 8.18 (d, J = 8.4 Hz, 2H, CH_{naph}), 11.10 (s, 1H, NC*H*N).

$^{13}C\{^1H\}$ NMR (300 K, 75.47 MHz, $CDCl_3$): δ (ppm) = 47.6 (NCH_2CH_2N), 50.1 (NCH_2Np), 122.9 (CH_{naph}), 125.3 (CH_{naph}), 126.5 (CH_{naph}), 127.7 (CH_{naph}), 127.9 ($C_{quart,\ naph}$), 128.6 (CH_{naph}), 129.0 (CH_{naph}), 130.2 (CH_{naph}), 131.2 ($C_{quart,\ naph}$), 133.9 ($C_{quart,\ naph}$), 159.2 (N*C*HN).

8.2.9 Synthesis of (*R*,*R*)-4,5-Dihydro-1,3-bis((1-naphthyl)ethyl)imidazolium Tetrafluoroborate, [SINpEtH]BF_4 (XLII)

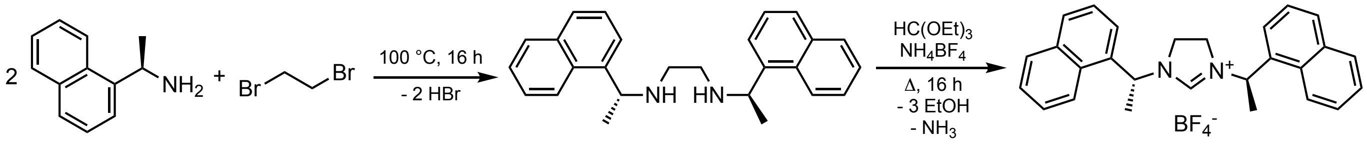

XLII

The reaction was performed following a procedure by Glorius and co-workers.[16]

a) Synthesis of (R,R)-N,N'-Bis(1-(1-naphthyl)ethyl)ethylenediamine

(*R*)-1-(1-Naphthyl)ethylamine (2.9261 g, 17.091 mmol, 2.0 equiv.) and 1,2-dibromoethane (1.6054 g, 8.5457 mmol, 1.0 equiv.) were added to a round-bottom flask and heated to 100 °C overnight (the mixture was stirred until a glassy solid formed after 20 minutes of heating). After cooling to room temperature, the solid was dissolved in NaOH (1 mol L^{-1}, 25 mL) and CH_2Cl_2 (25 mL). The pH was adjusted to 13 with NaOH (1 mol L^{-1}) and the phases were separated. The aqueous phase was extracted with CH_2Cl_2 (2x10 mL). The combined organic phases were dried with Na_2SO_4, filtered, and the solvent removed by rotary evaporation, yielding an orange-red oil.

b) Synthesis of R,R-4,5-Dihydro-1,3-bis(-1-(1-naphthyl)ethyl)imidazolium Tetrafluoroborate (**XLII**)

The crude diamine (a) (3.0887 g, 8.3816 mmol, 1.0 equiv.) was mixed with triethyl orthoformate (1.394 mL, 8.382 mmol, 1.0 equiv.) and finely ground ammonium tetrafluoroborate (0.8787 g, 8.382 mmol, 1.0 equiv.). The mixture was stirred at 120 °C overnight in an open flask to allow the evaporation of ethanol and ammonia formed in the reaction. After removal of all volatile components *in vacuo*, the crude product was dissolved in hot ethanol and precipitated by adding diethyl ether after cooling. After storage at 4 °C overnight, the precipitate was isolated by filtration and washed with diethyl ether.

Yield: 1.8435 g (47%).

^{1}H NMR (300.13 MHz, 300 K, $CDCl_3$): δ (ppm) = 1.94 (d, $^3J_{HH}$ = 6.8 Hz, 6H, Np-CH(CH_3)N), 3.49-3.79 (m, 4H, NCH_2CH_2N), 5.83 (q, $^3J_{HH}$ = 6.8 Hz, 2H, Np-C*H*(CH_3)N), 7.43-7.50 (m, 4H), 7.52-7.64 (m, 4H), 7.82-7.93 (m, 4H), 7.82-7.92 (m, 4H), 8.02 (d, J = 8.4 Hz, 2H), 8.62 (s, 1H, NC*H*N).

8.2.10 Synthesis of Ferrocenium Tetrakis(3,5-bis(trifluoromethyl)phenyl)borate, $[Cp_2Fe]BAr^F_4$

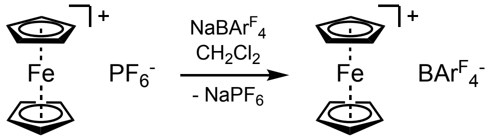

The synthesis of $[Cp_2Fe]BAr^F_4$ followed a procedure reported by Manríquez and co-workers.[17] In a round bottomed Schlenk flask equipped with a reflux condenser, $[Cp_2Fe]PF_6$ (1.482 g, 4.477 mmol) and $NaBAr^F_4$ (3.980 g, 4.491 mmol) were dissolved in dry CH_2Cl_2 (100 mL) and stirred for 30 minutes while refluxing. After cooling to room temperature, the solvent was removed *in vacuo* and the residue taken up in diethyl ether (100 mL). The mixture was filtered and the solid residue was washed with diethyl ether (2x15 mL). The filtrate was dried *in vacuo* to yield a blue powder which was purified by redissolving in CH_2Cl_2, filtering to remove a gray residue, and removing the solvent *in vacuo*.

Yield: 4.021 g (3.832 mmol, 86%).

Elemental analysis: calcd C 48.08, H 2.11; found C 47.50, H 2.33.

8.2.11 Synthesis of (Pentamethylcyclopentadienyl)(naphthalene)ruthenium(II) Hexafluoro-phosphate, $[(C_5Me_5)Ru(C_{10}H_8)]PF_6$ ([XXI]PF_6)

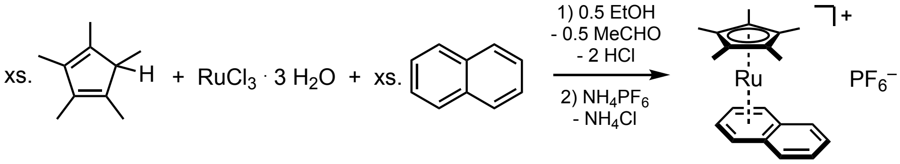

[XXI]PF_6

The synthesis of [**XXI**]PF_6 followed a modified procedure by Williams and co-workers.[18]

In a round bottomed Schlenk flask equipped with a reflux condenser, $RuCl_3 \cdot 2.4\ H_2O$ (2.500 g, 10.00 mmol) was dissolved in degassed ethanol (100 mL). Naphthalene (6.409 g, 50.00 mmol) and 1,2,3,4,5-pentamethylcyclopentadiene (8.11 mL, 50.0 mmol) were added to the solution and the mixture was stirred while refluxing overnight, yielding a black suspension. The solvent was removed *in vacuo* and the solid residue was extracted with water (200 mL) and diethyl ether (200 mL). The aqueous phase was washed with diethyl ether (3x50 mL). The organic phases were discarded. A saturated aqueous solution of NH_4PF_6 (4.075 g, 25.00 mmol) was added to the aqueous extraction phase, leading to the immediate precipitation of the product as a light orange solid. The crude product was isolated by filtration, dried, dissolved in acetone, and filtered over a pad of alumina. The solvent was removed by rotary evaporation and the residue recrystallized from hot acetone. The product was precipitated quantitatively by adding ethyl acetate (twice the volume of the acetone solution). After drying *in vacuo*, the product was obtained as a light yellow, crystalline solid.

Yield: 3.8044 g (7.468 mmol, 75%)

^{1}H NMR (300.13 MHz, 300 K, CD_2Cl_2): δ (ppm) = 1.63 (s, 15H, C_5Me_5), 5.92 (m, 2H, $C_{10}H_8$), 6.39 (m, 2H, $C_{10}H_8$), 7.48 (m, 2H, $C_{10}H_8$), 7.68 (m, 2H, $C_{10}H_8$).

8.2.12 Synthesis of Bis(1,2,3,4,5-pentamethylcyclopentadienyl Ruthenium(III) Dichloride), $[Cp^*RuCl_2]_2$

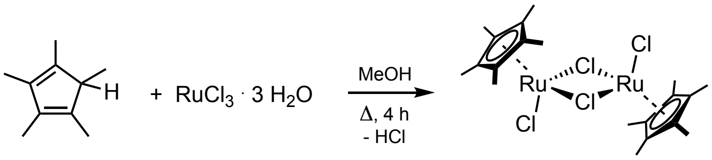

The synthesis followed a procedure by Suzuki and co-workers.[19]

Ruthenium(III) chloride hydrate (10.861 g, 41.538 mmol, 1.0 equiv.) was dissolved in degassed methanol (120 mL). In a counterflow of argon, 1,2,3,4,5-pentamethylcyclopentadiene (15.5 mL, 95.567 mmol, 2.3 equiv.) was added in one portion and the mixture was heated to reflux for four hours. Subsequently, the flask was cooled to –80 °C for 30 minutes and the mixture was filtered. The dark red-brown residue was washed with *n*-hexane (2x50 mL) and dried *in vacuo*.

Yield: 11.61 g (18.90 mmol, 91%).

8.2.13 Synthesis of Tetrakis(1,2,3,4,5-pentamethylcyclopentadienyl Ruthenium(II) Chloride), $[Cp^*RuCl]_4$

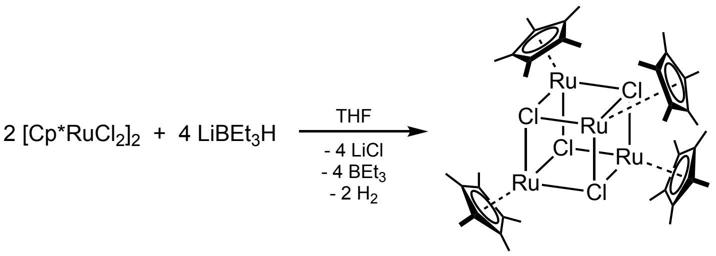

$[Cp^*RuCl]_4$ was prepared following a procedure by Fagan and co-workers.[20]

$[Cp^*RuCl_2]_2$ (11.61 g, 18.90 mmol, 1.0 equiv.) was dissolved in THF (150 mL) and a solution of $LiBEt_3H$ (1.0 mol L^{-1}, 37.8 mL, 37.80 mmol, 2.0 equiv.) was added dropwise. The mixture was stirred at room temperature overnight, whereupon a red-brown precipitate formed. The suspension was filtered and the precipitate was washed with THF (20 mL) and dried *in vacuo*.

Yield: 4.570 g (4.204 mmol, 45%).

^{1}H NMR (400.13 MHz, 300 K, C_6D_6): δ (ppm) = 1.67 (s, 60H).

8.2.14 (1,5-Cyclooctadiene)1,2,3,4,5-pentamethylcyclopentadienyl Ruthenium(II) Chloride, [Cp*RuCl(cod)] (XXIII)

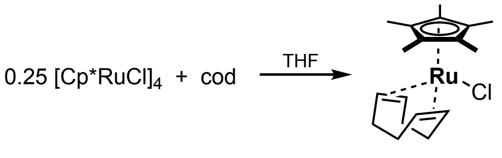

XXIII

[Cp*RuCl(cod)] was synthesized following a procedure by Fagan and co-workers.[20]

1,5-Cyclooctadiene (1.18 mL, 9.568 mmol, 1.3 equiv.) was added via syringe to a solution of [Cp*RuCl]$_4$ (2.000 g, 1.840 mmol, 0.25 equiv.) in THF (40 mL). The mixture was stirred at room temperature for one hour, yielding a clear orange solution. All volatiles were removed *in vacuo* and the yellow-orange residue was washed with *n*-hexane (1x10 mL, 2x5 mL) and dried *in vacuo*. The product was obtained as an orange, microcrystalline powder.

Yield: 2.568 g (6.759 mmol, 92%).

^{1}H NMR (300.13 MHz, 300 K, THF-d$_8$): δ (ppm) = 1.83 (s, 15H, $C_5(CH_3)_5$), 1.80-1.98 (m, 4H, cod), 2.14 (m, 2H, cod), 2.57 (m, 2H, cod), 3.69 (m, 2H, cod), 3.98 (m, 2H, cod).

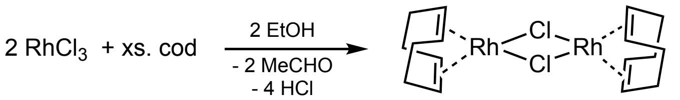

8.2.15 Synthesis of Bis(1,5-cyclooctadiene)dichlorodirhodium(I), [(cod)Rh(μ-Cl)]$_2$

$RhCl_3 \cdot 3\,H_2O$ (1.003 g, 3.895 mmol) was dissolved in a mixture of ethanol and water (5:1 by volume, 20 mL) and 1,5-cyclooctadiene (1.50 mL, 12.2 mmol) was added. The mixture was stirred under reflux overnight. An orange precipitate formed, which was isolated by filtration, washed with *n*-pentane, then with a mixture of methanol and water (1:5 by volume), and dried *in vacuo*.

The crude product was then purified by dissolving in hot CH_2Cl_2 (15 mL), cooling in an ice bath, and precipitating by adding diethyl ether. The product was obtained as a yellow-orange crystalline powder.

Yield: 765 mg (1.55 mmol, 80%).

^{1}H NMR (300.13 MHz, 300 K, $CDCl_3$): δ (ppm) = 1.75 (q, $^3J_{HH}$ = 8 Hz, 4H, cod), 2.50 (m, 4H, cod), 4.22 (s, 4H, cod).

Elemental analysis: calcd C 38.97, H 4.91; found C 39.26, H 4.87.

8.2.16 Synthesis of Bis(cymene)tetrachloridodiruthenium, [(cym)RuCl(μ-Cl)]$_2$

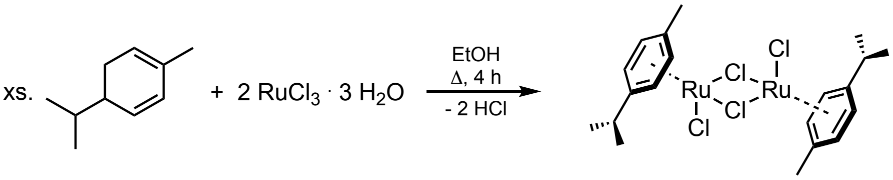

$RuCl_3 \cdot 3\ H_2O$ (1.99 g, 7.61 mmol, 1.0 equiv.) was dissolved in ethanol (100 mL). α-Phellandrene (10.0 mL, 62.1 mmol, 8.1 equiv.) was added and the solution was stirred while refluxing for four hours, yielding an orange solution and a black precipitate. The hot solution was filtered over a preheated glass frit and the residue was washed with ethanol. The filtrate was concentrated *in vacuo* to a volume of 80 mL and stored at –25 °C overnight, upon which the product crystallized as deep red blocks. The product was isolated by filtration, washed with *n*-hexane, and dried *in vacuo*.

Yield: 1.89 g (3.09 mmol, 81%).

^{1}H NMR (300.13 MHz, 300 K, $CDCl_3$): δ (ppm) = 1.23 (d, $^3J_{HH}$ = 6.9 Hz, 6H, $CH(CH_3)_2$), 2.11 (s, 3H, CH_3), 2.87 (heptet, $^3J_{HH}$ = 6.9 Hz, $CH(CH_3)_2$), 5.31 (d, $^3J_{HH}$ = 6.0 Hz, 2H, H_{cym}), 5.43 (d, $^3J_{HH}$ = 6.0 Hz, 2H, H_{cym}).

8.2.17 Synthesis of Bis(bis(trimethylsilyl)amido)iron, [Fe{N(SiMe$_3$)$_2$}$_2$]

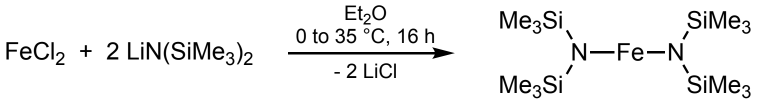

In a round bottomed Schlenk flask, anhydrous $FeCl_2$ (7.812 g, 61.36 mmol, 1.0 equiv.) and $LiN(SiMe_3)_2$ (22.60 g, 123.3 mmol, 2.0 equiv.) were dissolved in diethyl ether (200 mL) at 0 °C. The mixture was stirred overnight, allowing it to warm to room temperature. All volatiles were removed *in vacuo* and the residue was taken up in *n*-hexane (100 mL), yielding a dark green solution and a gray precipitate. The mixture was filtered over a glass frit into a small round bottomed Schlenk flask, which was subsequently equipped with a distillation bridge. After removing the *n*-hexane *in vacuo*, the crude product was purified by distillation at 150 °C. The product was obtained as a green oil which solidified upon cooling in the refrigerator.

Yield: 6.408 g (17.01 mmol, 28%).

^{1}H NMR (300.13 MHz, 300 K, C_6D_6): δ (ppm) = 65.6 (br).

8.2.18 Synthesis of Bis(bis(trimethylsilyl)amido)cobalt, $[Co\{N(SiMe_3)_2\}_2]_2$

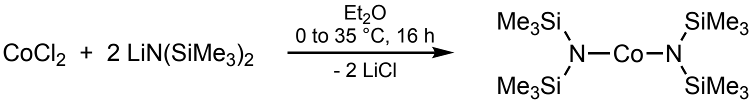

Anhydrous $CoCl_2$ (7.011 g, 54.00 mmol) was added to a three-neck Schlenk flask equipped with a reflux condenser and suspended in diethyl ether (100 mL). In a second Schlenk flask, $LiN(SiMe_3)_2$ (16.43 g, 98.19 mmol) was suspended in diethyl ether (100 mL) and subsequently added to the $CoCl_2$ suspension while cooling in an ice bath. The resulting turquoise suspension was then refluxed overnight. The solvent was removed *in vacuo*, yielding a green oil which was taken up in *n*-hexane (100 mL). After filtration, the solvent was removed *in vacuo*. The crude product was then distilled under reduced pressure (10^{-1} mbar, 150 °C). The green, oily product solidified into a brown solid upon cooling in the refrigerator.

Yield: 9.356 g (24.64 mmol, 46%).

Elemental analysis: calcd C 37.96, H 9.56, N 7.38; found C 37.71, H 9.00, N 7.25.

8.3 Experimental Details – Synthesis of Ruthenium Naphthalene Sandwich Complexes

8.3.1 Synthesis of Bis(1,2,3,4,5-pentamethylcyclopentadienyl)(naphthalene)-diruthenium(I), $[Cp^*Ru(C_{10}H_8)RuCp^*]$ (2)

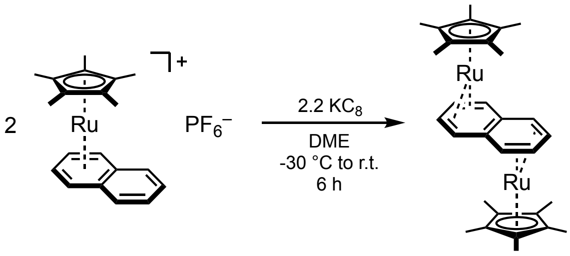

[**XXI**]PF6

2

$[Cp^*Ru(C_{10}H_8)]PF_6$ (3.800 g, 7.459 mmol, 2.0 equiv.) was suspended in DME (250 mL) and cooled to –30 °C. KC_8 (1.109 g, 8.205 mmol, 2.2 equiv.) was added and the mixture was stirred for six hours, allowing it to warm to room temperature. The resulting suspension was filtered over a glass frit and all volatile components were removed *in vacuo*. The residue was extracted with toluene. The deep red solution was concentrated to 20 mL and stored at –30 °C, whereupon dichroic red-green crystals formed.

Yield: 760 mg (1.265 mmol, 34%).

^{1}H NMR (300.13 MHz, 300 K, C_6D_6): δ (ppm) = 1.85 (s, 30H, $C_5(CH_3)_5$), 2.18 (m, 4H, $C_{10}H_8$), 4.89 (m, 4H, $C_{10}H_8$); $^{13}C\{^1H\}$ NMR (75.47 MHz, 300 K, C_6D_6): δ (ppm) = 11.6 ($C_5(CH_3)_5$), 60.9 ($C_{10}H_8$), 72.5 ($C_{10}H_8$), 85.8 ($C_5(CH_3)_5$).

UV-vis (THF solution): λ (nm) / ε (L mol^{-1} cm^{-1}): 492 ($1.81\cdot10^4$).

Elemental analysis: calcd. C 59.98, H 6.38, found C 59.90, H 6.45.

8.3.2 Synthesis of [Bis(1,2,3,4,5-pentamethylcyclopentadienyl)(naphthalene)diruthenium] tetrakis(3,5-bis(trifluoromethyl)phenyl)borate, [Cp*Ru($C_{10}H_8$)RuCp*]BAr$^F_4$ ([2]BAr$^F_4$)

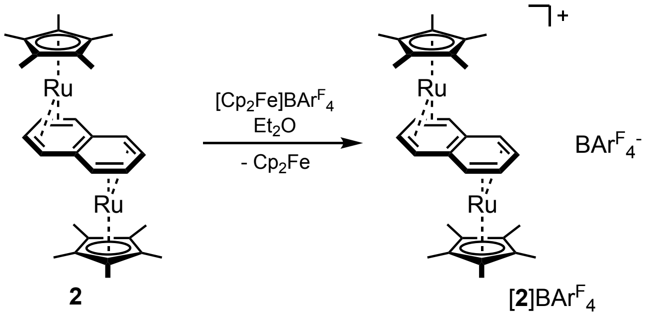

[Cp*Ru($C_{10}H_8$)RuCp*] (60.1 mg, 0.100 mmol, 1.0 equiv.) was dissolved in diethyl ether (15 mL) and [Cp_2Fe]BAr$^F_4$ (104.8 mg, 0.100 mmol, 1.0 equiv.) was added in one portion. An immediate color change from deep red to olive green was observed. The solvent was removed *in vacuo* and the residue was washed with *n*-hexane (3x5 mL). The remaining solid was extracted with diethyl ether, filtered, and dried *in vacuo* to yield a dark green microcrystalline powder.

Yield: 131.6 mg (0.0899 mmol, 90%).

UV-vis (THF solution): λ (nm) / ε (L mol^{-1} cm^{-1}): 609 ($2.79 \cdot 10^3$), 469 ($6.19 \cdot 10^3$).

Elemental analysis: calcd. C 50.87, H 3.44, found C 51.66, H 3.67.

Magnetic moment (Evans method, THF-d$_8$, 300 K): $\mu_{eff} = 1.3$ μ_B.

8.3.3 Synthesis of [Bis(1,2,3,4,5-pentamethylcyclopentadienyl)(naphthalene)-(hydrido)diruthenium] Tetrakis(3,5-bis(trifluoromethyl)phenyl)borate, [Cp*Ru($C_{10}H_8$)Ru(H)Cp*]BAr$^F_4$ ([2-H]BAr$^F_4$)

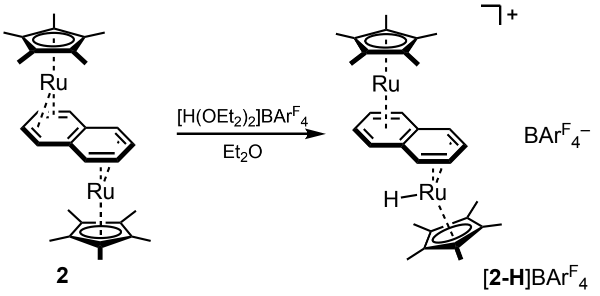

[Cp*Ru($C_{10}H_8$)RuCp*] (26.3 mg, 0.043 mmol, 1.0 equiv.) was dissolved in diethyl ether (10 mL) and cooled to –35 °C. A solution of [H(OEt_2)$_2$]BAr$^F_4$ (44.0 mg, 0.043 mmol, 1.0 equiv.) in diethyl ether (10 mL) was added dropwise, whereupon the color changed from deep red to yellow. The solution was concentrated to 10 mL, layered with 20 mL of *n*-hexane, and stored at –30 °C overnight. The product crystallized as colorless blocks, which were isolated by filtration and dried *in vacuo*.

Yield: 59.1 mg (91%).

^{1}H NMR (300.13 MHz, 300 K, THF-d$_8$): major isomer: δ (ppm) = –2.96 (s, 1H, Ru–H), 1.17 (s, 15H, Cp*), 1.41 (s, 15H, Cp*), 2.82 (m, 2H, H15/18 of $C_{10}H_8$), 3.78 (m, 2H, H11-14 of $C_{10}H_8$), 4.14 (m, 2H, H11-14 of $C_{10}H_8$), 4.86 (m, 2H, C16/17 of $C_{10}H_8$), 7.72 (s, 4H, H_{para} of $BAr^F{}_4$), 8.42 (s, 8H, H_{ortho} of $BAr^F{}_4$); minor isomer: –3.09 (s, 1H, Ru–H), 1.07 (s, 15H, Cp*), 1.28 (s, 15H, Cp*), 2.68 (m, 2H, H15/18 of $C_{10}H_8$), 3.75 (m, 4H, H11-14 of $C_{10}H_8$), 4.04 (m, 2H, H11-14 of $C_{10}H_8$) 4.69 (m, 2H, C16/17 of $C_{10}H_8$), 7.53 (s, 4H, H_{para} of $BAr^F{}_4$), 8.16 (s, 8H, H_{ortho} of $BAr^F{}_4$).

^{13}C{^{1}H} NMR (75.47 MHz, 300 K, THF-d$_8$): δ (ppm) = 9.6 ($C_5(\mathit{C}H_3)_5$), 10.2 ($C_5(\mathit{C}H_3)_5$), 48.6 (C15/18 of $C_{10}H_8$), 79.3 (C16/17 of $C_{10}H_8$), 79.5 ($C_{10}H_8$), 80.9 ($C_{10}H_8$), 92.9 ($\mathit{C}_5(CH_3)_5$), 93.5 ($\mathit{C}_5(CH_3)_5$), 118.1 (C_{para} of $BAr^F{}_4$), 123.9 (C_{meta} of $BAr^F{}_4$), 129.6 (m, $\mathit{C}F_3$ of $BAr^F{}_4$), 135.4 (C_{ortho} of $BAr^F{}_4$). C_{ipso} of $BAr^F{}_4$ was not observed in the ^{13}C{^{1}H} NMR spectrum, but the corresponding signal was observed at 162.8 ppm in the ^{1}H/^{13}C HMBC spectrum.

Elemental analysis: $C_{62}H_{51}BF_{24}Ru_2$ (1465.00): calcd. 50.83, H 3.51; found C 51.11, H 3.51.

8.3.4 Synthesis of Bis(dimethoxyethane)potassium (1,5-Cyclooctadiene)(1,2,3,4,5-penta-methylcyclopentadienyl)ruthenate(0), [K(dme)₂][Cp*Ru(cod)] (K3)

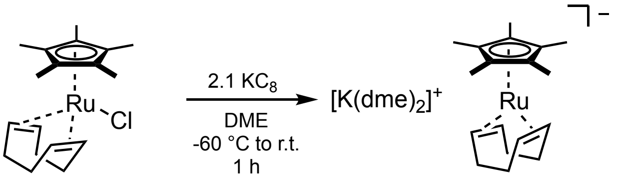

K3

[Cp*RuCl(cod)] (1.000 g, 2.632 mmol, 1.0 equiv.) was dissolved in DME (30 mL) and cooled to –60 °C. KC_8 (747.2 mg, 5.527 mmol, 2.1 equiv.) was added and the mixture was stirred for one hour, allowing it to warm to room temperature. The formed suspension was filtered and the resulting yellow solution was concentrated to dryness *in vacuo*. The solid residue was washed with several portions of *n*-hexane (3x10 mL) until the washing solution was colorless. The remaining colorless solid was dried *in vacuo*.

Yield: 530.3 mg (1.119 mmol, 43%).

^{1}H NMR (300 K, 400.13 MHz, THF-d$_8$): δ (ppm) = 1.54 (m, 4H, cod), 1.65 (m, 4H, cod), 1.73 (s, 15H, $C_5(C\mathit{H}_3)_5$), 1.83 (m, 4H, cod), 3.30 (s, 6H, $–OC\mathit{H}_3$), 3.46 (s, 4H, $–OC\mathit{H}_2C\mathit{H}_2O–$).

^{13}C{^{1}H} NMR (300 K, 100.61 MHz, THF-d$_8$): δ (ppm) = 10.3 ($C_5(\mathit{C}H_3)_5$), 34.5 ($\mathit{C}H_2$ (cod)), 51.8 ($\mathit{C}H$ (cod)), 57.9 ($\mathit{C}H_3$ (dme)), 71.8 ($\mathit{C}H_2$ (dme)), 85.2 ($\mathit{C}_5(CH_3)_5$).

Elemental analysis: calcd. C 55.78, H 7.87, found C 55.03, H 7.27.

8.3.5 Reaction of [K(dme)$_2$][Cp*Ru(cod)] (K3) with P$_4$

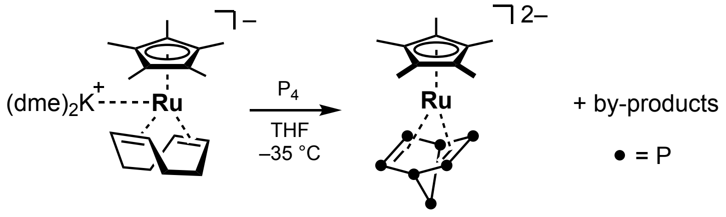

K3

[K(dme)$_2$][Cp*Ru(cod)] (213.0 mg, 0.450 mmol, 1.0 equiv.) was dissolved in THF (4 mL) and cooled to –35 °C. P_4 (55.7 mg, 0.450 mmol, 1.0 equiv.) was added, leading to a darkening of the red solution. The mixture was stored at –35 °C overnight before recording a ^{31}P NMR spectrum of the filtered reaction solution (see Figure 3.8 in Chapter 3).

^{31}P NMR (161.98 MHz, 300 K, THF / C_6D_6 capillary): δ (ppm) = –278.0 (s), –170.5 (m), –107.6 (m), –95.0 (m), 28.2 (m), 35-73 (br m), 86.6 (m).

8.4 Experimental Details – Synthesis of NHC Precursors and NHC-Silver Complexes

8.4.1 Synthesis of *R,R*-4,5-Dihydro-1,3-bis((1-naphthyl)ethyl)imidazolium Chloride, [SINpEtH]Cl (4)

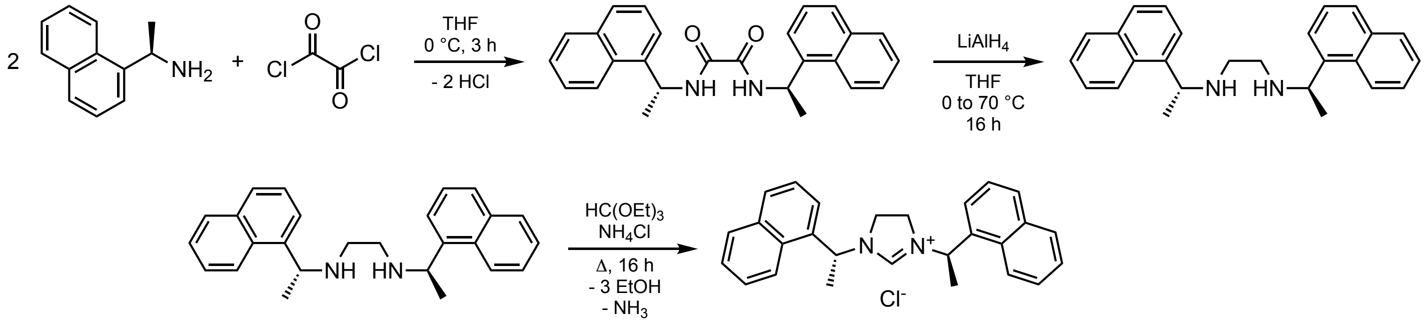

4

a) Synthesis of (R,R)-N,N'-Bis(1-(1-naphthyl)ethyl)oxalamide

The 1,2-diamide was prepared following a procedure by Fiksdahl and co-workers.[21]

(*R*)-1-(1-Naphthyl)ethylamine (3.9408 g, 23.010 mmol, 2.0 equiv.) was dissolved in dry THF (60 mL) and triethylamine (9.00 mL) was added. The solution was cooled to 0 °C and a mixture of oxalyl chloride (0.990 mL, 11.51 mmol, 1.0 equiv.) and dry THF (20 mL) was added dropwise, resulting in a cloudy suspension. After stirring at 0 °C for three hours, the mixture was filtered and the remaining solid was washed with THF until it was colorless. The solvent was removed *in vacuo* and the residue was washed with diethyl ether, yielding the product as a colorless solid.

Yield: 3.9616 g (9.990 mmol, 87%).

^{1}H NMR (300.13 MHz, 300 K, $CDCl_3$): δ (ppm) = 1.72 (d, 3JHH = 6.9 Hz, 6H, Np-CH(C*H*$_3$)NH-), 5.87 (dq, J = 8.4 Hz, 6.9 Hz, 2H, Np-C*H*(CH_3)NH-), 7.41-7.54 (m, 8H), 7.79 (d, J = 8.4 Hz, 4H), 7.86 (m, 2H), 8.01 (m, 2H).

b) Synthesis of (*R*,*R*)-*N*,*N'*-Bis(1-(1-naphthyl)ethyl)ethylenediamine

In a three-necked round-bottom Schlenk flask equipped with a reflux condenser and a dropping funnel, lithium aluminum hydride (3.780 g, 99.60 mmol, 10 equiv.) was suspended in dry THF (150 mL). In a separate Schlenk flask, the oxalamide from a) (3.9415 g, 9.9400 mmol, 1.0 equiv.) was dissolved in dry THF (150 mL) and transferred to the dropping funnel via cannula. The $LiAlH_4$ suspension was cooled to 0 °C and the oxalamide was added dropwise. The mixture was subsequently heated to reflux overnight, resulting in a slightly off-white color. Under cooling in an ice bath, excess $LiAlH_4$ was quenched by carefully adding an aqueous solution of 5 g of NaOH, which resulted in the vigorous release of hydrogen gas and the formation of a colorless precipitate. The mixture was diluted with water until two clear phases formed. The aqueous phase was extracted with THF (3x150 mL), the combined organic phases washed with brine and dried with $MgSO_4$. After filtration, the solvent was removed by rotary evaporation, yielding the crude product as an orange oil, which was purified by column chromatography (eluent: CH_2Cl_2 / MeOH 98:2 to 90:10; second band collected).
Yield: 2.9286 g (80%).
^{1}H NMR (300.13 MHz, 300 K, $CDCl_3$): δ (ppm) = 1.50 (d, $^3J_{HH}$ = 6.6 Hz, Np-CH(C*H*$_3$)NH-), 2.67 (s, 4H, -NH-C*H*$_2$-C*H*$_2$-NH-), 4.51 (q, $^3J_{HH}$ = 6.6 Hz, 2H, Np-C*H*(CH_3)NH-), 7.43-7.52 (m, 6H), 7.64 (d, J = 7.0 Hz, 2H), 7.76 (d, J = 8.2 Hz, 2H), 7.85-7.90 (m, 2H), 8.03-8.10 (m, 2H).

c) Synthesis of (*R*,*R*)-4,5-Dihydro-1,3-bis(-1-(1-naphthyl)ethyl)imidazolium Chloride (**4**)

0.416 g (7.785 mmol, 1.0 equiv.) of ammonium chloride was ground to a fine powder and suspended in 2 mL of ethanol. 2.869 g (7.785 mmol, 1.0 equiv.) of the diamine and 26 mL (ca. 20 equiv.) of triethyl orthoformate were added and the mixture was stirred at 120 °C overnight, leaving the flask open to release the formed ammonia and ethanol. All volatile components were subsequently removed *in vacuo* while warming to 45 °C. The resulting brown solid was dissolved in ca. 4 mL of ethanol and 30 mL of diethyl ether were added. Upon storage at 4 °C, a brown oil settled in the flask. The supernatant solution was decanted and the residue dried *in vacuo*, yielding **4** as a foamy, light brown solid.
Yield: 2.350 g (5.663 mmol, 73%).
^{1}H NMR (300.13 MHz, 300 K, $CDCl_3$): δ (ppm) = 2.02 (d, $^3J_{HH}$ = 6.8 Hz, 6H, Np-CH(C*H*$_3$)N), 3.23-3.62 (m, 4H, N-C*H*$_2$-C*H*$_2$-N), 6.19 (q, $^3J_{HH}$ = 6.8 Hz, 2H, Np-C*H*(CH_3)N),

7.39-7.49 (m, 4H), 7.56 (m, 2H), 7.67 (m, 2H), 7.82-7.92 (m, 4H), 8.32 (d, J = 8.6 Hz, 2H), 11.28 (s, 1H, NC*H*N).

8.4.2 Synthesis of 4,5-Dihydro-1,3-bis(1-naphthyl)imidazolium Bromide, [SINpH]Br (5)

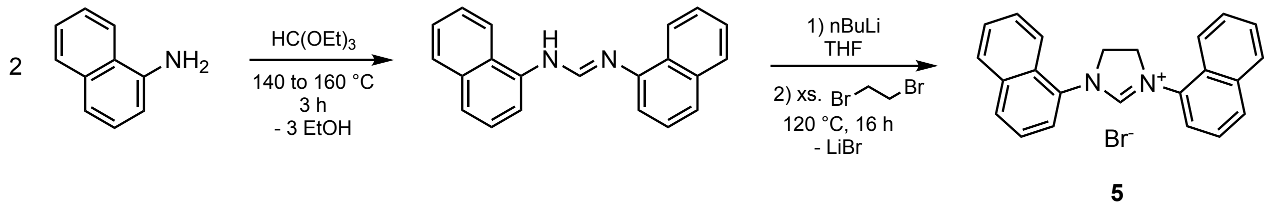

5

a) Synthesis of *N*,*N'*-Bis(1-naphthyl)formamidine

The formamidine was prepared following a procedure by Glorius and co-workers.[22]

1-Naphthylamine (19.49 g, 136.1 mmol, 2.0 equiv.) and triethyl orthoformate (11.4 mL, 68.5 mmol, 1.0 equiv.) were added to a flask and stirred at 140 °C for one hour and subsequently at 160 °C for another hour. The resulting solid was cooled to room temperature and ground to a fine powder with a mortar and pestle. The crude product was recrystallized from hot acetonitrile (10 mL), yielding a colorless crystalline powder.

Yield: 19.262 g (64.993 mmol, 96%)

^{1}H NMR (300.13 MHz, 300 K, DMSO-d$_6$): δ (ppm) = 7.10 (br, 1H), 7.43-7.69 (overlapping m, 9H), 7.91 (br, 2H), 8.23 (s, 1H), 8.33-8.39 (m, 2H), 10.12 (s, 1H).

b) Synthesis of 4,5-Dihydro-1,3-bis(1-naphthyl)imidazolium Bromide

The formamidine (a) (19.262 g, 64.993 mmol, 1.0 equiv.) was suspended in dry THF (200 mL) and *n*-butyllithium (2.5 mol L^{-1} solution in hexane, 26 mL) was added dropwise, yielding a fluorescent yellow solution. After stirring at room temperature for 20 minutes, the solvent was removed *in vacuo* and 1,2-dibromoethane (70 mL) was added under a stream of argon. The mixture was stirred while refluxing overnight, resulting in the formation of a light brown precipitate. After cooling to room temperature, diethyl ether (100 mL) was added to complete the precipitation of the product. The crude product was recrystallized from hot methanol (30 mL), filtered, washed with diethyl ether (3x40 mL), and dried *in vacuo*.

Yield: 17.636 g (43.728 mmol, 67%).

^{1}H NMR (300.13 MHz, 300 K, DMSO-d$_6$): δ (ppm) = 4.80 (s, 4H, N-CH_2-CH_2-N), 7.69-7.84 (m, 6H), 8.03 (dd, J = 7.3 Hz, 1.0 Hz, 2H), 8.16 (t, J = 8.2 Hz, 4H), 8.44 (d, J = 8.4 Hz, 2H), 9.55 (s, 1H, NC*H*N).

8.4.3 Synthesis of (1,3-Bis(1-naphthylmethyl)imidazolin-2-ylidene)silver Chloride, [(INpMe)AgCl] (6)

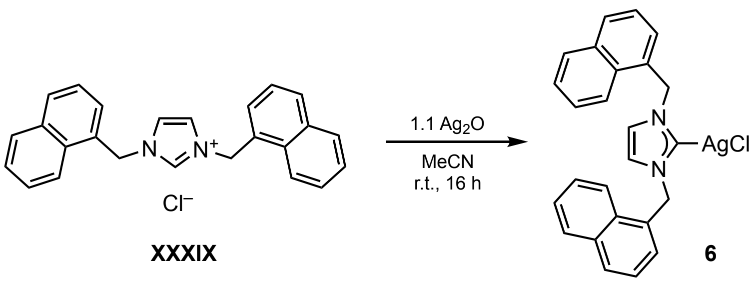

[INpMeH]Cl (384.9 mg, 1.000 mmol, 1.0 equiv.) and Ag_2O (254.9 mg, 1.100 mmol, 1.1 equiv.) were suspended in acetonitrile (50 mL) and stirred at room temperature overnight under strict exclusion of light. The resulting gray suspension was filtered, and the resulting colorless solution was concentrated to dryness *in vacuo*. The residue was taken up in CH_2Cl_2 and layered with *n*-hexane. The resulting crystalline solid was collected by filtration and dried *in vacuo*.

Yield: 128.4 mg (0.260 mmol, 26%).

^{1}H NMR (300.13 MHz, 300 K, $CDCl_3$): δ (ppm) = 5.75 (s, 4H, NCH_2Np), 6.73 (s, 4H, NCH_2CH_2N), 7.33 (d, J = 7.0 Hz, 2H, CH_{naph}), 7.46 (dd, J = 8.3 Hz, 7.0 Hz, 2H, CH_{naph}), 7.53 (overlapping m, 4H, CH_{naph}), 7.89 (overlapping m, 6H, CH_{naph}).

^{13}C{^{1}H} NMR (75.47 MHz, 300 K, $CDCl_3$): δ (ppm) = 54.1 (NCH_2Np), 121.2 (NCHCHN), 122.8 (CH_{naph}), 125.4 (CH_{naph}), 126.4 (CH_{naph}), 127.3 (CH_{naph}), 127.6 (CH_{naph}), 129.1 (CH_{naph}), 130.0 (CH_{naph}), 130.4 (C_{naph}), 131.0 (C_{naph}), 134.0 (C_{naph}). $C_{carbene}$ was not observed in the ^{13}C{^{1}H} NMR spectrum, but the corresponding signal was observed at 180.8 ppm in the ^{1}H/^{13}C HMBC spectrum (see section 4.3.1).

Elemental analysis: calcd. C 61.06, H 4.10, N 5.70; found C 61.55, H 4.23, N 5.85.

8.4.4 Synthesis of (1,3-Bis(1-naphthylmethyl)benzimidazol-2-ylidene)silver Chloride, (BNpMe)AgCl (7)

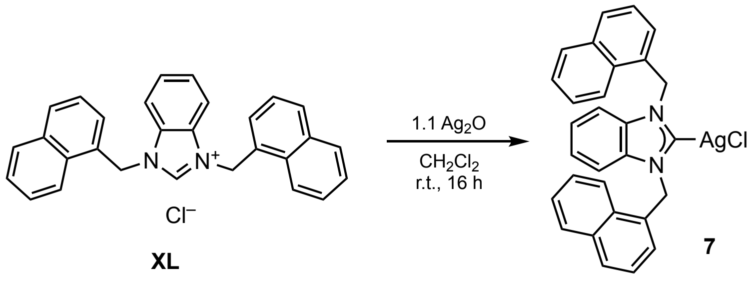

[BNpMeH]Cl (217.5 mg, 0.500 mmol, 1.0 equiv.) and Ag_2O (127.5 mg, 0.550 mmol, 1.1 equiv.) were suspended in CH_2Cl_2 (20 mL) and stirred at room temperature overnight under strict exclusion of light. The resulting gray suspension was filtered, and the resulting colorless solution was layered with *n*-hexane. The resulting crystalline solid was collected by filtration and dried *in vacuo*.

Yield: 121.5 mg (0.225 mmol, 45%).

^{1}H NMR (300.13 MHz, 300 K, CD_2Cl_2): δ (ppm) = 6.15 (s, 4H, NC*H*$_2$Np), 7.03 (d, J = 7.1 Hz, 2H, C*H*$_{naph}$), 7.26 (m, 4H, C*H*$_{backbone}$), 7.37 (t, J$_{HH}$ = 7.6 Hz, 2H, C*H*$_{naph}$), 7.56 (m, 4H, C*H*$_{naph}$), 7.85 (d, J = 8.3 Hz, 2H, C*H*$_{naph}$), 7.95 (m, 2H, C*H*$_{naph}$), 8.02 (m, 2H, C*H*$_{naph}$).

^{13}C{^{1}H} NMR (75.47 MHz, 300 K, CD_2Cl_2): δ (ppm) = 51.6 (N*C*H$_2$Np), 112.3 (*C*H$_{backbone}$), 122.4 (*C*H$_{naph}$), 124.6 (*C*H$_{backbone}$), 125.0 (*C*H$_{naph}$), 125.4 (*C*H$_{naph}$), 126.4 (*C*H$_{naph}$), 127.1 (*C*H$_{naph}$), 129.3 (*C*H$_{naph}$), 129.4 (*C*H$_{naph}$), 130.1 (*C*$_{naph}$), 130.6 (*C*$_{naph}$), 133.9 (*C*$_{naph}$), 134.7 (*C*$_{backbone}$). *C*$_{carbene}$ was not observed in the ^{13}C{^{1}H} NMR spectrum, but the corresponding signal was observed at 190.9 ppm in the ^{1}H/^{13}C HMBC spectrum (see section 4.3.2).

Elemental analysis: calcd. C 64.29, H 4.09, N 5.17; found C 64.58, H 4.21, N 4.99.

8.4.5 Synthesis of (1,3-Bis(1-naphthylmethyl)imidazolidin-2-ylidene)silver Chloride, [(SINpMe)AgCl] (8)

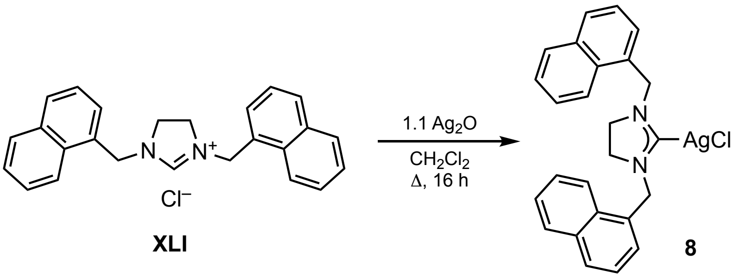

[SINpMeH]Cl (1.452 g, 3.753 mmol, 1.0 equiv.) and Ag_2O (1.031 g, 4.449 mmol, 1.2 equiv.) were suspended in CH_2Cl_2 (30 mL) and stirred at 40 °C overnight under strict exclusion of light. The resulting gray suspension was filtered, and the resulting colorless solution was concentrated *in vacuo* to a volume of 15 mL and layered with diethyl ether (30 mL). The resulting crystalline solid was collected by filtration and dried *in vacuo*.

Yield: 679 mg (1.38 mmol, 37%).

^{1}H NMR (400.13 MHz, 300 K, CD_2Cl_2): δ (ppm) = 3.40 (s, 4H, NC*H*$_2$C*H*$_2$N), 5.26 (s, 4H, NC*H*$_2$Np), 7.43-7.50 (m, 4H, C*H*$_{naph}$), 7.54-7.64 (m, 4H, C*H*$_{naph}$), 7.88 (d, J = 7.9 Hz, 2H, C*H*$_{naph}$), 7.93 (m, 2H, C*H*$_{naph}$), 8.16 (d, J = 8.2 Hz, 2H, C*H*$_{naph}$).

^{13}C{^{1}H} NMR (100.61 MHz, 300 K, CD_2Cl_2): δ (ppm) = 49.2 (N*C*H$_2$*C*H$_2$N), 53.9 (N*C*H$_2$Np), 123.7 (*C*H$_{naph}$), 125.8 (*C*H$_{naph}$), 126.6 (*C*H$_{naph}$), 127.2 (*C*H$_{naph}$), 129.3 (*C*H$_{naph}$), 129.6 (*C*H$_{naph}$), 131.1 (*C*$_{naph}$), 131.8 (*C*$_{naph}$), 134.4 (*C*$_{naph}$). *C*$_{carbene}$ was not observed in the ^{13}C{^{1}H} NMR spectrum, but the corresponding signal was observed at 205.3 ppm in the ^{1}H/^{13}C HMBC spectrum (see section 4.3.3).

Elemental analysis: calcd. C 60.81, H 4.45, N 5.67; found C 60.64, H 4.53, N 5.56.

8.4.6 Reaction of Silver Oxide with 1,3-Bis(1-(1-naphthyl)ethyl)imidazolinium Chloride

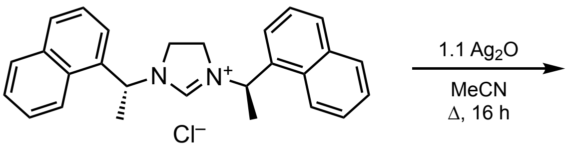

4

[SINpEtH]Cl (200.0 mg, 0.482 mmol, 1.0 equiv.) and Ag_2O (122.8 mg, 0.530 mmol, 1.1 equiv.) were mixed with acetonitrile (30 mL) and stirred at 80 °C overnight under strict light exclusion. After cooling to room temperature, the resulting suspension was filtered and layered with diethyl ether, resulting in the formation of a small amount of a grayish-brown solid which was collected by filtration.

8.4.7 Reaction of Silver Oxide with 1,3-Bis(1-naphthyl)imidazolinium Bromide

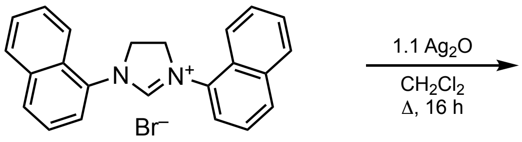

5

[SINpH]Br (60.0 mg, 0.159 mmol, 1.0 equiv.) and Ag_2O (38.8 mg, 0.167 mmol, 1.1 equiv.) were stirred in CH_2Cl_2 (15 mL) at room temperature overnight. The resulting suspension was filtered, yielding a light yellow solution. All volatiles were removed *in vacuo*, giving a very small amount of an off-white solid.

8.5 Experimental Details – Synthesis of NHC-Gold, Rhodium, and Ruthenium Complexes

8.5.1 Synthesis of (1,3-Bis(1-naphthylmethyl)imidazolidin-2-ylidene)gold(I) Chloride, [(SINpMe)AuCl] (9)

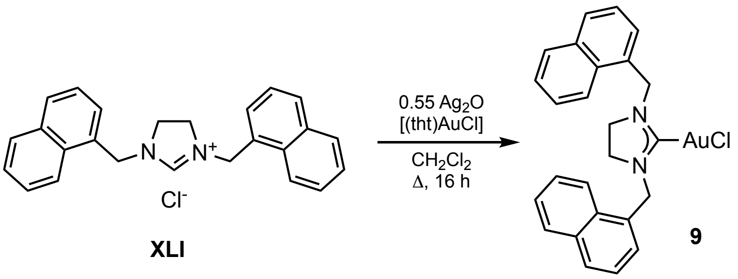

[SINpMeH]Cl (77.4 mg, 0.200 mmol, 1.0 equiv.), Ag_2O (25.5 mg, 0.110 mmol, 0.55 equiv.), and [(tht)AuCl] (64.1 mg, 0.200 mmol, 1.0 equiv.) were suspended in CH_2Cl_2 (20 mL) and stirred overnight under exclusion of light. The resulting off-white suspension was filtered over a pad of silica. In order to remove THT from the mixture, all volatiles were removed *in vacuo* and the residue was taken up in CH_2Cl_2 (7 mL). After layering with *n*-hexane (30 mL), the product crystallized as fine, colorless needles.

Yield: 53.5 mg (46%).

^{1}H NMR (400.13 MHz, 300 K, $CDCl_3$): δ (ppm) = 3.28 (s, 4H, $\mathrm{NC}\mathit{H}_2\mathrm{C}\mathit{H}_2\mathrm{N}$), 5.40 (s, 4H, $\mathrm{NC}\mathit{H}_2\mathrm{Np}$), 7.43 (m, 2H, $\mathrm{C}\mathit{H}_{\mathrm{naph}}$), 7.44 (s, 2H, $\mathrm{C}\mathit{H}_{\mathrm{naph}}$), 7.55 (m, 2H, $\mathrm{C}\mathit{H}_{\mathrm{naph}}$), 7.61 (m, 2H, $\mathrm{C}\mathit{H}_{\mathrm{naph}}$), 7.84 (m, 2H, $\mathrm{C}\mathit{H}_{\mathrm{naph}}$), 7.90 (m, 2H, $\mathrm{C}\mathit{H}_{\mathrm{naph}}$), 8.28 (d, 2H, $\mathrm{C}\mathit{H}_{\mathrm{naph}}$).

^{13}C{^{1}H} NMR (100.61 MHz, 300 K, $CDCl_3$): δ (ppm) = 48.0 ($\mathrm{N}\mathit{C}\mathrm{H}_2\mathit{C}\mathrm{H}_2\mathrm{N}$), 53.2 ($\mathrm{N}\mathit{C}\mathrm{H}_2\mathrm{Np}$), 123.5 ($\mathit{C}\mathrm{H}_{\mathrm{naph}}$), 125.3 ($\mathit{C}\mathrm{H}_{\mathrm{naph}}$), 126.3 ($\mathit{C}\mathrm{H}_{\mathrm{naph}}$), 127.1 ($\mathit{C}\mathrm{H}_{\mathrm{naph}}$), 127.4 ($\mathit{C}\mathrm{H}_{\mathrm{naph}}$), 129.0 ($\mathit{C}\mathrm{H}_{\mathrm{naph}}$), 129.5 ($\mathit{C}\mathrm{H}_{\mathrm{naph}}$), 130.2 ($\mathit{C}_{\mathrm{naph}}$), 131.5 ($\mathit{C}_{\mathrm{naph}}$), 134.0 ($\mathit{C}_{\mathrm{naph}}$). $\mathit{C}_{\mathrm{carbene}}$ was not observed in the ^{13}C{^{1}H} NMR spectrum, but the corresponding signal was observed at 194.0 ppm in the ^{1}H/^{13}C HMBC spectrum (see section 5.2.1).

Elemental analysis: calcd. C 60.81, H 4.45, N 5.67; found C 60.64, H 4.53, N 5.56.

8.5.2 Synthesis of (1,3-Bis(1-naphthylmethyl)benzimidazolidin-2-ylidene)gold(I) Chloride, [(BNpMe)AuCl] (10)

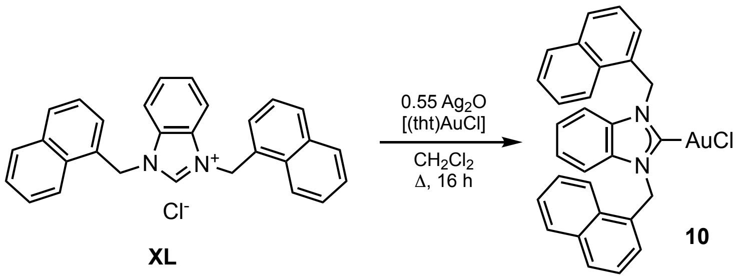

[BNpMeH]Cl (65.2 mg, 0.150 mmol, 1.0 equiv.), Ag_2O (19.1 mg, 0.083 mmol, 0.55 equiv.), and [(tht)AuCl] (48.1 mg, 0.150 mmol, 1.0 equiv.) were stirred in CH_2Cl_2 (15 mL) overnight under strict light exclusion. The resulting off-white suspension was filtered over a pad of silica and all volatiles were removed *in vacuo*. The residue was taken up in 5 mL of CH_2Cl_2 and layered with 15 mL of *n*-hexane, yielding the product as fine, colorless needles.

Yield: 39.8 mg (42%).

^{1}H NMR (400.13 MHz, 300 K, $CDCl_3$): δ (ppm) = 6.29 (s, 4H, NCH_2Np), 7.06 (d, 2H, CH_{naph}), 7.17 (overlapping m, 4H, $CH_{backbone}$), 7.37 (m, 2H, CH_{naph}), 7.56 (m, 2H, CH_{naph}), 7.61 (m, 2H, CH_{naph}), 7.84 (m, 2H, CH_{naph}), 7.92 (d, 2H, CH_{naph}), 8.19 (d, 2H, CH_{naph}).

^{13}C{^{1}H} NMR (100.61 MHz, 300 K, $CDCl_3$): δ (ppm) = 51.2 (NCH_2Np), 112.5 ($CH_{backbone}$), 122.6 (CH_{naph}), 124.8 (CH_{naph}), 124.9 ($CH_{backbone}$), 125.3 (CH_{naph}), 126.4 (CH_{naph}), 126.7 (CH_{naph}), 129.2 (CH_{naph}), 129.3 (CH_{naph}), 129.8 (C_{naph}), 133.7 (C_{naph}), 133.9 (C_{naph}), 133.9 ($C_{backbone}$), 181.0 ($C_{carbene}$).

8.5.3 Reaction of 9 with Sodium Tetrakis(3,5-bis(trifluoromethyl)phenyl)borate

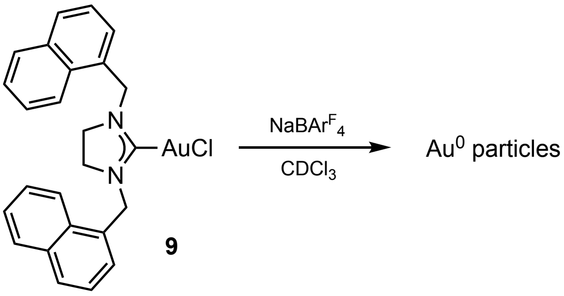

9

[(SINpMe)AuCl] (10.0 mg, 17.2 µmol, 1.0 equiv.) and NaBAr$^F_4$ (15.2 mg, 17.2 µmol, 1.0 equiv.) were dissolved in $CDCl_3$ (0.8 mL) and stirred at room temperature for two minutes. The resulting purple suspension was filtered and the pale purple filtrate was analyzed by NMR spectroscopy (see section 5.2.3).

8.5.4 Reaction of 9 with Silver Tetrafluoroborate

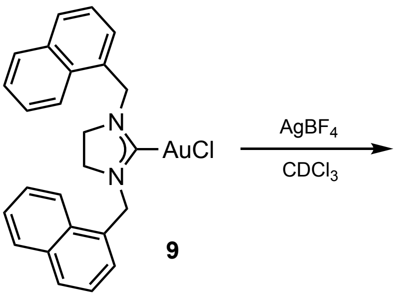

9

[(SINpMe)AuCl] (18.1 mg, 31.1 µmol, 1.0 equiv.) and $AgBF_4$ (6.0 mg, 31.1 µmol, 1.0 equiv.) were dissolved in $CDCl_3$ (0.8 mL) and stirred at room temperature for one hour. The mixture was analyzed by NMR spectroscopy (see section 5.2.3).

8.5.5 Synthesis of (1,3-Bis(1-naphthylmethyl)imidazolidin-2-ylidene)(1,5-cycloocta-diene)rhodium(I) Chloride, [(SINpMe)RhCl(cod)] (11)

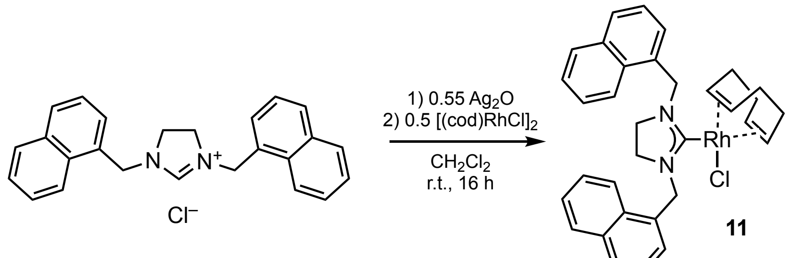

XLI

11

[SINpMeH]Cl (313.9 mg, 0.811 mmol, 1.0 equiv.) and Ag_2O (103.4 mg, 0.446 mmol, 0.55 equiv.) were suspended in CH_2Cl_2 (30 mL) and stirred for 30 minutes under exclusion of light. $[(cod)RhCl]_2$ (200.0 mg, 0.406 mmol, 0.50 equiv.) was added and the mixture was stirred overnight at room temperature under continuing light exclusion. All volatiles were removed *in vacuo* and the solid residue was taken up in THF (25 mL). The suspension was filtered and concentrated to 20 mL. Upon adding *n*-hexane (20 mL), a brown solid precipitated, which was removed by filtration. The clear yellow filtrate was concentrated *in vacuo*, yielding the product as a light yellow powder.

Yield: 352 mg (73%).

^{1}H NMR (300.13 MHz, 300 K, $CDCl_3$): δ (ppm) = 1.90 (m, 4H, cod), 2.26 (m, 4H, cod), 3.27 (m, 4H, NCH_2CH_2N), 3.66 (s, 2H, cod), 5.11 (s, 2H, cod), 5.92 (s, 4H, NCH_2Np), 7.48 (m, 2H, CH_{naph}), 7.55 (m, 2H, CH_{naph}), 7.64 (td, J = 7.7 Hz, 1.3 Hz, 2H, CH_{naph}), 7.84 (d, J = 8.0 Hz, 2H, CH_{naph}), 7.90 (d, J = 8.0 Hz, 2H, CH_{naph}), 8.45 (d, J = 8.4 Hz, 2H, CH_{naph}).

^{13}C{^{1}H} NMR (75.47 MHz, 300 K, $CDCl_3$): δ (ppm) = 28.6 (CH$_{2\ \text{cod}}$), 32.9 (CH$_{2\ \text{cod}}$), 48.6 (NCH$_2\mathit{C}$H$_2$N), 52.6 (NCH$_2$Np), 68.6 (CH$_{\text{cod}}$), 99.7 (CH$_{\text{cod}}$), 123.9 (CH$_{\text{naph}}$), 125.4 (CH$_{\text{naph}}$), 126.1 (CH$_{\text{naph}}$), 126.7 (CH$_{\text{naph}}$), 128.6 (CH$_{\text{naph}}$), 128.7 (CH$_{\text{naph}}$), 131.7 (C_{naph}), 132.1 (C_{naph}), 133.8 (C_{naph}). $\mathit{C}_{\text{carbene}}$ was not observed in the ^{13}C{^{1}H} NMR spectrum, but the corresponding signal was observed at 214.1 ppm in the ^{1}H/^{13}C HMBC spectrum (see section 4.3.2).

Elemental analysis: calcd. C 66.39, H 5.74, N 4.69; found C 65.92, H 5.82, N 4.44.

8.5.6 Synthesis of (1,3-Bis(1-(1-naphthyl)ethyl)imidazolidin-2-ylidene)(1,5-cyclooctadiene)rhodium(I) Chloride, [(SINpEt)RhCl(cod)] (12)

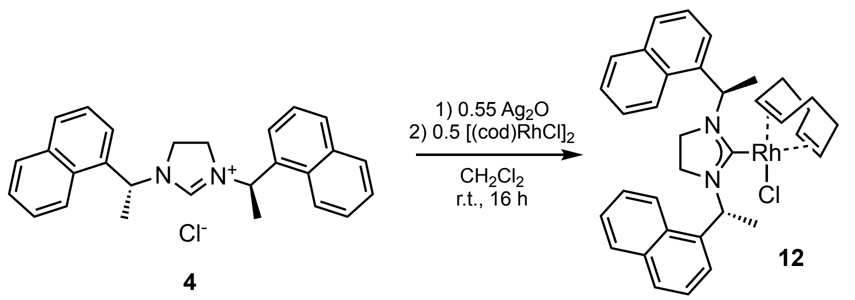

[SINpEtH]Cl (202.0 mg, 0.487 mmol, 1.0 equiv.), Ag_2O (60.0 mg, 0.259 mmol, 0.53 equiv.), and $[(cod)RhCl]_2$ (120.0 mg, 0.243 mmol, 0.50 equiv.) were suspended in CH_2Cl_2 (20 mL) and stirred at room temperature for 20 hours under strict light exclusion. The mixture was concentrated to a volume of 1 mL and separated by column chromatography (SiO_2, eluent: *n*-hexane/ethyl acetate 10:1 to 1:10). From the first and second band, unreacted $[(cod)RhCl]_2$ was recovered, while the third band contained **12**, which was isolated as a yellow powder upon removal of the eluent *in vacuo*.

Yield: 187.0 mg (61%).

^{1}H NMR (300.13 MHz, 300 K, $CDCl_3$): δ (ppm) = 0.82 (m, 1H, C*H*$_2$ (cod)), 1.17 (m, 1H, C*H*$_2$ (cod)), 1.43 (m, 1H, C*H*$_2$ (cod)), 1.57 (m, 1H, C*H*$_2$ (cod)), 1.66 (m, 1H, 1.69 (d, 3H, NCH(C*H*$_3$)Np), 1.83 (m, 1H, C*H*$_2$ (cod)), 1.89 (d, 3H, NCH(C*H*$_3$)Np), 2.25 (m, 1H, C*H*$_2$ (cod)), 2.33 (m, 1H, C*H*$_2$ (cod)), 2.91 (m, 1H, C*H* (cod)), 3.40 (m, 1H, NC*H*$_2$C*H*$_2$N), 3.51 (m, 1H, C*H* (cod)), 3.69 (m, 2H, NC*H*$_2$C*H*$_2$N), 3.89 (m, 1H, NC*H*$_2$C*H*$_2$N), 5.00 (m, 1H, C*H* (cod)), 5.09 (m, 1H, C*H* (cod)), 7.04 (q, 1H, NC*H*(CH$_3$)Np), 7.33 (d, 1H, C*H*$_{\text{naph}}$), 7.45 (d, 1H, C*H*$_{\text{naph}}$), 7.49 (d, 1H, C*H*$_{\text{naph}}$), 7.54 (m, 2H, C*H*$_{\text{naph}}$), 7.56 (m, 1H, C*H*$_{\text{naph}}$), 7.68 (m, 1H, C*H*$_{\text{naph}}$), 7.73 (m, 1H, C*H*$_{\text{naph}}$), 7.80 (d, 1H, C*H*$_{\text{naph}}$), 7.84 (m, 2H, C*H*$_{\text{naph}}$), 7.85 (m, 1H, NC*H*(CH$_3$)Np), 7.90 (d, 1H, C*H*$_{\text{naph}}$), 8.53 (d, 1H, C*H*$_{\text{naph}}$), 9.24 (d, 1H, C*H*$_{\text{naph}}$).

^{13}C{^{1}H} NMR (75.47 MHz, 300 K, $CDCl_3$): δ (ppm) = 20.0 (NCH(*C*H$_3$)Np), 20.5 (NCH(*C*H$_3$)Np), 27.3 (*C*H$_2$ (cod)), 29.4 (*C*H$_2$ (cod)), 32.1 (*C*H$_2$ (cod)), 32.6 (*C*H$_2$ (cod)), 44.4 (N*C*H$_2$*C*H$_2$N), 46.4 (N*C*H$_2$*C*H$_2$N), 53.8 (N*C*H(CH$_3$)Np), 56.2 (N*C*H(CH$_3$)Np), 66.7 (*C*H (cod)), 70.0 (*C*H (cod)), 98.2 (*C*H (cod)), 99.4 (*C*H (cod)), 121.4 (*C*H$_{\text{naph}}$), 123.9 (*C*H$_{\text{naph}}$), 124.0 (*C*H$_{\text{naph}}$), 124.6 (*C*H$_{\text{naph}}$), 125.3 (*C*H$_{\text{naph}}$), 126.0 (*C*H$_{\text{naph}}$), 126.1 (*C*H$_{\text{naph}}$), 126.2 (*C*H$_{\text{naph}}$), 126.4 (*C*H$_{\text{naph}}$), 127.0 (*C*H$_{\text{naph}}$), 127.5 (*C*H$_{\text{naph}}$), 128.3 (*C*H$_{\text{naph}}$), 128.7 (*C*H$_{\text{naph}}$), 128.9 (*C*H$_{\text{naph}}$), 130.4 (*C*$_{\text{naph}}$), 131.5 (*C*$_{\text{naph}}$), 134.0 (*C*$_{\text{naph}}$), 134.1 (*C*$_{\text{naph}}$), 135.9 (*C*$_{\text{naph}}$), 142.0 (*C*$_{\text{naph}}$), 213.0 (*C*$_{\text{carbene}}$).

Elemental analysis: calcd. C 67.26, H 6.13, N 4.48; found C 65.10, H 5.98, N 4.10.

8.5.7 Synthesis of (1,3-Bis(1-naphthylmethyl)benzimidazolin-2-ylidene)(1,5-cycloocta-diene)rhodium(I) Chloride, [(BNpMe)RhCl(cod)] (13)

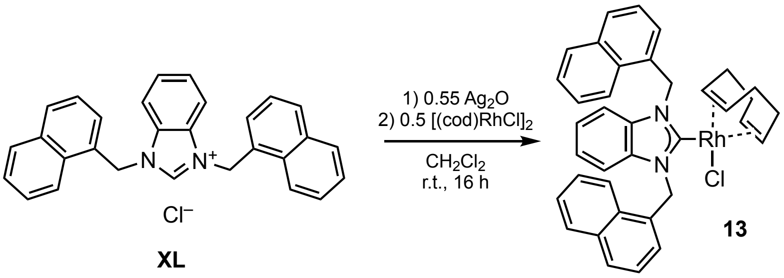

$[BNpMeH]Cl$ (88.2 mg, 0.200 mmol, 1.0 equiv.) and Ag_2O (25.8 mg, 0.110 mmol, 0.55 equiv.) were suspended in THF (10 mL) and stirred for 30 minutes under exclusion of light. $[(cod)RhCl]_2$ (50.0 mg, 0.100 mmol, 0.50 equiv.) was added and the mixture was stirred overnight at room temperature under continuing light exclusion. All volatiles were removed *in vacuo*. The crude product was purified by column chromatography (SiO_2, eluent: *n*-hexane/CH_2Cl_2 4:1 to pure CH_2Cl_2).

Yield: 86.6 mg (67%).

^1H NMR (300.13 MHz, 300 K, $CDCl_3$): δ (ppm) = 1.47-1.76 (overlapping m, 6H, CH_2 (cod)), 1.93-2.08 (m, 2H, CH_2 (cod)), 3.31 (m, 2H, C*H* (cod)), 5.07 (m, 2H, C*H* (cod)), 6.31 (d, J_{HH} = 16.7 Hz, 2H, NCH_2Np), 6.96-7.09 (m, 6H, overlapping CH_{naph} and $CH_{backbone}$), 7.28 (d, J_{HH} = 16.7 Hz, 2H, NCH_2Np), 7.36 (t, J_{HH} = 7.5 Hz, 2H, CH_{naph}), 7.64 (m, 2H, CH_{naph}), 7.74 (m, 2H, CH_{naph}), 7.84 (d, J = 8.3 Hz, 2H, CH_{naph}), 7.98 (d, J = 8.3 Hz, 2H, CH_{naph}), 8.42 (d, J = 8.3 Hz, 2H, CH_{naph}).

$^{13}C\{^1H\}$ NMR (75.47 MHz, 300 K, $CDCl_3$): δ (ppm) = 28.3 (CH_2 (cod)), 32.6 (CH_2 (cod)), 50.2 (NCH_2Np), 69.3 (*C*H (cod)), 100.5 (*C*H (cod)), 111.0 ($CH_{backbone}$), 122.8 ($CH_{backbone}$), 122.8 (CH_{naph}), 123.6 (CH_{naph}), 125.4 (CH_{naph}), 126.3 (CH_{naph}), 126.9 (CH_{naph}), 128.2 (CH_{naph}), 129.0 (CH_{naph}), 130.6 (C_{naph}), 131.9 (C_{naph}), 133.7 (C_{naph}), 135.4 ($C_{backbone}$), 199.1 (d, $^1J_{CRh}$ = 51.2 Hz, $C_{carbene}$).

Elemental analysis: calcd. C 66.39, H 5.74, N 4.69; found C 65.92, H 5.82, N 4.44.

8.5.8 Reaction of 11 with Sodium Tetrakis(3,5-bis(trifluoromethyl)phenyl)borate

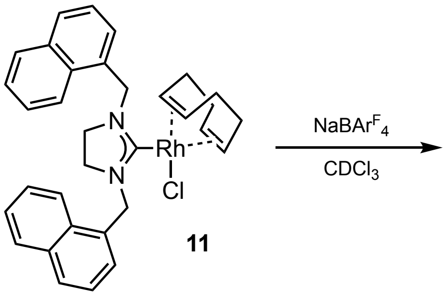

[(SINpMe)RhCl(cod)] (29.9 mg, 50.0 µmol, 1.0 equiv.) and NaBAr^F$_4$ (44.3 mg, 50.0 µmol, 1.0 equiv.) were stirred in $CDCl_3$ (1 mL) at room temperature for 15 minutes, during which time a color change from yellow to orange was observed. The mixture was filtered and analyzed by NMR spectroscopy (see section 5.3.4).

8.5.9 Reaction of 13 with Silver Tetrafluoroborate

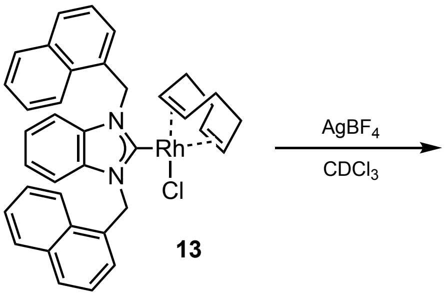

[(BNpMe)RhCl(cod)] (32.3 mg, 50.0 µmol, 1.0 equiv.) and $AgBF_4$ (9.7 mg, 50 µmol, 1.0 equiv.) were stirred in $CDCl_3$ (0.8 mL) at room temperature for 15 minutes. The mixture was filtered and analyzed by NMR spectroscopy (see section 5.3.4).

8.5.10 Synthesis of (1,3-Bis(1-naphthyl)benzimidazolidin-2-ylidene)(*p*-cymene)ruthenium(II) Dichloride, [(BNpMe)RuCl₂(cym)] (15)

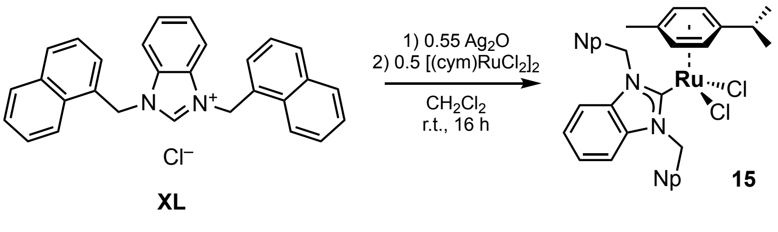

[BNpMeH]Cl (869.9 mg, 2.000 mmol, 1.0 equiv.), Ag_2O (243.3 mg, 1.050 mmol, 0.53 equiv.), and $[(cym)RuCl_2]_2$ (612.4 mg, 1.000 mmol, 0.50 equiv.) were suspended in CH_2Cl_2 (30 mL) and stirred at room temperature overnight under exclusion of light. After filtration, all volatiles were removed *in vacuo*, yielding **15** as a bright red solid.

Yield: 1.3213 g (94%).

^{1}H NMR (300.13 MHz, 300 K, $CDCl_3$): δ (ppm) = 0.76 (d, $^3J_{HH}$ = 6.9 Hz, 6H, $CH(CH_3)_2$ (cym)), 1.51 (s, 3H, CH_3 (cym)), 2.10 (septet, $^3J_{HH}$ = 6.9 Hz, 1H, $CH(CH_3)_2$ (cym)), 4.94 (d, $^3J_{HH}$ = 6.1

Hz, 2H, C*H*arene (cym)), 5.17 (d, $^3J_{HH}$ = 6.1 Hz, 2H, C*H*arene (cym)), 6.00 (d, J = 18.5 Hz, 2H, NC*H*$_2$Ar), 6.73 (d, J = 7.1 Hz, 2H, C*H*naph), 7.16 (s, 4H, C*H*backbone), 7.42 (m, 2H, C*H*naph), 7.53 (d, J = 18.5 Hz, 2H, NC*H*$_2$Ar), 7.64 (m, 2H, C*H*naph), 7.70 (m, 2H, C*H*naph), 7.85 (d, J = 8.2 Hz, 2H, C*H*naph), 7.97 (m, 2H, C*H*naph), 8.29 (d, J = 8.2 Hz, 2H, C*H*naph).

^{13}C{^{1}H} NMR (75.47 MHz, 300 K, CDCl$_3$): δ (ppm) = 17.8 (*C*H$_3$ (cym)), 22.3 (CH(*C*H$_3$)$_2$ (cym)), 30.5 (*C*H(CH$_3$)$_2$ (cym)), 50.6 (N*C*H$_2$Ar), 84.9 (*C*Harene (cym)), 85.6 (*C*Harene (cym)), 96.6 (*C*quat (cym)), 105.5 (*C*quat (cym)), 111.0 (*C*Hbackbone), 121.5 (*C*Hnaph), 123.1 (*C*Hnaph), 123.6 (*C*Hbackbone), 125.1 (*C*Hnaph), 126.7 (*C*Hnaph), 127.2 (*C*Hnaph), 128.1 (*C*Hnaph), 128.9 (*C*Hnaph), 130.5 (*C*naph), 133.4 (*C*naph), 133.8 (*C*naph), 136.0 (*C*backbone), 192.6 (*C*carbene).

Elemental analysis: calcd: C 66.47, H 5.15, N 3.98; found: C 64.24, H 4.88, N 3.78.

8.5.11 Synthesis of (1,3-Bis(1-naphthyl)imidazolidin-2-ylidene)(*p*-cymene)-ruthenium(II) Dichloride, [(SINpMe)RuCl$_2$(cym)] (16)

The synthesis of **16** followed a procedure by Peris and co-workers.[23]

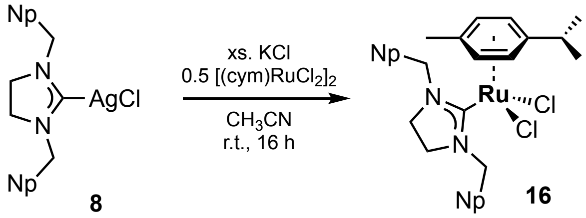

[(SINpMe)AgCl] (32.3 mg, 0.065 mmol, 1.0 equiv.), [(cym)RuCl$_2$]$_2$ (20.0 mg, 0.033 mmol, 0.50 equiv.), and KCl (48.7 mg, 0.653 mmol, 10 equiv.) were suspended in acetonitrile (3 mL) and stirred overnight at room temperature. The mixture was filtered, yielding a yellow solution. Slow diffusion of diethyl ether into the CH$_3$CN solution gave red crystals suitable for X-ray diffraction.

^{1}H NMR (300.13 MHz, 300 K, CDCl$_3$): δ (ppm) = 0.99 (d, $^3J_{HH}$ = 6.9 Hz, 6H, CH(C*H*$_3$)$_2$ (cym)), 1.84 (s, 3H, C*H*$_3$ (cym)), 2.46 (septet, $^3J_{HH}$ = 6.9 Hz, 1H, C*H*(CH$_3$)$_2$ (cym)), 3.63 (s, 2H, NC*H*$_2$C*H*$_2$N), 3.95 (s, 2H, NC*H*$_2$C*H*$_2$N), 5.10 (d, $^3J_{HH}$ = 6.0 Hz, C*H*arene (cym)), 5.31 (d, $^3J_{HH}$ = 6.0 Hz, C*H*arene (cym)), 5.39 (d, J = 16.5 Hz, 2H, NC*H*$_2$Np), 6.15 (d, J = 16.5 Hz, 2H, NC*H*$_2$Np), 7.59 (overlapping m, 8H, C*H*naph), 7.86 (m, 2H, C*H*naph), 7.93 (m, 2H, C*H*naph), 8.16 (m, 2H, C*H*naph).

8.5.12 Synthesis of (1,3-Bis(1-naphthyl)imidazolin-2-ylidene)(*p*-cymene)-ruthenium(II) dichloride, [(cym)RuCl$_2$(INpMe)] (17)

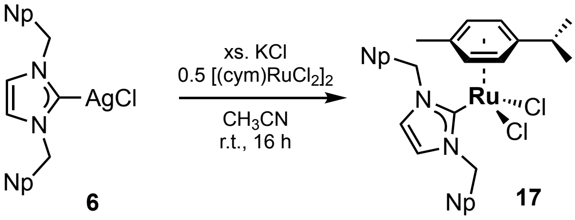

The synthesis of **17** followed a procedure by Peris and co-workers.[23]

[(INpMe)AgCl] (32.1 mg, 0.065 mmol, 1.0 equiv.), [(cym)RuCl$_2$]$_2$ (20.0 mg, 0.033 mmol, 0.50 equiv.), and KCl (48.7 mg, 0.653 mmol, 10 equiv.) were suspended in acetonitrile (3 mL) and stirred at room temperature overnight under exclusion of light. After filtration, all volatiles were removed *in vacuo* and the residue was extracted with CH$_2$Cl$_2$. Layering with diethyl ether gave a small amount of a reddish powder.

^{1}H NMR (300.13 MHz, 300 K, CDCl$_3$): δ (ppm) = 0.96 (d, $^3J_{HH}$ = 6.9 Hz, 6H, CH(CH_3)$_2$ (cym)), 1.75 (s, 3H, CH_3 (cym)), 2.45 (septet, $^3J_{HH}$ = 6.9 Hz, 1H, CH(CH$_3$)$_2$ (cym)), 4.96 (d, $^3J_{HH}$ = 6.0 Hz, 2H, CH_{arene} (cym)), 5.21 (d, $^3J_{HH}$ = 6.0 Hz, 2H, CH_{arene} (cym)), 6.98 (s, 4H, NCHCHN), 6.03 (br, 2H, NCH_2Ar), 6.68 (br, 2H, NCH_2Ar), 7.18 (dd, J = 0.9 Hz, 7.1 Hz, 2H, CH_{naph}), 7.53 (m, 2H, CH_{naph}), 7.60 (overlapping m, 4H, CH_{naph}), 7.88 (d, J = 8.3 Hz, 2H, CH_{naph}), 7.93 (m, 2H, CH_{naph}), 8.14 (m, 2H, CH_{naph}).

8.5.13 Synthesis of (1-(1-Naphthylmethyl)-3-((1-naphthyl)methyl)benzimidazolidin-2-ylidene)diphenylruthenium(II), [RuPh$_2$(BNpMe*)] (18)

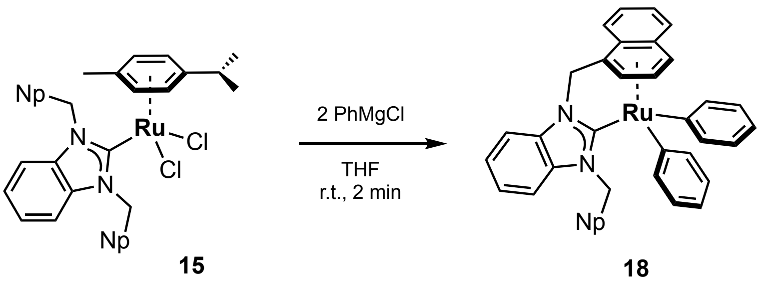

[(BNpMe)RuCl$_2$(cym)] (211.4 mg, 0.30 mmol, 1.0 equiv.) was suspended in THF (7 mL). PhMgCl (2 mol L^{-1} in THF, 0.30 mL, 0.60 mmol, 2.0 equiv.) was added and the mixture was stirred for two minutes, whereupon a clear, deep red solution formed. The mixture was filtered and all volatiles were removed *in vacuo*. After washing with *n*-hexane, the residue was extracted with toluene. The extract was concentrated to a volume of 10 mL and stored at –30 °C, whereupon **18** crystallized as red blocks.

Yield: 108.9 mg (56%).

^{1}H NMR (300.13 MHz, 300 K, C_6D_6): δ (ppm) = 3.79 (d, J = 12.5 Hz, 1H, NC*H*$_2$Ar), 4.88 (d, J = 12.5 Hz, 1H, NC*H*$_2$Ar), 5.10 (d, J = 5.3 Hz, 1H, C*H*$_{\mathrm{naph}}$), 5.26 (d, J = 17.1 Hz, 1H, NC*H*$_2$Ar), 5.49 (dd, J = 5.3 Hz, 6.6 Hz, 1H, C*H*$_{\mathrm{naph}}$), 5.56 (d, J = 17.1 Hz, 1H, NC*H*$_2$Ar), 5.68 (d, J = 6.6 Hz, 1H, NC*H*$_2$Ar), 6.31 (d, J = 7.1 Hz, 1H, C*H*$_{\mathrm{naph}}$), 6.36 (m, 1H, C*H*$_{\mathrm{naph}}$), 6.44 (t, J = 7.3 Hz, 1H, C*H*$_{\mathrm{naph}}$), 6.63 (t, J = 7.6 Hz, 1H, C*H*$_{\mathrm{naph}}$), 6.75 (m, 1H, C*H*$_{\mathrm{naph}}$), 6.93 (m, 1H, C*H*$_{\mathrm{naph}}$), 7.12 (m, 1H, C*H*$_{\mathrm{naph}}$), 7.21 (m, 1H, C*H*$_{\mathrm{naph}}$), 7.27 (m, 1H, C*H*$_{\mathrm{naph}}$), 7.34 (m, 1H, C*H*$_{\mathrm{naph}}$), 7.47 (m, 1H, C*H*$_{\mathrm{naph}}$), 7.56 (m, 1H, C*H*$_{\mathrm{naph}}$).

8.5.14 Catalytic Hydrosilylation of 1-Hexene

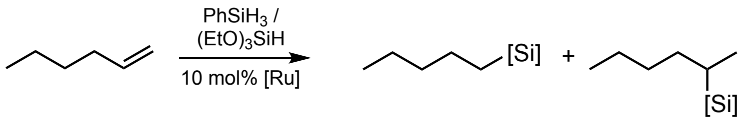

Aliquots of 1-hexene (12.6 µL, 0.10 mmol, 1.0 equiv.) and triethoxysilane (18.5 µL, 0.10 mmol, 1.0 equiv.) were each added to two sample vials and dissolved in toluene (1 mL). To the first vial, [RuPh$_2$(BNpMe*)] (7.0 mg, 0.010 mmol, 10 mol%) was added, while [(BNpMe)RuCl$_2$(cym)] (6.5 mg, 0.010 mmol, 10 mol%) was added to the second. The solutions were stirred at room temperature for 15 hours. After quenching with 1 mL of a saturated $NaHCO_3$ solution, *n*-pentadecane (50 µL) and *n*-hexane (1 mL) were added, the solutions filtered over pads of basic Al_2O_3, and analyzed by gas chromatography (see section 5.4.5).

In a subsequent set of reactions, 1-hexene (12.6 µL, 0.10 mmol, 1.0 equiv.) and phenylsilane (12.4 µL, 0.10 mmol, 1.0 equiv.) were reacted with 10 mol% of [RuPh$_2$(BNpMe*)] and [(BNpMe)RuCl$_2$(cym)], respectively. Reaction and work-up conditions were identical.

8.6 Experimental Details – Synthesis of NHC-Iron and -Cobalt Complexes

8.6.1 Synthesis of Bis(1,3-bis(1-naphthylmethyl)imidazolidin-2-ylidene)tetrachlorido-diiron(II), [(SINpMe)FeCl$_2$]$_2$ (23)

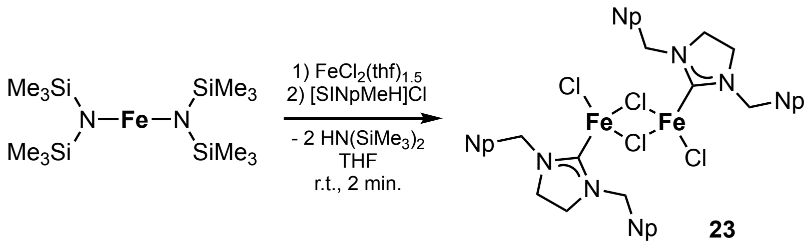

23

[Fe{N(SiMe$_3$)$_2$}$_2$] (75.4 mg, 0.200 mmol, 1.0 equiv.) and FeCl$_2$(thf)$_{1.5}$ (47.0 mg, 0.200 mmol, 1.0 equiv.) were dissolved in THF (8 mL) and stirred for ten minutes at room temperature, until a clear, light orange solution formed. Subsequently, [SINpMeH]Cl (154.8 mg, 0.400 mmol, 2.0 equiv.) was added and the mixture was shaken vigorously for ten seconds. All volatiles were immediately removed *in vacuo*. The remaining off-white solid was washed with 2 mL of *n*-hexane. The residue was taken up in toluene. After filtration, the pale yellowish toluene solution was concentrated *in vacuo* and stored at –35 °C, whereupon colorless crystals formed. The product was isolated by filtration and dried *in vacuo*. After drying, the product contains one equivalent of toluene.

Yield: 93.0 mg (41%).

^{1}H NMR (300.13 MHz, 300 K, THF-d_8): δ (ppm) = –20.5 (br), –13.6 (br), 6.3 (br), 7.0 (br s), 7.4 (br), 7.5 (br), 7.6 (br), 7.9 (br), 7.9 (br), 8.4 (br).

UV-vis (THF solution): λ (nm) / ε (L mol^{-1} cm^{-1}): 226 ($1.03 \cdot 10^5$), 282 ($2.98 \cdot 10^4$).

Elemental analysis: calcd. C 67.51, H 5.31, N 4.92; found C 68.79, H 5.28, N 5.33.

8.6.2 Synthesis of Bis(1,3-bis(1-naphthylmethyl)imidazolidin-2-ylidene)tetrachlorido-dicobalt(II), [(SINpMe)CoCl$_2$]$_2$ (24)

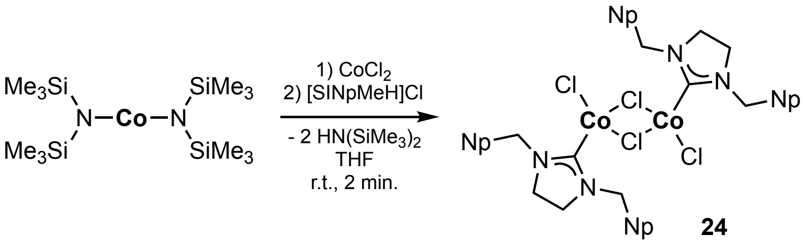

[Co{N(SiMe$_3$)$_2$}$_2$] (82.4 mg, 0.217 mmol, 1.0 equiv.) and CoCl$_2$ (28.2 mg, 0.217 mmol, 1.0 equiv.) were dissolved in THF (5 mL) and stirred for five minutes at room temperature. Subsequently, [SINpMeH]Cl (168.1 mg, 0.434 mmol, 2.0 equiv.) was added and the mixture was shaken vigorously for ten seconds. All volatiles were immediately removed *in vacuo*. The remaining blue solid was washed with 2 mL of *n*-hexane. The residue was taken up in toluene. After filtration, the blue-green toluene solution was concentrated *in vacuo* to a volume of 6 mL and stored at –35 °C, whereupon turquoise crystals formed. The product was isolated by filtration and dried *in vacuo*. After drying, the product contains 0.9 equivalents of toluene.

Yield: 37.1 mg (15%).

^{1}H NMR (300.13 MHz, 300 K, THF-d_8): δ (ppm) = –4.9 (br), –2.5 (br), 4.2 (br), 6.4 (br), 6.7 (br), 6.7 (br), 6.9 (br), 7.0 (br), 7.0 (br), 7.1 (m), 7.2 (m), 7.3 (br), 7.5 (br), 7.6 (br), 7.7 (br).

Elemental analysis: calcd. C 67.14, H 5.28, N 4.89; found C 67.42, H 5.20, N 4.96.

UV-vis (THF solution): λ (nm) / ε (L mol^{-1} cm^{-1}): 225 ($1.66 \cdot 10^5$), 282 ($4.28 \cdot 10^4$), 647 (40.1).

8.6.3 Synthesis of Bis(bis(trimethylsilyl)amido)(1,3-bis(1-naphthyl)imidazolidin-2-ylidene)iron(II), $[(\mathrm{SINp})\mathrm{Fe}\{\mathrm{N}(\mathrm{SiMe_3})_2\}_2]$ (25)

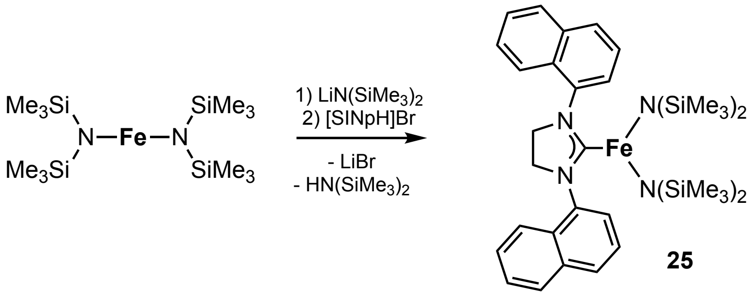

25

$[\mathrm{Fe}\{\mathrm{N}(\mathrm{SiMe_3})_2\}_2]$ (750.0 mg, 1.991 mmol, 1.0 equiv.) and $\mathrm{LiN}(\mathrm{SiMe_3})_2$ (466.1 mg, 1.991 mmol, 1.0 equiv.) were dissolved in toluene (10 mL) and stirred for 10 minutes. [SINpH]Br (807.1 mg, 1.991 mmol, 1.0 equiv.) was added and the mixture was stirred for one hour at room temperature. All volatiles were removed *in vacuo*. The solid residue was washed with cold *n*-pentane (1 mL) and subsequently extracted with toluene. After filtration, the solvent was removed *in vacuo*, yielding the product as a pale yellow solid.

Yield: 398.4 mg (29%).

^{1}H NMR (300.13 MHz, 300 K, C_6D_6): δ (ppm) = –25 to –18 (br); –13.2 (br s); –8.2 (br s) –4.7 (br s); 0.0 (br s); 0.6 (s); 1.4 (s); 1.6 (s); 1.8 (s); 3.7 (br s); 7.6 (s); 7.7 (s); 12.0 to 16.8 (br).

UV-vis (Et_2O solution): λ (nm) / ε (L mol^{-1} cm^{-1}): 228 ($8.52\cdot10^4$), 294 ($3.52\cdot10^4$).

Elemental analysis: calcd. C 60.14, H 7.79, N 8.02; found C 61.63, H 7.43, N 7.72.

Magnetic moment (Evans method, C_6D_6, 300 K): $\mu_{\mathrm{eff}} = 4.8\ \mu_B$.

8.6.4 Synthesis of Bis(bis(trimethylsilyl)amido)(1,3-bis(1-naphthylmethyl)imidazolidin-2-ylidene)iron(II), $[(\mathrm{BNpMe})\mathrm{Fe}\{\mathrm{N}(\mathrm{SiMe_3})_2\}_2]$ (26)

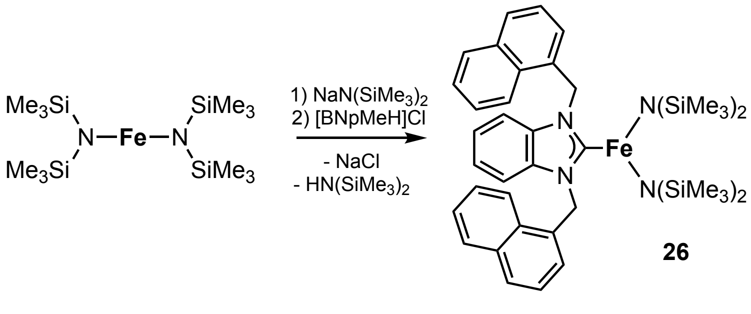

26

$[\mathrm{Fe}\{\mathrm{N}(\mathrm{SiMe_3})_2\}_2]$ (376.6 mg, 1.000 mmol, 1.0 equiv.) and $\mathrm{NaN}(\mathrm{SiMe_3})_2$ (183.4 mg, 1.000 mmol, 1.0 equiv.) were dissolved in toluene (10 mL) and stirred for 10 minutes. [BNpMeH]Cl (435.0 mg, 1.000 mmol, 1.0 equiv.) was added and the mixture was stirred for one hour at room temperature. All volatiles were removed *in vacuo*. The solid residue was washed with cold *n*-pentane (1 mL) and subsequently extracted with toluene. After filtration, the solvent was removed *in vacuo*, yielding the product as a pale yellow solid.

Yield: 558.1 mg (0.720 mmol, 72%).

^{1}H NMR (300.13 MHz, 300 K, C_6D_6): δ (ppm) = –65.5 (br s); –13.8 (br s); –8.6 (br s); –2.9 (br s); –1.8 (br s); 1.5 (br s); 5.6 (br); 7.2 (br s); 11.3 (br s); 21.4 (br s); 42.5 (br s).

UV-vis (Et_2O solution): λ (nm) / ε (L mol^{-1} cm^{-1}): 225 ($1.88 \cdot 10^5$), 282 ($5.70 \cdot 10^4$), 411 ($7.88 \cdot 10^3$).

Elemental analysis: calcd. C 63.53, H 7.54, N 7.23; found C 63.62, H 7.24, N 7.07.

Magnetic moment (Evans method, C_6D_6, 300 K): $\mu_{eff} = 4.7\ \mu_B$.

8.6.5 Synthesis of Bis(bis(trimethylsilyl)amido)(1,3-bis(1-naphthylmethyl)imidazolidin-2-ylidene)iron(II), [(SINpMe)Fe{N(SiMe$_3$)$_2$}$_2$] (27)

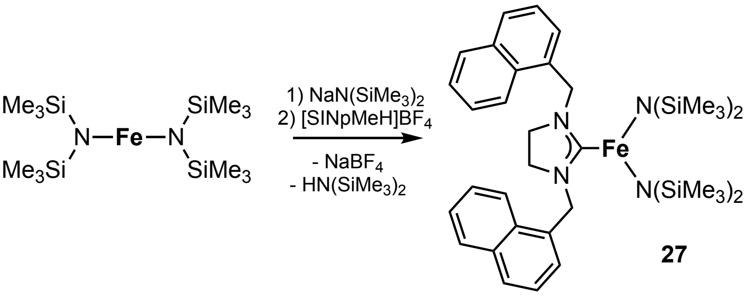

[Fe{N($SiMe_3$)$_2$}$_2$] 376.6 mg, 1.000 mmol, 1.0 equiv.) and NaN($SiMe_3$)$_2$ (183.4 mg, 1.000 mmol, 1.0 equiv.) were dissolved in toluene (10 mL) and stirred for 10 minutes. [SINpMeH]BF_4 (438.3 mg, 1.000 mmol, 1.0 equiv.) was added and the mixture was stirred for one hour at room temperature. All volatiles were removed *in vacuo*. The solid residue was washed with cold *n*-pentane (1 mL) and subsequently extracted with toluene. After filtration, the solvent was removed *in vacuo*, yielding the product as a pale yellow solid.

Yield: 508.9 mg (70%).

^{1}H NMR (300.13 MHz, 300 K, C_6D_6): δ (ppm) = –26.8 (br s); –15.1 (s); –5.6 (br s); –2.3 (s); 0.2 (s); 1.9 (s); 2.1 (s); 3.3 (d); 4.5 (s); 5.6 (s); 2.5 to 6 (br); 7.0 (s); 86 to 103 (br).

UV-vis (Et_2O solution): λ (nm) / ε (L mol^{-1} cm^{-1}): 225 ($1.82 \cdot 10^5$), 281 ($6.71 \cdot 10^4$).

Elemental analysis: calcd. C 61.12, H 8.04, N 7.71; found C 61.11, H 7.64, N 7.63.

Magnetic moment (Evans method, C_6D_6, 300 K): $\mu_{eff} = 4.4\ \mu_B$

8.6.6 Synthesis of Bis(bis(trimethylsilyl)amido)((*R*,*R*)-1,3-bis(1-(1-naphthyl)ethyl)-imidazolidin-2-ylidene)iron(II), [(SINpEt)Fe{N(SiMe$_3$)$_2$}$_2$] (28)

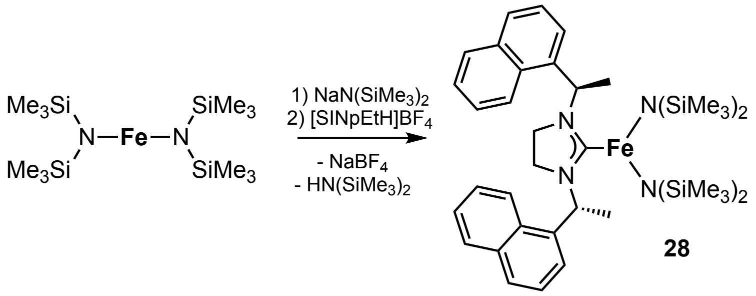

[Fe{N(SiMe$_3$)$_2$}$_2$] (376.6 mg, 1.000 mmol, 1.0 equiv.) and NaN(SiMe$_3$)$_2$ (183.4 mg, 1.000 mmol, 1.0 equiv.) were dissolved in toluene (5 mL) and stirred for 10 minutes. [SINpEtH]BF$_4$ (466.3 mg, 1.000 mmol, 1.0 equiv.) was added and the mixture was stirred for one hour at room temperature. All volatiles were removed *in vacuo*. The solid residue was washed with cold *n*-pentane (1 mL) and subsequently extracted with toluene. After filtration, the solvent was removed *in vacuo*, yielding the product as a pale yellow solid.

Yield: 513.5 mg (0.680 mmol, 68%).

^{1}H NMR (300.13 MHz, 300 K, C_6D_6): δ (ppm) = –26.9 (br s); –15.3 (s); –5.7 (br s); –2.3 (s); 0.1 (s); 0.9 (t); 1.3 (s); 1.9 (s); 4.4 (br s); 4.5 (s); 5.6 (s); 2.5 to 6.5 (br); 85 to 100 (br).

UV-vis (Et_2O solution): λ (nm) / ε (L mol^{-1} cm^{-1}): 224 ($1.60 \cdot 10^5$), 281 ($3.38 \cdot 10^4$).

Elemental analysis: calcd. C 62.03, H 8.28, N 7.42; found C 62.56, H 7.86, N 7.02.

8.6.7 Synthesis of Bis(bis(trimethylsilyl)amido)(1,3-bis(1-naphthyl)imidazolidin-2-ylidene)cobalt(II), [(SINp)Co{N(SiMe$_3$)$_2$}$_2$] (21)

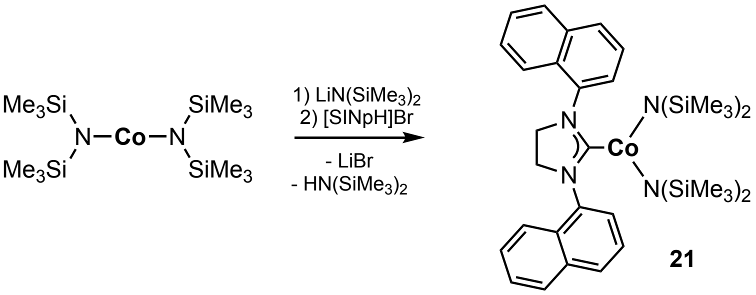

[Co{N(SiMe$_3$)$_2$}$_2$] (750.0 mg, 1.975 mmol, 1.0 equiv.) and LiN(SiMe$_3$)$_2$ (462.3 mg, 1.975 mmol, 1.0 equiv.) were dissolved in toluene (10 mL) and stirred for 10 minutes. [SINpH]Br (796.6 mg, 1.975 mmol, 1.0 equiv.) was added and the mixture was stirred for one hour at room temperature. All volatiles were removed *in vacuo*. The solid residue was washed with cold *n*-pentane (1 mL) and subsequently extracted with toluene. After filtration, the solvent was removed *in vacuo*, yielding the product as a green solid.

Yield: 262.4 mg (19%).

^{1}H NMR (300.13 MHz, 300 K, C_6D_6): δ (ppm) = –29.8 (br s); –20.7 (br s); –10.1 (br s); –3.3 (br s); 3.9 (br s); 46.7 (br s); 107.5 (br s); 110.2 (br s); 113.3 (br s).

UV-vis (Et_2O solution): λ (nm) / ε (L mol^{-1} cm^{-1}): 224 ($1.77 \cdot 10^5$), 285 ($4.47 \cdot 10^4$), 647 (134), 719 (89.2).

Elemental analysis: calcd.: C 59.87, H 7.75, N 7.98; found: C 60.61, H 7.52, N 7.73.

Magnetic moment (Evans method, C_6D_6, 300 K): $\mu_{eff} = 5.0\ \mu_B$.

8.6.8 Synthesis of Bis(bis(trimethylsilyl)amido)(1,3-bis(1-naphthylmethyl)imidazolin-2-ylidene)cobalt(II), [(INpMe)Co{N(SiMe₃)₂}₂] (29)

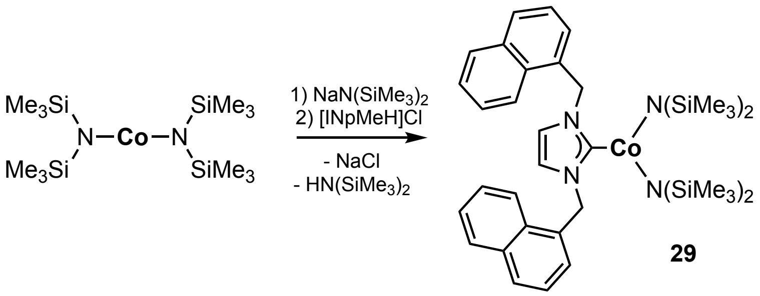

29

[Co{N($SiMe_3$)$_2$}$_2$] (57.0 mg, 0.150 mmol, 1.0 equiv.) and NaN($SiMe_3$)$_2$ (27.5 mg, 0.150 mmol, 1.0 equiv.) were dissolved in toluene (10 mL) and stirred for 10 minutes. [INpMeH]Cl (57.7 mg, 0.150 mmol, 1.0 equiv.) was added and the mixture was stirred for one hour at room temperature. All volatiles were removed *in vacuo*. The solid residue was washed with cold *n*-pentane (1 mL) and subsequently extracted with toluene. After filtration, the solvent was removed *in vacuo*, yielding the product as a green solid.

Yield: 80.8 mg (74%).

^{1}H NMR (300.13 MHz, 300 K, C_6D_6): δ (ppm) = –17.2 (br s); –5.2 (br s); –3.2 (s); 0.0 (d); 0.4 (s); 1.4 (br s); 1.8 (t); 41.0 (br s); 42.7 (s); 52.0 to 58.2 (br); 59.3 (s).

Elemental analysis: calcd. C 61.03, H 7.75, N 7.69; found C 61.49, H 7.48, N 7.59.

8.6.9 Synthesis of Bis(bis(trimethylsilyl)amido)(1,3-bis(1-naphthylmethyl)imidazolidin-2-ylidene)cobalt(II), [(BNpMe)Co{N(SiMe₃)₂}₂] (30)

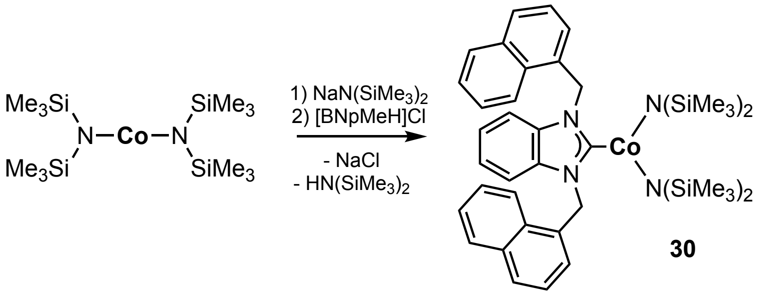

30

[Co{N(SiMe$_3$)$_2$}$_2$] (379.7 mg, 1.000 mmol, 1.0 equiv.) and NaN(SiMe$_3$)$_2$ (183.4 mg, 1.000 mmol, 1.0 equiv.) were dissolved in toluene (10 mL) and stirred for 10 minutes. [BNpMeH]Cl (435.0 mg, 1.000 mmol, 1.0 equiv.) was added and the mixture was stirred for one hour at room temperature. All volatiles were removed *in vacuo*. The solid residue was washed with cold *n*-pentane (1 mL) and subsequently extracted with toluene. After filtration, the solvent was removed *in vacuo*, yielding the product as a green solid.

Yield: 622.6 mg (80%).

^{1}H NMR (300.13 MHz, 300 K, C$_6$D$_6$): δ (ppm) = –18.2 (br s); –6.9 (br s); –3.3 (br s); 0.2 (s); 0.4 (s); 1.0 (s); 1.3 (s); 2.2 (s); 3.2 (s); 3.5 (s); 4.0 (s); 4.6 (d); 7.1 (d); 32.5 (br s); 37.2 to 40.2 (br).

UV-vis (Et$_2$O solution): λ (nm) / ε (L mol^{-1} cm^{-1}): 225 ($1.82\cdot10^5$), 282 ($4.30\cdot10^4$), 607 (130), 642 (120), 707 (212).

Elemental analysis: calcd. C 63.28, H 7.51, N 7.20; found C 63.34, H 7.34, N 7.01.

Magnetic moment (Evans method, C$_6$D$_6$, 300 K): $\mu_{\text{eff}} = 4.3\ \mu_B$.

8.6.10 Synthesis of Bis(bis(trimethylsilyl)amido)(1,3-bis(1-naphthylmethyl)imidazolidin-2-ylidene)cobalt(II), [(SINpMe)Co{N(SiMe₃)₂}₂] (31)

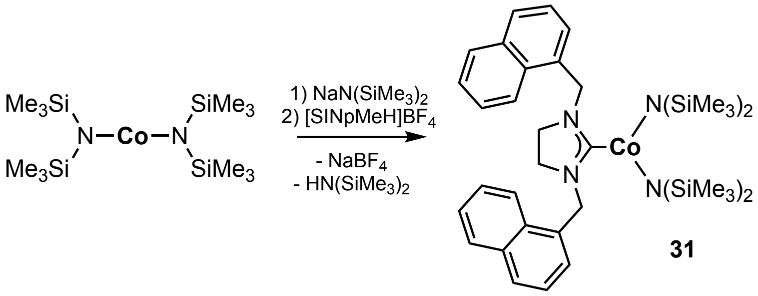

31

[Co{N(SiMe$_3$)$_2$}$_2$] (379.7 mg, 1.000 mmol, 1.0 equiv.) and NaN(SiMe$_3$)$_2$ (183.4 mg, 1.000 mmol, 1.0 equiv.) were dissolved in toluene (10 mL) and stirred for 10 minutes. [SINpMeH]BF$_4$ (438.3 mg, 1.000 mmol, 1.0 equiv.) was added and the mixture was stirred for one hour at room temperature. All volatiles were removed *in vacuo*. The solid residue was washed with cold *n*-pentane (1 mL) and subsequently extracted with toluene. After filtration, the solvent was removed *in vacuo*, yielding the product as a green solid.

Yield: 554.9 mg (76%).

^{1}H NMR (300.13 MHz, 300 K, C_6D_6): δ (ppm) = –17.1 (br s); –7.1 (s); –6.7 (br s); 0.1 (s); 1.3 (m); 2.1 (m); 3.4 (d); 4.0 (d); 23.2 (br s); 36.9 (br s); 99.0 (br s).

UV-vis (Et_2O solution): λ (nm) / ε (L mol^{-1} cm^{-1}): 224 ($1.78 \cdot 10^5$), 281 ($4.43 \cdot 10^4$), 605 (103), 641 (109), 703 (147).

Elemental analysis: calcd. C 60.86, H 8.01, N 7.67; found C 60.93, H 7.72, N 7.46.

Magnetic moment (Evans method, C_6D_6, 300 K): $\mu_{eff} = 4.7\ \mu_B$.

8.6.11 Synthesis of Bis(bis(trimethylsilyl)amido)((*R*,*R*)-1,3-bis(1-(1-naphthyl)ethyl)-imidazolidin-2-ylidene)cobalt(II), [(SINpEt)Co{N(SiMe₃)₂}₂] (32)

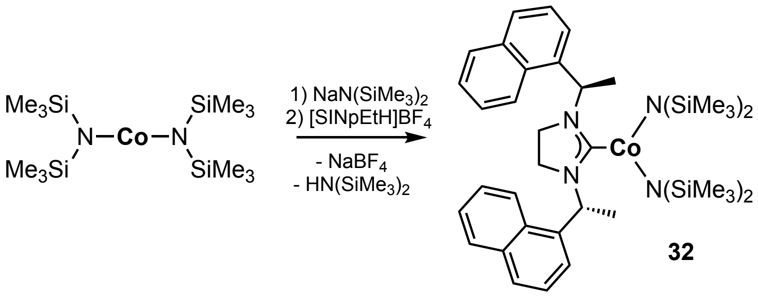

[Co{N(SiMe$_3$)$_2$}$_2$] (379.7 mg, 1.000 mmol, 1.0 equiv.) and NaN(SiMe$_3$)$_2$ (183.4 mg, 1.000 mmol, 1.0 equiv.) were dissolved in toluene (10 mL) and stirred for 10 minutes. [SINpEtH]BF$_4$ (466.3 mg, 1.000 mmol, 1.0 equiv.) was added and the mixture was stirred for one hour at room temperature. All volatiles were removed *in vacuo*. The solid residue was washed with cold *n*-pentane (1 mL) and subsequently extracted with toluene. After filtration, the solvent was removed *in vacuo*, yielding the product as a green solid.

Yield: 470.1 mg (62%).

^{1}H NMR (300.13 MHz, 300 K, C_6D_6): δ (ppm) = –60.3 (br s); –36.6 (br); –26.5 (s); –6.9 (s); –3.6 (s); –1.5 (s); 0.1 (s); 4.5 (s); 2.3 to 9.4 (br); 23.4 (br s); 40.6 (br s); 97.1 (br s); 113.4 (br s).

UV-vis (Et_2O solution): λ (nm) / ε (L mol^{-1} cm^{-1}): 224 ($1.61 \cdot 10^5$), 281 ($4.13 \cdot 10^4$), 613 (73.6), 647 (109), 712 (135).

Elemental analysis: calcd. C 61.78, H 8.24, N 7.39; found C 62.70, H 8.01, N 7.02.

8.6.12 Reaction of 24 with KC_8 to [{K(18-crown-6)}{(SINpMe)$CoCl_3$}] (35)

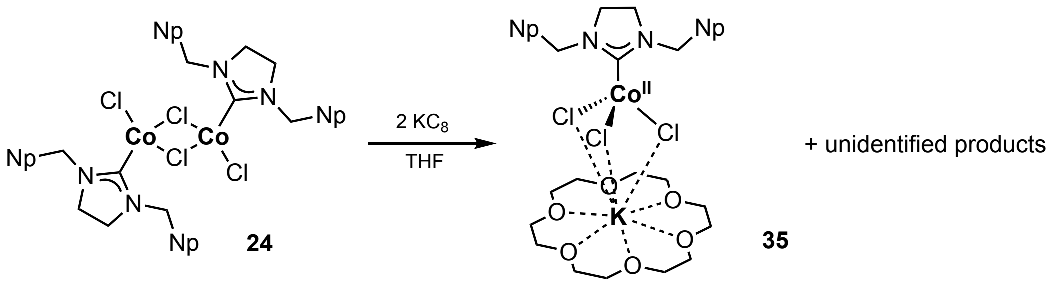

[(SINpMe)$CoCl_2$]$_2$ (57.2 mg, 0.100 mmol, 1.00 equiv.) and 18-crown-6 (29.1 mg, 0.110 mmol, 1.10 equiv.) were dissolved in THF (4 mL). KC_8 (14.2 mg, 0.105 mmol, 1.05 equiv.) was added and the suspension was stirred at room temperature overnight. After filtration, all volatiles were removed from the olive-green filtrate, and the residue was fractionally extracted with *n*-hexane, diethyl ether, and toluene. While the hexane and ether extracts were olive-green in color, the toluene extract showed a distinct turquoise coloration. X-ray quality crystals of **35** were obtained from the toluene fraction by slow evaporation of the solvent over activated charcoal.

8.6.13 Reduction of 21, 25, 27, and 31

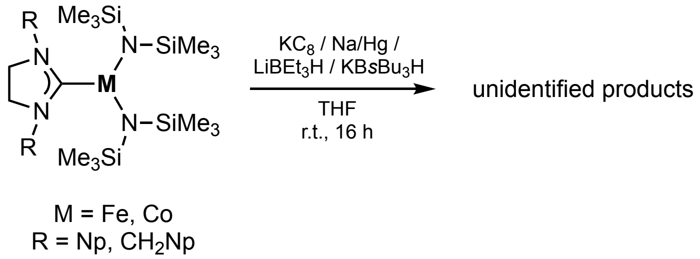

General procedure: 0.050 mmol (1.0 equiv.) of metal complex was dissolved in THF (2 mL). 0.055 mmol (1.1 equiv.) of reducing agent was added and the mixture was stirred at room temperature overnight. The mixture was filtered and all volatiles were removed *in vacuo*. The residue was fractionally extracted with *n*-hexane, diethyl ether, toluene, and THF. The hexane and ether extracts were subjected to slow solvent evaporation over activated charcoal. *n*-Hexane was allowed to slowly diffuse into the toluene and THF extracts.

In a second set of reactions, 0.050 mmol (1.0 equiv.) of metal complex was reacted with 0.110 mmol (2.2 equiv.) of reducing agent under otherwise identical conditions.

21, **25**, **27**, and **31** were all reacted with 1.1 and 2.2 equiv. of KC_8 and Na/Hg (0.5 wt%), respectively. The iron complexes **25** and **27** were reacted with 1.1 and 2.2 equiv. of lithium triethylborohydride and potassium tri-*sec*-butylborohydride as well, yielding the degradation products **33** and **34** which were identified by X-ray crystallography (see section 6.7.1).

8.7 References

[1] a) SCALE3ABS, CrysAlisPro, Agilent Technologies Inc., Oxford, UK, **2015**; b) G. M. Sheldrick, SADABS, Bruker AXS, Madison, USA, 2007.

[2] a) R. C. Clark, J. S. Reid, *Acta Crystallogr.*, **1995**, *A51*, 887; b) CrysAlisPro, Agilent Technologies Inc., Oxford, UK, **2015**.

[3] G. M. Sheldrick, *Acta Crystallogr.*, **2015**, *A71*, 3.

[4] G. M. Sheldrick, *Acta Crystallogr.*, **2008**, *A64*, 112.

[5] Gaussian 09, Revision E.01, M. J. Frisch, G. W. Trucks, H. B. Schlegel, G. E. Scuseria, M. A. Robb, J. R. Cheeseman, G. Scalmani, V. Barone, G. A. Petersson, H. Nakatsuji, X. Li, M. Caricato, A. Marenich, J. Bloino, B. G. Janesko, R. Gomperts, B. Mennucci, H. P. Hratchian, J. V. Ortiz, A. F. Izmaylov, J. L. Sonnenberg, D. Williams-Young, F. Ding, F. Lipparini, F. Egidi, J. Goings, B. Peng, A. Petrone, T. Henderson, D. Ranasinghe, V. G. Zakrzewski, J. Gao, N. Rega, G. Zheng, W. Liang, M. Hada, M. Ehara, K. Toyota, R. Fukuda, J. Hasegawa, M. Ishida, T. Nakajima, Y. Honda, O. Kitao, H. Nakai, T. Vreven, K. Throssell, J. A. Montgomery, Jr., J. E. Peralta, F. Ogliaro, M. Bearpark, J. J. Heyd, E. Brothers, K. N. Kudin, V. N. Staroverov, T. Keith, R. Kobayashi, J. Normand, K. Raghavachari, A. Rendell, J. C. Burant, S. S. Iyengar, J. Tomasi, M. Cossi, J. M. Millam, M. Klene, C. Adamo, R. Cammi, J. W. Ochterski, R. L. Martin, K. Morokuma, O. Farkas, J. B. Foresman, and D. J. Fox, Gaussian, Inc., Wallingford CT, **2016**.

[6] a) C. Lee, W. Yang, R. G. Parr, *Phys. Rev. B: Condens. Matter Mater. Phys.* **1988**, *37*, 785; b) A. D. Becke, *J. Chem. Phys.* **1993**, *98*, 1372.

[7] a) A. Schäfer, H. Horn, R. Ahlrichs, *J. Chem. Phys.* **1992**, *97*, 2571; b) F. Weigend, R. Ahlrichs, *Phys. Chem. Chem. Phys.* **2005**, *7*, 3297.

[8] S. Grimme, J. Antony, S. Ehrlich, H. Krieg, *J. Chem. Phys.* 2010, **132**, 154104.

[9] a) A. D. Becke, *J. Chem. Phys.* **1993**, *98*, 5648; b) P. J. Stephens, F. J. Devlin, C. F. Chabalowski, M. J. Frisch, *J. Phys. Chem.* **1994**, *98*, 11623.

[10] J. Tomasi, B. Mennucci, R. Cammi, *Chem. Rev.* **2005**, *105*, 2999.

[11] GaussView 5.0.9: R. Dennington, T. A. Keith, J. M. Millam, Semichem Inc. Shawnee Mission, KS, **2016**.

[12] R. S. Threlkel, J. E. Bercaw, P. F. Seidler, J. M. Stryker, R. G. Bergman, *Org. Synth.* **1987**, *65*, 42-43.

[13] H. Song, N. Yan, Z. Fei, K. J. Kilpin, R. Scopelliti, X. Li, P. J. Dyson, *Catalysis Today* **2012**, *183*, 172- 177.

[14] a) O. V. Starikova, G. V. Dolgushin, L. I. Larina, P. E. Ushakov, T. N. Komarova, V. A. Lopyrev, *Russ. J. Org. Chem.* **2003**, *39*, 1467-1470; b) Y. Gök, N. Gürbüz, I. Özdemir, B. Cetinkaya, E. Cetinkaya, *Appl. Organometal. Chem.* **2005**, *19*, 870- 874.

[15] S. Yasar, I. Özdemir, B. Cetinkaya, J.-L. Renaud, C. Bruneau, *Eur. J. Org. Chem.* **2008**, 2142-2149.

[16] S. Urban, N. Ortega, F. Glorius, *Angew. Chem. Int. Ed.* **2011**, *50*, 3803-3806.

[17] I. Chávez, A. Alvarez-Carena, E. Molins, A. Roig, W. Maniukiewicz, A. Arancibia, V. Arancibia, H. Brand, J. M. Manríquez, *J. Organomet. Chem.* **2000**, *601*, 126-132.

[18] B. T. Loughrey, B. V. Cunning, P. C. Healy, C. L. Brown, P. G. Parsons, M. L. Williams, *Chem. Asian J.* **2012**, *7*, 112-121.

[19] N. Oshima, H. Suzuki, Y. Moro-Oka, *Chem. Lett.* **1984**, 1161-1164.

[20] P. J. Fagan, W. S. Mahoney, J. C. Calabrese, I. D. Williams, *Organometallics* **1990**, *9*, 1843-1852.

[21] R. B. Strand, T. Helgerud, T. Solvang, C. A. Sperger, A. Fiksdahl, *Tetrahedron: Asymmetry* **2011**, *22*, 1994-2006.

[22] K. Hirano, S. Urban, C. Wang, F. Glorius, *Org. Lett.* **2009**, *11*, 1019-1022.

[23] S. Sabater, J. A. Mata, E. Peris, *ACS Catal.* **2014**, *4*, 2038-2047.

A. Crystallographic Data

A.1. Crystal Data and Structure Refinement – [K{Cp*Ru($C_{10}H_8$)}]$_n$ (K1)

Empirical formula	$C_{20}H_{23}KRu$
Formula weight	403.55
Temperature/K	123.0(1)
Crystal system	monoclinic
Space group	$P2_1/c$
a/Å	9.8241(2)
b/Å	15.5584(4)
c/Å	11.6868(3)
α/°	90
β/°	105.383(2)
γ/°	90
Volume/Å^3	1722.30(7)
Z	4
ρ_{calc}g/cm^3	1.556
μ/mm^{-1}	9.456
F(000)	824.0
Crystal size/mm^3	0.5 × 0.5 × 0.2
Radiation	CuKα (λ = 1.54178)
2Θ range for data collection/°	9.336 to 152.592
Index ranges	$-9 \leq h \leq 12$, $-15 \leq k \leq 19$, $-14 \leq l \leq 14$
Reflections collected	7870
Independent reflections	3529 [R_{int} = 0.0373, R_{sigma} = 0.0466]
Data/restraints/parameters	3529/0/267
Goodness-of-fit on F^2	1.023
Final R indexes [I>=2σ (I)]	R_1 = 0.0277, wR_2 = 0.0651
Final R indexes [all data]	R_1 = 0.0364, wR_2 = 0.0696
Largest diff. peak/hole / e Å^{-3}	0.48/-0.68

A.2. Crystal Data and Structure Refinement – [Cp*Ru($C_{10}H_8$)RuCp*] (2)

Empirical formula	$C_{30}H_{38}Ru_2$
Formula weight	600.74
Temperature/K	123.0(1)
Crystal system	monoclinic
Space group	$P2_1/n$
a/Å	8.6703(3)
b/Å	11.0228(3)
c/Å	13.1457(4)
α/°	90
β/°	91.186(3)
γ/°	90
Volume/Å^3	1256.08(7)
Z	2
ρ_{calc}g/cm^3	1.588
μ/mm^{-1}	9.828
F(000)	612.0
Crystal size/mm^3	0.2 × 0.2 × 0.1
Radiation	CuKα (λ = 1.54178)
2Θ range for data collection/°	10.474 to 153.054
Index ranges	$-10 \leq h \leq 10$, $-13 \leq k \leq 13$, $-16 \leq l \leq 15$
Reflections collected	8009
Independent reflections	2565 [R_{int} = 0.0442, R_{sigma} = 0.0304]
Data/restraints/parameters	2565/0/145
Goodness-of-fit on F^2	1.094
Final R indexes [I>=2σ (I)]	R_1 = 0.0610, wR_2 = 0.1631
Final R indexes [all data]	R_1 = 0.0634, wR_2 = 0.1640
Largest diff. peak/hole / e Å^{-3}	3.25/-1.85

A.3. Crystal Data and Structure Refinement – [Cp*Ru($C_{10}H_8$)RuCp*]BAr$^F_4$ ([2]BAr$^F_4$)

Empirical formula	$C_{124}H_{100}B_2F_{48}Ru_4$
Formula weight	2927.93
Temperature/K	123.1(2)
Crystal system	triclinic
Space group	*P*–1
a/Å	10.52733(11)
b/Å	23.1371(2)
c/Å	24.6760(3)
α/°	87.0962(9)
β/°	89.0569(9)
γ/°	87.5307(9)
Volume/Å^3	5996.46(12)
Z	2
ρ_{calc}g/cm^3	1.622
μ/mm^{-1}	5.110
F(000)	2924.0
Crystal size/mm^3	0.181 × 0.128 × 0.09
Radiation	CuKα (λ = 1.54184)
2Θ range for data collection/°	7.658 to 133.508
Index ranges	$-12 \leq h \leq 12$, $-19 \leq k \leq 27$, $-29 \leq l \leq 29$
Reflections collected	67882
Independent reflections	21058 [R_{int} = 0.0348, R_{sigma} = 0.0347]
Data/restraints/parameters	21058/0/1623
Goodness-of-fit on F^2	1.027
Final R indexes [I>=2σ (I)]	R_1 = 0.0358, wR_2 = 0.0845
Final R indexes [all data]	R_1 = 0.0439, wR_2 = 0.0891
Largest diff. peak/hole / e Å^{-3}	2.73/-0.85

A.4. Crystal Data and Structure Refinement – [Cp*Ru($C_{10}H_8$)Ru(H)Cp*]PF_6 ([2-H]PF_6)

Empirical formula	$C_{68}H_{94}F_{12}O_2P_2Ru_4$
Formula weight	1637.65
Temperature/K	123.0(6)
Crystal system	triclinic
Space group	*P*–1
a/Å	12.2572(3)
b/Å	12.5519(3)
c/Å	12.7014(4)
α/°	115.951(3)
β/°	100.575(3)
γ/°	98.837(2)
Volume/Å^3	1665.66(9)
Z	1
ρ_{calc}g/cm^3	1.633
μ/mm^{-1}	8.316
F(000)	832.0
Crystal size/mm^3	0.2198 × 0.1267 × 0.0775
Radiation	CuKα (λ = 1.54184)
2Θ range for data collection/°	7.608 to 133.61
Index ranges	$-14 \leq h \leq 14$, $-14 \leq k \leq 14$, $-15 \leq l \leq 14$
Reflections collected	24106
Independent reflections	5845 [R_{int} = 0.0305, R_{sigma} = 0.0241]
Data/restraints/parameters	5845/48/447
Goodness-of-fit on F^2	1.014
Final R indexes [I>=2σ (I)]	R_1 = 0.0199, wR_2 = 0.0477
Final R indexes [all data]	R_1 = 0.0219, wR_2 = 0.0488
Largest diff. peak/hole / e Å^{-3}	0.67/-0.41

A.1. Crystal Data and Structure Refinement – [(INpMe)AgCl] (6)

Empirical formula	$C_{50}H_{40}Ag_2Cl_2N_4$
Formula weight	983.50
Temperature/K	123.00(14)
Crystal system	triclinic
Space group	*P*–1
a/Å	7.9326(3)
b/Å	9.9043(3)
c/Å	14.4375(4)
α/°	92.908(3)
β/°	94.896(3)
γ/°	112.163(3)
Volume/Å^3	1042.43(6)
Z	1
ρ_{calc}g/cm^3	1.567
μ/mm^{-1}	9.026
F(000)	496.0
Crystal size/mm^3	0.2664 × 0.224 × 0.0808
Radiation	CuKα (λ = 1.54184)
2Θ range for data collection/°	9.682 to 133.276
Index ranges	$-9 \leq h \leq 9$, $-11 \leq k \leq 11$, $-17 \leq l \leq 16$
Reflections collected	11182
Independent reflections	3659 [R_{int} = 0.0279, R_{sigma} = 0.0273]
Data/restraints/parameters	3659/0/262
Goodness-of-fit on F^2	1.050
Final R indexes [I>=2σ (I)]	R_1 = 0.0260, wR_2 = 0.0641
Final R indexes [all data]	R_1 = 0.0272, wR_2 = 0.0648
Largest diff. peak/hole / e Å^{-3}	0.78/-0.59

A.5. Crystal Data and Structure Refinement – [(BNpMe)AgCl] (7)

Empirical formula	$C_{29}H_{22}N_2ClAg$
Formula weight	541.80
Temperature/K	123.0(1)
Crystal system	hexagonal
Space group	$P6_1$
a/Å	21.3509(5)
b/Å	21.3509(5)
c/Å	9.2588(3)
α/°	90
β/°	90
γ/°	120
Volume/Å^3	3655.3(2)
Z	6
ρ_{calc}g/cm^3	1.477
μ/mm^{-1}	7.782
F(000)	1644.0
Crystal size/mm^3	0.622 × 0.045 × 0.029
Radiation	CuKα (λ = 1.54184)
2Θ range for data collection/°	8.282 to 147.044
Index ranges	$-26 \leq h \leq 24$, $-23 \leq k \leq 19$, $-11 \leq l \leq 11$
Reflections collected	13852
Independent reflections	4673 [R_{int} = 0.0704, R_{sigma} = 0.0786]
Data/restraints/parameters	4673/1/298
Goodness-of-fit on F^2	1.024
Final R indexes [I>=2σ (I)]	R_1 = 0.0559, wR_2 = 0.1318
Final R indexes [all data]	R_1 = 0.0630, wR_2 = 0.1367
Largest diff. peak/hole / e Å^{-3}	1.57/-0.74
Flack parameter	-0.009(19)

A.6. Crystal Data and Structure Refinement – [(SINpMe)AgCl] (8)

Empirical formula	$C_{25}H_{22}N_2ClAg$
Formula weight	493.76
Temperature/K	123.0(1)
Crystal system	monoclinic
Space group	*I*2/a
a/Å	25.5487(7)
b/Å	7.23816(16)
c/Å	22.3654(6)
α/°	90
β/°	95.433(2)
γ/°	90
Volume/Å^3	4117.37(19)
Z	8
ρ_{calc}g/cm^3	1.593
μ/mm^{-1}	9.141
F(000)	2000.0
Crystal size/mm^3	0.3882 × 0.0479 × 0.0404
Radiation	CuKα (λ = 1.54184)
2Θ range for data collection/°	10.052 to 148.748
Index ranges	$-31 \leq h \leq 28$, $-8 \leq k \leq 9$, $-27 \leq l \leq 27$
Reflections collected	19159
Independent reflections	4140 [$R_{int} = 0.0514$, $R_{sigma} = 0.0310$]
Data/restraints/parameters	4140/0/262
Goodness-of-fit on F^2	1.075
Final R indexes [I>=2σ (I)]	$R_1 = 0.0377$, $wR_2 = 0.1028$
Final R indexes [all data]	$R_1 = 0.0412$, $wR_2 = 0.1071$
Largest diff. peak/hole / e Å^{-3}	1.07/-0.68

A.7. Crystal Data and Structure Refinement – [(SINpMe)AuCl] (9)

Empirical formula	$C_{50}H_{44}N_4Cl_2Au_2$
Formula weight	1165.72
Temperature/K	123.0(1)
Crystal system	monoclinic
Space group	*I*2/a
a/Å	25.4666(4)
b/Å	7.30092(10)
c/Å	22.3006(4)
α/°	90
β/°	95.7811(15)
γ/°	90
Volume/Å^3	4125.24(11)
Z	4
ρ_{calc}g/cm^3	1.877
μ/mm^{-1}	14.690
F(000)	2256.0
Crystal size/mm^3	0.3 × 0.05 × 0.05
Radiation	CuKα (λ = 1.54184)
2Θ range for data collection/°	10.056 to 133.504
Index ranges	$-29 \leq h \leq 30$, $-8 \leq k \leq 8$, $-26 \leq l \leq 26$
Reflections collected	21938
Independent reflections	3639 [R_{int} = 0.0448, R_{sigma} = 0.0233]
Data/restraints/parameters	3639/0/262
Goodness-of-fit on F^2	0.966
Final R indexes [I>=2σ (I)]	R_1 = 0.0240, wR_2 = 0.0676
Final R indexes [all data]	R_1 = 0.0259, wR_2 = 0.0701
Largest diff. peak/hole / e Å^{-3}	1.39/-1.29

A.8. Crystal Data and Structure Refinement – [(SINpMe)RhCl(cod)] (11)

Empirical formula	$C_{40}H_{41.5}ClN_2Rh$
Formula weight	688.61
Temperature/K	123.0(1)
Crystal system	monoclinic
Space group	$P2_1/c$
a/Å	19.3574(3)
b/Å	13.7194(2)
c/Å	12.3445(2)
α/°	90
β/°	99.7830(10)
γ/°	90
Volume/Å^3	3230.68(9)
Z	4
ρ_{calc}g/cm^3	1.416
μ/mm^{-1}	5.263
F(000)	1430.0
Crystal size/mm^3	0.52 × 0.141 × 0.083
Radiation	CuKα (λ = 1.54184)
2Θ range for data collection/°	9.272 to 147.576
Index ranges	$-24 \leq h \leq 23$, $-16 \leq k \leq 15$, $-15 \leq l \leq 15$
Reflections collected	94746
Independent reflections	6482 [R_{int} = 0.0643, R_{sigma} = 0.0197]
Data/restraints/parameters	6482/0/438
Goodness-of-fit on F^2	1.283
Final R indexes [I>=2σ (I)]	R_1 = 0.0517, wR_2 = 0.1210
Final R indexes [all data]	R_1 = 0.0537, wR_2 = 0.1220
Largest diff. peak/hole / e Å^{-3}	1.50/-0.81

A.9. Crystal Data and Structure Refinement – [(BNpMe)RhCl(cod)] (13)

Empirical formula	$C_{37}H_{34}N_2ClRh$
Formula weight	645.02
Temperature/K	123.0(1)
Crystal system	triclinic
Space group	*P*–1
a/Å	11.34104(15)
b/Å	11.97834(15)
c/Å	13.0011(2)
α/°	64.4058(14)
β/°	67.5407(14)
γ/°	82.1178(11)
Volume/Å^3	1471.21(4)
Z	2
ρ_{calc}g/cm^3	1.456
μ/mm^{-1}	5.741
F(000)	664.0
Crystal size/mm^3	0.5098 × 0.3221 × 0.1118
Radiation	CuKα (λ = 1.54184)
2Θ range for data collection/°	8.086 to 133.58
Index ranges	$-13 \leq h \leq 13$, $-14 \leq k \leq 14$, $-15 \leq l \leq 15$
Reflections collected	68991
Independent reflections	5207 [R_{int} = 0.0392, R_{sigma} = 0.0146]
Data/restraints/parameters	5207/282/442
Goodness-of-fit on F^2	1.161
Final R indexes [I>=2σ (I)]	R_1 = 0.0255, wR_2 = 0.0691
Final R indexes [all data]	R_1 = 0.0265, wR_2 = 0.0766
Largest diff. peak/hole / e Å^{-3}	0.69/-0.66

A.10. Crystal Data and Structure Refinement – [(BNpMe)RuCl$_2$(cym)] (15)

Empirical formula	$C_{44}H_{41}Cl_4N_2ORu$
Formula weight	856.66
Temperature/K	123.0(1)
Crystal system	monoclinic
Space group	$P2_1/n$
a/Å	15.4300(2)
b/Å	11.13329(12)
c/Å	24.1165(3)
α/°	90
β/°	105.7246(14)
γ/°	90
Volume/Å^3	3987.85(9)
Z	4
ρ_{calc}g/cm^3	1.427
μ/mm^{-1}	5.927
F(000)	1756.0
Crystal size/mm^3	0.3545 × 0.229 × 0.1403
Radiation	CuKα (λ = 1.54184)
2Θ range for data collection/°	7.888 to 133.592
Index ranges	$-17 \leq h \leq 18$, $-13 \leq k \leq 11$, $-28 \leq l \leq 28$
Reflections collected	34684
Independent reflections	7031 [R_{int} = 0.0332, R_{sigma} = 0.0221]
Data/restraints/parameters	7031/0/465
Goodness-of-fit on F^2	1.070
Final R indexes [I>=2σ (I)]	R_1 = 0.0456, wR_2 = 0.1196
Final R indexes [all data]	R_1 = 0.0471, wR_2 = 0.1208
Largest diff. peak/hole / e Å^{-3}	1.83/-0.69

A.11. Crystal Data and Structure Refinement – [(SINpMe)RuCl$_2$(cym)] (16)

Empirical formula	$C_{35}H_{36}N_2Cl_2Ru$
Formula weight	656.63
Temperature/K	123.0(1)
Crystal system	orthorhombic
Space group	*P*bca
a/Å	17.2127(4)
b/Å	12.7519(3)
c/Å	26.6289(5)
α/°	90
β/°	90
γ/°	90
Volume/Å^3	5844.9(2)
Z	8
ρ_{calc}g/cm^3	1.492
μ/mm^{-1}	6.227
F(000)	2704.0
Crystal size/mm^3	0.2619 × 0.0854 × 0.0582
Radiation	CuKα (λ = 1.54184)
2Θ range for data collection/°	8.396 to 147.236
Index ranges	$-20 \leq h \leq 21$, $-15 \leq k \leq 15$, $-31 \leq l \leq 32$
Reflections collected	33315
Independent reflections	5797 [R_{int} = 0.0359, R_{sigma} = 0.0210]
Data/restraints/parameters	5797/0/364
Goodness-of-fit on F^2	1.073
Final R indexes [I>=2σ (I)]	R_1 = 0.0391, wR_2 = 0.1019
Final R indexes [all data]	R_1 = 0.0415, wR_2 = 0.1037
Largest diff. peak/hole / e Å^{-3}	0.95/-0.61

A.12. Crystal Data and Structure Refinement – [(BNpMe*)RuPh$_2$] (18)

Empirical formula	$C_{48}H_{40}N_2Ru$
Formula weight	745.89
Temperature/K	123.0(1)
Crystal system	monoclinic
Space group	$P2_1/c$
a/Å	11.31198(19)
b/Å	20.5994(3)
c/Å	15.9490(3)
α/°	90
β/°	109.0241(18)
γ/°	90
Volume/Å^3	3513.45(10)
Z	4
ρ_{calc}g/cm^3	1.410
μ/mm^{-1}	3.892
F(000)	1544.0
Crystal size/mm^3	0.5407 × 0.4008 × 0.3143
Radiation	CuKα (λ = 1.54184)
2Θ range for data collection/°	7.266 to 133.192
Index ranges	$-13 \leq h \leq 13$, $-24 \leq k \leq 23$, $-18 \leq l \leq 18$
Reflections collected	35028
Independent reflections	6185 [R_{int} = 0.0327, R_{sigma} = 0.0211]
Data/restraints/parameters	6185/0/461
Goodness-of-fit on F^2	1.190
Final R indexes [I>=2σ (I)]	R_1 = 0.0237, wR_2 = 0.0695
Final R indexes [all data]	R_1 = 0.0244, wR_2 = 0.0700
Largest diff. peak/hole / e Å^{-3}	0.37/-0.63

A.13. Crystal Data and Structure Refinement – $[(\mathrm{SINp})\mathrm{FeBr}(\mu\text{-}\mathrm{Br})_2\mathrm{Fe}\{\mathrm{N}(\mathrm{SiMe}_3)_2\}(\mathrm{SINp})]$ (19)

Empirical formula	$C_{52}H_{54}N_5Si_2Fe_2Br_3$
Formula weight	1156.61
Temperature/K	123.0(1)
Crystal system	monoclinic
Space group	$P2_1/c$
a/Å	19.5513(10)
b/Å	12.1162(5)
c/Å	23.6560(12)
α/°	90
β/°	111.620(6)
γ/°	90
Volume/Å^3	5209.6(5)
Z	4
ρ_{calc}g/cm^3	1.475
μ/mm^{-1}	7.902
F(000)	2344.0
Crystal size/mm^3	0.095 × 0.059 × 0.049
Radiation	CuKα (λ = 1.54184)
2Θ range for data collection/°	7.712 to 147.362
Index ranges	$-24 \leq h \leq 22, -14 \leq k \leq 10, -26 \leq l \leq 28$
Reflections collected	21045
Independent reflections	10145 [$R_{int} = 0.0755$, $R_{sigma} = 0.1067$]
Data/restraints/parameters	10145/0/583
Goodness-of-fit on F^2	1.016
Final R indexes [I>=2σ (I)]	$R_1 = 0.0580$, $wR_2 = 0.1175$
Final R indexes [all data]	$R_1 = 0.1071$, $wR_2 = 0.1387$
Largest diff. peak/hole / e Å^{-3}	1.11/-0.77

A.14. Crystal Data and Structure Refinement – [(SINp)FeBr(μ-Br)]$_2$ (20)

Empirical formula	$C_{46}H_{36}Br_4Fe_2N_4$
Formula weight	1076.13
Temperature/K	123.0(1)
Crystal system	monoclinic
Space group	$P2_1/n$
a/Å	15.3970(2)
b/Å	12.8637(2)
c/Å	22.0424(4)
α/°	90
β/°	99.9557(16)
γ/°	90
Volume/Å^3	4300.00(13)
Z	4
ρ_{calc}g/cm^3	1.662
μ/mm^{-1}	10.051
F(000)	2128.0
Crystal size/mm^3	0.147 × 0.076 × 0.04
Radiation	CuKα (λ = 1.54184)
2Θ range for data collection/°	7.666 to 147.042
Index ranges	$-18 \le h \le 18$, $-15 \le k \le 15$, $-27 \le l \le 26$
Reflections collected	29927
Independent reflections	8456 [R_{int} = 0.0343, R_{sigma} = 0.0306]
Data/restraints/parameters	8456/0/505
Goodness-of-fit on F^2	1.071
Final R indexes [I>=2σ (I)]	R_1 = 0.0703, wR_2 = 0.1998
Final R indexes [all data]	R_1 = 0.0816, wR_2 = 0.2106
Largest diff. peak/hole / e Å^{-3}	2.40/-3.34

A.15. Crystal Data and Structure Refinement – [(SINp)Co{N(SiMe$_3$)$_2$}$_2$] (21)

Empirical formula	$C_{35}H_{54}N_4Si_4Co$
Formula weight	702.11
Temperature/K	123.0(1)
Crystal system	monoclinic
Space group	*C*2/c
a/Å	11.90769(17)
b/Å	18.8013(3)
c/Å	17.9296(3)
α/°	90
β/°	103.6666(14)
γ/°	90
Volume/Å^3	3900.44(10)
Z	4
ρ_{calc}g/cm^3	1.196
μ/mm^{-1}	4.836
F(000)	1500.0
Crystal size/mm^3	0.301 × 0.124 × 0.09
Radiation	CuKα (λ = 1.54184)
2Θ range for data collection/°	8.974 to 147.008
Index ranges	$-14 \leq h \leq 14$, $-22 \leq k \leq 22$, $-22 \leq l \leq 22$
Reflections collected	14015
Independent reflections	3872 [R_{int} = 0.0186, R_{sigma} = 0.0154]
Data/restraints/parameters	3872/0/206
Goodness-of-fit on F^2	1.055
Final R indexes [I>=2σ (I)]	R_1 = 0.0252, wR_2 = 0.0703
Final R indexes [all data]	R_1 = 0.0255, wR_2 = 0.0706
Largest diff. peak/hole / e Å^{-3}	0.25/-0.28

A.16. Crystal Data and Structure Refinement – [(SINp)CoBr(μ-Br)$_2$Co{N(SiMe$_3$)$_2$}(SINp)] (22)

Empirical formula	$C_{52}H_{54}N_5Si_2Co_2Br_3$
Formula weight	1162.77
Temperature/K	123.0(1)
Crystal system	monoclinic
Space group	$P2_1/c$
a/Å	19.3738(4)
b/Å	12.10978(19)
c/Å	23.5941(5)
α/°	90
β/°	111.282(3)
γ/°	90
Volume/Å^3	5157.99(19)
Z	4
ρ_{calc}g/cm^3	1.497
μ/mm^{-1}	8.508
F(000)	2352.0
Crystal size/mm^3	0.194 × 0.141 × 0.045
Radiation	CuKα (λ = 1.54184)
2Θ range for data collection/°	7.75 to 146.952
Index ranges	$-22 \leq h \leq 23$, $-14 \leq k \leq 10$, $-29 \leq l \leq 27$
Reflections collected	21686
Independent reflections	9993 [R_{int} = 0.0226, R_{sigma} = 0.0283]
Data/restraints/parameters	9993/102/583
Goodness-of-fit on F^2	1.018
Final R indexes [I>=2σ (I)]	R_1 = 0.0331, wR_2 = 0.0794
Final R indexes [all data]	R_1 = 0.0390, wR_2 = 0.0827
Largest diff. peak/hole / e Å^{-3}	0.89/-0.57

A.17. Crystal Data and Structure Refinement – [(SINpMe)FeCl(μ-Cl)]$_2$ (23)

Empirical formula	$C_{32}H_{30}Cl_2FeN_2$
Formula weight	569.33
Temperature/K	123.0(1)
Crystal system	monoclinic
Space group	$P2_1/c$
a/Å	15.1600(2)
b/Å	8.9072(2)
c/Å	20.6596(3)
α/°	90
β/°	99.245(2)
γ/°	90
Volume/Å^3	2753.49(8)
Z	4
ρ_{calc}g/cm^3	1.373
μ/mm^{-1}	6.351
F(000)	1184.0
Crystal size/mm^3	0.105 × 0.08 × 0.066
Radiation	CuKα (λ = 1.54184)
2Θ range for data collection/°	8.672 to 146.96
Index ranges	$-18 \leq h \leq 17$, $-8 \leq k \leq 10$, $-25 \leq l \leq 25$
Reflections collected	22452
Independent reflections	5432 [R_{int} = 0.0331, R_{sigma} = 0.0262]
Data/restraints/parameters	5432/0/335
Goodness-of-fit on F^2	1.031
Final R indexes [I>=2σ (I)]	R_1 = 0.0389, wR_2 = 0.0963
Final R indexes [all data]	R_1 = 0.0465, wR_2 = 0.1012
Largest diff. peak/hole / e Å^{-3}	0.90/-0.30

A.18. Crystal Data and Structure Refinement – [(SINpMe)CoCl(μ-Cl)]$_2$ (24)

Empirical formula	$C_{32}H_{30}Cl_2CoN_2$
Formula weight	572.41
Temperature/K	123.0(1)
Crystal system	monoclinic
Space group	$P2_1/c$
a/Å	15.0141(10)
b/Å	8.9618(7)
c/Å	20.5892(14)
α/°	90
β/°	98.805(6)
γ/°	90
Volume/Å^3	2737.7(3)
Z	4
ρ_{calc}g/cm^3	1.389
μ/mm^{-1}	6.885
F(000)	1188.0
Crystal size/mm^3	0.103 × 0.09 × 0.077
Radiation	CuKα (λ = 1.54184)
2Θ range for data collection/°	8.692 to 148.514
Index ranges	$-17 \leq h \leq 18$, $-11 \leq k \leq 7$, $-21 \leq l \leq 25$
Reflections collected	10247
Independent reflections	5290 [R_{int} = 0.0335, R_{sigma} = 0.0453]
Data/restraints/parameters	5290/66/323
Goodness-of-fit on F^2	1.029
Final R indexes [I>=2σ (I)]	R_1 = 0.0791, wR_2 = 0.2166
Final R indexes [all data]	R_1 = 0.1063, wR_2 = 0.2437
Largest diff. peak/hole / e Å^{-3}	1.39/-0.48

A.19. Crystal Data and Structure Refinement – $[(\mathrm{SINp})\mathrm{Fe}\{\mathrm{N}(\mathrm{SiMe}_3)_2\}_2]$ (25)

Empirical formula	$C_{37.5}H_{60}FeN_4Si_4$
Formula weight	735.10
Temperature/K	123.0(1)
Crystal system	triclinic
Space group	*P*–1
a/Å	11.1726(9)
b/Å	11.7629(9)
c/Å	18.0901(14)
α/°	89.439(6)
β/°	73.629(7)
γ/°	67.642(7)
Volume/Å^3	2096.8(3)
Z	2
ρ_{calc}g/cm^3	1.164
μ/mm^{-1}	4.195
F(000)	790.0
Crystal size/mm^3	0.192 × 0.17 × 0.144
Radiation	CuKα (λ = 1.54184)
2Θ range for data collection/°	8.176 to 147.102
Index ranges	$-13 \leq h \leq 13$, $-11 \leq k \leq 14$, $-21 \leq l \leq 21$
Reflections collected	16542
Independent reflections	8087 [R_{int} = 0.0325, R_{sigma} = 0.0428]
Data/restraints/parameters	8087/24/447
Goodness-of-fit on F^2	1.017
Final R indexes [I>=2σ (I)]	R_1 = 0.0356, wR_2 = 0.0868
Final R indexes [all data]	R_1 = 0.0420, wR_2 = 0.0918
Largest diff. peak/hole / e Å^{-3}	0.51/-0.50

A.20. Crystal Data and Structure Refinement – [(BNpMe)Fe{N($SiMe_3$)$_2$}$_2$] (26)

Empirical formula	$C_{44}H_{65}FeN_4Si_4$
Formula weight	818.21
Temperature/K	123.0(1)
Crystal system	monoclinic
Space group	$P2_1/c$
a/Å	17.5264(6)
b/Å	12.0646(4)
c/Å	23.5174(9)
α/°	90
β/°	107.487(4)
γ/°	90
Volume/Å^3	4742.9(3)
Z	4
ρ_{calc}g/cm^3	1.146
μ/mm^{-1}	2.775
F(000)	1756.0
Crystal size/mm^3	0.257 × 0.189 × 0.133
Radiation	? (λ = 1.39222)
2Θ range for data collection/°	4.774 to 120.72
Index ranges	$-21 \leq h \leq 21$, $-14 \leq k \leq 14$, $-29 \leq l \leq 28$
Reflections collected	40679
Independent reflections	9514 [R_{int} = 0.0658, R_{sigma} = 0.0494]
Data/restraints/parameters	9514/48/570
Goodness-of-fit on F^2	1.037
Final R indexes [I>=2σ (I)]	R_1 = 0.0453, wR_2 = 0.1106
Final R indexes [all data]	R_1 = 0.0629, wR_2 = 0.1266
Largest diff. peak/hole / e Å^{-3}	0.46/-0.60

A.21. Crystal Data and Structure Refinement – [(SINpMe)Fe{N(SiMe$_3$)$_2$}$_2$] (27)

Empirical formula	$C_{37}H_{58}N_4Si_4Fe$
Formula weight	727.08
Temperature/K	123.0(1)
Crystal system	orthorhombic
Space group	$P2_12_12_1$
a/Å	12.8784(3)
b/Å	12.9878(4)
c/Å	25.1917(6)
α/°	90
β/°	90
γ/°	90
Volume/Å^3	4213.62(19)
Z	4
ρ_{calc}g/cm^3	1.146
μ/mm^{-1}	3.080
F(000)	1560.0
Crystal size/mm^3	0.279 × 0.177 × 0.117
Radiation	? (λ = 1.39222)
2Θ range for data collection/°	6.336 to 121.272
Index ranges	$-15 \le h \le 16$, $-15 \le k \le 15$, $-31 \le l \le 30$
Reflections collected	61412
Independent reflections	8496 [R_{int} = 0.0704, R_{sigma} = 0.0392]
Data/restraints/parameters	8496/0/427
Goodness-of-fit on F^2	1.013
Final R indexes [I>=2σ (I)]	R_1 = 0.0353, wR_2 = 0.0836
Final R indexes [all data]	R_1 = 0.0435, wR_2 = 0.0894
Largest diff. peak/hole / e Å^{-3}	0.33/-0.24
Flack parameter	-0.007(2)

A.22. Crystal Data and Structure Refinement – [(INpMe)Co{N(SiMe$_3$)$_2$}$_2$] (29)

Empirical formula	$C_{37}H_{56}N_4Si_4Co$
Formula weight	728.14
Temperature/K	123.0(1)
Crystal system	orthorhombic
Space group	$P2_12_12_1$
a/Å	13.0021(2)
b/Å	13.2453(2)
c/Å	23.9240(4)
α/°	90
β/°	90
γ/°	90
Volume/Å^3	4120.11(11)
Z	4
ρ_{calc}g/cm^3	1.174
μ/mm^{-1}	4.596
F(000)	1556.0
Crystal size/mm^3	0.158 × 0.122 × 0.092
Radiation	CuKα (λ = 1.54184)
2Θ range for data collection/°	7.39 to 147.78
Index ranges	$-15 \leq h \leq 15$, $-15 \leq k \leq 16$, $-27 \leq l \leq 29$
Reflections collected	35926
Independent reflections	8194 [R_{int} = 0.0610, R_{sigma} = 0.0430]
Data/restraints/parameters	8194/0/427
Goodness-of-fit on F^2	1.049
Final R indexes [I>=2σ (I)]	R_1 = 0.0436, wR_2 = 0.1045
Final R indexes [all data]	R_1 = 0.0515, wR_2 = 0.1109
Largest diff. peak/hole / e Å^{-3}	0.54/-0.28
Flack parameter	-0.036(3)

A.23. Crystal Data and Structure Refinement – [(BNpMe)Co{N(SiMe$_3$)$_2$}$_2$] (30)

Empirical formula	$C_{41}H_{58}CoN_4Si_4$
Formula weight	778.20
Temperature/K	123.0(3)
Crystal system	triclinic
Space group	*P*–1
a/Å	10.4411(5)
b/Å	11.5917(7)
c/Å	20.4343(10)
α/°	79.582(5)
β/°	89.846(4)
γ/°	67.277(5)
Volume/Å^3	2237.4(2)
Z	2
ρ_{calc}g/cm^3	1.155
μ/mm^{-1}	3.205
F(000)	830.0
Crystal size/mm^3	0.331 × 0.227 × 0.154
Radiation	? (λ = 1.39222)
2Θ range for data collection/°	7.612 to 121.002
Index ranges	$-12 \leq h \leq 12$, $-14 \leq k \leq 14$, $-23 \leq l \leq 25$
Reflections collected	16032
Independent reflections	8661 [R_{int} = 0.0431, R_{sigma} = 0.0613]
Data/restraints/parameters	8661/0/463
Goodness-of-fit on F^2	1.053
Final R indexes [I>=2σ (I)]	R_1 = 0.0486, wR_2 = 0.1167
Final R indexes [all data]	R_1 = 0.0594, wR_2 = 0.1301
Largest diff. peak/hole / e Å^{-3}	0.42/-0.49

A.24. Crystal Data and Structure Refinement – [(SINpMe)Co{N(SiMe$_3$)$_2$}$_2$] (31)

Empirical formula	$C_{37}H_{58}CoN_4Si_4$
Formula weight	730.16
Temperature/K	123.0(1)
Crystal system	orthorhombic
Space group	$P2_12_12_1$
a/Å	12.8978(4)
b/Å	12.9905(2)
c/Å	25.0678(6)
α/°	90
β/°	90
γ/°	90
Volume/Å^3	4200.08(18)
Z	4
ρ_{calc}g/cm^3	1.155
μ/mm^{-1}	3.390
F(000)	1564.0
Crystal size/mm^3	0.398 × 0.27 × 0.224
Radiation	? (λ = 1.39222)
2Θ range for data collection/°	6.368 to 120.514
Index ranges	$-15 \leq h \leq 14$, $-16 \leq k \leq 16$, $-30 \leq l \leq 29$
Reflections collected	31347
Independent reflections	8289 [R_{int} = 0.0490, R_{sigma} = 0.0404]
Data/restraints/parameters	8289/0/427
Goodness-of-fit on F^2	1.081
Final R indexes [I>=2σ (I)]	R_1 = 0.0501, wR_2 = 0.1281
Final R indexes [all data]	R_1 = 0.0543, wR_2 = 0.1314
Largest diff. peak/hole / e Å^{-3}	0.41/-0.32
Flack parameter	0.019(3)

A.25. Crystal Data and Structure Refinement – [(SINpEt)Co{N(SiMe$_3$)$_2$}$_2$] (32)

Empirical formula	$C_{156}H_{248}Co_4N_{16}Si_{16}$
Formula weight	3032.85
Temperature/K	123.0(1)
Crystal system	monoclinic
Space group	$P2_1$
a/Å	20.8098(3)
b/Å	14.3539(2)
c/Å	29.3346(4)
α/°	90
β/°	100.1770(10)
γ/°	90
Volume/Å^3	8624.4(2)
Z	2
ρ_{calc}g/cm^3	1.168
μ/mm^{-1}	4.408
F(000)	3256.0
Crystal size/mm^3	0.321 × 0.218 × 0.171
Radiation	CuKα (λ = 1.54184)
2Θ range for data collection/°	6.84 to 147.294
Index ranges	$-25 \le h \le 25$, $-13 \le k \le 17$, $-35 \le l \le 36$
Reflections collected	51069
Independent reflections	26805 [R_{int} = 0.1607, R_{sigma} = 0.1042]
Data/restraints/parameters	26805/1/1785
Goodness-of-fit on F^2	1.164
Final R indexes [I>=2σ (I)]	R_1 = 0.0935, wR_2 = 0.2484
Final R indexes [all data]	R_1 = 0.1075, wR_2 = 0.2766
Largest diff. peak/hole / e Å^{-3}	1.32/-1.17
Flack parameter	0.001(4)

A.26. Crystal Data and Structure Refinement – Compound 33

Empirical formula	$C_{58}H_{66}B_2N_4$
Formula weight	840.76
Temperature/K	123.0(1)
Crystal system	orthorhombic
Space group	$P\mathrm{na}2_1$
a/Å	18.2448(3)
b/Å	7.7885(2)
c/Å	32.8465(6)
α/°	90
β/°	90
γ/°	90
Volume/Å^3	4667.48(17)
Z	4
ρ_{calc}g/cm^3	1.196
μ/mm^{-1}	0.517
F(000)	1808.0
Crystal size/mm^3	0.213 × 0.125 × 0.058
Radiation	CuKα (λ = 1.54184)
2Θ range for data collection/°	9.696 to 147.516
Index ranges	$-21 \leq h \leq 22$, $-9 \leq k \leq 9$, $-28 \leq l \leq 39$
Reflections collected	20019
Independent reflections	7189 [R_{int} = 0.0277, R_{sigma} = 0.0286]
Data/restraints/parameters	7189/1/583
Goodness-of-fit on F^2	1.060
Final R indexes [I>=2σ (I)]	R_1 = 0.0385, wR_2 = 0.0961
Final R indexes [all data]	R_1 = 0.0428, wR_2 = 0.0998
Largest diff. peak/hole / e Å^{-3}	0.19/-0.21
Flack parameter	0.4(3)

A.27. Crystal Data and Structure Refinement – Compound 34

Empirical formula	$C_{24}H_{36}BLiN_2O$
Formula weight	386.30
Temperature/K	123.0(1)
Crystal system	monoclinic
Space group	$P2_1/n$
a/Å	8.4832(3)
b/Å	18.0019(6)
c/Å	14.9454(8)
α/°	90
β/°	102.216(4)
γ/°	90
Volume/Å^3	2230.69(16)
Z	4
ρ_{calc}g/cm^3	1.150
μ/mm^{-1}	0.516
F(000)	840.0
Crystal size/mm^3	0.169 × 0.131 × 0.117
Radiation	CuKα (λ = 1.54184)
2Θ range for data collection/°	7.794 to 146.934
Index ranges	$-10 \leq h \leq 10$, $-22 \leq k \leq 22$, $-18 \leq l \leq 18$
Reflections collected	9792
Independent reflections	4381 [$R_{int} = 0.0217$, $R_{sigma} = 0.0263$]
Data/restraints/parameters	4381/0/265
Goodness-of-fit on F^2	1.036
Final R indexes [I>=2σ (I)]	$R_1 = 0.0456$, $wR_2 = 0.1228$
Final R indexes [all data]	$R_1 = 0.0503$, $wR_2 = 0.1281$
Largest diff. peak/hole / e Å^{-3}	0.90/-0.29

A.28. Crystal Data and Structure Refinement – [K(18-crown-6){(SINpMe)CoCl$_3$}] (35)

Empirical formula	$C_{37}H_{46}Cl_3CoKN_2O_6$
Formula weight	819.14
Temperature/K	123.0(1)
Crystal system	orthorhombic
Space group	$P2_12_12_1$
a/Å	11.27940(10)
b/Å	15.5019(2)
c/Å	22.2078(3)
α/°	90
β/°	90
γ/°	90
Volume/Å^3	3883.08(8)
Z	4
ρ_{calc}g/cm^3	1.401
μ/mm^{-1}	6.700
F(000)	1708.0
Crystal size/mm^3	0.145 × 0.132 × 0.105
Radiation	CuKα (λ = 1.54184)
2Θ range for data collection/°	6.954 to 147.866
Index ranges	$-13 \leq h \leq 13$, $-19 \leq k \leq 18$, $-27 \leq l \leq 22$
Reflections collected	38710
Independent reflections	7750 [R_{int} = 0.0440, R_{sigma} = 0.0286]
Data/restraints/parameters	7750/0/451
Goodness-of-fit on F^2	1.061
Final R indexes [I>=2σ (I)]	R_1 = 0.0509, wR_2 = 0.1184
Final R indexes [all data]	R_1 = 0.0522, wR_2 = 0.1191
Largest diff. peak/hole / e Å^{-3}	0.62/-0.48
Flack parameter	0.3231(15)

B. NMR Spectra

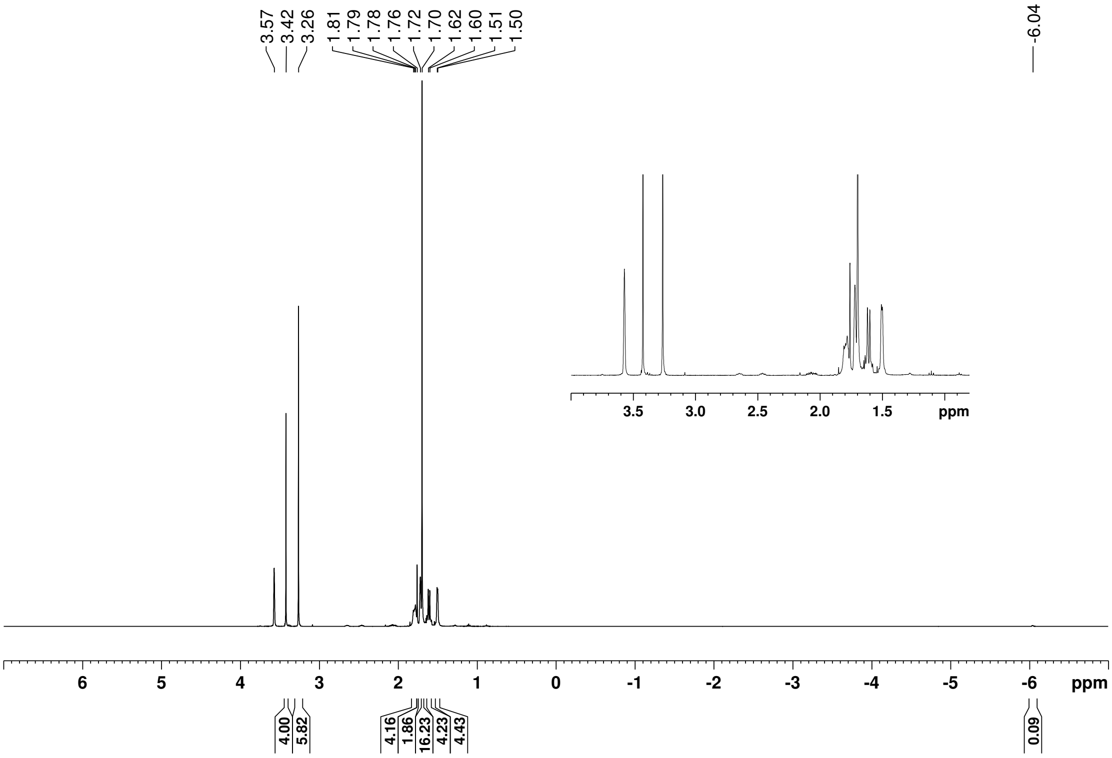

Figure B.1. ^{1}H NMR spectrum of [K(dme)$_2$][Cp*Ru(cod)] (**K3**) (300 K, 400.13 MHz, THF-d$_8$).

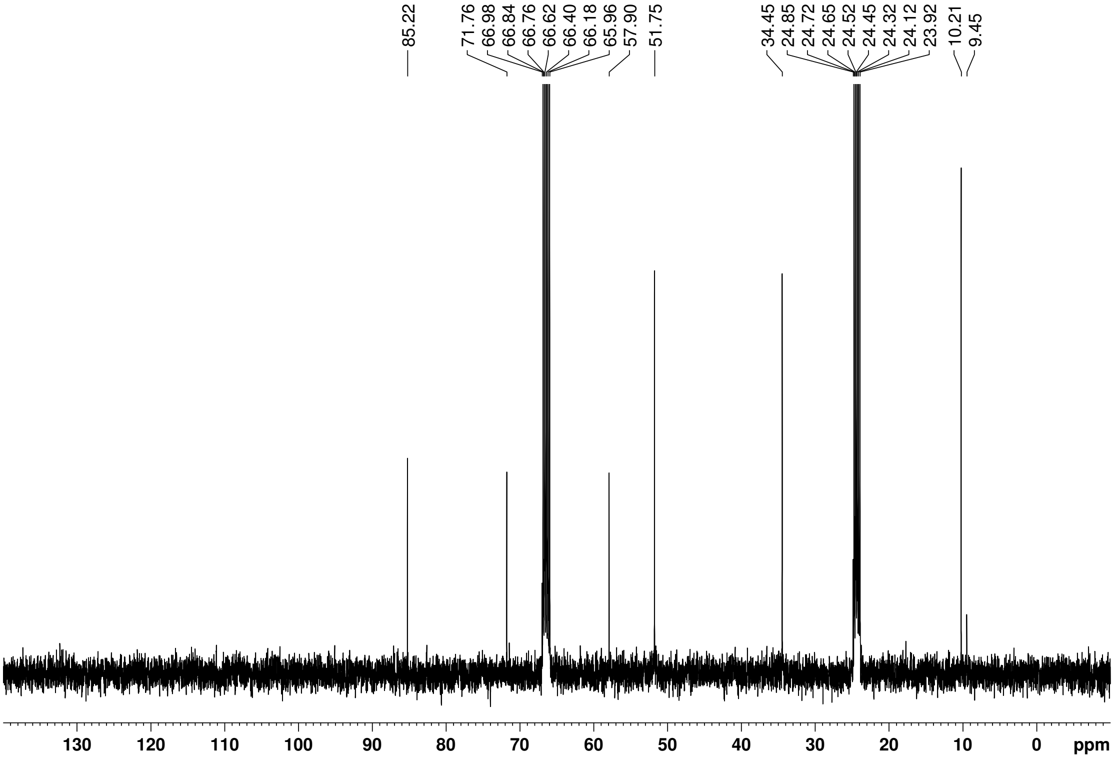

Figure B.2. ^{13}C{^{1}H} NMR spectrum of [K(dme)$_2$][Cp*Ru(cod)] (**K3**) (300 K, 100.61 MHz, THF-d$_8$).

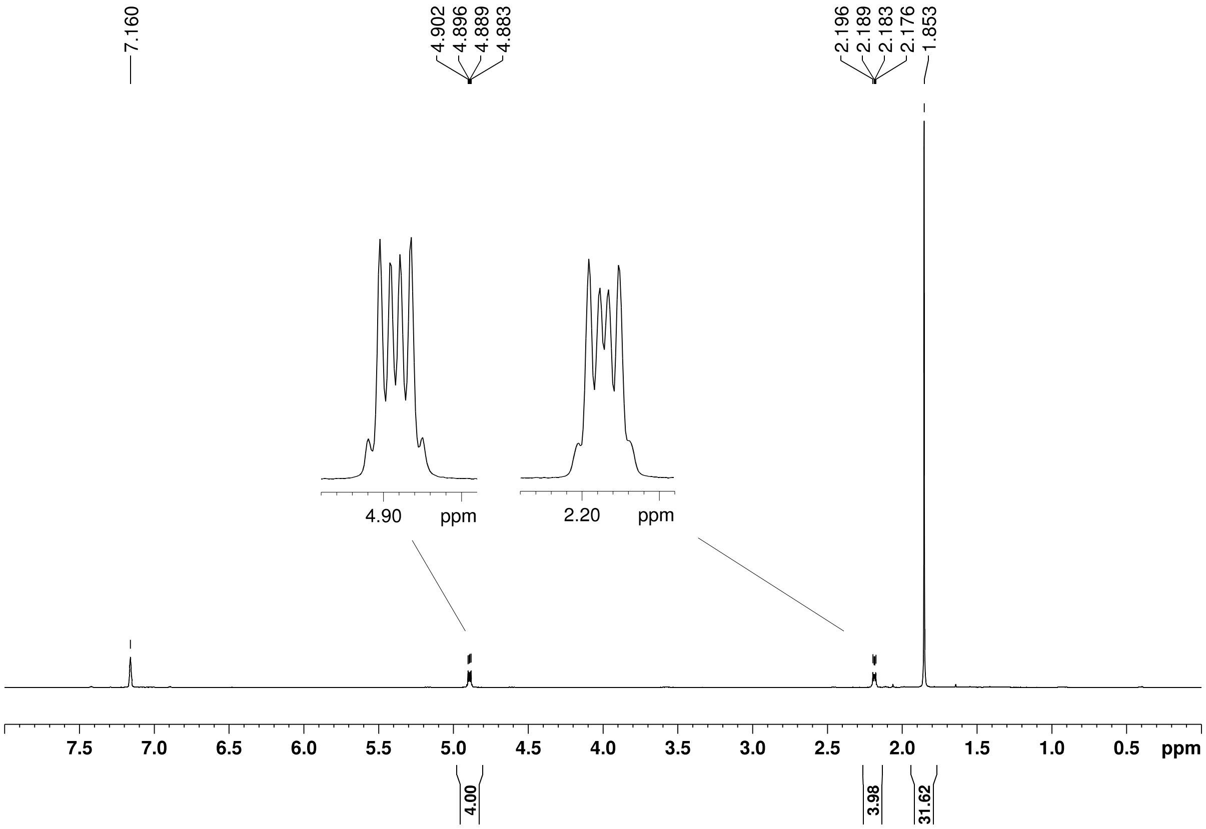

Figure B.3. ^{1}H NMR spectrum of [Cp*Ru(μ-$C_{10}H_8$)RuCp*] (**2**) (300 K, 300.13 MHz, C_6D_6).

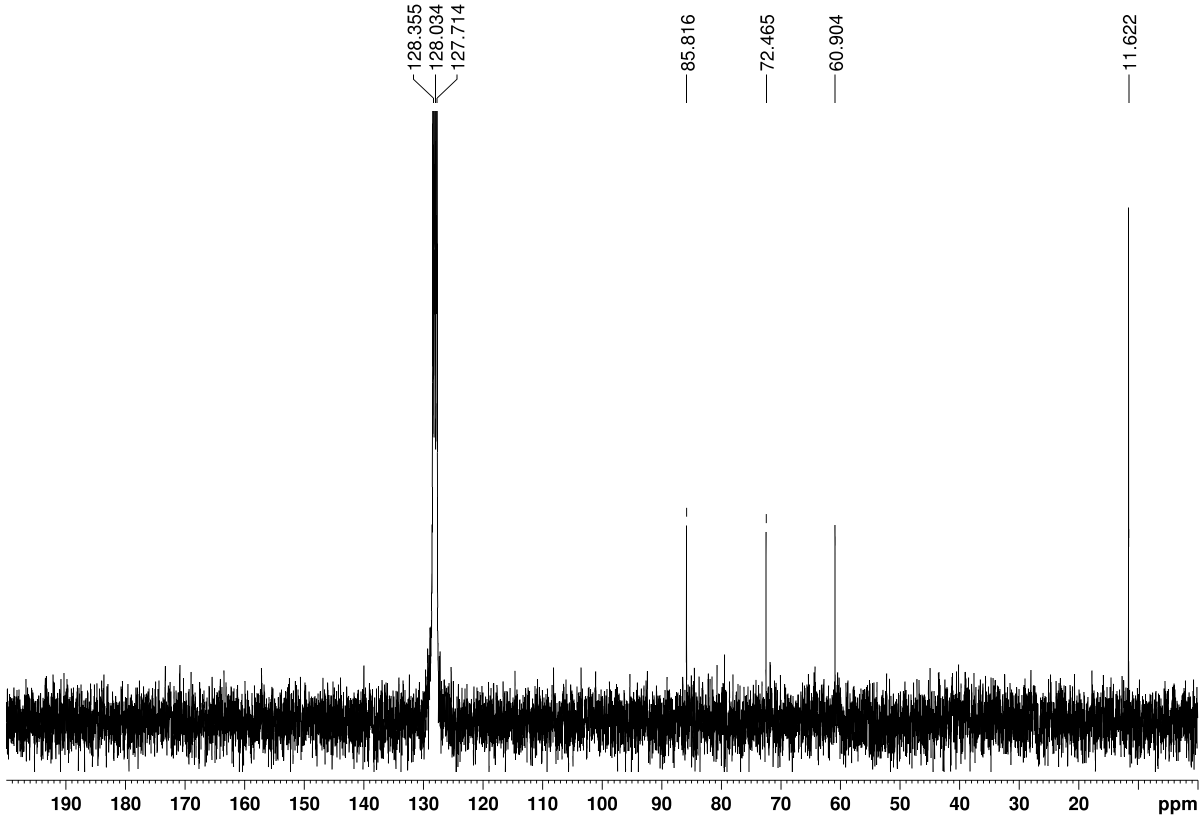

Figure B.4. ^{13}C{^{1}H} NMR spectrum of [Cp*Ru(μ-$C_{10}H_8$)RuCp*] (**2**) (300 K, 75.47 MHz, C_6D_6).

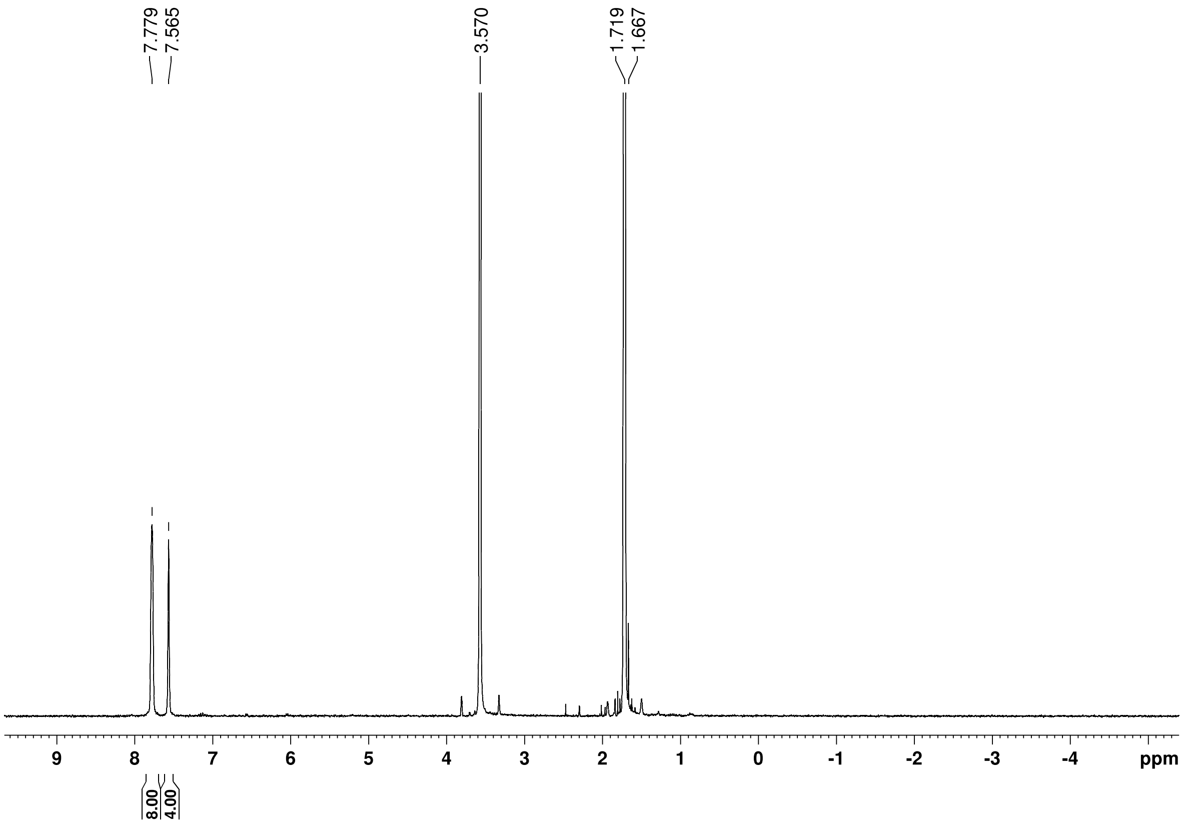

Figure B.5. ^{1}H NMR spectrum of [Cp*Ru(μ-$C_{10}H_8$)RuCp*]BAr$^F_4$ ([**2**]BAr$^F_4$) (300 K, 400.13 MHz, THF-d_8).

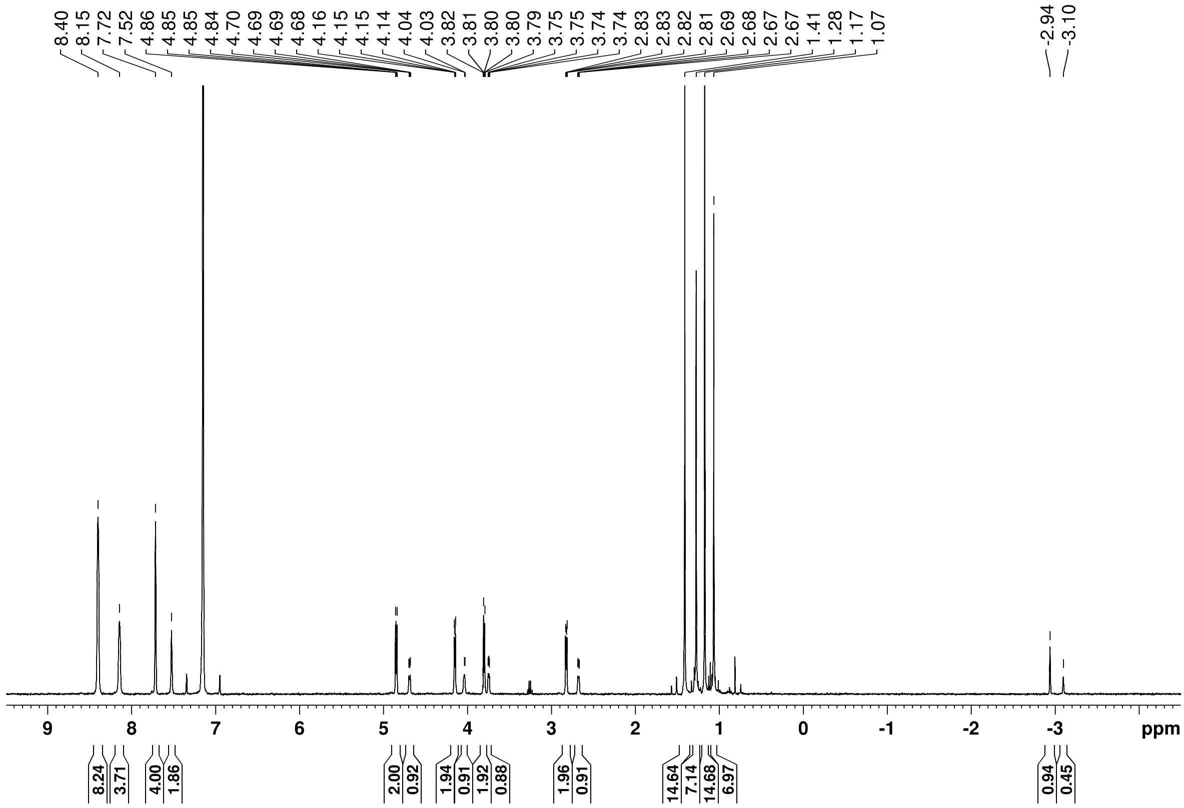

Figure B.6. ^{1}H NMR spectrum of [Cp*Ru(μ-$C_{10}H_8$)Ru(H)Cp*]BAr$^F_4$ ([**2-H**]BAr$^F_4$) recorded after five minutes (300 K, 300.13 MHz, THF-d_8).

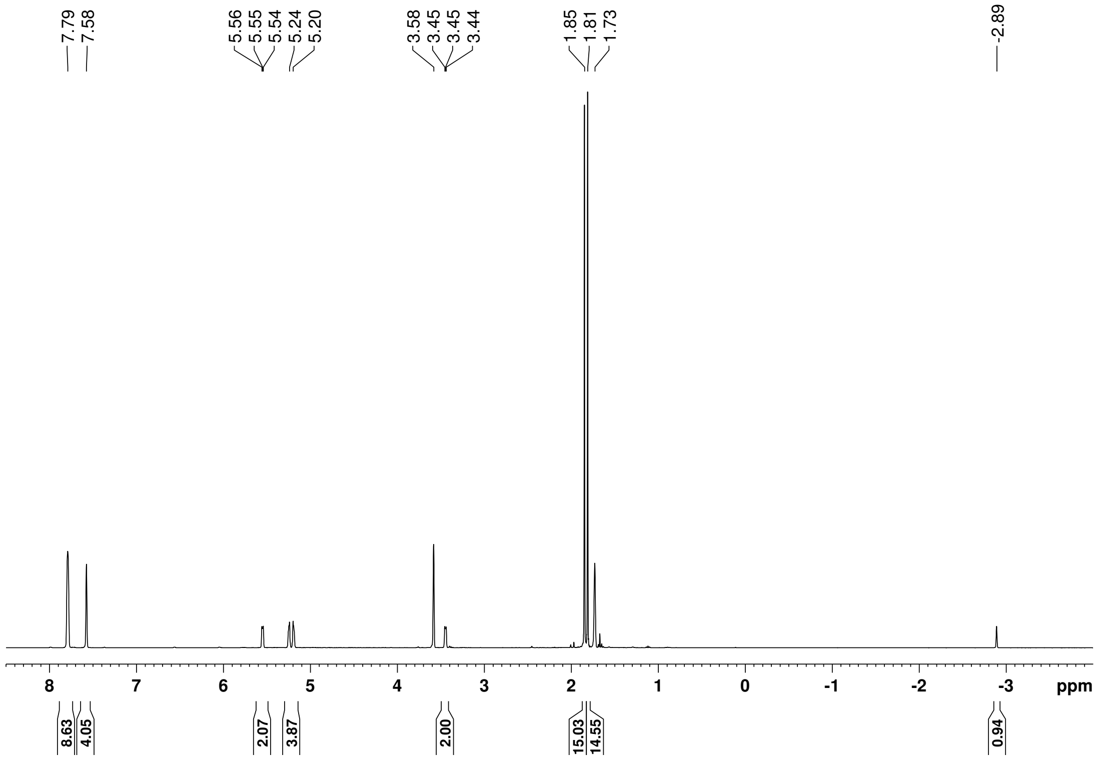

Figure B.7. ^{1}H NMR spectrum of [Cp*Ru(μ-$C_{10}H_8$)Ru(H)Cp*]BAr$^F_4$ ([**2-H**]BAr$^F_4$) recorded after one day (300 K, 300.13 MHz, THF-d_8).

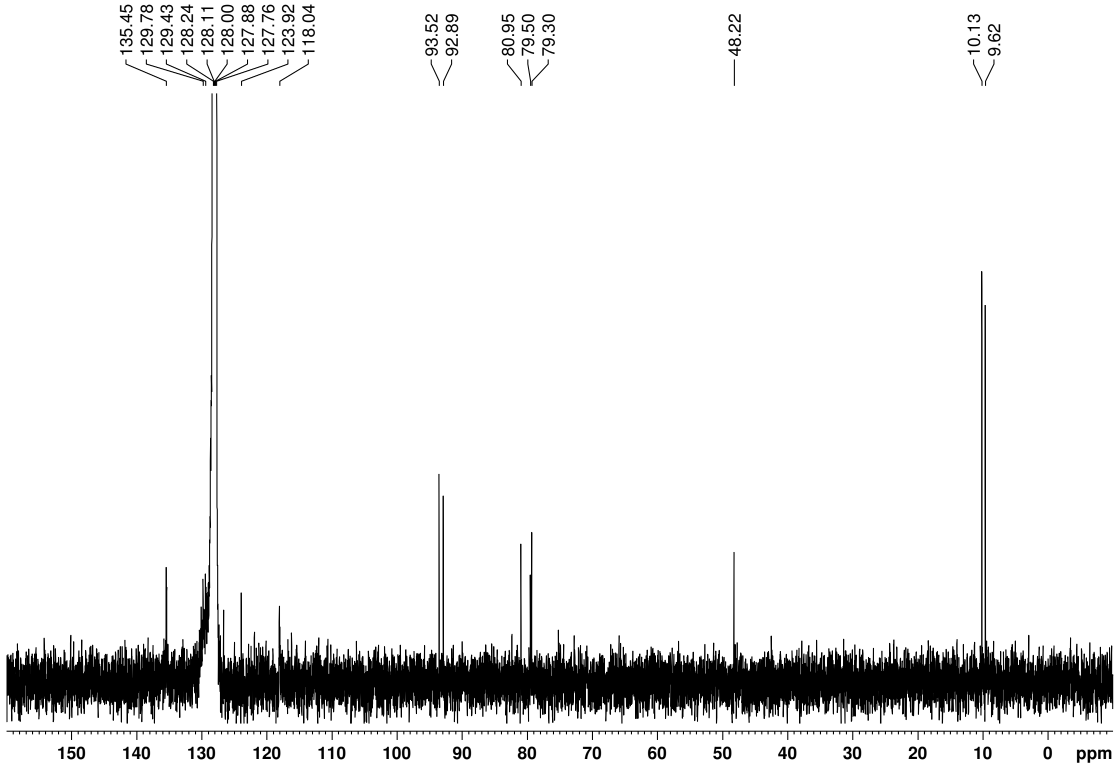

Figure B.8. $^{13}C\{^1H\}$ NMR spectrum of [Cp*Ru(μ-$C_{10}H_8$)Ru(H)Cp*]BAr$^F_4$ ([**2-H**]BAr$^F_4$) (300 K, 75.47 MHz, THF-d_8).

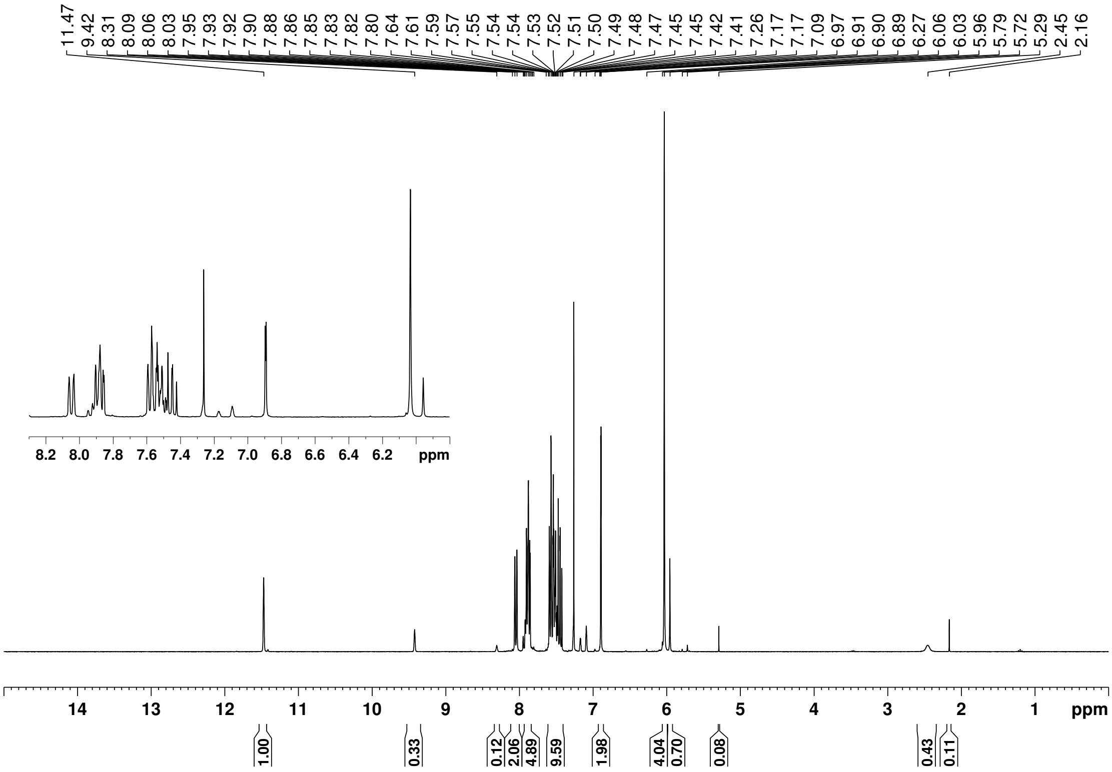

Figure B.9. ^{1}H NMR spectrum of [INpMeH|Cl (**XXXIX**) (300 K, 300.13 MHz, $CDCl_3$).

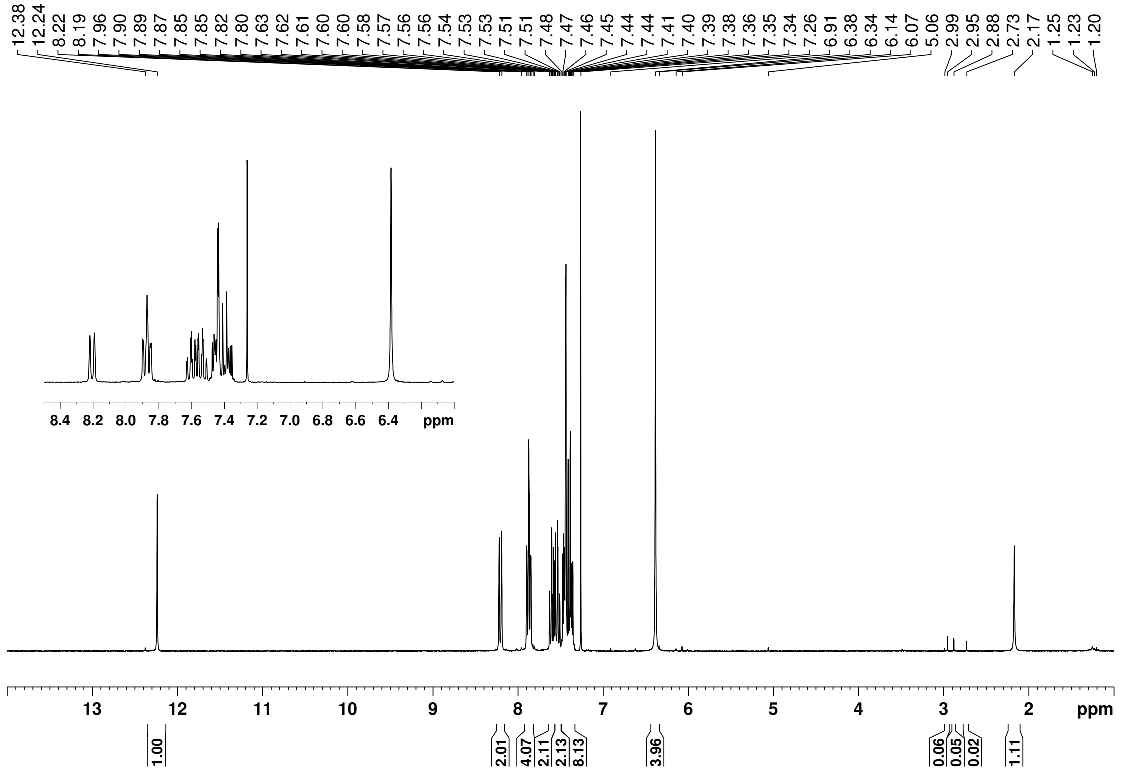

Figure B.10. ^{1}H NMR spectrum of [BNpMeH|Cl (**XL**) (300 K, 300.13 MHz, $CDCl_3$).

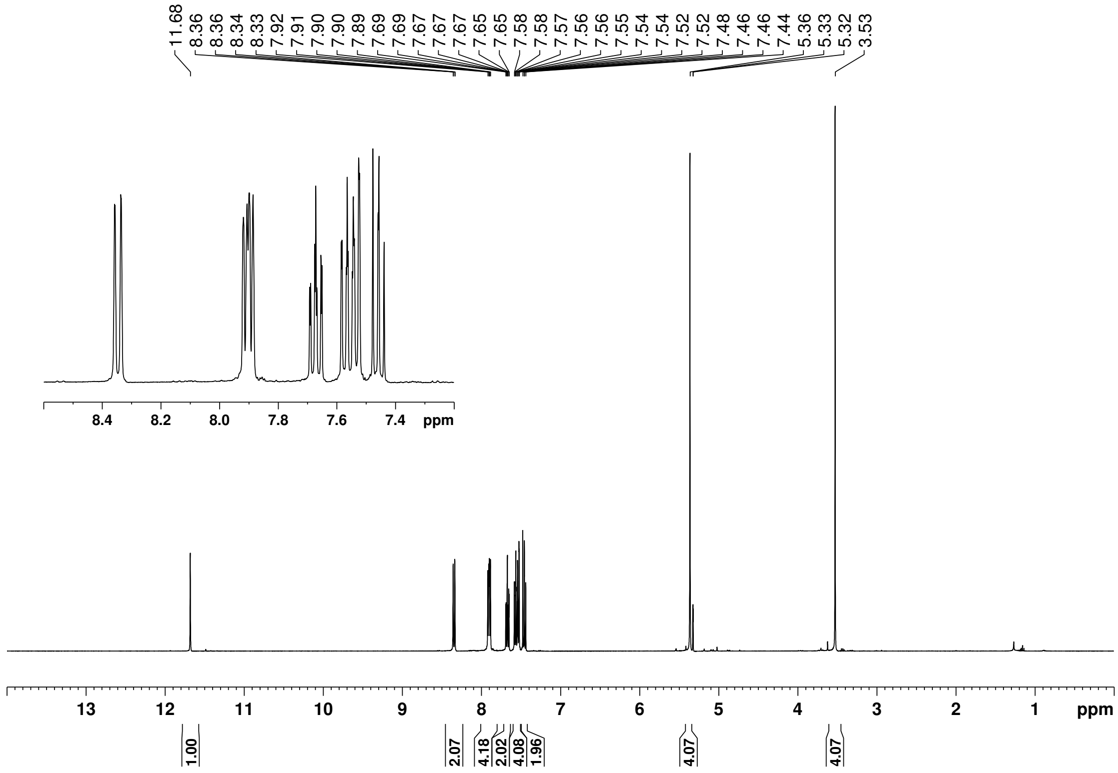

Figure B.11. ^{1}H NMR spectrum of [SINpMeH|Cl (**XLI**) (300 K, 300.13 MHz, $CDCl_3$).

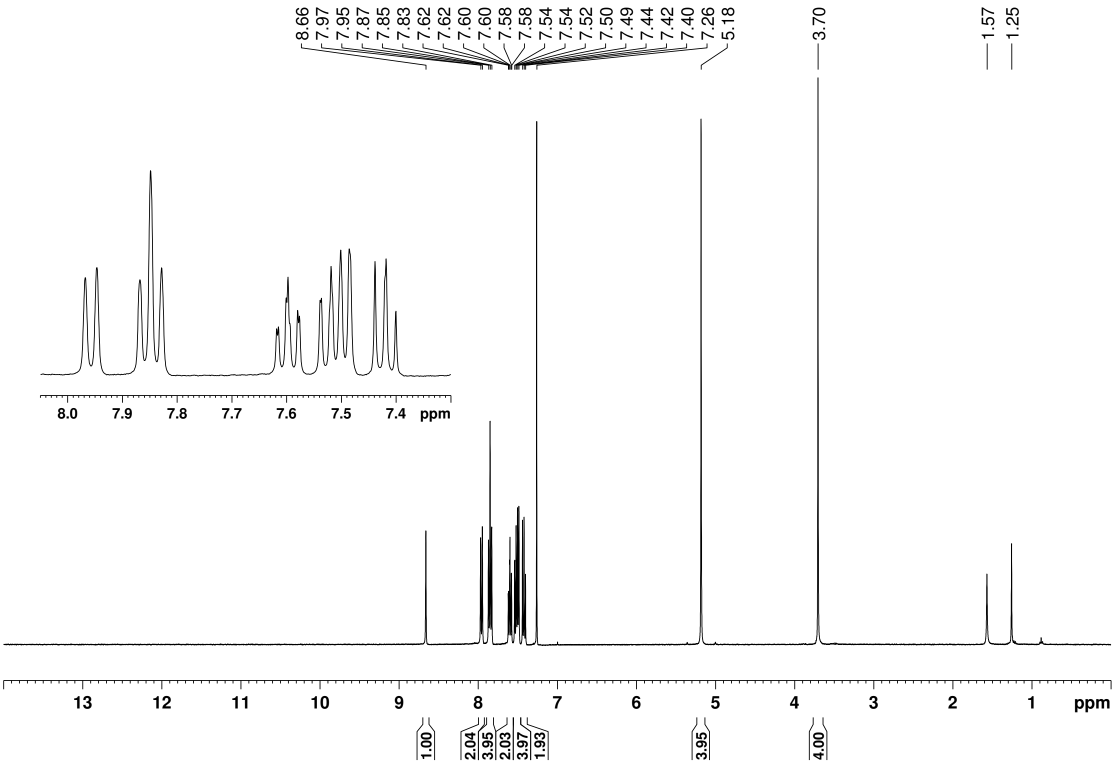

Figure B.12. ^{1}H NMR spectrum of [SINpMeH|BF_4 (**XLI'**) (300 K, 300.13 MHz, $CDCl_3$).

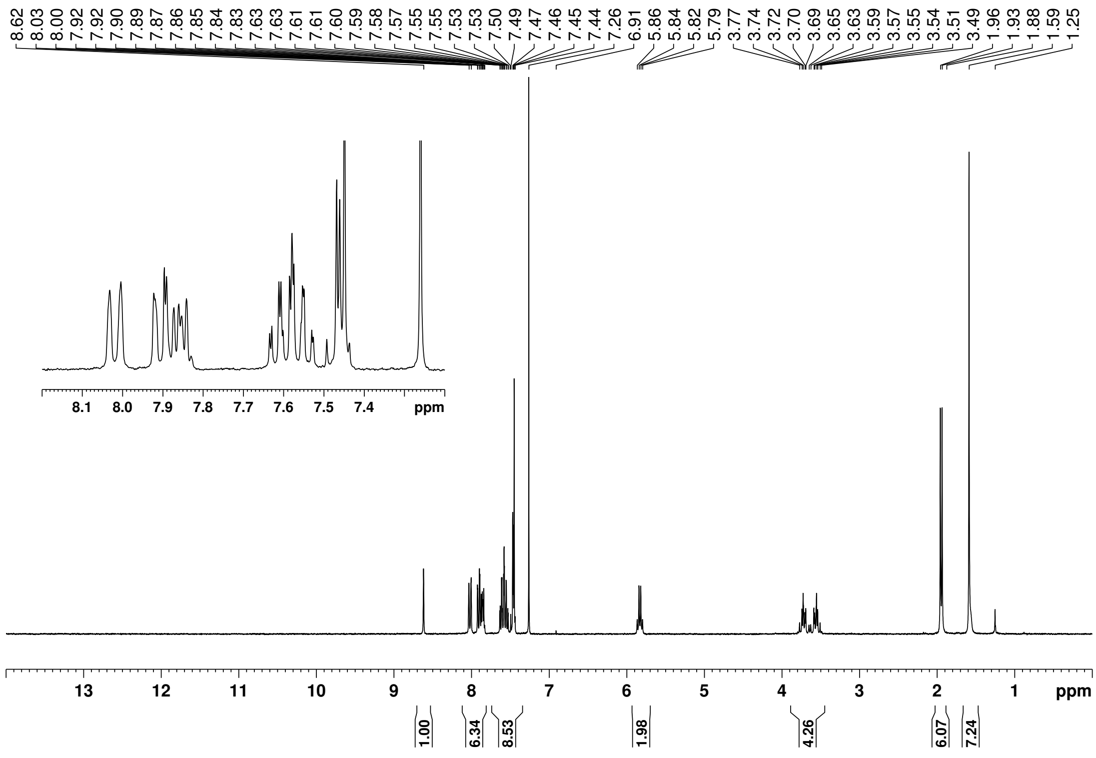

Figure B.13. ^{1}H NMR spectrum of [SINpEtH|BF$_4$ (**XLII**) (300 K, 300.13 MHz, CDCl$_3$).

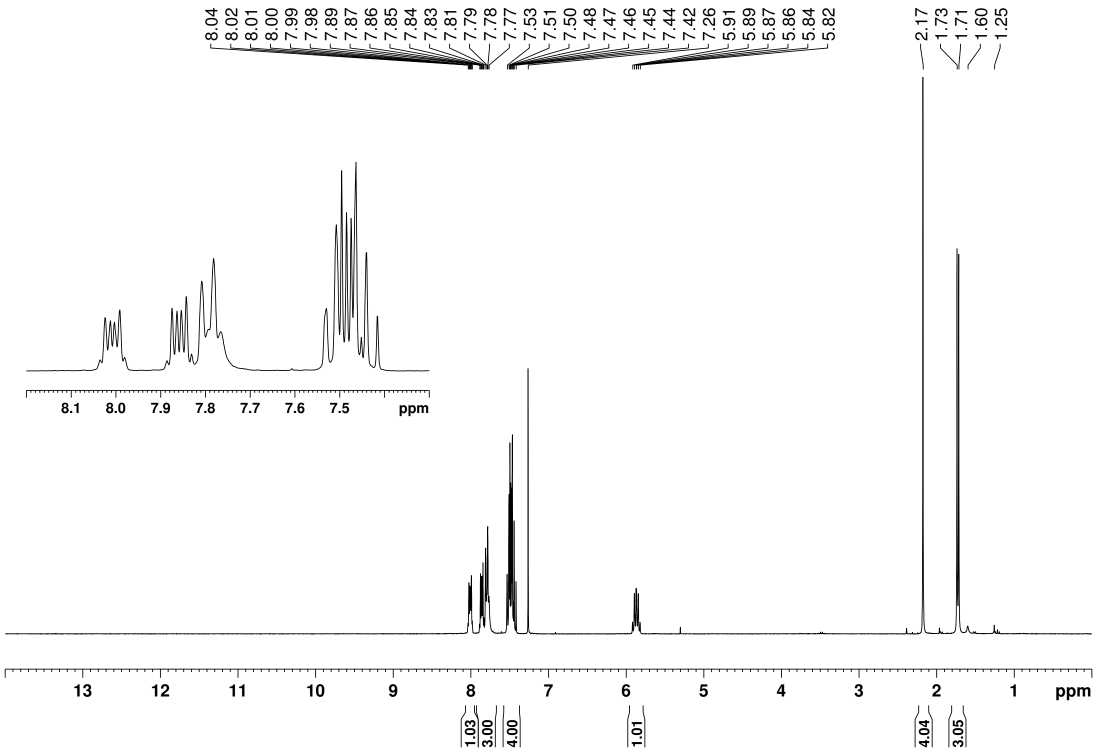

Figure B.14. ^{1}H NMR spectrum of *N*,*N'*-bis(1-naphthylmethyl)oxalamide (300 K, 300.13 MHz, CDCl$_3$).

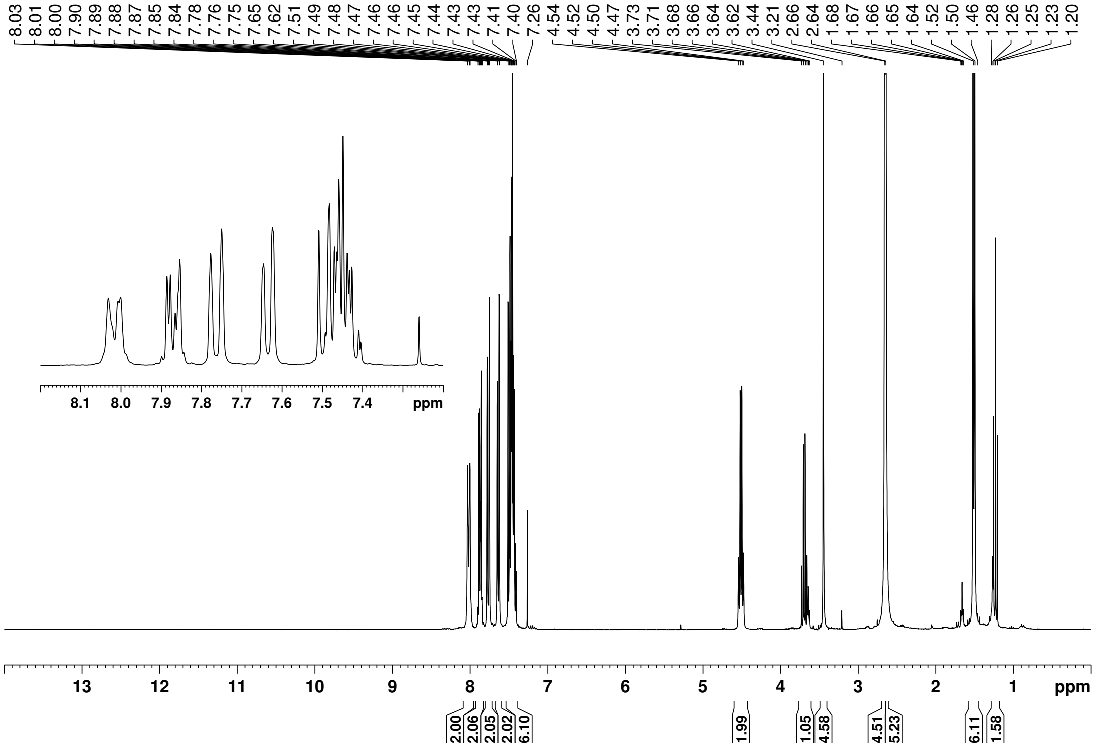

Figure B.15. ^{1}H NMR spectrum of *N*,*N'*-bis(1-naphthylmethyl)ethylenediamine (300 K, 300.13 MHz, $CDCl_3$).

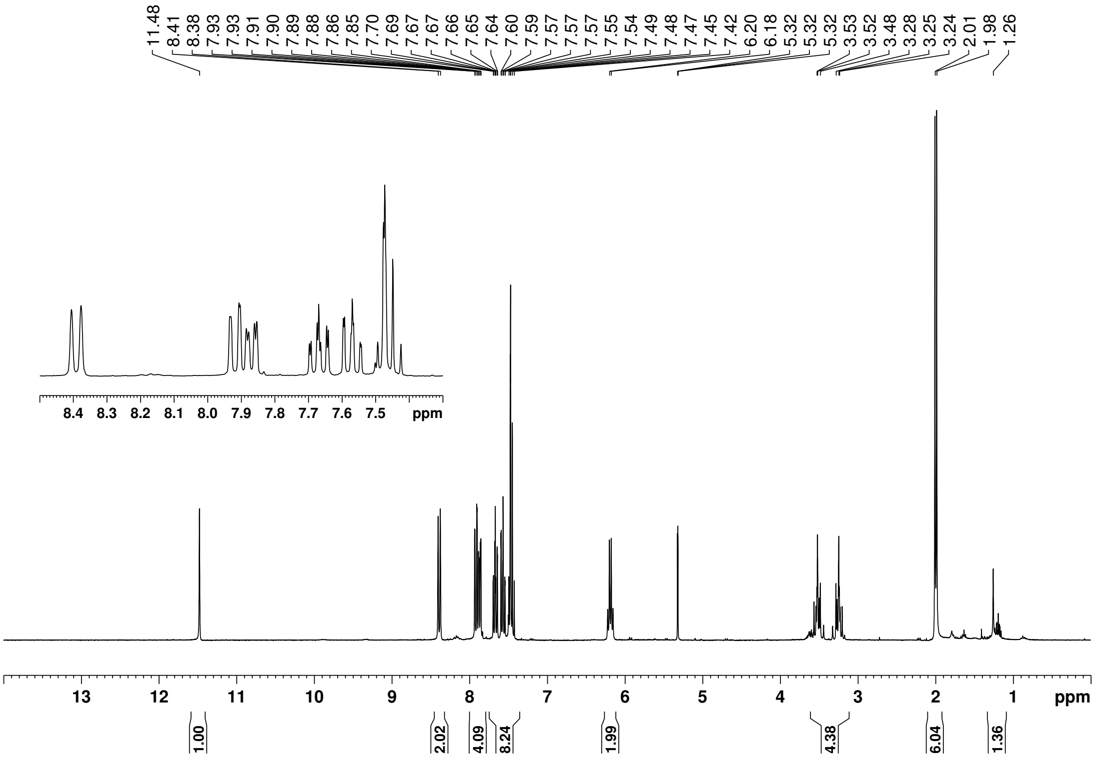

Figure B.16. ^{1}H NMR spectrum of [SINpEtH]Cl (**4**) (300 K, 300.13 MHz, $CDCl_3$).

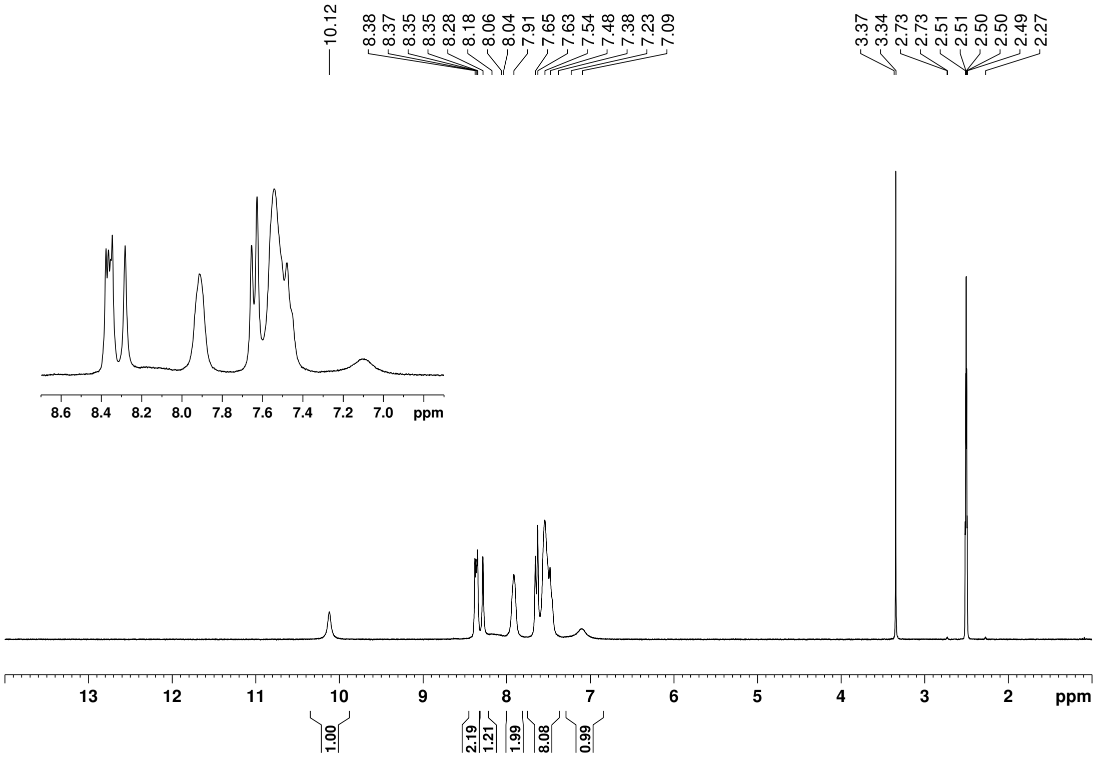

Figure B.17. ^{1}H NMR spectrum of bis(1-naphthyl)formamide (300 K, 300.13 MHz, DMSO-d$_6$).

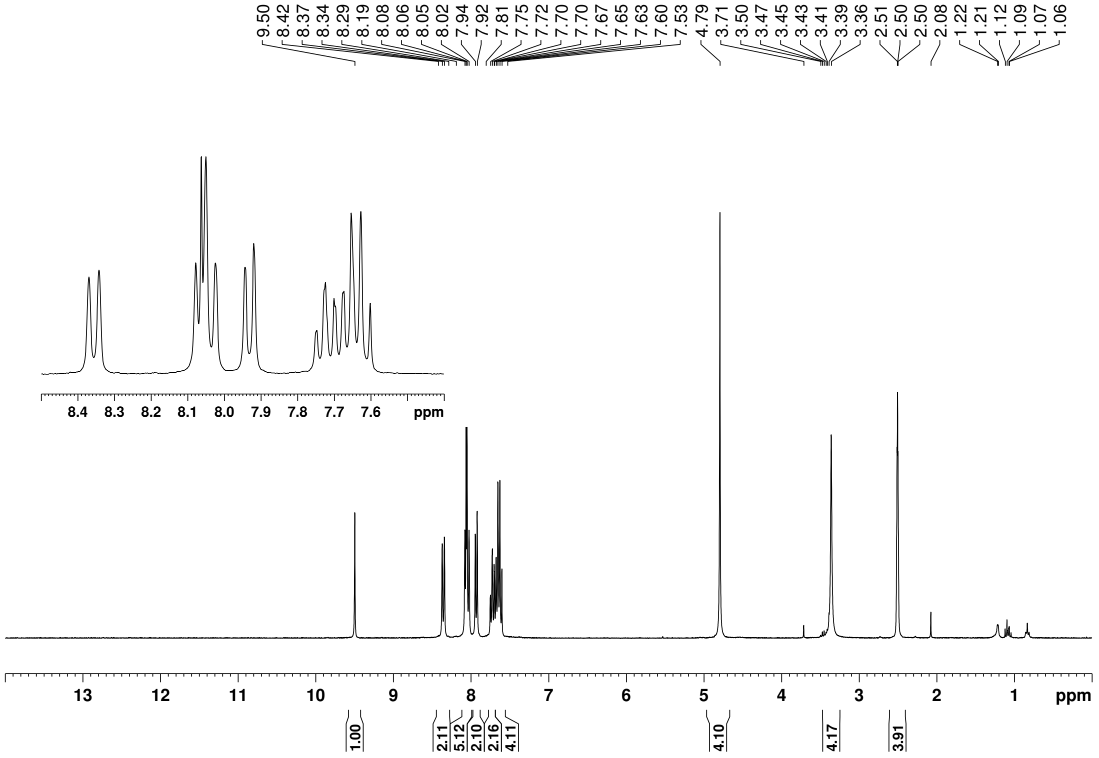

Figure B.18. ^{1}H NMR spectrum of [SINpH]Br (**5**) (300 K, 300.13 MHz, DMSO-d$_6$).

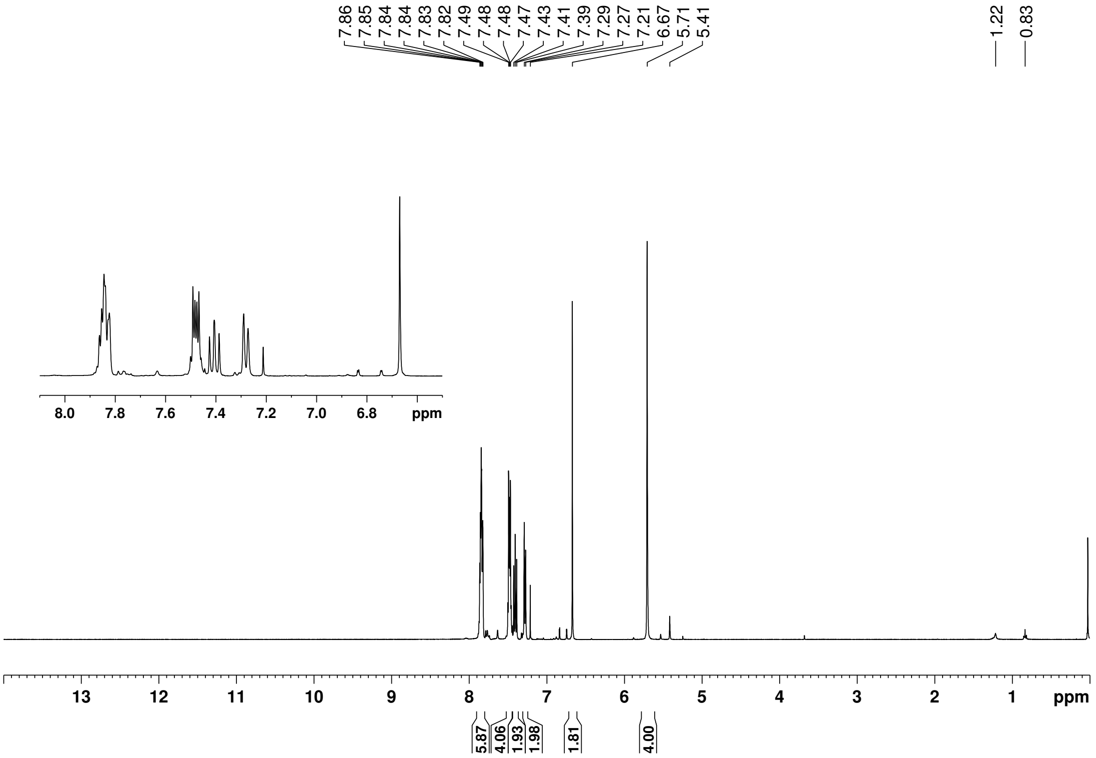

Figure B.19. ^{1}H NMR spectrum of [(INpMe)AgCl] (**6**) (300 K, 300.13 MHz, CDCl$_3$).

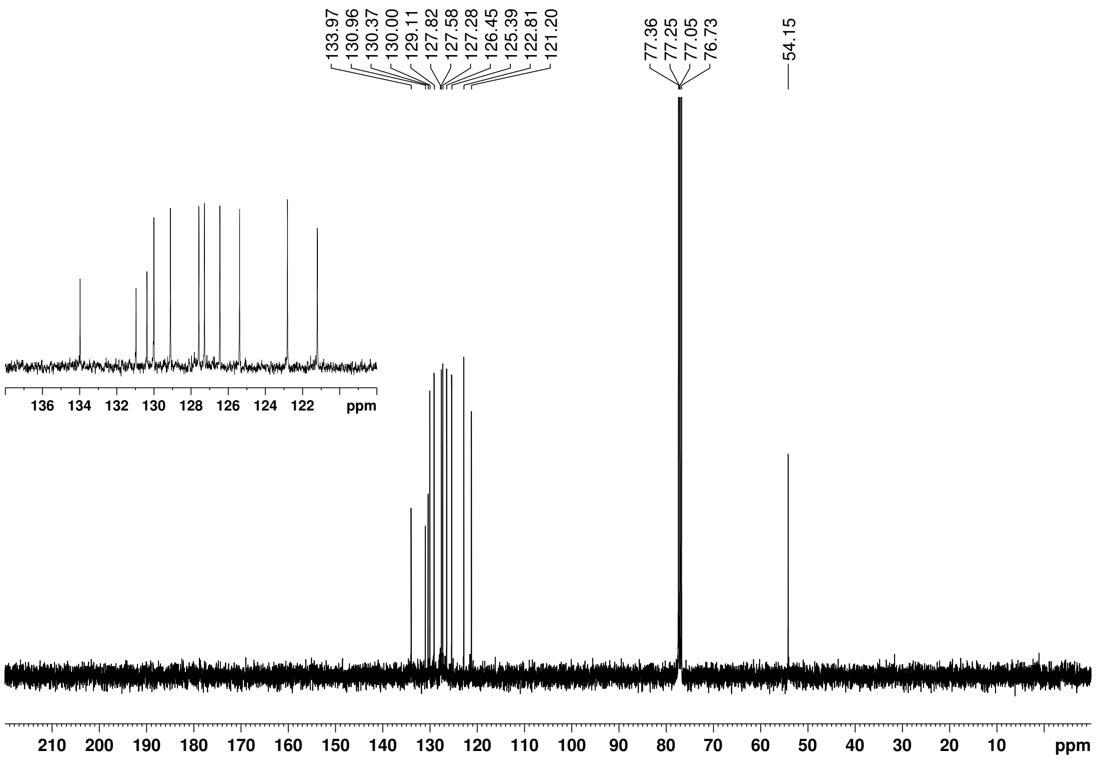

Figure B.20. ^{13}C{^{1}H} NMR spectrum of [(INpMe)AgCl] (**6**) (300 K, 75.47 MHz, CDCl$_3$).

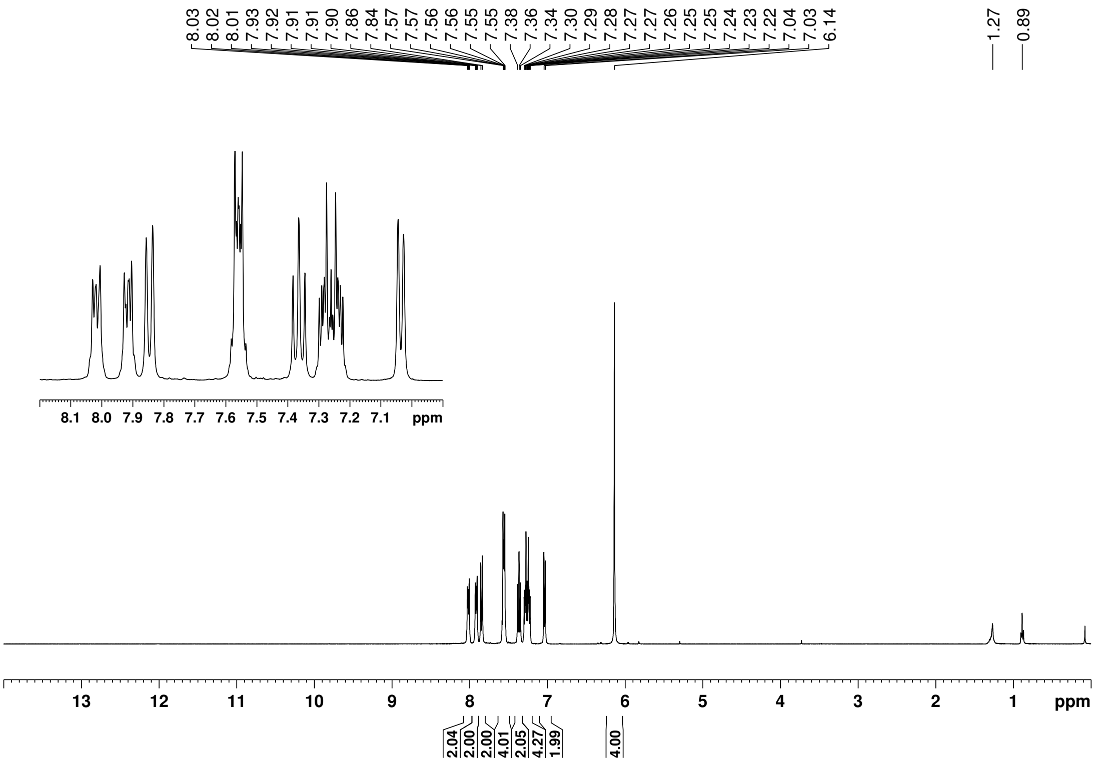

Figure B.21. ^{1}H NMR spectrum of [(BNpMe)AgCl] (**7**) (300 K, 300.13 MHz, CD_2Cl_2).

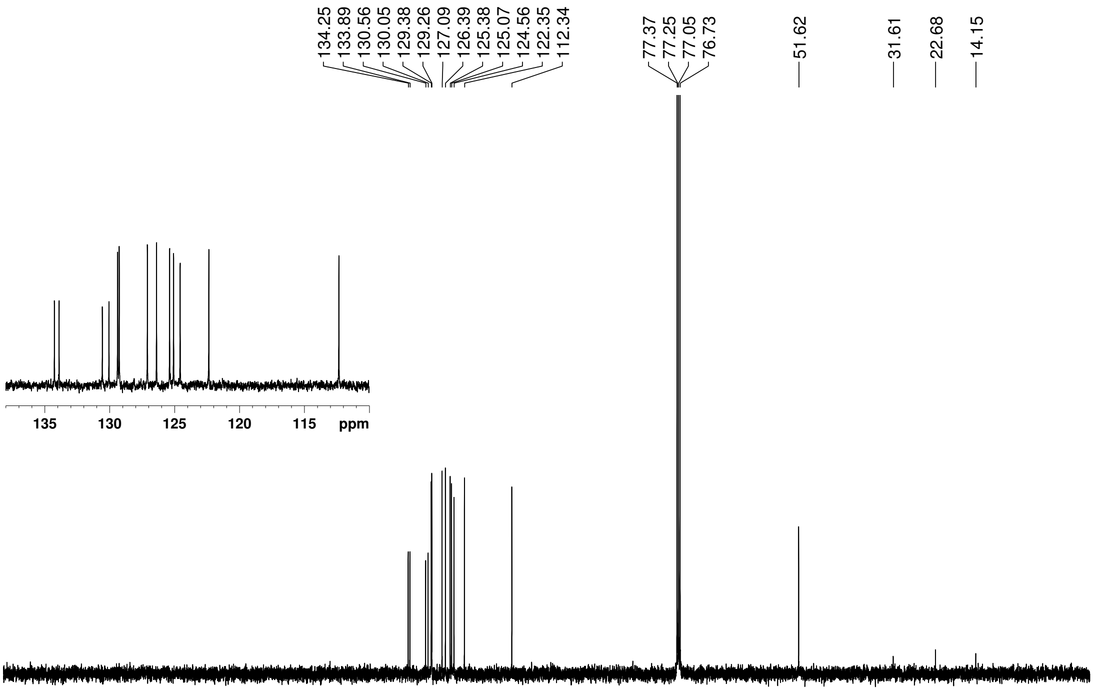

Figure B.22. $^{13}C\{^1H\}$ NMR spectrum of [(BNpMe)AgCl] (**7**) (300 K, 75.47 MHz, CD_2Cl_2).

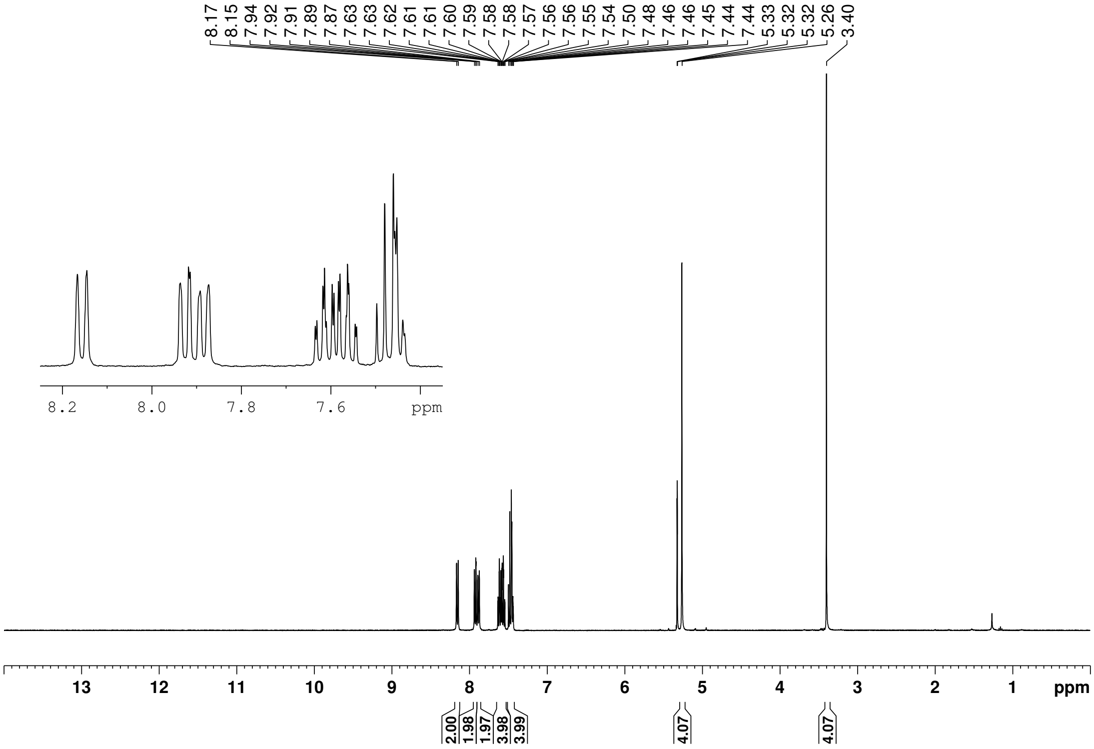

Figure B.23. ^{1}H NMR spectrum of [(SINpMe)AgCl] (**8**) (300 K, 400.13 MHz, CD_2Cl_2).

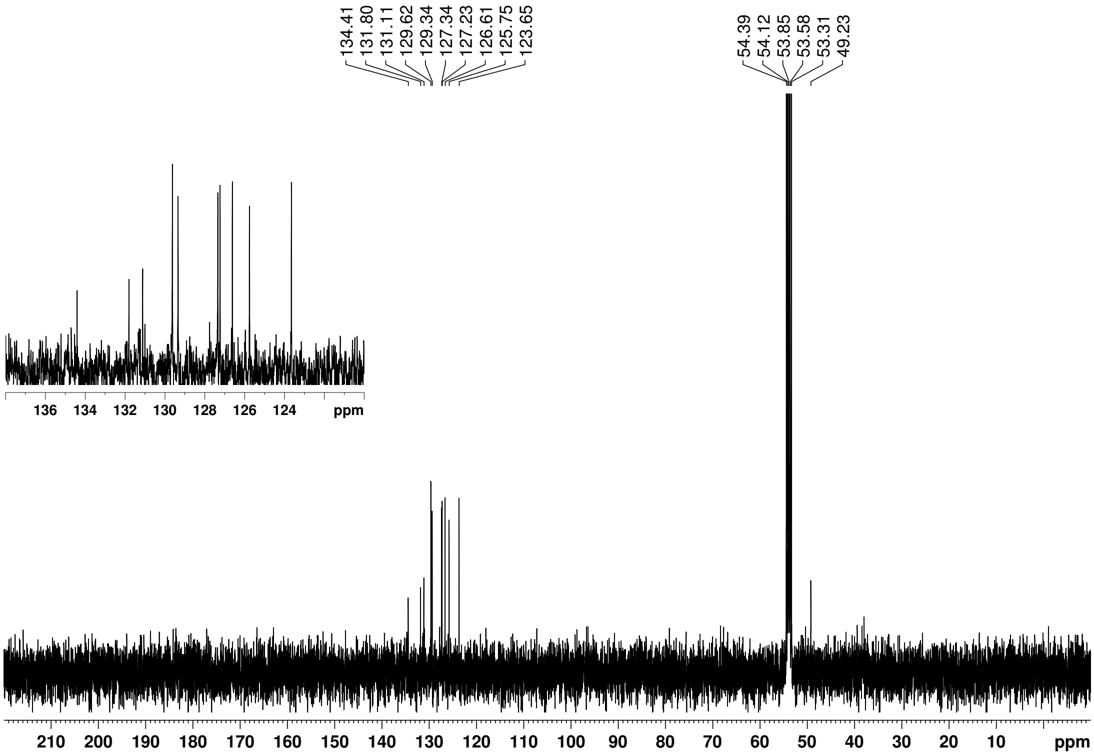

Figure B.24. $^{13}C\{^1H\}$ NMR spectrum of [(SINpMe)AgCl] (**8**) (300 K, 100.61 MHz, CD_2Cl_2).

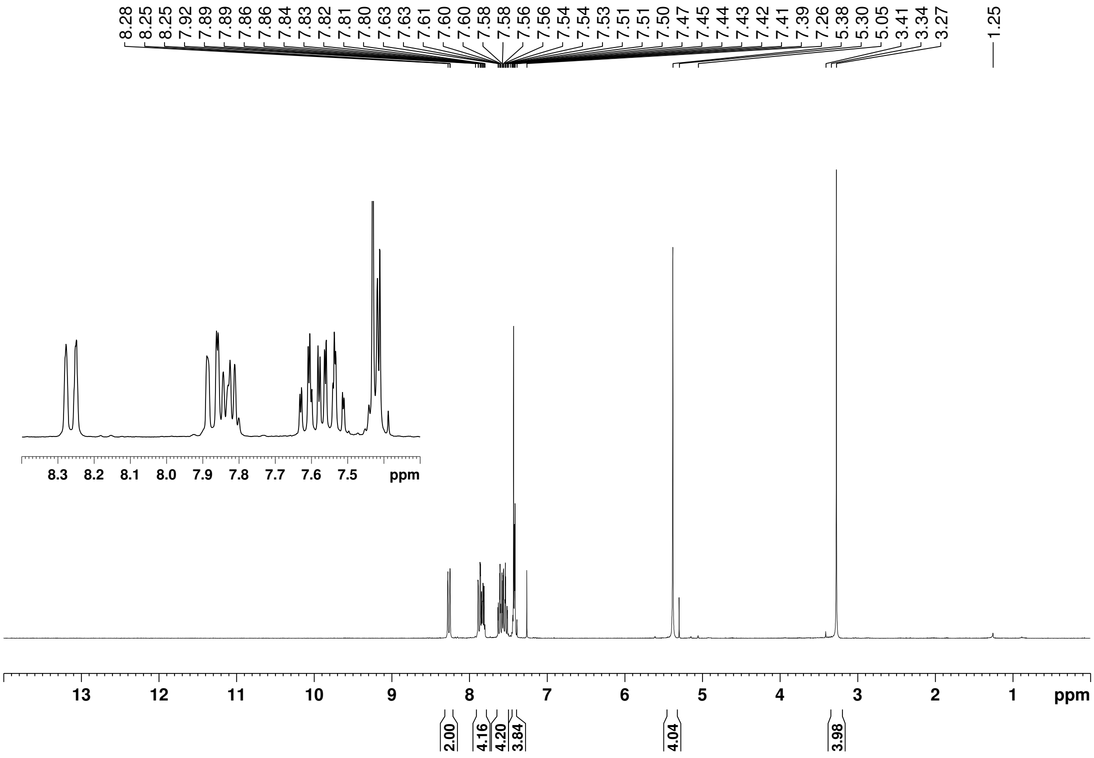

Figure B.25. ^{1}H NMR spectrum of [(SINpMe)AuCl] (**9**) (300 K, 400.13 MHz, CDCl$_3$).

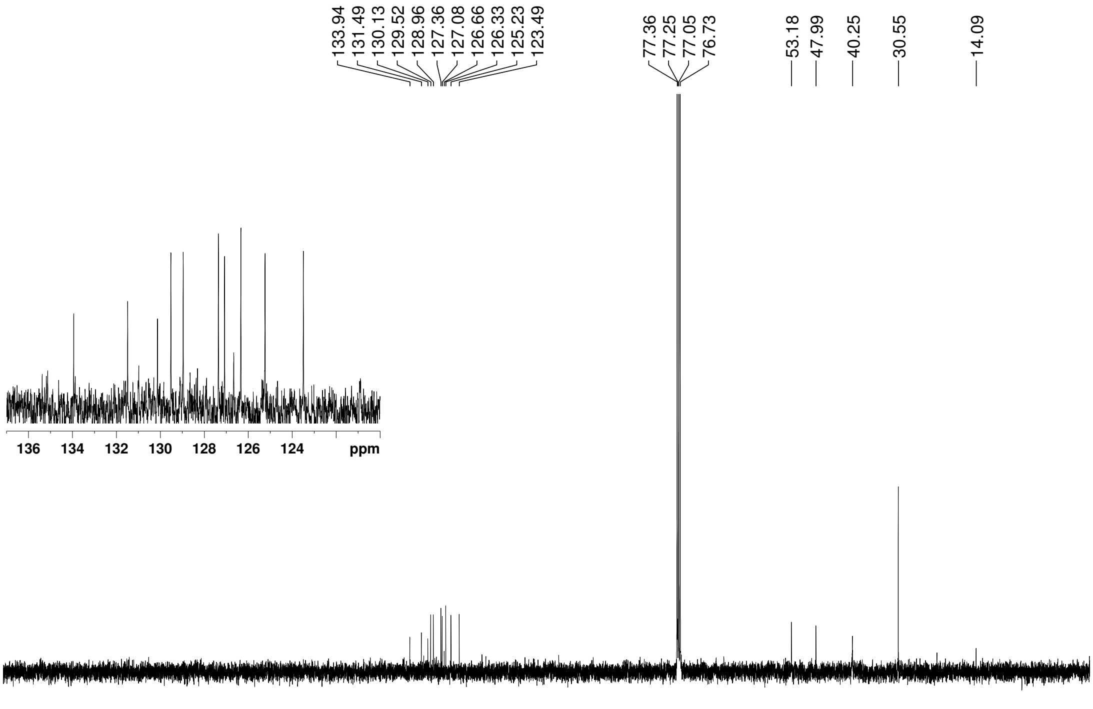

Figure B.26. ^{13}C{^{1}H} NMR spectrum of [(SINpMe)AuCl] (**9**) (300 K, 100.61 MHz, CDCl$_3$).

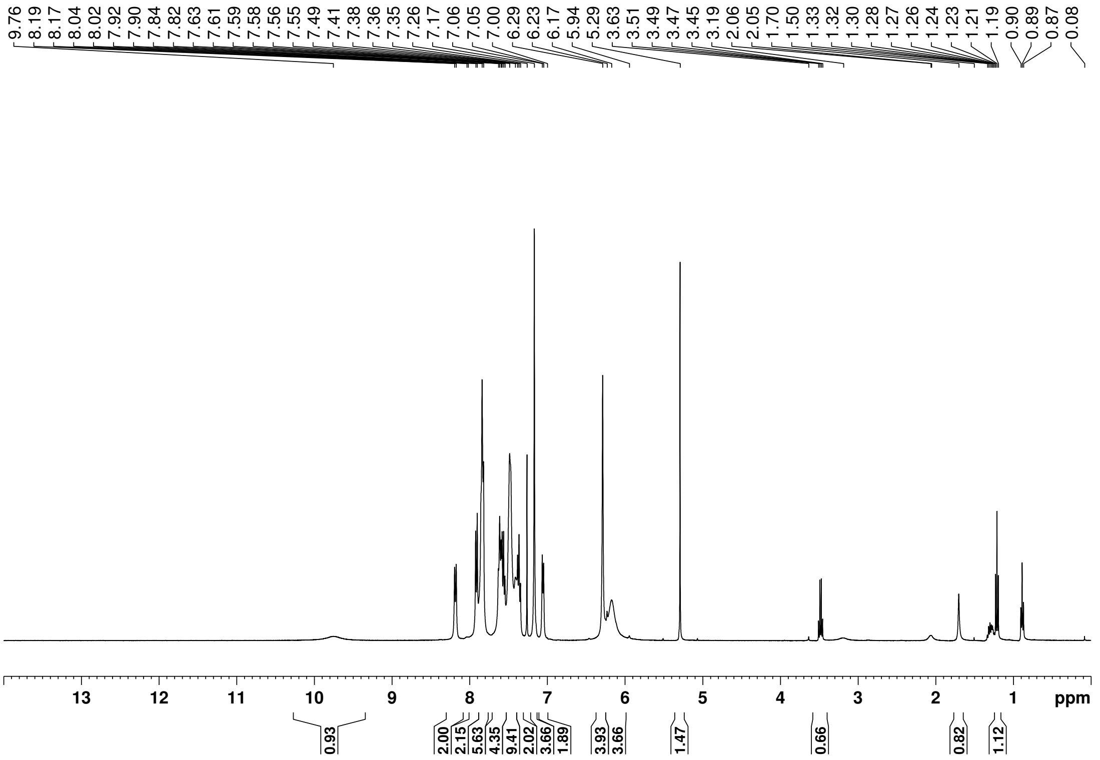

Figure B.27. ^{1}H NMR spectrum of [(BNpMe)AuCl] (**10**) (300 K, 400.13 MHz, CDCl$_3$).

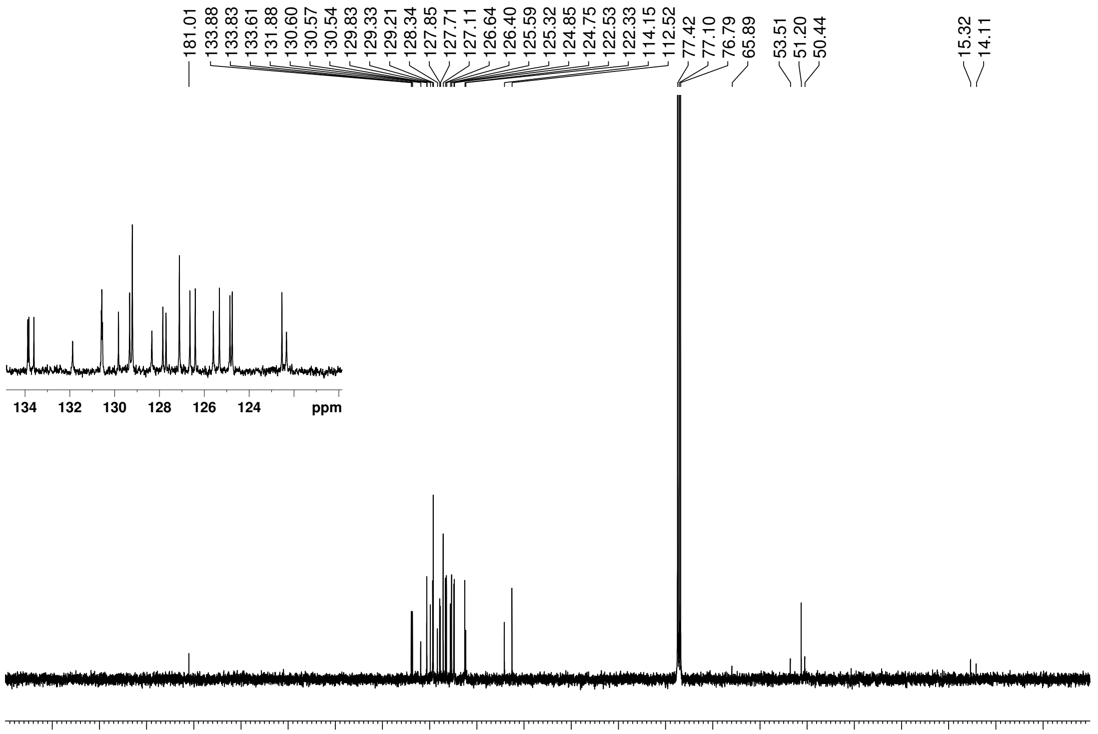

Figure B.28. ^{13}C{^{1}H} NMR spectrum of [(BNpMe)AuCl] (**10**) (300 K, 100.61 MHz, CDCl$_3$).

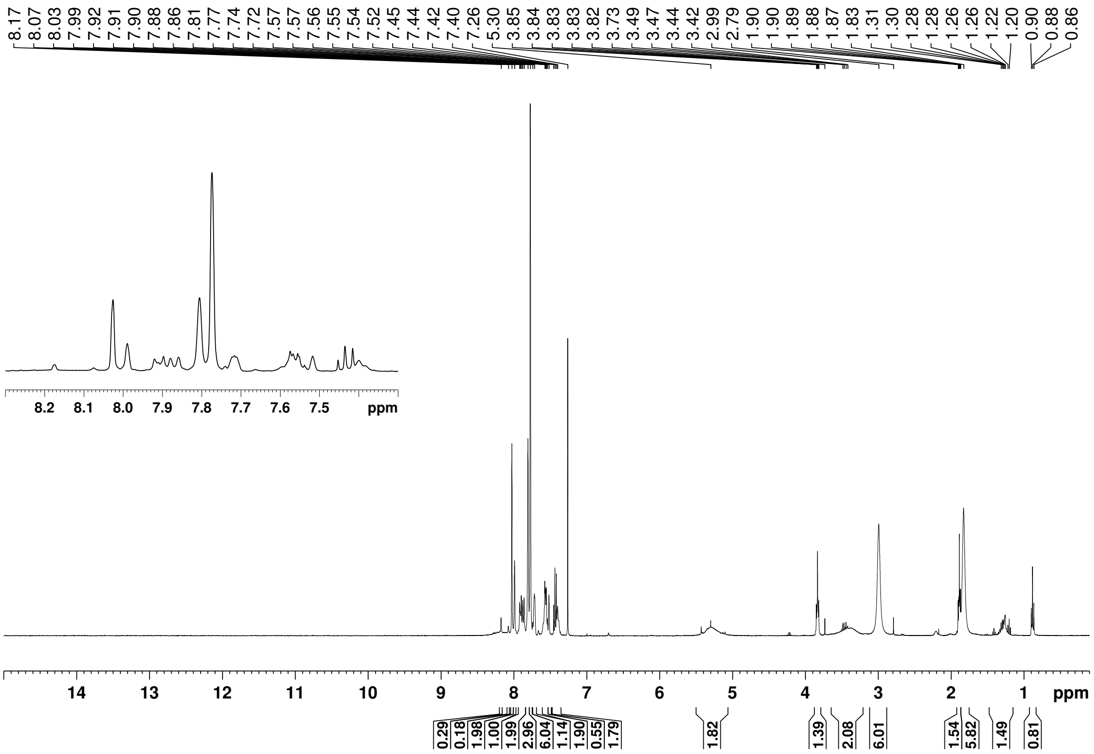

Figure B.29. ^{1}H NMR spectrum of the reaction mixture of **9** and NaBAr$^F{}_4$ (300 K, 300.13 MHz, CDCl$_3$).

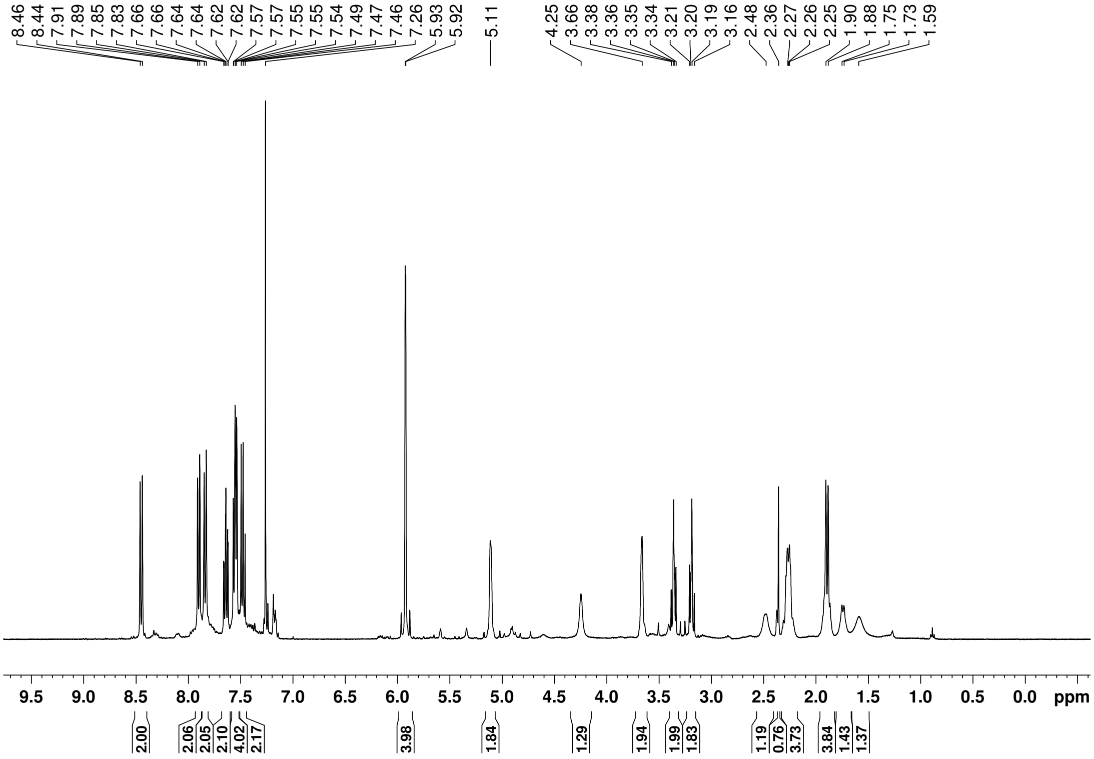

Figure B.30. ^{1}H NMR spectrum of [(SINpMe)RhCl(cod)] (**11**) (300 K, 300.13 MHz, CDCl$_3$).

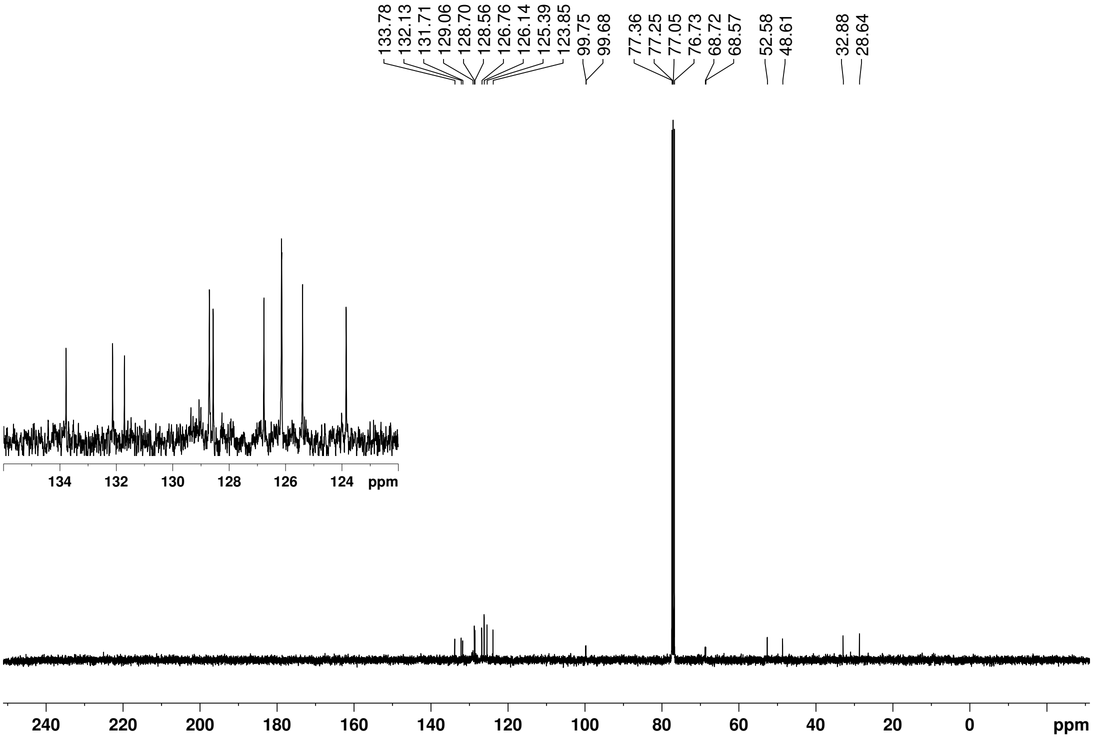

Figure B.31. $^{13}C\{^1H\}$ NMR spectrum of [(SINpMe)RhCl(cod)] (**11**) (300 K, 75.47 MHz, $CDCl_3$).

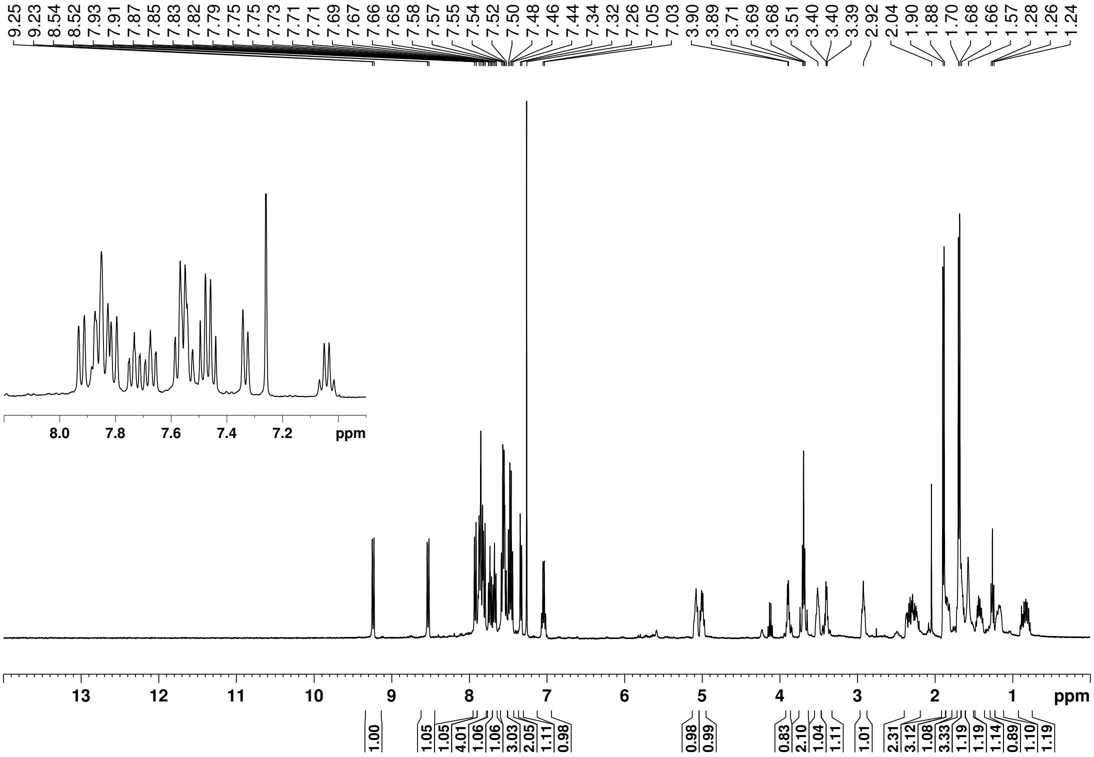

Figure B.32. ^1H NMR spectrum of [(SINpEt)RhCl(cod)] (**12**) (300 K, 300.13 MHz, $CDCl_3$).

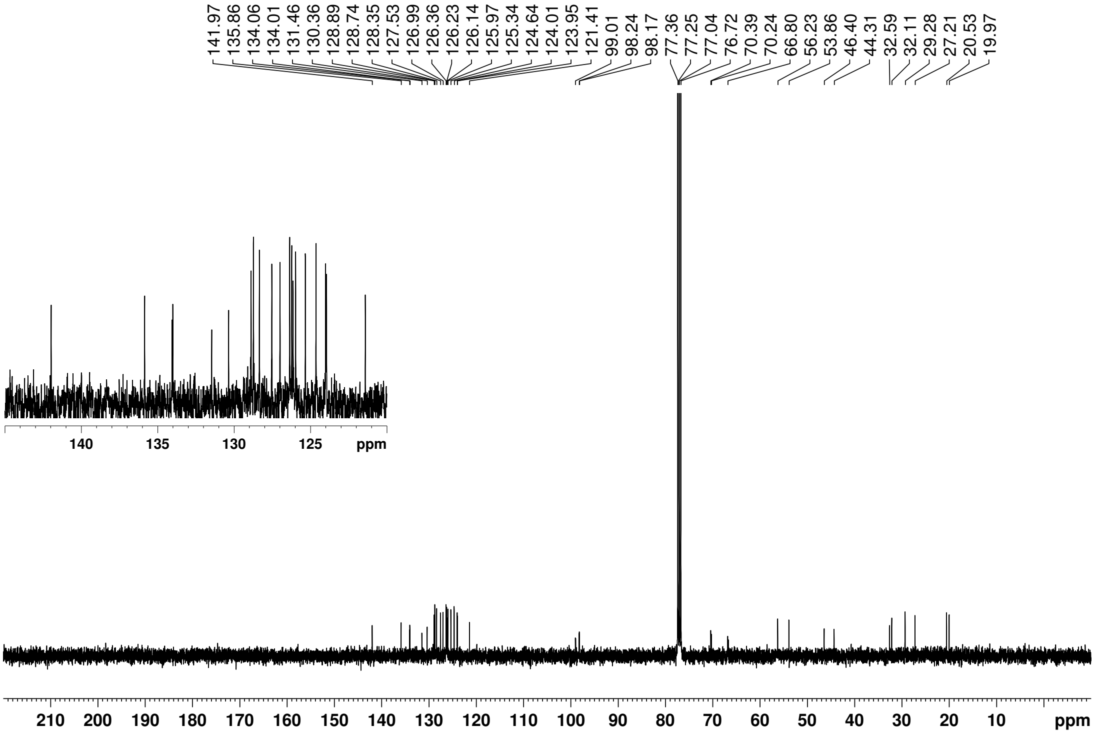

Figure B.33. $^{13}C\{^{1}H\}$ NMR spectrum of [(SINpEt)RhCl(cod)] (**12**) (300 K, 75.47 MHz, $CDCl_3$).

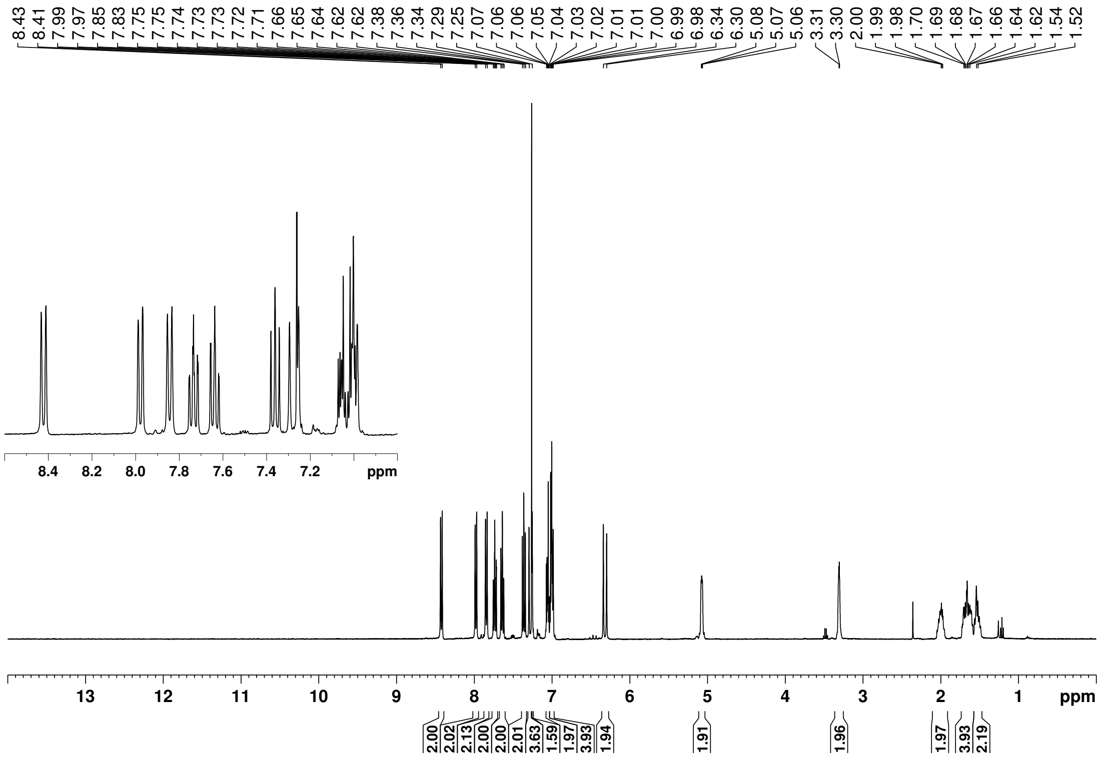

Figure B.34. ^{1}H NMR spectrum of [(BNpMe)RhCl(cod)] (**13**) (300 K, 300.13 MHz, $CDCl_3$).

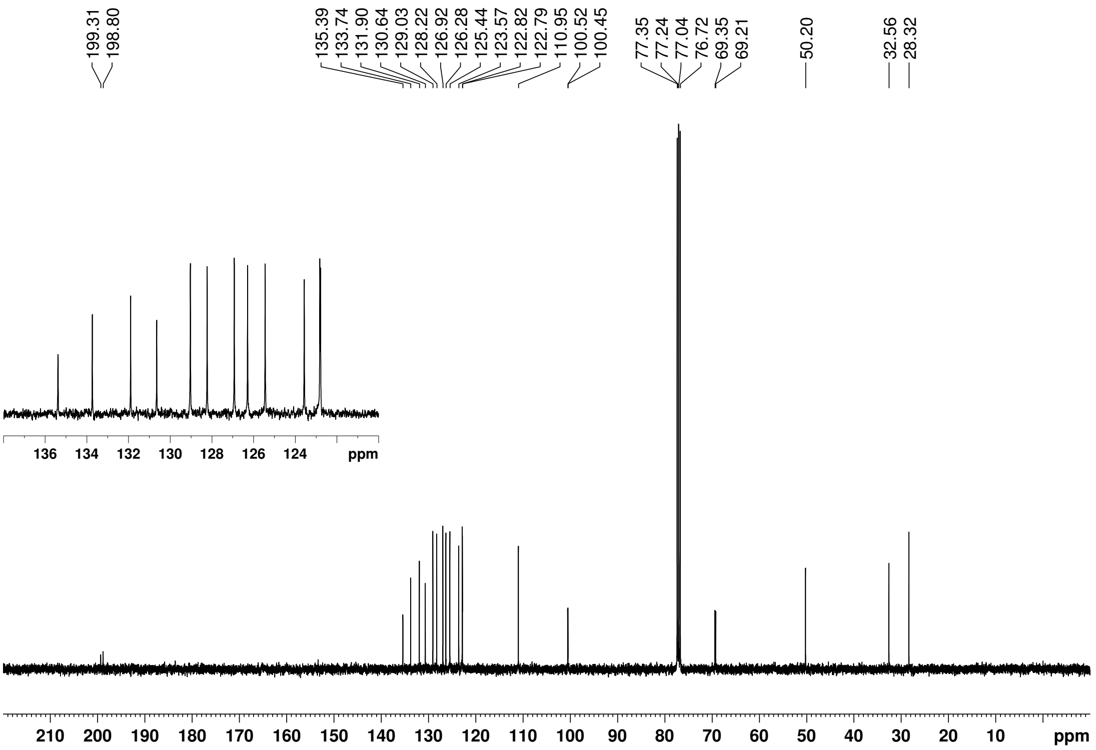

Figure B.35. ^{13}C{^{1}H} NMR spectrum of [(BNpMe)RhCl(cod)] (**13**) (300 K, 75.47 MHz, CDCl$_3$).

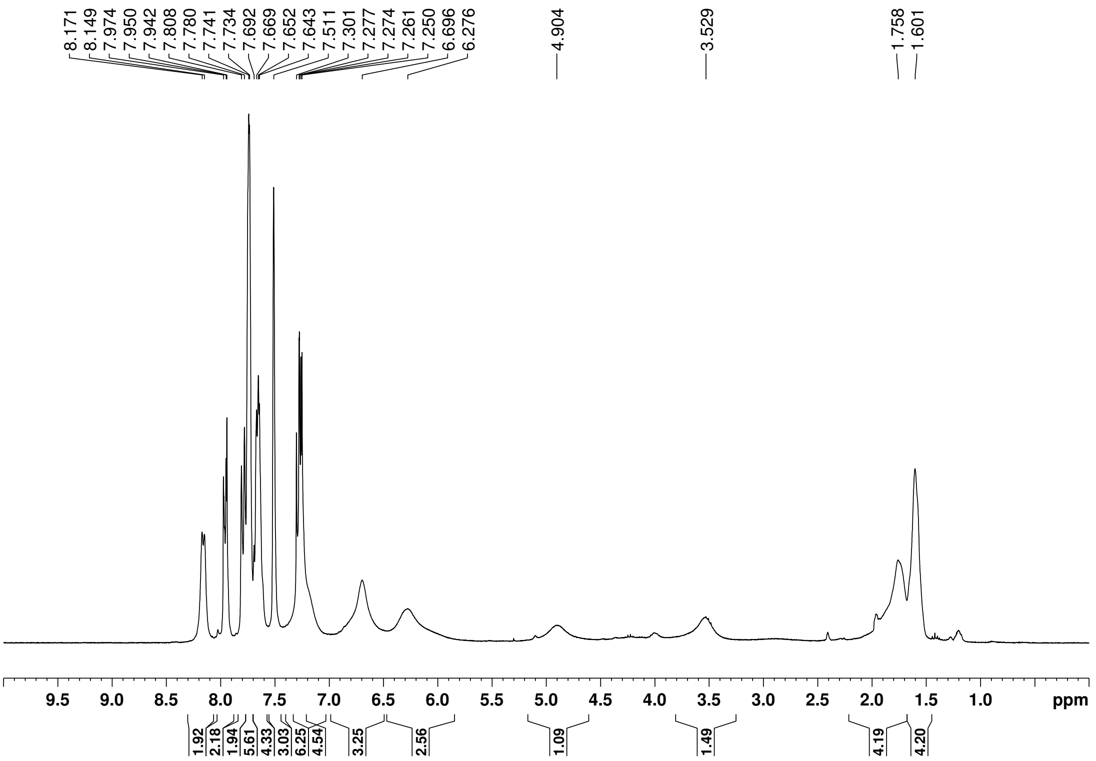

Figure B.36. ^{1}H NMR spectrum of the reaction of [(BNpMe)RhCl(cod)] with NaBAr$^{F}_{4}$ (**14a**) (300 K, 300.13 MHz, CDCl$_3$).

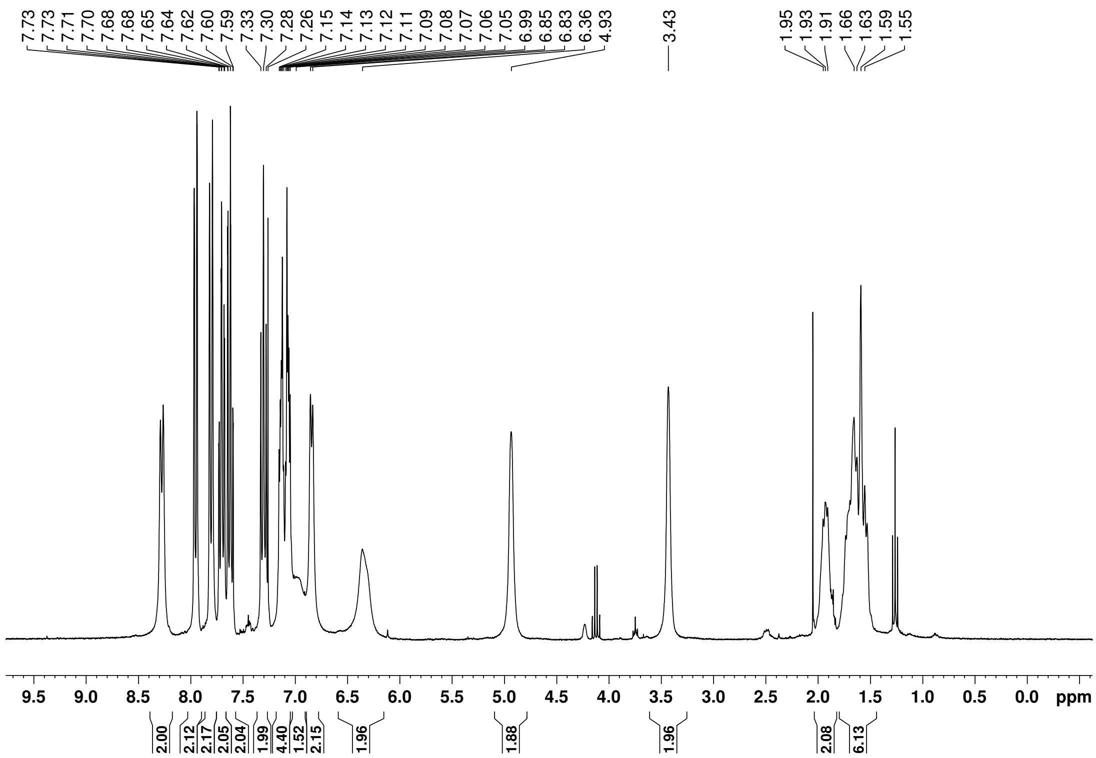

Figure B.37. ^{1}H NMR spectrum of the reaction of [(SINpMe)RhCl(cod)] with $AgBF_4$ (**14b**) (300 K, 300.13 MHz, $CDCl_3$).

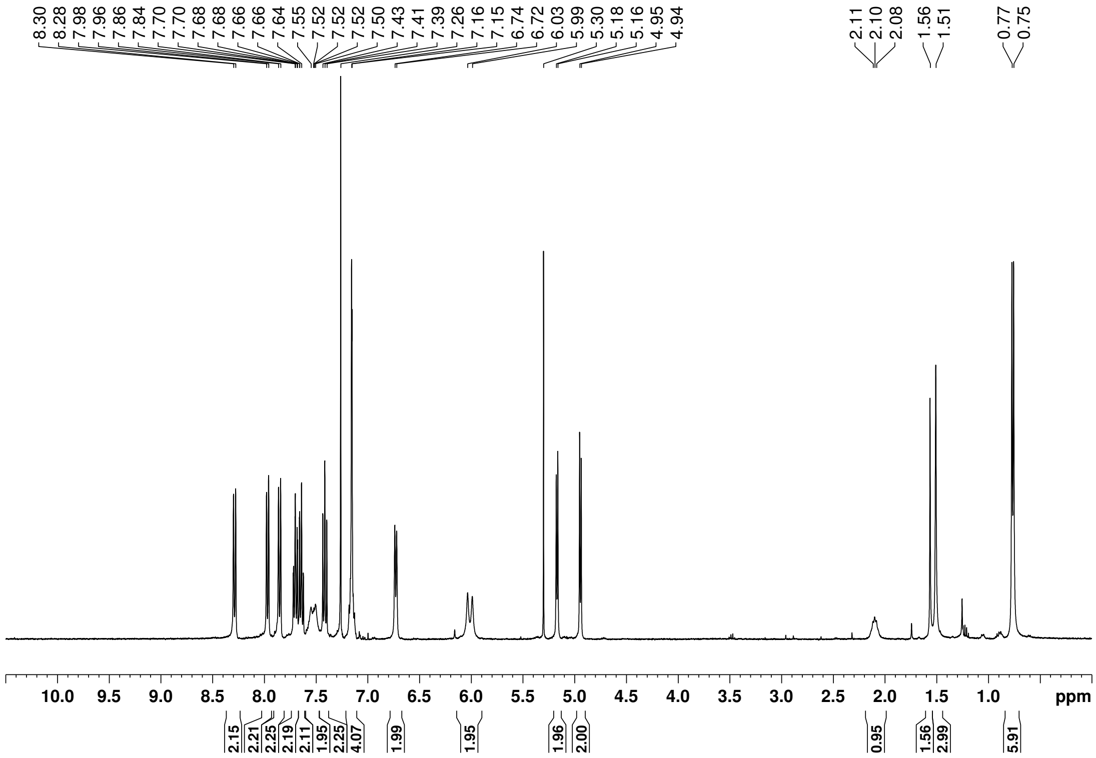

Figure B.38. ^{1}H NMR spectrum of [(cym)RuCl$_2$(BNpMe)] (**15**) (300 K, 300.13 MHz, $CDCl_3$).

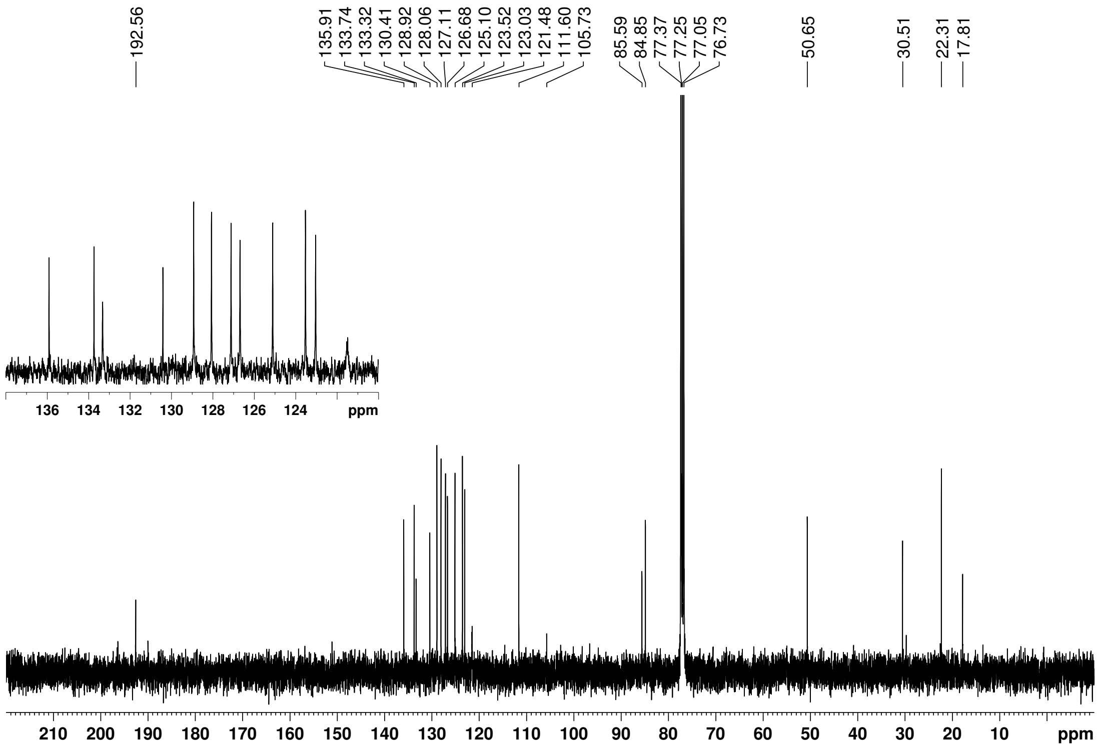

Figure B.39. $^{13}C\{^1H\}$ NMR spectrum of [(cym)$RuCl_2$(BNpMe)] (**15**) (300 K, 75.47 MHz, $CDCl_3$).

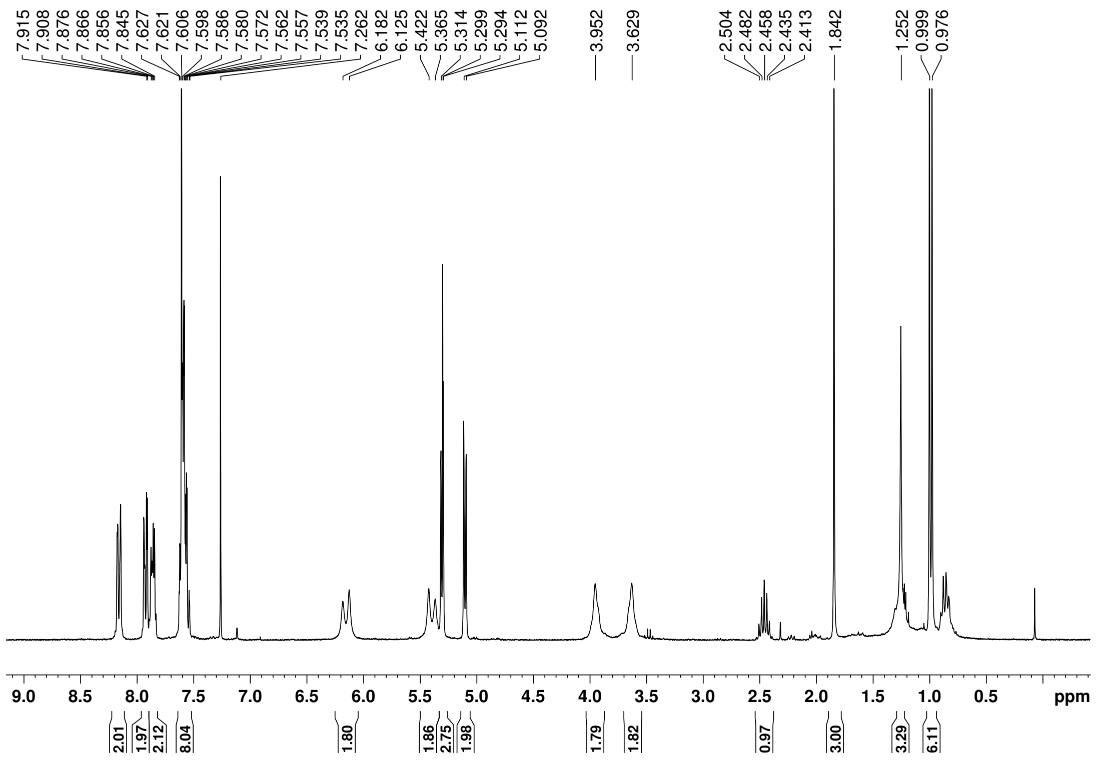

Figure B.40. ^1H NMR spectrum of [(cym)$RuCl_2$(SINpMe)] (**16**) (300 K, 300.13 MHz, $CDCl_3$).

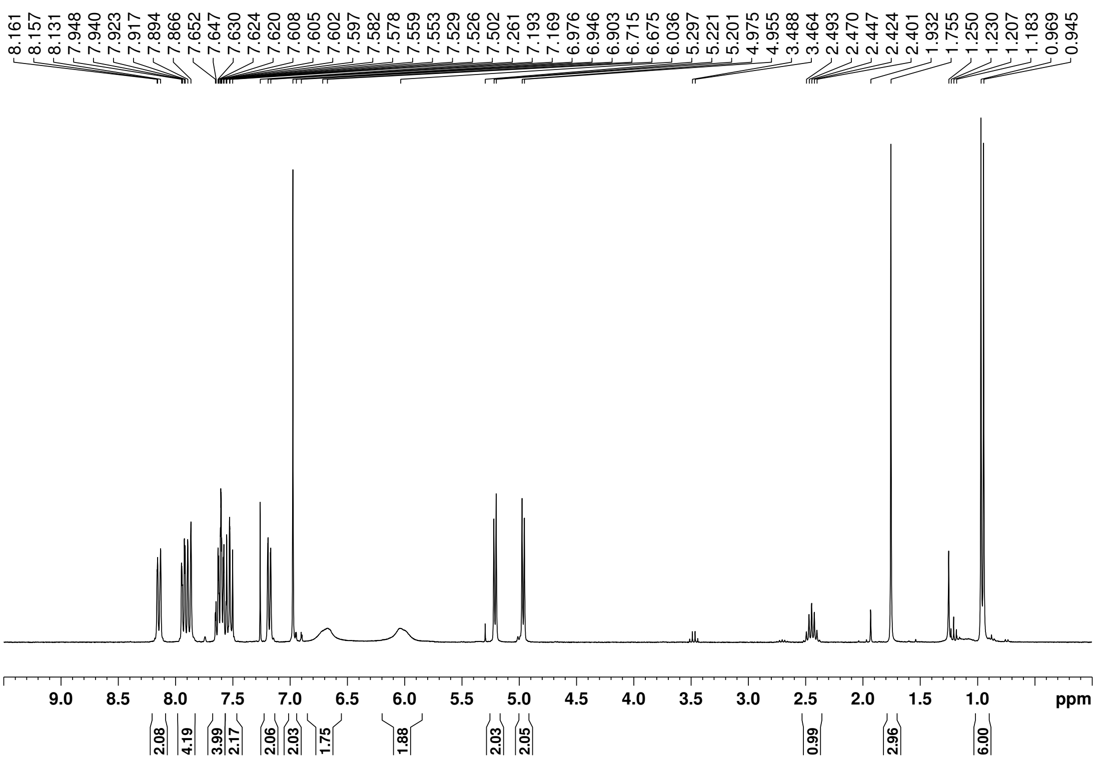

Figure B.41. ^{1}H NMR spectrum of [(cym)RuCl$_2$(INpMe)] (**17**) (300 K, 300.13 MHz, CDCl$_3$).

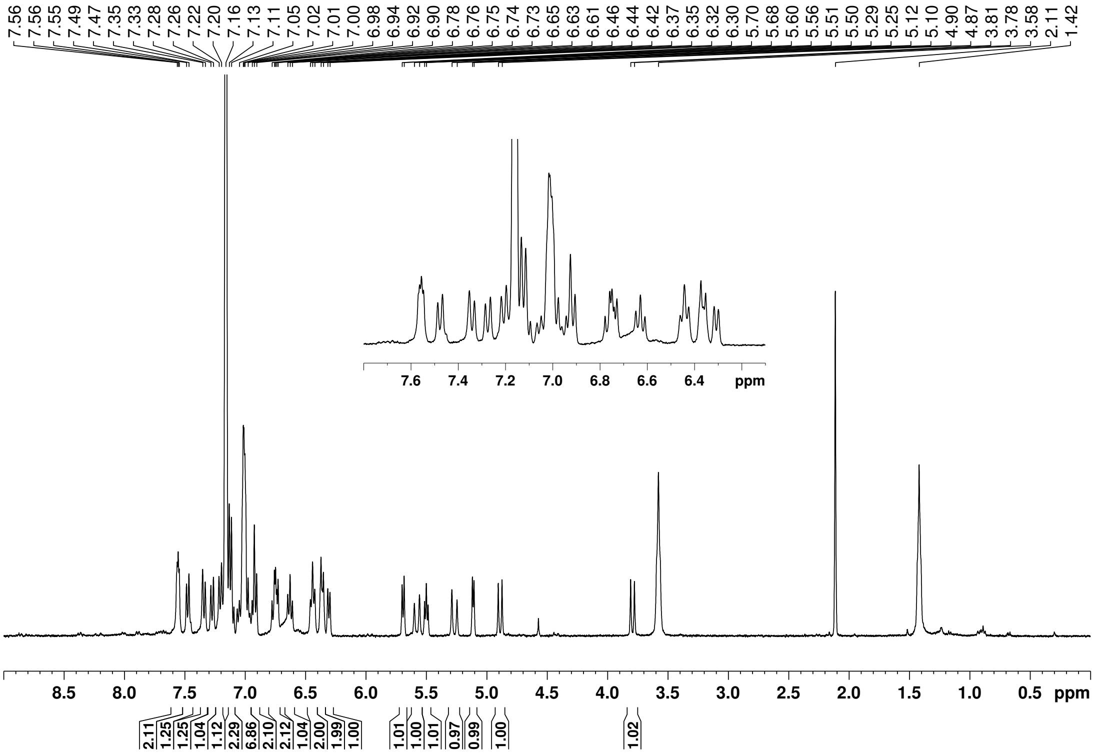

Figure B.42. ^{1}H NMR spectrum of [(BNpMe*)RuPh$_2$] (**18**) (300 K, 300.13 MHz, C$_6$D$_6$).

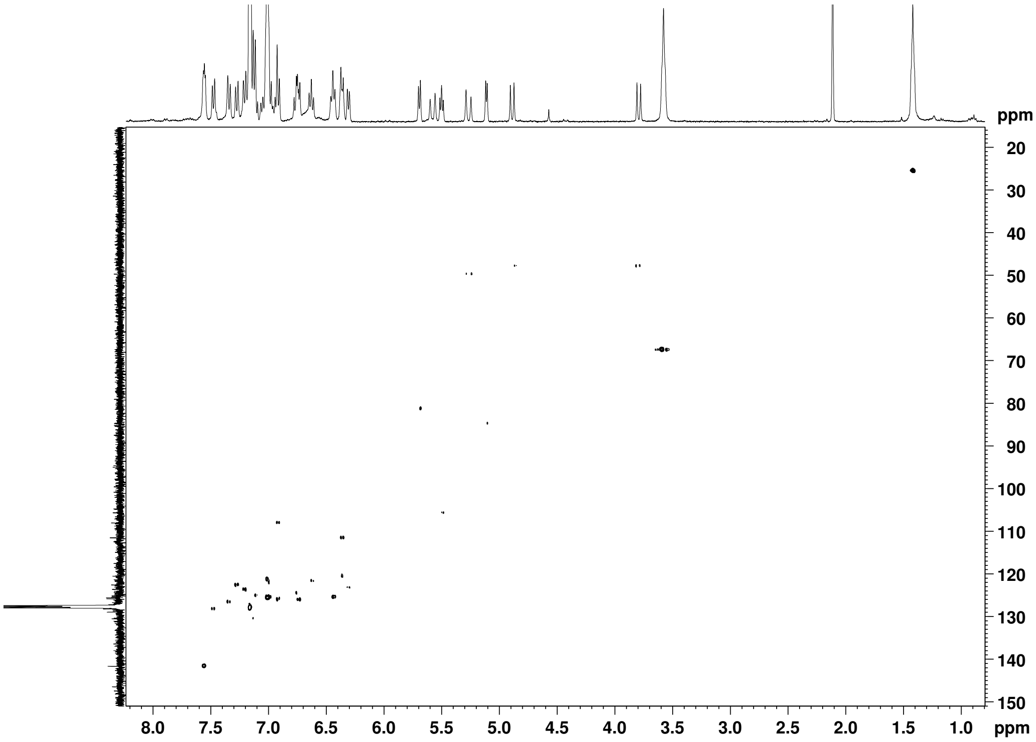

Figure B.43. $^{1}H/^{13}C$ HSQC NMR spectrum of **18** (300 K, C_6D_6).

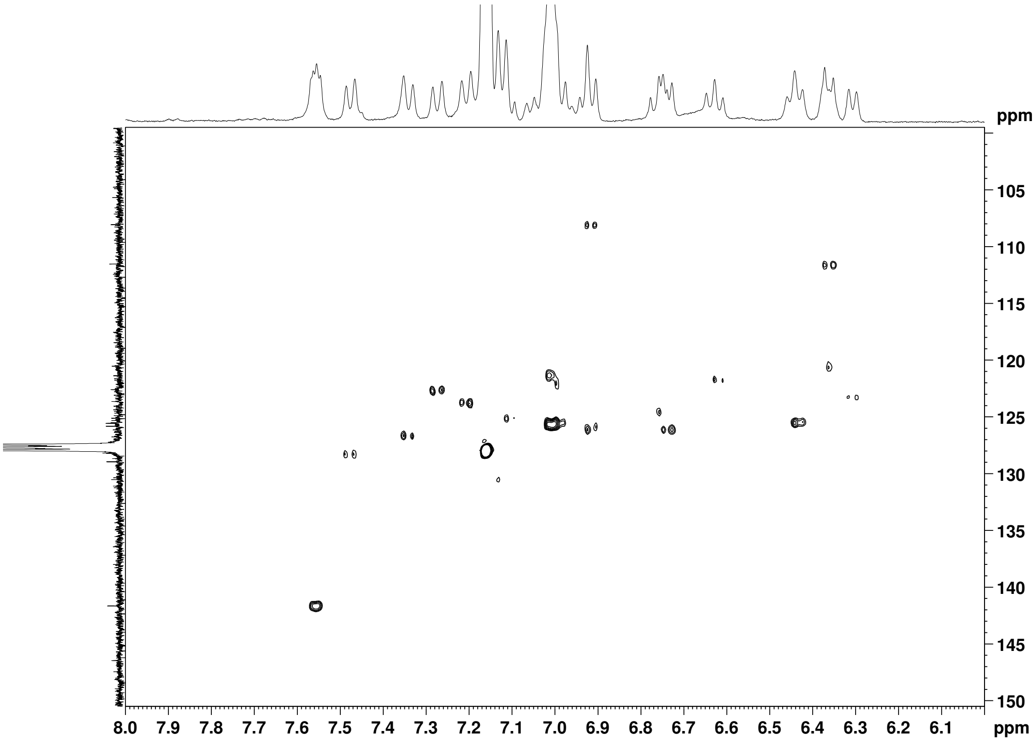

Figure B.44. $^{1}H/^{13}C$ HSQC NMR spectrum of **18** (C_6D_6; aromatic region).

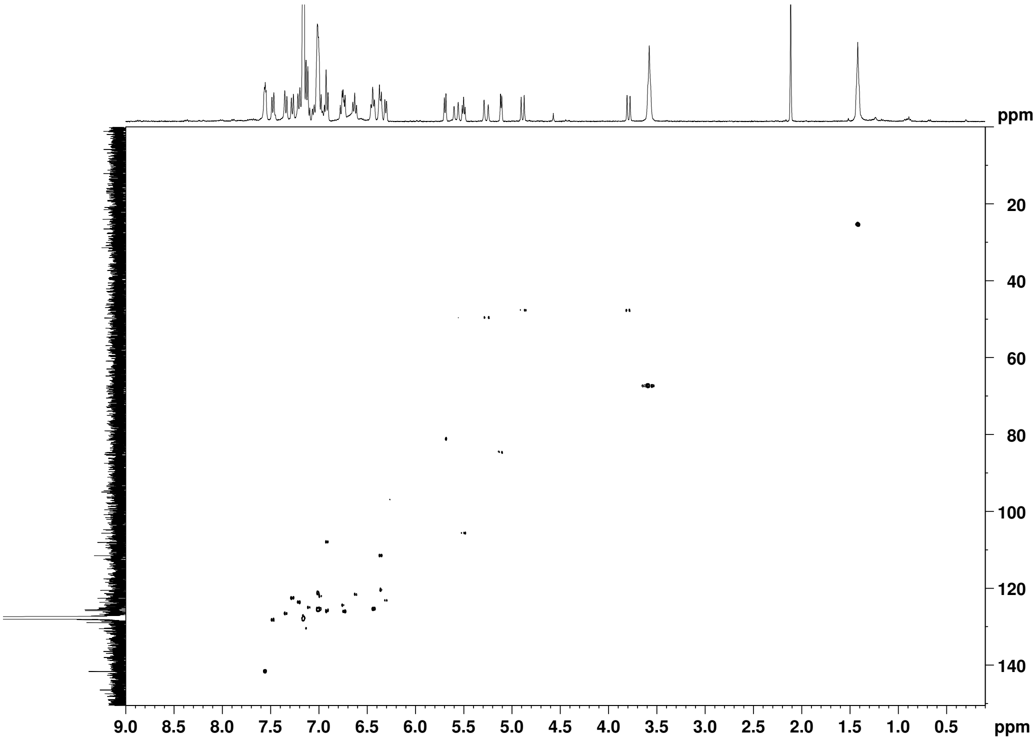

Figure B.45. $^1H/^{13}C$ HMBC NMR spectrum of **18** (300 K, C_6D_6).

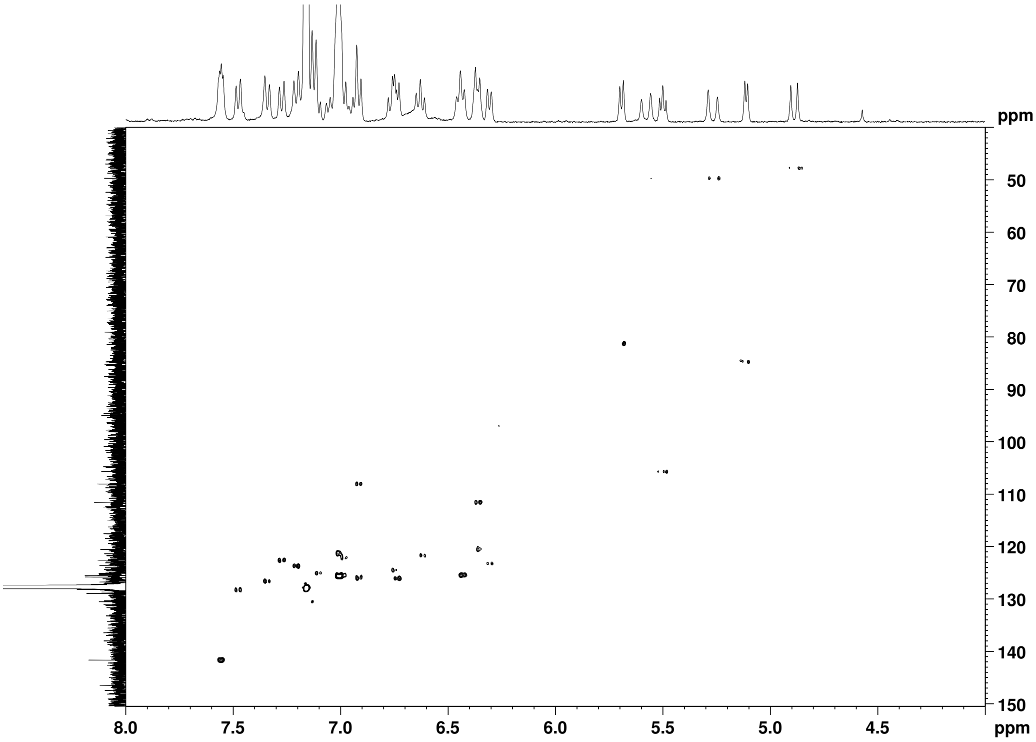

Figure B.46. $^1H/^{13}C$ HMBC NMR spectrum of **18** (C_6D_6; aromatic region).

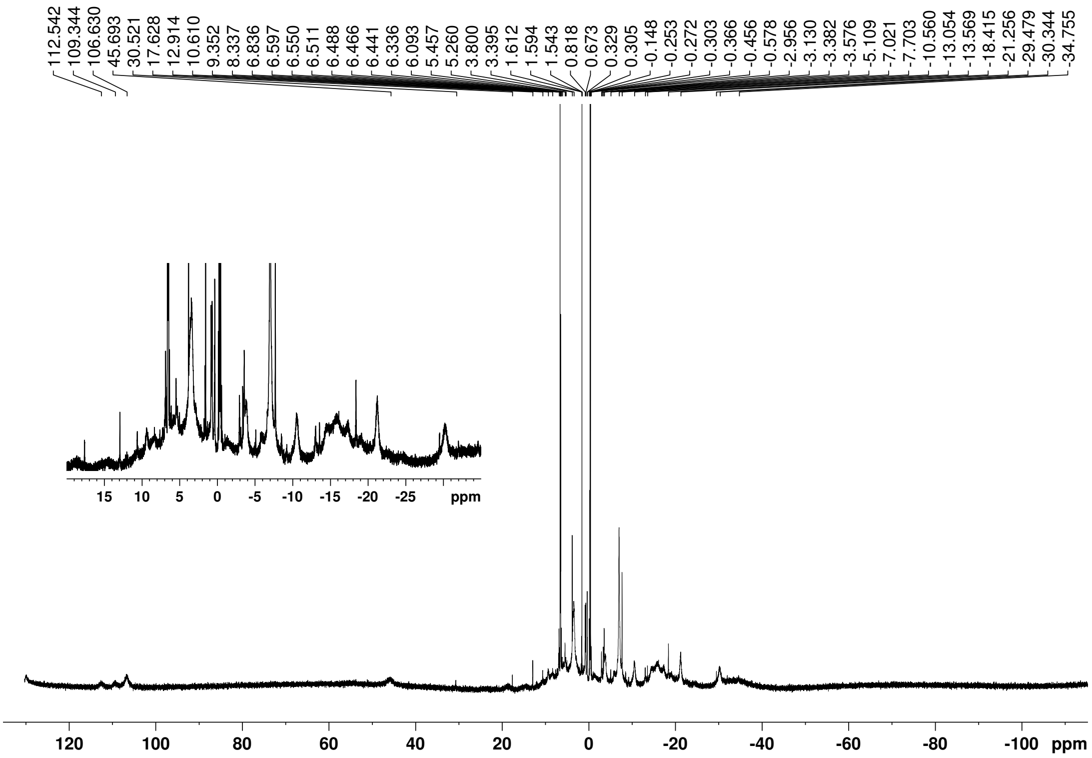

Figure B.47. ^{1}H NMR spectrum of [(SINp)Co{N(SiMe$_3$)$_2$}$_2$] (**21**) (300 K, 300.13 MHz, C_6D_6).

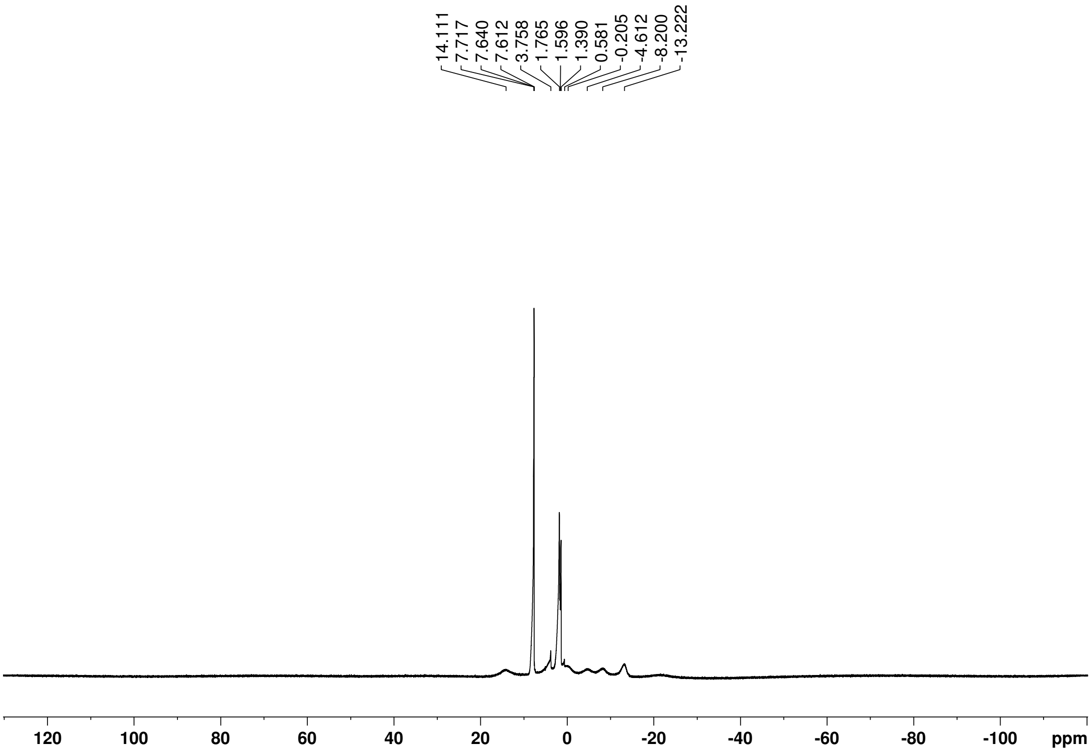

Figure B.48. ^{1}H NMR spectrum of [(SINp)Fe{N(SiMe$_3$)$_2$}$_2$] (**25**) (300 K, 300.13 MHz, C_6D_6).

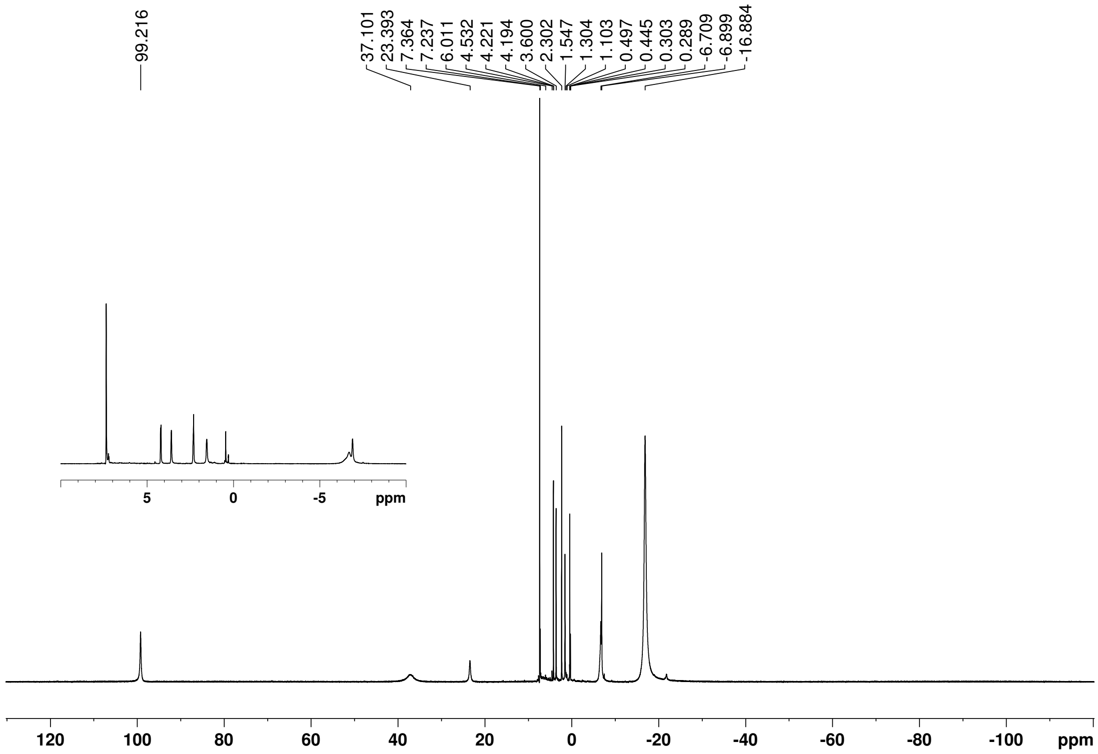

Figure B.49. ^{1}H NMR spectrum of [(BNpMe)Fe{N(SiMe$_3$)$_2$}$_2$] (**26**) (300 K, 300.13 MHz, C_6D_6).

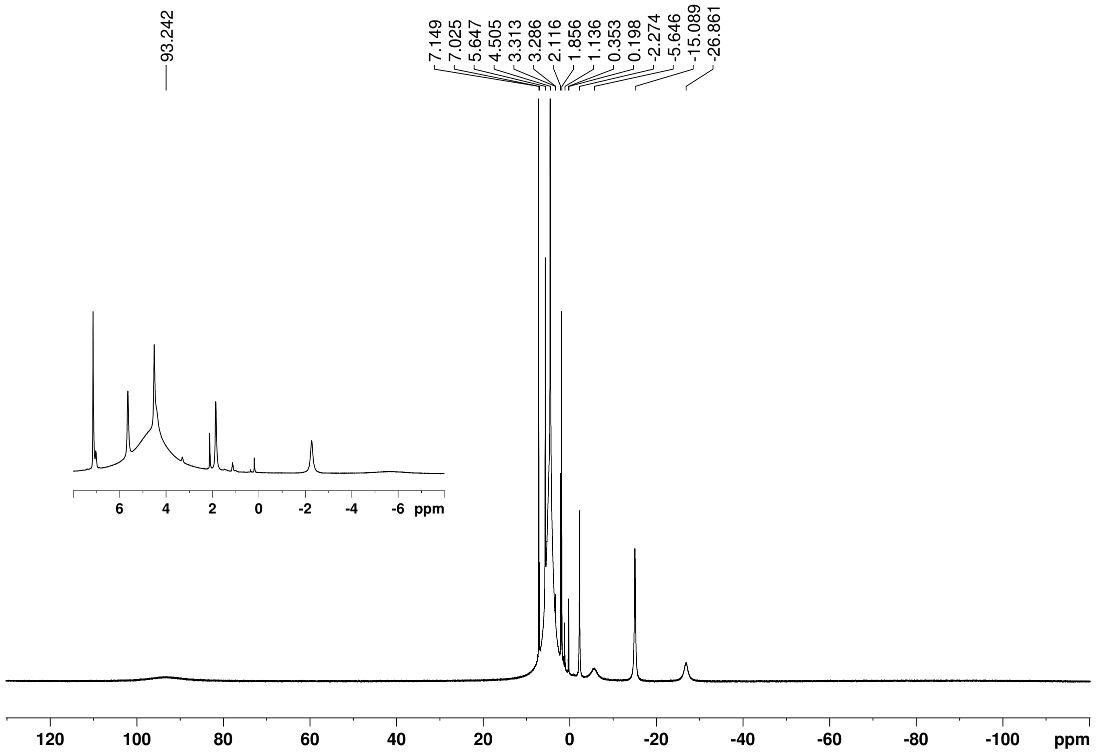

Figure B.50. ^{1}H NMR spectrum of [(SINpMe)Fe{N(SiMe$_3$)$_2$}$_2$] (**27**) (300 K, 300.13 MHz, C_6D_6).

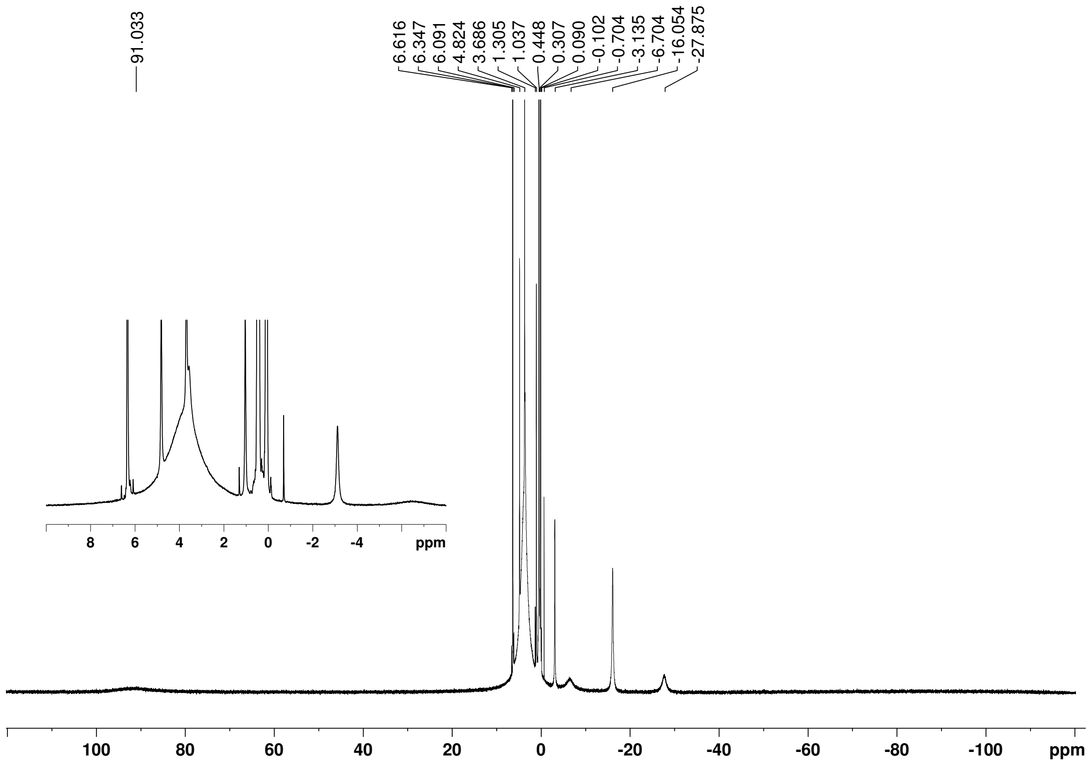

Figure B.51. ^{1}H NMR spectrum of [(SINpEt)Fe{N(SiMe$_3$)$_2$}$_2$] (**28**) (300 K, 300.13 MHz, C_6D_6).

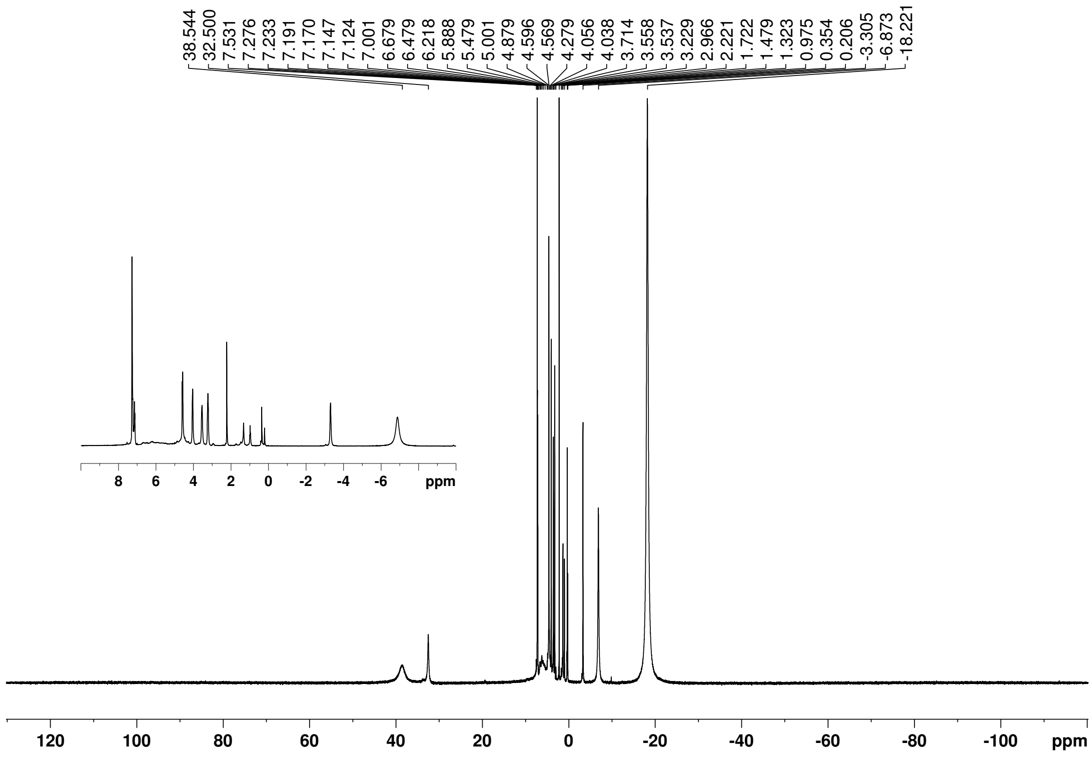

Figure B.52. ^{1}H NMR spectrum of [(INpMe)Co{N(SiMe$_3$)$_2$}$_2$] (**29**) (300 K, 300.13 MHz, C_6D_6).

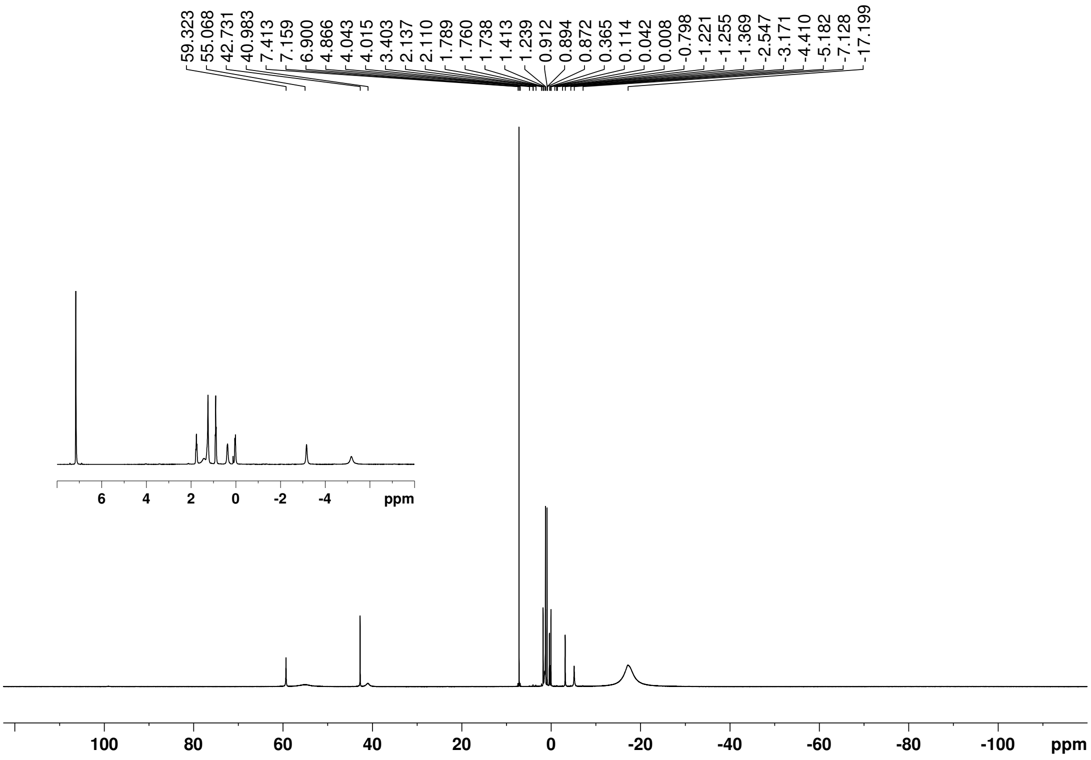

Figure B.53. ^{1}H NMR spectrum of [(BNpMe)Co{N(SiMe$_3$)$_2$}$_2$] (**30**) (300 K, 300.13 MHz, C_6D_6).

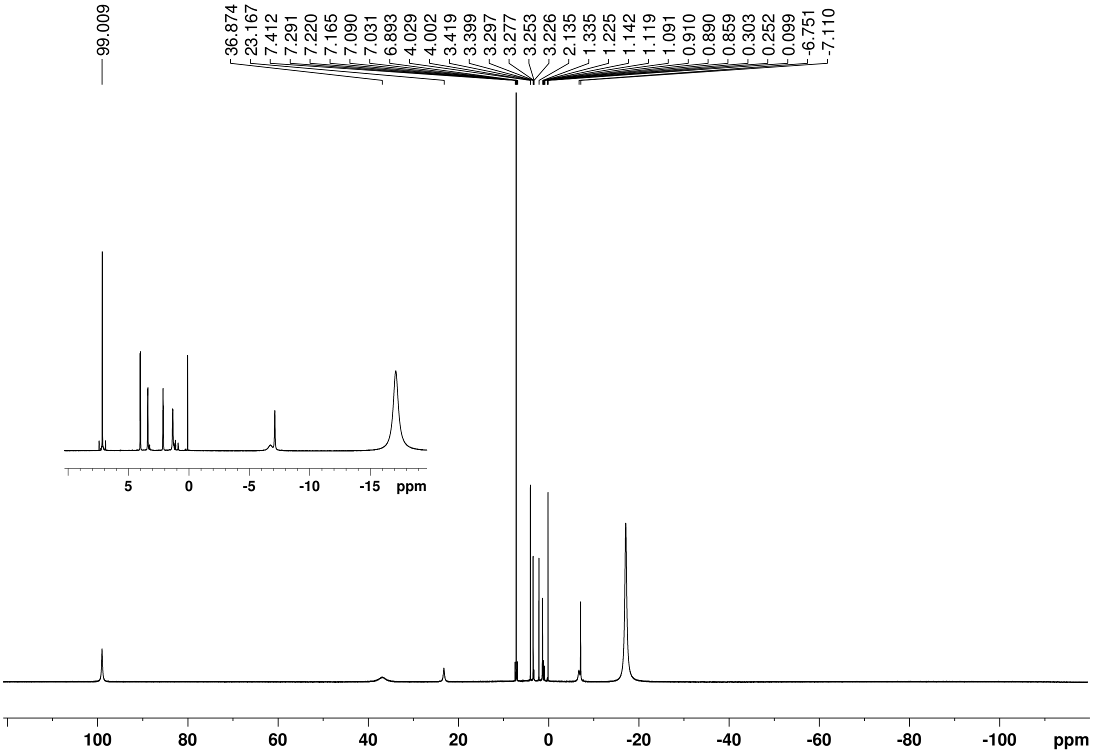

Figure B.54. ^{1}H NMR spectrum of [(SINpMe)Co{N(SiMe$_3$)$_2$}$_2$] (**31**) (300 K, 300.13 MHz, C_6D_6).

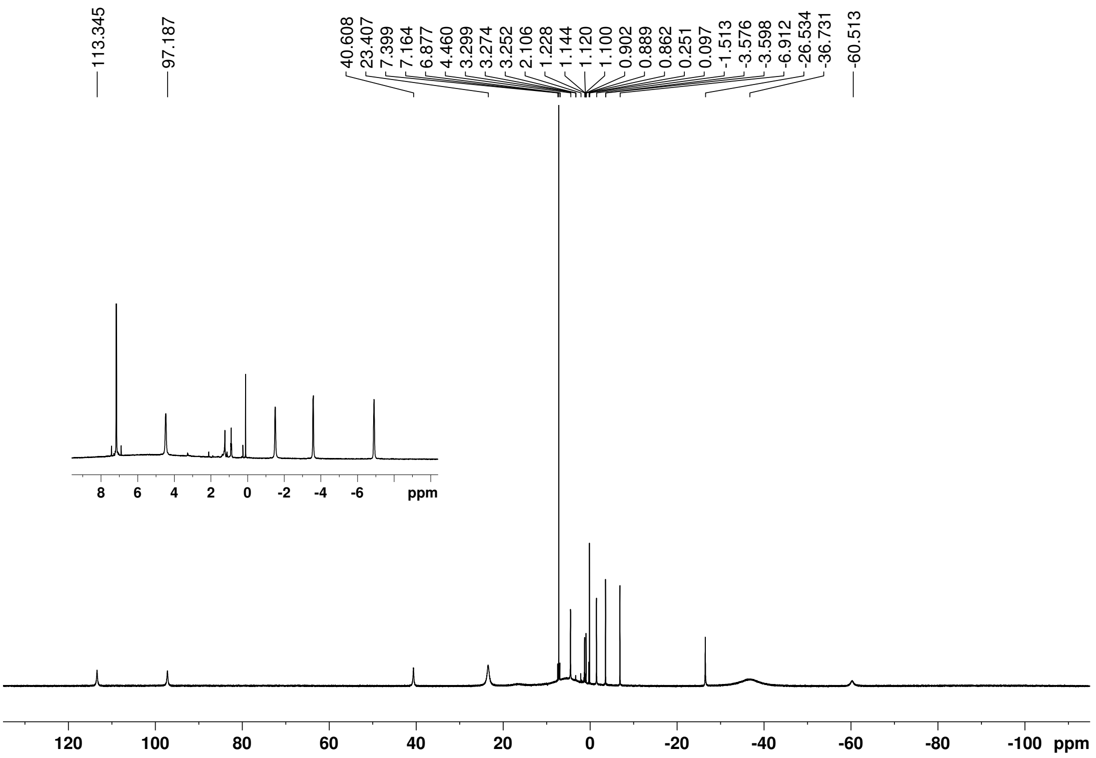

Figure B.55. ^{1}H NMR spectrum of [(SINpEt)Co{N(SiMe$_3$)$_2$}$_2$] (**32**) (300 K, 300.13 MHz, C_6D_6).

Table 6.2. ^{1}H NMR chemical shifts of Fe and Co NHC amide complexes.

Compound	^{1}H NMR (C_6D_6)
[(SINp)Co{N(SiMe$_3$)$_2$}$_2$] (**21**)	-29.8 (br s); -20.7 (br s); -10.1 (br s); -3.3 (br s); 3.9 (br s); 46.7 (br s); 107.5 (br s); 110.2 (br s); 113.3 (br s)
[(INpMe)Co{N(SiMe$_3$)$_2$}$_2$] (**29**)	-17.2 (br s); -5.2 (br s); -3.2 (s); 0.0 (d); 0.4 (s); 1.4 (br s); 1.8 (t); 41.0 (br s); 42.7 (s); 52.0 to 58.2 (br); 59.3 (s)
[(BNpMe)Co{N(SiMe$_3$)$_2$}$_2$] (**30**)	-18.2 (br s); -6.9 (br s); -3.3 (br s); 0.2 (s); 0.4 (s); 1.0 (s); 1.3 (s); 2.2 (s); 3.2 (s); 3.5 (s); 4.0 (s); 4.6 (d); 7.1 (d); 32.5 (br s); 37.2 to 40.2 (br)
[(SINpMe)Co{N(SiMe$_3$)$_2$}$_2$] (**31**)	-17.1 (br s); -7.1 (s); -6.7 (br s); 0.1 (s); 1.3 (m); 2.1 (m); 3.4 (d); 4.0 (d); 23.2 (br s); 36.9 (br s); 99.0 (br s)
[(SINpEt)Co{N(SiMe$_3$)$_2$}$_2$] (**32**)	-60.3 (br s); -36.6 (br); -26.5 (s); -6.9 (s); -3.6 (s); -1.5 (s); 0.1 (s); 4.5 (s); 2.3 to 9.4 (br); 23.4 (br s); 40.6 (br s); 97.1 (br s); 113.4 (br s)
[(SINp)Fe{N(SiMe$_3$)$_2$}$_2$] (**25**)	-25 to -18 (br); -13.2 (br s); -8.2 (br s); -4.7 (br s); 0.0 (br s); 0.6 (s); 1.4 (s); 1.6 (s); 1.8 (s); 3.7 (br s); 7.6 (s); 7.7 (s); 12.0 to 16.8 (br)
[(BNpMe)Fe{N(SiMe$_3$)$_2$}$_2$] (**26**)	-65.5 (br s); -13.8 (br s); -8.6 (br s); -2.9 (br s); -1.8 (br s); 1.5 (br s); 5.6 (br); 7.19 (br s); 11.3 (br s); 21.4 (br s); 42.5 (br s)
[(SINpMe)Fe{N(SiMe$_3$)$_2$}$_2$] (**27**)	-26.8 (br s); -15.1 (s); -5.6 (br s); -2.3 (s); 0.2 (s); 1.9 (s); 2.1 (s); 3.3 (d); 4.5 (s); 5.6 (s); 2.5 to 6 (br); 7.0 (s); 86 to 103 (br)
[(SINpEt)Fe{N(SiMe$_3$)$_2$}$_2$] (**28**)	-26.9 (br s); -15.3 (s); -5.7 (br s); -2.3 (s); 0.1 (s); 0.9 (t); 1.3 (s); 1.9 (s); 4.4 (br s); 4.5 (s); 5.6 (s); 2.5 to 6.5 (br); 85 to 100 (br)

Danksagung

Mein besonderer Dank gilt Prof. Dr. Robert Wolf für die spannende Aufgabenstellung, die hervorragenden Arbeitsbedingungen und die ausgezeichnete Betreuung während der Doktorarbeit.

Bei Prof. Dr. Manfred Scheer bedanke ich mich für die Übernahme des Zweitgutachtens. Prof. Dr. Frank-Michael Matysik und Prof. Dr. Rainer Müller danke ich für die Übernahme der Drittprüferschaft und des Vorsitzes des Promotionsausschusses.

Weiter möchte ich mich bei den Leitern und Mitarbeitern der zentralen Analytik und der Werkstätten bedanken, insbesondere Dr. Michael Bodensteiner (Röntgenstrukturanalyse), Annette Schramm, Georgine Stühler und Fritz Kastner (NMR-Abteilung), Barbara Baumann, Wilhelmine Krutina und Helmut Schüller (Elementaranalyse) sowie Markus Lindner (Glasbläserei).

Bei meinen Kooperationspartnern Prof. Dr. František Hartl (University of Reading), Prof. Dr. Bas de Bruin (Universiteit van Amsterdam), Dr. Daniel Paul (WWU Münster), Dr. Tim Gieshoff (Universität Regensburg) und Jan Gerkens (Universität Göttingen) bedanke ich mich für ihre wertvollen Beiträge. Christian Rödl (Universität Regensburg) gilt mein besonderer Dank für die Durchführung der DFT-Rechnungen in Kapitel 3.

Außerdem möchte ich mich bei meinen Kollegen aus dem AK Wolf, unseren Auszubildenden, Bachelorstudenten und Praktikanten bedanken: Dr. Markus Plois, Dr. Jennifer Bissmeyer, Dr. Babak Rezaei Rad, Dr. Stefan Pelties, Dr. Bernd Mühldorf, Vanessa Tomanek, Philipp Büschelberger, Christian Rödl, Anna Kohl, Anne-Kathrin Wiegel, Anna Weigl, Dr. Uttam Chakraborty, Christian Hoidn, Franziska Urban, Nadine Maue, Veronica Scheidler, Julia Leitl, Uli Lennert, Thomas Maier, Gabriele Hierlmeier, Christoph Ziegler, Julia Märsch, Marion Till und Thomas Wagner. Vielen Dank für die gute Zusammenarbeit, die spannenden Diskussionen, Grillabende, Hüttenwochenenden und generell für die tolle Zeit!

Bei den Kollegen der Nachbar-Arbeitskreise Díaz, Garcia, Fleischer, Jacobi und Scheer bedanke ich mich für die schöne gemeinsame Zeit und die gegenseitige Unterstützung.

Außerdem bedanke ich mich bei allen Freunden und Kommilitonen, die mich während des Studiums und der Promotion begleitet haben.

Besonders möchte ich mich bei meiner Familie für ihre ständige Unterstützung während des Studiums und der Promotion bedanken.

Mein größter Dank gilt meiner Freundin Jana für ihre unendliche Geduld und grenzenlose Unterstützung in allen Lebenslagen.

Dirk Herrmann

Beethovenstr. 4
93053 Regensburg

0170/226 3426
dirk_herrmann@gmx.net

Geburtsdatum: 28.11.1986

Ausbildung

Universität Regensburg	**Promotion zum Dr. rer. nat.** (11/2012-08/2018) *Metallorganische Chemie:* „Synthesis, Characterization, and Reactivity of Transition Metal Complexes Stabilized by Naphthalene and Naphthyl-substituted N-heterocyclic Carbenes” *Analyse* der hergestellten Verbindungen mit modernen Methoden (NMR-Spektroskopie, Röntgenkristallographie, Cyclovoltammetrie, UV-Vis-Spektroskopie, Spektroelektrochemie, IR-Spektroskopie, Elementaranalyse, Gaschromatographie) Note: magna cum laude (1.0)
Universität Regensburg	**Master of Science** (10/2011-09/2012) Fächer: Anorganische Chemie / Organische Chemie / Physikalische Chemie Masterarbeit: „Synthesis and Characterization of Hemi-cage Complexes of Copper, Vanadium, Titanium, and Neodymium with a Hexadentate Polypyridyl Ligand” Gesamtnote: 1.1
University of Arkansas	**Bachelor of Science** (08/2010-08/2011) Dual Bachelor Degree im Rahmen des ATLANTIS-Austauschprogramms Kurse in Academic Writing, Basic Economics Cumulative GPA: 4.0 (entspricht Note 1.0)
Universität Regensburg	**Bachelor of Science** (10/2007-09/2011) Bachelorarbeit: Synthese von Elektrolytmaterialien für Lithium-Ionen-Akkus (Institut für Physikalische und Theoretische Chemie; Note 1.0) Gesamtnote: 1.6
Humboldt-Gymnasium Vaterstetten	**Allgemeine Hochschulreife** (2006) Leistungskurse: Mathematik, Englisch Weitere Abiturfächer: Physik, Geschichte Abiturnote: 1.3

Tätigkeiten und Auslandsaufenthalte

Schlenk Metallic Pigments GmbH Barnsdorf / Roth	**Laborleiter Forschung & Entwicklung** (seit 05/2018) Fachliche und disziplinarische Führung eines Teams mit drei Labormitarbeitern Leitung von Projekten in Produkt- und Technologieentwicklung Produktionssupport

Schlenk Metallic Pigments GmbH Barnsdorf / Roth	**Trainee Forschung & Entwicklung** (09/2017-04/2018) Forschung & Entwicklung / Qualitätskontrolle / Produktion / Vertrieb
Universität Regensburg Institut für Anorganische Chemie	**Wissenschaftlicher Mitarbeiter** (11/2012-10/2016) Elektrochemische Messungen für den Arbeitskreis Betreuung von Praktika, Bachelorarbeiten und Forschungspraktikanten Koordination Einkauf von Geräten und Chemikalien IT-Systemadministration und Betreuung der Arbeitskreis-Website
Universität Regensburg Institut für Anorganische Chemie	**Wissenschaftliche Hilfskraft** (01/2012-08/2012) Synthese und Charakterisierung hochempfindlicher Metallkomplexe Gestaltung der Arbeitskreis-Website
University of Arkansas Fayetteville, AR, USA	**Auslandsjahr** (08/2010-08/2011) Im Rahmen des ATLANTIS-Dual-Bachelor-Programms Forschungsprojekt in der anorganischen Chemie
Dublin City University Dublin, Irland	**Auslandssemester** (09/2009-01/2010) Im Rahmen des ERASMUS-Programms
Universität Regensburg Institut für Physikalische und Theoretische Chemie	**Studentische Hilfskraft** (10/2008-08/2010) Herstellung von Additiven für Lithium-Ionen-Akkus Durchführung elektrochemischer Messungen Übersetzung von wissenschaftlichen Artikeln ins Englische
Bayerisches Rotes Kreuz Kreisverband Regensburg	**Zivildienst** (09/2006-05/2007)

Kenntnisse

Qualifikationen	**Statistische Versuchsplanung (DoE)** und allgemeine **Statistik** **Qualitätssicherungsmanagement** in der analytischen Chemie Nachweis der umfassenden **Sachkunde** nach §5 i. V. m. §2 **ChemVerbotsV** **Sicherheit** in Laboratorien
Methodenkenntnisse	**Kanban, 5S, QFD**
EDV-Kenntnisse	**(statistische) Datenanalyse und –visualisierung** (XLStat, Design Expert, Origin) **Messsoftware** zur chemischen Analyse: Elektrochemie, Spektroskopie (NMR, UV-Vis, IR), Kristallographie, Rheologie **Python / HTML / PHP / MySQL** (Grundkenntnisse) **MS Office, ChemOffice** (fundierte Kenntnisse)
Sprachkenntnisse	**Deutsch** (Muttersprache) **Englisch** (verhandlungssicher) **Spanisch** (Grundkenntnisse)

Ehrenamtliche Tätigkeiten

Alumniverein Chemie der Universität Regensburg e.V.: **Mitglied im Vorstand** (seit 2014)

Evang.-Luth. Petrikirche Baldham bei München: **Jugendleiter** (2002-2008)

Betreuung von Kinder- und Jugendgruppen, Freizeiten und weiteren Veranstaltungen
Mitglied im Jugendausschuss der Gemeinde

Regensburg, 10.09.2018

Wissenschaftliche Publikationen

D. Herrmann, C. Rödl, B. de Bruin, F. Hartl, R. Wolf, „Synthesis, electronic structure, and redox properties of the diruthenium sandwich complexes [Cp*Ru(μ-$C_{10}H_8$)RuCp*]x (x = 0, 1+; Cp* = C_5Me_5; $C_{10}H_8$ = naphthalene), *Dalton Trans.* **2018**, *47*, 11058-11069.

S. Pelties, T. Maier, **D. Herrmann**, B. de Bruin, C. Rebreyend, S. Gärtner, I. G. Shenderovich, R. Wolf, „Selective P_4 Activation by a Highly Reduced Cobaltate: Synthesis of Dicobalt Tetraphosphido Complexes", *Chem. Eur. J.* **2017**, *23*, 6094-6102.

A.-K. Wiegel, B. Rezaei Rad, **D. Herrmann**, R. Wolf, „Synthesis and Characterization of Tetra(pyridyl)cyclobutadiene Iron Complexes [Cp*Fe(C_4py_4)]$^-$ (py = 3-pyridyl and 4-pyridyl, Cp* = C_5Me_5), *Z. Anorg. Allg. Chem.* **2015**, *641*, 2065-2070.

S. Pelties, **D. Herrmann**, B. de Bruin, F. Hartl, R. Wolf, „Selective P_4 Activation by an organometallic nickel(I) radical: Formation of a dinuclear nickel(II) tetraphosphide and related di- and trichalcogenides", *Chem. Commun.* **2014**, *50*, 7014-7016.

B. Rezaei Rad, **D. Herrmann**, C. Lescop, R. Wolf, „A tetradentate metalloligand: Synthesis and coordination behaviour of a 2-pyridyl-substituted cyclobutadiene iron complex", *Dalton Trans.* **2014**, *43*, 4247-4250.

Konferenzbeiträge

„Transition Metal Complexes of Naphthyl-substituted *N*-heterocyclic Carbenes"
Posterpräsentation, 27th International Conference on Organometallic Chemistry, 17.-22. Juli 2016, Melbourne, Australien

"Metal Complexes with Naphthyl-substituted N-heterocyclic Carbenes"
Vortrag, wissenschaftliches Kolloquium anorganischer Arbeitskreise, 23.-28. August 2015, Hirschegg, Österreich

"Dinuclear Iron and Ruthenium Complexes Containing Naphthalene as a Bridging Ligand"
Posterpräsentation, 14th International Symposium on Inorganic Ring Systems, 26.-31. Juli 2015, Regensburg

"Naphthalene as a Bridging Ligand in Bimetallic Iron and Ruthenium Complexes"
Vortrag, 13. Ferrocen-Kolloquium, 22.-24. Februar 2015, Leipzig

"Synthesis and Electrochemical Properties of the Diruthenium Sandwich Complex [Cp*Ru(μ-$C_{10}H_8$)RuCp*]"
Posterpräsentation, 17. Vortragstagung der Wöhler-Vereinigung für Anorganische Chemie, 24.-26. September 2014, Saarbrücken

"Synthese niedervalenter Ruthenium-Polyarenkomplexe"
Vortrag, wissenschaftliches Kyolloquium anorganischer Arbeitskreise, 25.-30. August 2013, Hirschegg, Österreich

Eidesstattliche Erklärung

Ich erkläre hiermit an Eides statt, dass ich die vorliegende Arbeit ohne unzulässige Hilfe Dritter und ohne Benutzung anderer als der angegebenen Hilfsmittel angefertigt habe; die aus anderen Quellen direkt oder indirekt übernommenen Daten und Konzepte sind unter Angabe des Literaturzitats gekennzeichnet.

Dirk Herrmann